INFLUENCE OF THE KELVIN-HELMHOLTZ INSTABILITY ON THE PLASMA TRANSPORT AT THE MAGNETOSPHERIC BOUNDARY

A

THESIS

Presented to the Faculty

of the University of Alaska Fairbanks

in Partial Fulfillment of the Requirements

for the Degree of

DOCTOR OF PHILOSOPHY

By

Katariina Nykyri, M.S

Fairbanks, Alaska

December 2002

INFLUENCE OF THE KELVIN-HELMHOLTZ INSTABILITY ON THE PLASMA TRANSPORT AT THE MAGNETOSPHERIC BOUNDARY

By

Katariina Nykyri

RECOMMENDED:

Advisory Committee Chair

Department Head

APPROVED:

Dean, College of Science, Engineering and Mathematics

Dean of the Graduate School

Date

Abstract

The Kelvin-Helmholtz (KH) instability has long been suggested as a mechanism for viscous interaction at the magnetospheric boundary but it was not expected to produce significant mass transport. Satellite observations show that the density, temperature, particle pressure and total pressure of the plasma sheet are strongly correlated with those of the solar wind on a time scale of $\sim$ 2 hours. I present a systematic 2-D study of reconnection in KH flow vortices using MHD and Hall-MHD approximations depending on magnetosheath and magnetospheric plasma and field properties. The presented results show that the Kelvin-Helmholtz instability can be a major plasma transport mechanism during times of strongly northward IMF providing a source of plasma into the low latitude boundary layer and plasma sheet on a time scale of $\sim$ 2 hours. I have also analyzed Equator-S and Cluster satellite data at the dawnside magnetospheric flank and compared these results with MHD simulations in order to distinguish signatures caused by Kelvin-Helmholtz instability. In addition I have discussed typical ionospheric signatures caused by KH instability.

Contents

List of Figures . . . vii
List of Tables . . . xvi
List of Appendices . . . xvii
Acknowledgements . . . xviii

1 Introduction **1**
1.1 Interaction Between Solar Wind and Planetary Environments . . . 2
1.2 Magnetospheric Boundary Layers . . . 5
1.3 The Tearing Mode and Kelvin-Helmholtz Instabilitites . . . 6
1.3.1 The Tearing Mode Instability . . . 7
1.3.2 The Kelvin-Helmholtz Instability (KHI) . . . 8
1.4 Motivation of the Thesis . . . 18
1.5 Outline of the Thesis . . . 23

2 Numerical Method **25**
2.1 MHD Simulations . . . 26
2.2 Hall-MHD Simulations . . . 27

3 Plasma Transport at the Magnetospheric Boundary due to Reconnection in Kelvin-Helmholtz Vortices: MHD approximation **29**
3.1 Introduction . . . 29
3.2 Numerical Method . . . 30
3.3 Results . . . 35
3.4 Discussion and Conclusions . . . 40

4 Influence of the Hall Term on KH Instability and Reconnection inside KH Vortices **42**
4.1 Introduction 42
4.2 Numerical Method 45
4.3 Demonstration of the Hall Effect (Simulation Results Without Background B_z) 49
4.3.1 Magnetic Field Asymmetry (CASE 1) 49
4.3.2 Magnetic Field and Density Asymmetry (CASE 2) 52
4.4 Results of the Plasma Transport 52
4.4.1 Demonstration of Plasma Transport and Growth Rates (CASES 3-7) 56
4.4.2 Comparison of Plasma Transport and Growth Rates Between MHD and Hall-MHD Simulations (CASES 8-12) 57
4.4.3 Demonstration of the Wavelength Effect on the Plasma Transport (CASES 13-17) 60
4.5 Turbulence in the Ion Inertia Scale 63
4.6 Discussion and Conclusions 64

5 Ionospheric Signatures of the Kelvin-Helmholtz Instability **70**
5.1 Introduction 70
5.2 Numerical Method 73
5.2.1 Magnetic field line tracing 74
5.3 Results 75
5.3.1 Comparison of Auroral Bright Spots with MHD Simulation results . 77
5.3.2 Comparison of Super DARN radar observations with MHD Simulation results 78
5.4 Discussion and Conclusions 80

6 Equator-S Observations at the LLBL on March 10th 1998: FTE's or Kelvin-Helmholtz waves? **82**
6.1 Introduction 82
6.2 Numerical Method 83
6.2.1 Data analysis 84

6.2.2 2-D MHD models 84
6.3 Observations 86
6.4 Simulations 88
6.4.1 Kelvin-Helmholtz Instability, KHI 88
6.4.2 Flux Transfer Event, FTE 92
6.5 Discussion and Conclusions 94

7 Cluster Observations of the Kelvin-Helmholtz Instability on 3rd of July 2001 and Comparison with MHD Simulations 97
7.1 Introduction 97
7.2 Observations 101
7.2.1 Current Sheet Crossings 102
7.2.2 Intervals with Reconnection Signatures: Accelerated Flow or Alfvén Waves? 107
7.2.3 Intervals with Accelerated Flow 122
7.2.4 Flux Transfer Events or Reconnection inside the KH Vortices? . . . 140
7.3 Simulations 140
7.4 Discussion and Conclusions 150

8 Summary and Discussion 154
8.1 Results 154
8.1.1 Plasma Transport in KH Vortices in MHD Approximation 155
8.1.2 Reconnection Inside KH Vortices in the Hall-MHD Approximation . 156
8.1.3 Ionospheric Signatures of the Kelvin-Helmholtz Instability 157
8.1.4 Equator-S Observations of the Kelvin-Helmholtz Instability 158
8.1.5 Cluster Observations of the Kelvin-Helmholtz Instability 158
8.2 Summary and Future Work 159

A From Boltzmann Equation to MHD 163

B Magnetic Field Frozen into the Electron Fluid 166

Bibliography 168

List of Figures

1.1 Magnetospheric boundary layers and currents [*Crooker et al., 1999*]. 4

1.2 A) represents velocity shear layer with anti-parallel magnetic field components. When $\mathbf{k} \cdot \mathbf{B} > \mathbf{k} \cdot \mathbf{V}_{\mathbf{Alfvén}}$ KH mode becomes unstable (B). When $\mathbf{k} \cdot \mathbf{B} < \mathbf{k} \cdot \mathbf{V}_{\mathbf{Alfvén}}$ the tearing mode becomes unstable (C). 13

1.3 A) shows snapshot of magnetic field lines, field vectors, and B_z (color code) on the left and plasma velocity (arrows), field lines, and plasma density (color scale) on the right at 358 seconds into the evolution of the KH mode. B) represents current density (left) and reconnection electric field (right). . . . 14

1.4 Data along the slices at $y = 2$ and $y = -3$ of the configurations shown in Figure 1.3. 16

2.1 Task at time $t = t_{n+1}$ uses information from surrounding gridpoints at $t = t_n$ and it's value at the same gridpoint at $t = t_{n-1}$. 28

3.1 Sketch of the evolution of magnetic reconnection in the Kelvin-Helmholtz vortex. 32

3.2 Illustration of basic geometries for the occurrence of KH instabilities on the magnetospheric flank: (a) The **k** vector of the KH mode is in the equatorial plane and the magnetospheric and the magnetosheath fields have a small x component; (b) the magnetospheric and magnetosheath fields are along the z direction and the **k** vector has a component out of the equatorial plane (the upper index s denotes simulation coordinates); (c) illustration of the KH mode at the magnetospheric boundary. In the cases (a) and (b) the angle between the **k** vector and the magnetic field is $90° - \varphi$. 33

3.3 Panel (A) to (C) present the time evolution of Kelvin-Helmholtz wave for CASE 5. The yellow line is the marker for original boundary and yellow asterisks present plasma elements that mark the original boundary $y = 0$. The color measures plasma density, lines are magnetic field lines and arrows are velocity vectors. Panel (D) shows an example of $A_z(t_2)$ versus $-\int \eta J_z dt$ for plot (A) to determine the appropriate boundaries (yellow line in the color plots). 36

3.4 Magnetic field vectors (arrows), magnetic field lines and z-component of the current density (color code) for CASE 5 at time $\sim 74.5\ \tau_A$. 37

3.5 Mass entry velocity as a function of time for CASE 5 ($\varphi = 10\ °$ and magnetosheath field strength 24 nT). 39

3.6 Maximum mass entry velocities with error bars as a function of φ for the cases of Table 3.1. The scale on the right axis presents the equivalent diffusion coefficient assuming a boundary layer width of 1000 km. 39

4.1 KH vortex at $t/\tau_A \approx 60$ and at $t/\tau_A \approx 82$. Lines are magnetic field lines projected to x, y -plane and arrows are electron velocity vectors. Color code represents electron current (left) and z component of the magnetic field (right). 50

4.2 KH vortex at $t/\tau_A \approx 60$ and at $t/\tau_A \approx 82$. Lines are magnetic field lines projected to x, y -plane and arrows are plasma velocity vectors. Color code represents ion current (left) and total current (right). 51

4.3 KH vortex at $t/\tau_A \approx 63$ and at $t/\tau_A \approx 81$. Lines are magnetic field lines projected to x, y -plane and arrows are electron velocity vectors. Color code represents plasma density. 53

4.4 KH vortex at $t/\tau_A \approx 63$ and at $t/\tau_A \approx 81$. Lines are magnetic field lines projected to x, y -plane and arrows are electron velocity vectors. Color code represents electron current (left) and z component of the magnetic field (right). 54

4.5 KH vortex at $t/\tau_A \approx 63$ and at $t/\tau_A \approx 81$. Lines are magnetic field lines projected to x, y -plane and arrows are plasma velocity vectors. Color code represents ion current (left) and total current (right). 55

4.6 KH vortex at $t/\tau_A \approx 62$ and at $t/\tau_A \approx 107$ for CASE 5. Lines are magnetic field lines projected to x, y -plane and arrows are electron velocity vectors. Color code represents plasma density (upper panel) and z-component of the magnetic field (lower panel). 58

4.7 A) Mass transport velocity as a function of time for $\varphi = 10°$. B) Mass transport velocity as a function of φ. C) Growth of KH instability for $\varphi = 3°, 5°, 10°, 15°$ and $25°$. 59

4.8 A) Mass transport velocity as a function of φ for MHD and Hall-MHD. B) Growth of KH instability for $\varphi = 3°, 5°, 10°, 15°$ and $25°$. for Hall-MHD approximation. C) Growth of KH instability for MHD approximation. . . . 61

4.9 A) Mass transport velocity as a function of φ for short wavelength ($ka = 0.25$, $\lambda = 0.4R_E$) Hall-MHD. B) Growth rates of KH instability for $\varphi = 3°$, $5°, 10°, 15°$ for Hall-MHD approximation. 62

4.10 KH vortex for $\varphi = 5$ at $t/\tau_A \approx 93$. A) shows electron velocity (arrows) and plasma density (color code). B) represents z-component of the magnetic field. C) is a magnified domain of figure A). 65

4.11 A) is a magnified domain of figure 4.10 A). B) shows plasma velocity vectors (arrows), and ion current (color code) on left and total current on right. C) depicts magnetic field vectors (arrows) and electron current (color code) on left, and z-component of the plasma velocity on right. 66

4.12 A) represents comparison of KH growth rates between theory and Hall-MHD and MHD simulations for $ka = 2\pi/a\lambda = 0.12$. B) shows comparison between KH growth rates between theory and Hall-MHD simulations for $ka = 0.25$. 68

5.1 KH-vortex at the magnetospheric inertial frame at $\tau_A = 51$ (A), at $\tau_A = 60$ (B), and at $\tau_A = 71$ (C). 76

5.2 Polar UVI image of auroral luminosity on March 10 1998 at 14:12:28 UT. . 79

6.1 Plasma and magnetic field observations in GSE coordinates on March 10, 1998 from 13:00 to 13:36 UT. Shading illustrates regions with excellent Walen relation and de HT frame. Figure 6.1b has test of the Walen relation (left) and HT frame (right) during the same time interval as in Figure 6.1a. . . . 87

6.2 Tests of the Walen relation (left) and HT frame (right) during the interval from 13:17:29 UT to 13:17:48 UT on March 10, 1998 89

6.3 Results from the MHD simulation at t = 116. The left hand side shows magnetic field vectors and the z-component of the current density (color code). The right hand side depicts plasma velocity and plasma density (color code). Black lines represent magnetic field lines projected into x, y -plane. . 90

6.4 A) has plasma and magnetic field properties in cut through simulation box at y = -13.6 at t = 406 s. The upper panel panel of B) has the test for the Walen relation (left) and HT frame (right) from x = -20.0 to x = 20.0. The lower panel in B) has the test for the Walen relation (left) and HT frame (right) from x = -7.8 to x = -0.2. 91

6.5 Time evolution of the 2-D magnetic reconnection. Arrows represent plasma velocity, black lines are magnetic field lines and the background color is B_y-component of the magnetic field. 93

6.6 A) represents measurements of the magnetic field and plasma properties in simulation box at x=6.0, y = 2.0 and z = 65.0 as a function of time. B) has corresponding tests for the Walen relation and HT frame. 95

7.1 Cluster orbits during polar cusp crossings (right) and tail crossings (left). The size of the perfect tetrahedron in the cusp is 600 km and in the tail, 2000 km *[European Space Agency, 2001]*. 100
7.2 A) represents plasma (left) and magnetic field (right) observations along Cluster orbit on 3rd of July 2001 between 00:00-12:00 UT. The shaded regions indicate intervals when SC1 observed current sheets. The upper right box shows the Cluster constellation. B) shows boundary normal directions (black vectors) and de HT velocities (red vectors) during shaded intervals. 104
7.3 A) represents plasma (left) and magnetic field (right) observations along Cluster orbit on 3rd of July 2001 between 00:00-12:00 UT. The shaded regions indicate intervals when SC3 observed current sheets. The upper right box shows the Cluster constellation. B) shows boundary normal directions and de HT velocities during the shaded intervals. 105
7.4 A) represents plasma (left) and magnetic field (right) observations along Cluster orbit on 3rd of July 2001 between 00:00-12:00 UT. The shaded regions indicate intervals when SC4 observed current sheets. The upper right box shows the Cluster constellation. B) shows boundary normal directions and de HT velocities during the shaded intervals. 106
7.5 Plasma (left) and magnetic field (right) observations along Cluster orbit on 3rd of July 2001 between 05:00-8:30 UT. The shaded regions indicate intervals when SC1 observed reconnection signatures. The upper right box shows the Cluster constellation. 108
7.6 Boundary normal directions (black vectors) and de HT velocities (red vectors) during the intervals (illustrated in Figure 7.5) with reconnection signatures observed by SC1 between 05:00-8:30 UT and plotted along the trajectory of SC3, SC1, and SC4. 109
7.7 Plasma (left) and magnetic field (right) observations along Cluster orbit on 3rd of July 2001 for brief 20 s period between 06:40-06:40:22 UT in variance E coordinates chosen by SC1. The upper right box shows the Cluster constellation and de HT frame velocity in GSM and in variance E coordinates observed by SC1. 110

7.8 Walen relations (left) and de HT frames (right) observed by SC1 for a 6.5 minute period between 6:36-06:42:30 UT in A) and for a brief 20 second period in B). 112

7.9 Plasma (left) and magnetic field (right) observations along Cluster orbit on 3rd of July 2001 for brief 20 s period between 06:40-06:40:22 UT in variance E coordinates chosen by SC3. The upper right box shows the Cluster constellation and de HT frame velocity in GSM and in variance E coordinates observed by SC3. 114

7.10 Walen relations (left) and de HT frames (right) observed by SC3 for a 6.5 minute period between 6:36-06:42:30 UT in A) and for a brief 20 second period in B). 115

7.11 Plasma (left) and magnetic field (right) observations along Cluster orbit on 3rd of July 2001 for brief 20 s period between 06:40-06:40:22 UT in variance E coordinates chosen by SC4. The upper right box shows the Cluster constellation and de HT frame velocity in GSM and in variance E coordinates observed by SC4. 116

7.12 Walen relations (left) and de HT frames (right) observed by SC4 for a 6.5 minute period between 6:36-06:42:30 UT in A) and for a brief 20 second period in B). 118

7.13 Cluster plasma (left) and magnetic field (right) observations between 6:36-06:42:30 UT. The shaded regions indicate regions with reconnection signatures. 120

7.14 The data shown in this figure are the same as in Figure 7.4 but the shaded intervals that indicate reconnection signatures are here based on SC3 data. 121

7.15 Boundary normal directions (black vectors) and de HT velocities (red vectors) during the intervals (illustrated in Figure 7.7) with reconnection signatures observed by SC3 between 05:00-8:30 UT and plotted along the trajectory of SC3, SC1 and SC4. 123

7.16 A) Represents Cluster plasma (left) and magnetic field (right) observations between 04:54:00-06:06:00 UT. The shaded regions indicate regions with reconnection signatures and accelerated flow observed by SC1. B) represents boundary normal directions and de HT frame velocities during shaded intervals along the trajectory of SC1. 124

7.17 A) Represents Cluster plasma (left) and magnetic field (right) observations between 05:40:06-05:40:27 UT in variance E coordinates determined by SC1. The top right boxes show the Cluster constellation and de HT frame velocities in GSM and in variance E coordinates. B) represents the Walen relation (left) and de HT frame (right) for this interval. 126

7.18 A) Represents Cluster plasma (left) and magnetic field (right) observations between 05:36-05:42 UT in variance E coordinates determined by SC1. The top right boxes show the Cluster constellation and de HT frame velocities in GSM and in variance E coordinates. B) represents the Walen relation (left) and de HT frame (right) for this interval. 127

7.19 A) Represents Cluster plasma (left) and magnetic field (right) observations between 05:40:06-05:40:27 UT in variance E coordinates determined by SC3. The top right boxes show the Cluster constellation and de HT frame velocities in GSM and in variance E coordinates. B) shows the Walen relation (left) and de HT frame (right) for this interval. C) Represents Cluster plasma and magnetic field observations between 05:36-05:42 UT in variance E coordinates determined by SC3. D) represents the Walen relation (left) and de HT frame (right) for this interval. 129

7.20 A) Represents Cluster plasma (left) and magnetic field (right) observations between 05:40:06-05:40:27 UT in variance E coordinates determined by SC4. The top right boxes show the Cluster constellation and de HT frame velocities in GSM and in variance E coordinates. B) Represents Cluster plasma and magnetic field observations between 05:36-05:42 UT in variance E coordinates determined by SC4. 131

7.21 A) Represents Cluster plasma (left) and magnetic field (right) observations between 05:48:34-05:48:54 UT in variance E coordinates determined by SC1. The top right boxes show the Cluster constellation and de HT frame velocities in GSM and in variance E coordinates. B) represents the Walen relation (left) and de HT frame (right) for this interval. 133

7.22 A) Represents Cluster plasma (left) and magnetic field (right) observations between 05:45-05:51 UT in variance E coordinates determined by SC1. The top right boxes show the Cluster constellation and de HT frame velocities in GSM and in variance E coordinates. B) represents the Walen relation (left) and de HT frame (right) for this interval. 134

7.23 A) Represents Cluster plasma (left) and magnetic field (right) observations between 05:48:34-05:48:54 UT in variance E coordinates determined by SC3. The top right boxes show the Cluster constellation and de HT frame velocities in GSM and in variance E coordinates. B) represents the Walen relation (left) and de HT frame (right) for this interval. 136

7.24 A) Represents Cluster plasma (left) and magnetic field (right) observations between 05:45-05:51 UT in variance E coordinates determined by SC3. The top right boxes show the Cluster constellation and de HT frame velocities in GSM and in variance E coordinates. B) represents the Walen relation (left) and de HT frame (right) for this interval. 137

7.25 A) Represents Cluster plasma (left) and magnetic field (right) observations between 05:48:34-05:48:54 UT in variance E coordinates determined by SC4. The top right boxes show the Cluster constellation and de HT frame velocities in GSM and in variance E coordinates. B) Represents Cluster plasma and magnetic field observations between 05:45-05:51 UT in variance E coordinates determined by SC4. 138

7.26 A) Represents Cluster plasma (left) and magnetic field (right) observations between 05:50:38-05:51:02 UT in variance E coordinates determined by SC1. The top right boxes show the Cluster constellation and de HT frame velocities in GSM and in variance E coordinates. B) represents the Walen relation (left) and de HT frame (right) for this interval. 141

7.27 A) Represents Cluster plasma (left) and magnetic field (right) observations between 05:50:38-05:51:02 UT in variance E coordinates determined by SC3. The top right boxes show the Cluster constellation and de HT frame velocities in GSM and in variance E coordinates. B) represents the Walen relation (left) and de HT frame (right) for this interval. 142

7.28 Represents Cluster plasma (left) and magnetic field (right) observations between 04:54-06:06 UT in variance E coordinates determined by SC1. Note the bipolar signatures in normal components of the magnetic field, b_i. . . . 143

7.29 Simulation geometry. 145

7.30 Kelvin-Helmholtz vortex at $t \sim 110$. Magnetic field (arrows) and z-component of the current density (color code) are plotted on left and plasma velocity (arrows) and density (color code) are represented on the right. 147

7.31 A) represents plasma and magnetic field measurements observed by virtual spacecraft traveling through the simulation box (Figure 7.22) from x = -20 to x = 20 at y = 1.2. Walen relation and de Hoffman teller frame for this interval are plotted in B). 148

7.32 A) represents plasma and magnetic field measurements observed by virtual spacecraft traveling through the simulation box (Figure 7.30) from x = -20 to $x = 20$ at $y = 3.2$. The Walen relation (left) and de HT frame (right) for this interval are plotted in B). 149

7.33 A) shows Walen relation and de HT frame measured by virtual spacecraft at $y = 1.2$ from $x = 14.2$ to $x = 15.8$. B) shows Walen relation and de HT frame measured by virtual spacecraft at $y = 3.2$ from $x = 11.2$ to $x = 12.8$. 151

List of Tables

3.1 Simulation Runs 32
3.2 Simulation Normalization 34

4.1 Simulation Normalization 46
4.2 Simulation Runs 48

5.1 Input for magnetic field line tracing 75
5.2 Simulation Results 77

6.1 Properties of reconnection and the KH instability. 94

List of Tables

Acknowledgements

In the immortal words of Finnish movie director, Aki Kaurismäki, "I would first like to thank myself and then the judges". The past four years in Fairbanks, Alaska have been the best years of my life. Even though I love my family and friends in Finland very much, I think it is necessary for the personal growth of a human being to leave the safe environment of home and move to a different culture for a while. Indeed, this was the case for me. I have been very fortunate to meet interesting and kind people from all around the world here at the UAF. Many of these people have become very close friends of mine and therefore it is little sad to leave Fairbanks.

First I would like to thank Professor Antonius Otto, my thesis advisor, for his great intellect, outstanding knowledge in our field and beyond, constant encouragement, advice, support, great sense of humor, and enthusiasm towards my work during past three years. I have been extremely fortunate to study space science under his guidance. I think he is one of the smartest people on this planet and should get the Nobel Prize. I would also like to thank Isabel, Antonius' wife, for inviting students to their house and organizing great parties. While getting a Ph.D, it is important also, to relax and enjoy good wine with friends. Several Thanksgiving dinners, barbecues and Friday "meetings" most definitely served this purpose. Thank you for these!

My sincere appreciation also goes to Professor Dirk Lummerzheim, whose helpful suggestions improved the quality of my thesis. I would also like to thank him for his interesting conversations of the aurora, space science and aviation, as well as his help and advice for using his programs developed for the Polar UVI pictures.

I would also like to thank the other committee members– Professors John Olson, Roger Smith and Brenton Watkins– for their invaluable time spent in committee meetings and reading this document. Also, the math physics class taught by Professor Olson was wonderful and helped me to understand for the first time the essence of the calculus of variations.

I am also very grateful for Professors Jörg Büchner and Berndt Nikutowski at the Max Planck Institute für Aeronomie in Germany for inviting me to work there with the Cluster satellite data on fall 2001. I would also like to acknowledge their collaboration with the Equator-S and Cluster observations, as well as thank them for the wonderful time in

Germany. In addition I would like to thank Professor Wolfgang Baumjohann for providing the Equator-S magnetometer data, as well as Dr. Lynn Kistler and Dr. Chris Mouikis who provided the Equator-S plasma velocity moments.

My deep thanks go to Professors André Balogh and Karl-Heinz Glaßmeier for providing the Cluster magnetometer data, and to Professor Henri Rème for the opportunity to use the plasma velocity moments from the Cluster CIS instrument. I would also like to thank Dr. Harri Laakso for the valuable discussions of the Cluster observations.

My special thanks go to my high school math teacher, Pentti Hangasmaa, who is an exceptional teacher and who's talent inspired me, not only to appreciate the beauty of mathematics but also to study and work hard.

My gratitude also extends to Professors Tuija Pulkkinen and Hannu Koskinen who opened the door of Space Physics for me when I was studying theoretical physics at the University of Helsinki in Finland.

I am greatly indebted to my husband, Mikko Nykyri for his love, continuous support, encouragement, his knowledge in computers and operating systems, and unwavering belief in my abilities. Being separated by Atlantic ocean for four years is tough, but on the other hand, phone companies need money too. As a compromise between flying to Finland or to Alaska, we have spent our Christmas holidays in warm California, Arizona, Nevada and Mexico–which is not a bad idea when considering the temperature, and amount of sunlight available in Fairbanks and in Helsinki during Christmas time. This way I also had an opportunity to travel in the US: hike the Grand Canyon, visit the ghost town and win a grand in Black Jack in Las Vegas. I also learned that Malibu beach is not filled with life guards wearing red bathing suites.

I would also like to thank my mom, Lahja Havansi, from whom I inherited my creativity and an attitude which prevents me to leave the office before I have completed the task I set for myself (Thank god for coffee, Red Bull and chocolate). I guess one can also call this Finnish SISU. Thank you mom! Now I have to thank my father, Kari Korkiakoski, as well. Thank you father for constantly reminding me that it is important for mental well-being to do regular exercise and enjoy good beer. Now when I have my Ph.D my next goal is to win you in Marathon. I beat you in Chess already when I was 9. I would also like to thank my wonderful sisters Kristiina and Johanna Postareff, whose continuous support, encouragement and colorful lifestyles reminded me that there is life outside the world of physics. I would also like to thank Pär-Erik Postareff and Kia Postareff, my sisters children for being so adorable, and who might become future scientists (Pärre, I know you want to become a rock star but wouldn't it be much cooler to figure out the Grand Unified Theory?).

My sincere appreciation also goes to Reijo Nykyri, my father in law, who is very good in English language and who helped me to find grammar mistakes in this thesis. I would also like to send my kind thanks to Irja Nykyri, my mother in law, who takes good care of me when I am in Finland and for raising such a wonderful son.

I am very thankful for my fellow graduate students for making it a delight to arrive at the office every morning. I have been very fortunate to share the office with the coolest people in the world! In particular my thanks go to Laura Peticolas–who made me feel at home when I first started working at the Geophysical Institute, and with whom I discussed lot's of physics problems and who organized great parties; to Fred Hall–the fresh prince of Fairbanks whose vast knowledge in Linux, physics, rap music, and Star Trek trivia broadened my horizons; to John Styers–whose "Wildebeest incident" and "going deaf" jokes made me laugh even if my code had just stopped running, and who helped me to formulate some of the sentences in this thesis; to Cliff Cole–who is always on the good mood and who kept me informed of the developments of the US politics. I also want to thank Karen Remick–a fellow evening time worker, with whom I often had late night dinners and who conveniently always had coke in the fridge and who helped me to drive in the down town Fairbanks (believe me, there is a down town in Fairbanks:)); Fernanda SaoSabbas–with whom I was buried in the library for two months studying for the comprehensive exams and with whom I had great discussions starting from hair coloring to the general relativity; Dana Moudry–for kindly letting me borrow her Latex books and helping with Latex problems; Kim Nielsen–with whom I spent numerous Wednesday evenings relaxing my brain at the University pub and in the Marlin; and last but not least I would like to thank Keith Carney–for making the best cheese cake in the world and for bringing me cookies and movies when I needed a break from writing this thesis. Our friendship made these years of my graduate study unforgettable.

My sincere thanks go also to Irene Downes, the administrative assistant of the physics department and a good friend, who made me feel welcome when I first moved to Fairbanks and who invited students to her house for dinner and movie nights. Thank you for taking such a good care of us!

I would also like to thank John Petersen, an excellent teacher, who was teaching me and other graduate students during our first year in the program, how to teach physics laboratory experiments to undergraduate students. Even a theoretician should know how to determine the permeability of free space with the use of a current balance! My kind thanks go also to Professor Channon Price, who is able to solve any physics problem there exists. When I was studying for physics comprehensive exams, and got stucked with a problem I knew where to find help.

This thesis work was supported by grants from the National Aeronautics and Space Administration, the National Science Foundation, The Finnish Cultural Foundation, The Finnish Academy and The Jenny and Antti Wihuri Foundation of Finland. The computations were supported at the Arctic Region Supercomputer Center. Without the support of the Finnish Cultural Foundation and Finnish Academy I could not have been able to afford to live in an apartment with running water. Thank you for making my life comfortable!

Chapter 1

Introduction

The most beautiful manifestation of the relationship between Sun and Earth, the northern lights, can be seen during the dark nights in the northern sky (and southern sky in southern hemisphere). The Latin term for northern lights –Aurora Borealis–was first used by Galileo Galilei on 1619, which meant "the goddess of the dawn." Being Italian, Galileo probably never saw the aurora himself, since the phenomena occurring in the middle of the night, and in high latitudes hardly resembles dawn.

Therefore, it is not surprising at all that the people of the north didn't use the term aurora from the "burning, trembling and dancing arcs across the sky", but tied the auroral phenomena closely to their own mythological beliefs. Norse mythology calls aurora the "bridge Bifrost" across which the gods could travel from Heaven to Earth. Finnish mythology refers to river, Rutja, which stood in fire marking the boundary between the realms of the living and the dead. A Norwegian folk-legend suggest that the aurora is a celestial dance by souls of dead maidens. Some Eskimo people in Northern America believe that aurora is produced by spirits playing a game of celestial football with the skull of a walrus (and some believe that spirits of walrus were using human skulls for their game!!). The Australian aborigines have also reported the "Aurora Australis." as a "dance of gods across the sky." The Chinese dragon legends may also have originated from the aurora–as the twisting, snake-like auroral arcs are observed moving rapidly in the sky [*Rasinkangas et al.*, 1998].

There are several other descriptions of the aurora by people of different nationalities and tribes within these nationalities throughout history. However, common features for all these auroral interpretations is a description of movement and light, which is also emphasized in a modern Finnish word for aurora, "revontuli", which means fox-fire. The cause for these beautiful auroral displays lies within a complicated interaction between magnetized solar wind and Earth's magnetic field.

In 1601 English physician and natural philosopher William Gilbert was the first one to illustrate that Earth behaves like a giant magnet [*Kivelson and Russel*, 1995]. The magnetic field points down towards the surface of the Earth in the northern hemisphere, and away from it in the southern hemisphere. Without the influence of the sun –or to be more precise–, without the influence of the magnetized solar wind, Earth's magnetosphere would really be more spherical. Biermann explained in 1951 that comets have two tails due to the continuous stream of particles from the sun, one tail following the orbit of the comet and the other one lagging behind about $5°$ from the radial direction. In 1957 Hannes Alfvén postulated that the solar wind was magnetized, and in 1958 E. W. Parker presented the first theory for the supersonic, continuous solar wind [*Kivelson and Russel*, 1995]. When the space race begun in late 1950s between Russians and Americans, several satellites were launched to near Earth space, and the observations made by these space crafts confirmed Parker's solution for supersonic solar wind to be true. Another surprise was the discovery of the Earth's elongated magnetotail formed by the interaction of the Earth's dipolar magnetic field and magnetized solar wind. The following years of space exploration were flowering with discoveries: bow shock; magnetospheric boundary layers; field aligned currents above the auroral regions; ionosphere. By now, spacecraft have passed all the planets in our solar system except for Pluto, and have revealed that also Mercury, Jupiter, Saturn, Uranus and Neptune all have intrinsic magnetic fields and thus magnetospheres.

1.1 Interaction Between Solar Wind and Planetary Environments

Dynamical processes between magnetized solar wind and planetary magnetic fields determine the plasma, momentum and energy transport from the solar wind into the magnetospheres. Since the magnitude of the intrinsic magnetic field, rotation period, tilt of the rotation axis, mass, dipole tilt and distance from the sun vary for different planets significantly, also the plasma environments of these planets can be very dissimilar. The plasma in Earth's magnetosphere consists mainly on protons and electrons, and the main source for these particles are solar wind and terrestrial ionosphere. For Jupiter the primary plasma source is the volcanic activity on its moon, Io.

The solar wind is the highly conducting, expanding solar corona, where electrons and protons are moving closely together with solar magnetic field frozen into it. This frozen-in condition can break in reconnection where two plasma elements that initially located in the same flux tube can move into a different flux tubes. Parker's solution for solar wind expansion was based on the idea, that solar corona cannot be in a static equilibrium but either collapses or expands. Parker's assumption of plasma isothermality and simplistic equation of state causes his solution to predict higher density values at 1 AU than observed. However, the essential point in his solution is that at certain point, the subsonic solar wind turns into a supersonic solar wind flow. When solar wind is approaching a planet, the pressure is enhanced in front of the obstacle. This pressure increase tries to redistribute itself by a compressional wave. Since the solar wind speed is faster than the speed of the compressional wave, a shock front is formed which, in turn, will slow, heat, and deflect plasma around the planet [*Kivelson and Russel*, 1995]. The obstacle for solar wind flow is not the actual planet but its magnetosphere or ionosphere. The word magnetosphere is also extended to surroundings of unmagnetized planets like Venus and Mars, but even in these cases the solar wind flow is not free but is deflected by their ionospheres. In addition, our solar system forms a magnetospheric-like cavity in the interstellar medium, similarly to our milky way -galaxy in the intergalactic medium.

The solar wind starts already deviating from its original direction at the bow shock where it's velocity is drastically reduced. The magnetosheath is a turbulent region between the bow shock and the magnetosphere. The location of the outer boundary of magnetosphere, magnetopause, is determined by the pressure balance between the dynamic pressure of the solar wind and the magnetic pressure of the planet's magnetic field. Inside the magnetopause the magnetic field becomes stronger and more steady. Since the magnetic field is changing direction at the magnetopause and at the tail plasma sheet there have to exist currents according to $\nabla \times \mathbf{B} = \mu_0 \mathbf{J}$.

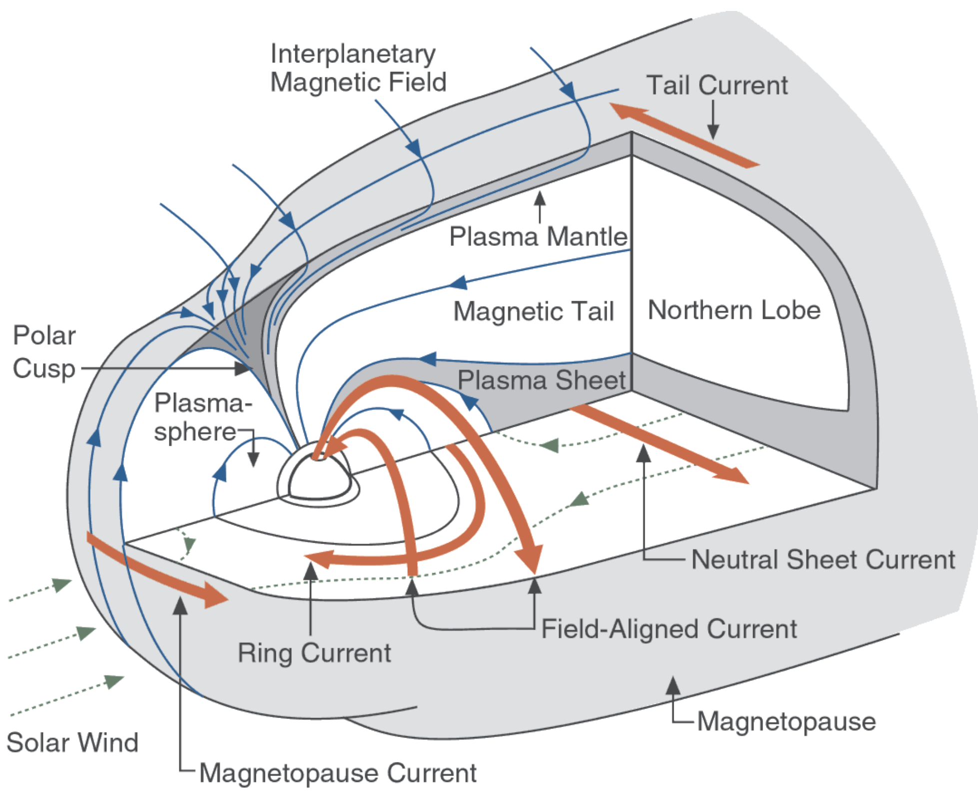

Figure 1.1. Magnetospheric boundary layers and currents [*Crooker et al.*, 1999].

1.2 Magnetospheric Boundary Layers

The magnetopause is not a "plasma proof" shield, but magnetosheath material can enter the boundary layers of the magnetosphere. There are various instabilities that can contribute to this transport at the magnetopause but most important, macroscopic processes are magnetic reconnection [*Dungey*, 1961] and viscous interaction [*Axford and Hines*, 1961; *Miura*, 1984].

Plasma entering the magnetosphere doesn't get evenly distributed, but forms regions of different temperatures and densities. Figure 1.1 presents the magnetospheric boundary and current layers. According to plasma flow, magnetic field and plasma composition, Earth's magnetosphere can be divided into the magnetopause current layer, the low latitude boundary layer (LLBL), the high latitude boundary layer or plasma mantle (HLBL), the entry layer, the cusp, the magnetotail current layer, the plasma sheet boundary layer, tail lobes, the plasma sheet, the plasma sphere, and the ring current.

In this thesis I will concentrate on the processes at the low latitude boundary layer. The low latitude boundary layer, LLBL, contains a mix of magnetosheath and magnetospheric plasma, and the flow velocities in LLBL have intermediate values from those of the magnetosheath and the magnetosphere. During dayside reconnection the entire LLBL is on open field lines, while for northward IMF its inner part may be on closed field lines [*Scholer and Treumann*, 1997]. Magnetic reconnection, impulsive penetration, and wave effects have been considered as plausible formation mechanisms of the LLBL, and have been discussed by several authors [*Song and Russell*, 1992; *Miura*, 1984, 1992, 1995; *Thomas and Winske*, 1991, 1993; *Fujimoto and Terasawa*, 1994, 1995; *Scholer and Treumann*, 1997]. For southward IMF the formation of LLBL is well understood by dayside reconnection [*Sonnerup et al.*, 1981; *La Belle-Hamer et al.*, 1988; *Lee and Fu*, 1986]. For northward IMF, high latitude reconnection has been the most dominant candidate for formation of the LLBL [*Scholer and Treumann*, 1997]. According to *Scholer and Treumann* [1997] anomalous diffusive processes cannot sustain the LLBL since gradient driven non-classical processes, drift and current instabilities become weaker towards the flanks of the magnetopause. The Kelvin-Helmholtz instability can operate along flanks of the magnetopause under certain conditions and has been suggested to cause viscous momentum transport and be the source of the LLBL during northward IMF conditions [*Miura*, 1984, 1992, 1995; *Thomas and Winske*, 1991, 1993;

Fujimoto and Terasawa, 1994, 1995]. However, *Scholer and Treumann* [1997] conclude that although the KH instability might provide some mixing at the magnetopause, it has not yet been convincingly identified as being important for the presence and dynamics of the LLBL. The KH mode is an ideal plasma instability and has therefore not been expected to produce a significant mass transport. This thesis will provide new evidence of importance of the Kelvin-Helmholtz Instability for being one of the main generators of the low latitude boundary layer and source for cold dense plasma sheet during northward IMF conditions.

1.3 The Tearing Mode and Kelvin-Helmholtz Instabilitites

Instabilitity is a growing amplitude of a small perturbation from an initial equilibrium. These non-equilibrium stages arise from the sources of free energy, that in the near Earth space are available due to the interaction of the solar wind and Earth's magnetosphere. On macroscopic scale mass, momentum and energy transport from the solar wind generates gradients and inhomogeneities of the plasma, and on the microscopic scale it leads to deformations of the local plasma distribution functions [*Treumann and Baumjohann*, 1997]. The most important instabilities on macroscopic scales are the tearing mode and Kelvin-Helmholtz (KH) instability. They are of fundamental importance for many space plasma system varying from our magnetosphere to stellar atmospheres, active galactic nuclei and accretion disks.

The plasma, energy and momentum transport from the solar wind into the magnetosphere is well understood for southward interplanetary magnetic field, IMF, as the magnetic merging at the subsolar magnetopause opens the Earth's magnetic field. Opened magnetic flux is pulled by solar wind into the Earth's magnetotail, and it piles up until an unloading process, a magnetospheric substorm releases this energy. A beautiful end result of this unloading process can be seen as intensified aurora in high latitudes.

For northward IMF the plasma transport has been a long standing mystery. KH instability has been observed operating at the magnetospheric flanks by several satellite measurements and it's contribution to energy and momentum transport is widely studied and understood. However, the KH mode is an ideal instability, i.e., it cannot transport mass across magnetic field lines or alter the magnetic topology. The work presented in this thesis will illustrate that KH instability can be a major mass transport mechanism during periods of strongly northward IMF. In order to comprehend the plasma transport associated with KH modes it's important to understand the basic properties of the tearing mode and Kelvin-Helmholtz Instability.

1.3.1 The Tearing Mode Instability

The free energy for tearing instability is the magnetic energy that becomes available due to the magnetic shear of the anti-parallel magnetic field components. In ideal MHD the magnetic field is frozen into a plasma flow and the Ohm's law can be expressed as $\mathbf{E} = -\mathbf{v} \times \mathbf{B}$. Diffusion and annihilation of magnetic fields is only possible when the plasma is non-ideal, i.e., due the resistivity, η. The resistivity arises due to the collisional term, $\eta\mathbf{J}$, in generalized Ohm's law, with $\eta = \frac{m_e \nu_c}{n_e e^2}$, where ν_c is the collision frequency. By using Ampere's law (without displacement current), Faraday's law and resistive Ohm's law, $\mathbf{E} = \eta\mathbf{J} - \mathbf{v} \times \mathbf{B}$, one can derive the induction equation of the magnetic field (assuming that η is constant):

$$\frac{\partial \mathbf{B}}{\partial t} = \nabla \times (\mathbf{v} \times \mathbf{B}) + \frac{\mathbf{1}}{\mu_{\mathbf{0}}\sigma}\nabla^{\mathbf{2}}\mathbf{B} \tag{1.1}$$

In diffusion region the convective, $\nabla\times(\mathbf{v}\times\mathbf{B})$, term becomes negligible and the induction equation becomes diffusion equation:

$$\frac{\partial \mathbf{B}}{\partial t} = \frac{1}{\mu_0\sigma}\nabla^2\mathbf{B} \tag{1.2}$$

By replacing the temporal and spatial derivatives, with τ_d and L_0 respectively, one can derive the characteristic diffusion time of the magnetic field,$\tau_d = L^2\sigma\mu_0$.

The resistive tearing instability happens on a time scale that is much larger than the Alfvén transit time,$\tau_A = L_0/v_A$, and is much smaller than the diffusion time, τ_d such that the Lundqvist number $R = \tau_d/\tau_A >> 1$. It develops in a small region where oppositely orientated magnetic field components, ($\mathbf{B_1} = -\mathbf{B_2}$), approach each other. In this region the wave vector of the instability is perpendicular to the magnetic field, $\mathbf{k} \cdot \mathbf{B}$ =0, and the resistivity is non-zero. The tearing mode leads to formation of magnetic islands which grow during the linear phase with an exponential growth rate, the maximum growth rate scales as $\sqrt{\eta}$ [*Chen*, 1997]. Tearing mode can also operate on the collisionless regime, where the reconnection is caused by kinetic instabilities [*Treumann and Baumjohann*, 1997].

The tearing mode operates in a variety of plasma physical fields. In the Earth's magnetosphere the most widely studied tearing mode areas are the dayside reconnection [*Sonnerup et al.*, 1981; *La Belle-Hamer et al.*, 1988; *Lee and Fu*, 1986], flux transfer events [*Lee and Fu*, 1985; *Scholer*, 1988; *Sibeck and Smith*, 1992; *Elphic*, 1995; *Otto and Arendt*, 1991; *Lee et al.*, 1993] and tail reconnection [*Kan*, 1998; *Scholer et al.*, 1991; *Scholer and Otto*, 1991]. There are also numerous simulation and theory studies of magnetic reconnection assuming different plasma approximations and geometries [*Birn and Hesse*, 2001; *Hesse et al.*, 2001; *Liu and Hu*, 1988; *Ma and Bhattacharjee*, 2001; *Pritchett*, 2001; *Shay et al.*, 2001; *Drake*, 1995; *Lee*, 1995; *Schindler*, 1995; *Schindler et al.*, 1987; *Otto*, 1989, 1990b; *Otto et al.*, 1990; *Scholer and Otto*, 1991; *Scholer et al.*, 1991; *Otto*, 1992; *Ma et al.*, 1994; *La Belle-Hamer et al.*, 1995; *Ma et al.*, 1995; *Otto*, 1995a,b,c; *Otto et al.*, 1995; *Wiechen et al.*, 1995, 1996; *Chen et al.*, 1997; *Wiechen et al.*, 1997; *Otto*, 1998; *Schopper and Otto*, 1999; *Otto*, 2001; *Birn et al.*, 2001].

1.3.2 The Kelvin-Helmholtz Instability (KHI)

The free energy for the Kelvin-Helmholtz instability is the kinetic energy that becomes available due to the velocity shear of anti parallel velocity components ($\mathbf{V_1} = -\mathbf{V_2}$) across a plane boundary. An ordinary non viscous fluid is always KH unstable in the presence of the velocity shear, and its growth rate, for a simple case with uniform density, is $q = kV_0/2$, where $V_0 = (\mathbf{V_1} - \mathbf{V_2})$ is the difference of the velocities across the shear flow layer and $k = 2\pi/\lambda$ is the wave number. This indicates that short wave lengths (small λ) grow fastest, and that large velocity shear increases the growth rate. Fluid Kelvin-Helmholtz vortices can be seen always when a velocity shear is present: in uprising cigarette smoke; in the intersection of two rivers (i.e. Chena and Tanana river in Alaska); on the ocean and lakes; in a coffee cup when one pours cream into it; in cloud formations. Also, aeroplane wings can get into a stall when the critical angle of attack is exceeded due to the Kelvin-Helmholtz Instability.

Chandrasekhar [1961] derived theoretical growth rates for the Kelvin-Helmholtz mode with several fluid and plasma profiles. His results indicate that KH instability is stabilized when velocity shear is parallel to the magnetic field, because it requires additional energy to twist the magnetic field in the boundary or vortex motion.

The onset condition for the KH mode in an ideal, incompressible plasma with a discontinuous (arbitrarily thin) velocity shear layer is

$$\frac{m_0 n_1 n_2}{n_1 + n_2} [\mathbf{k} \cdot \Delta\mathbf{V}]^2 > \frac{1}{\mu_0} \left[(\mathbf{k} \cdot \mathbf{B}_1)^2 + (\mathbf{k} \cdot \mathbf{B}_2)^2 \right] \tag{1.3}$$

where m_0 is the ion mass, n is number density, $\Delta\mathbf{V} = (\mathbf{V}_1 - \mathbf{V}_2)$ is the velocity shear, $\mathbf{B}$ is magnetic field strength, and the indices denote plasma properties on the two sides of the boundary. One can see that the KH instability is stabilized for large magnetic field values along the $\mathbf{k}$ -vector of the instability. In a plasma with constant density and constant $|\mathbf{k} \cdot \mathbf{B}|$ this relation becomes

$$(\mathbf{k} \cdot \mathbf{V}_0)^2 > (\mathbf{k} \cdot \mathbf{v}_A)^2 \tag{1.4}$$

with $\mathbf{V}_0 = \frac{1}{2}(\mathbf{V}_1 - \mathbf{V}_2)$ and with $\mathbf{v_A} = \boldsymbol{\alpha_1} \mathbf{v_{A_1}} + \boldsymbol{\alpha_2} \mathbf{v_{A_2}}$. Thus the velocity shear along $\mathbf{k}$ must be larger than a typical Alfvén speed along $\mathbf{k}$ for instability. Note that $\mathbf{k} \cdot \mathbf{B}$ can have different signs across the boundary.

For a very thin boundary we expect the KH mode to propagate in a frame moving with a velocity of

$$V_{kh} = V_{sh} \frac{\rho_{sh}}{\rho_{sh} + \rho_{sp}},$$

[*Chandrasekhar*, 1961].

The growth rate q of the KH wave is given by (provided that the onset condition is satisfied)

$$q = [\alpha_1 \alpha_2 [(\mathbf{V_1} - \mathbf{V_2}) \cdot \mathbf{k}]^2 - \alpha_1 (\mathbf{V_{A1}} \cdot \mathbf{k})^2 - \alpha_2 (\mathbf{V_{A2}} \cdot \mathbf{k})^2]^{1/2} \tag{1.5}$$

[*Chandrasekhar*, 1961] where the indices refer to the two sides of the shear flow layer, $\alpha_i = \rho_i/(\rho_1 + \rho_2)$, and $\mathbf{V_{Ai}} = \mathbf{B_i}/\sqrt{4\pi\rho_i}$.

The Kelvin-Helmholtz growth rate and onset conditions have been derived above assuming ideal, incompressible plasma and infinitely thin boundary layer thickness. In reality (and in computer simulations), a finite thickness of the shear layer stabilizes the KH mode for small wavelengths. Also, compressibility ($\nabla \cdot \mathbf{V} \neq \mathbf{0}$) of plasma has a stabilizing effect on KH mode [*Miura and Pritchett*, 1982].

There have been several numerical simulation studies of the Kelvin-Helmholtz instability. These simulations are carried using MHD [*Miura and Pritchett*, 1982; *Miura*, 1984, 1987, 1992; *Chen et al.*, 1997; *Otto and Fairfield*, 2000; *Keller and Lysak*, 1999], Hall-MHD [*Huba*, 1994, 1996; *Fujimoto and Terasawa*, 1991], hybrid and kinetic codes [*Terasawa et al.*, 1992; *Thomas and Winske*, 1993; *Fujimoto and Terasawa*, 1994, 1995; *Thomas*, 1995]. The main objective of these studies have been to understand the non-linear evolution of the KH instabiliy at the magnetopause and its effect on the momentum and energy transport and diffusion. I will introduce the main results of the MHD simulations below, and discuss the Hall-MHD and particle simulations in the introduction of Chapter 4.

Miura and Pritchett [1982] used 2-D MHD simulations in transverse ($\mathbf{B_0} \perp \mathbf{V_0}$) and parallel ($\mathbf{B_0} \parallel \mathbf{V_0}$) configurations in homogeneous, compressible plasma. They found that only modes with $ka < 2$ are unstable, where a is the scale length of the shear layer. The fastest growing modes occur for $ka \approx$ 0.5-1.0. Both compressibility and magnetic field parallel to the flow are found to be stabilizing effects [*Miura and Pritchett*, 1982]. Since $v = (\lambda\omega)/2\pi$ and the fastest growing wavelength $\lambda \approx 4\pi a$, the fastest growing KH mode has a frequency of $V_0/2a$ at the magnetopause boundary, which overlaps with the frequency range of geomagnetic pulsations (Pc 3-5).

Miura [1984] used 2-D MHD simulations in a homogeneous, compressible plasma in transverse and parallel configurations in order to estimate nonlinear momentum and energy transport due to the Kelvin-Helmholtz instability. He found that Kelvin-Helmholtz instability acts quite differently in these two configurations. In transverse configuration the viscous interaction is due to the hydrodynamic Reynolds stress, and it could account for a convection potential drop over the polar cap of 10-30 kV. In parallel configuration the viscous interaction is mostly caused by hydromagnetic Maxwell stress, which gives rise to transport 2-3 times larger than that of the transverse case.

Miura [1987] used 2-D MHD simulations including plasma and magnetic field gradients in the initial configuration. Results indicate that the magnetopause current layer is highly nonlinearly corrugated by the KH instability resulting in formation of a plasma blob; a wide velocity boundary layer is formed just inside the magnetopause current layer by the anomalous momentum transport; plasma flow is accelerated by the KH instability due to the increase in the electric field drift $\mathbf{E}\times\mathbf{B}$; an increased electric field drift amplifies the total voltage drop across velocity boundary layer. Magnetosheath plasma momentum is diffused into the the magnetosphere by anomalous tangential stresses that reach few percent of the magnetosheath flow momentum flux. The value of anomalous viscosity increases rapidly between magnetosheath Alfvén Mach numbers (V_0/V_A) 2.5-5.

Miura [1992] studied the influence of the sonic Mach number, $M_s = V_0/V_s$, on the anomalous viscosity produced by the Kelvin-Helmholtz instability (V_s is the magnetosheath sound speed). For all sonic Mach numbers a velocity boundary layer is formed inside the magnetopause caused by the momentum transport by the Kelvin-Helmholtz instability, and it becomes wider for a smaller sonic Mach number. The boundary layer becomes more highly nonlinearly corrugated by the instability for a smaller sonic Mach number, and the anomalous viscosity by the Reynolds stress associated with the instability decreases as the absolute magnitude of M_s increases. Energy and momentum fluxes transported into the magnetosphere by KH instability for $1.0< M_s <3.0$ are 0.045 $V_0 p_0$ and 0.083 p_0 respectively (p_0 is the undisturbed plasma pressure). These results suggest that dayside and dawn-dusk side magnetopauses are the most viscous parts of the boundary.

Chen et al. [1997]; *Chen* [1997] studied mutual interaction of the tearing mode and KH instability with 2-D and 3-D MHD simulations. They found that for sub-Alfvénic flow the reconnection rate decreases with increasing velocity shear. Growth of KH modes for shear flow less than the Alfvén velocity was found to be impossible unless η is very large. Similarly, if shear flow is super-Alfvénic, the tearing mode is stabilized. The information that reconnection operates, propagates with Alfvén speed along the magnetic field. Figure 1.2 illustrates that if the plasma flow is faster than the local Alfvén speed this information cannot propagate away from the reconnection side and thus only the KH mode will grow into a non-linear stage. Thus the tearing and KH instabilities can operate simultaneously, but only in different planes. In 3-D the nonlinear interaction of the KH mode and tearing mode can lead to current sheet thinning and formation of multiple current layers. KH vortices can induce multiple current layer reconnection in 3-D configuration and the mutual interaction of neighboring tearing islands leads to fast growth of the tearing mode. This 3-D vortex-induced tearing instability can cause highly efficient mixing of plasma and complex current layer structures [*Chen*, 1997].

Keller and Lysak [1999] studied the momentum transport associated with the KH instability in a compressional plasma for different configurations. They also observed mass transport but didn't quantify it in detail. In disagreement with results by *Miura* [1984] they found more momentum transport for perpendicular configuration. This is due to the fact that *Keller and Lysak* [1999] had a stronger magnetic field along the **k**-vector of the instability for the parallel cases with respect to the simulations of *Miura* [1984]. This large **B** along the **k**-vector stabilized the instability before the Maxwell stresses developed, which increased the momentum transport in *Miura* [1984] simulation.

Probably the most convincing case for the existence of the Kelvin-Helmholtz instability at the magnetospheric boundary has been presented by *Fairfield et al.* [2000] and *Otto and Fairfield* [2000] to which we will refer as F1 and O1 in the following. On March 24, 1995, the Geotail spacecraft observed large fluctuations of the magnetic field and plasma properties at the dusk side magnetospheric flank. At the time the spacecraft moved from the magnetosheath into the LLBL about 15 R_E tailward of the dusk meridian. A remarkable property of the observations reported by F1 is a strongly fluctuating magnetic field with brief periods of negative B_z components, although the interplanetary magnetic field (IMF) remained strongly northward and largely parallel to the plasma sheet magnetic field during the entire event. The field fluctuations and the plasma properties show a clear quasi-periodic behavior with a period of 2–3 min. The quasi-periodic signatures were observed through the entire transition of the LLBL lasting for about 5 hours during which the IMF remained fairly constant with a strong northward field component. A detailed account of the overall dynamics and the signatures obtained from KH simulations is found in O1. Here I will only discuss the most important observational aspects. These results are also published by *Otto and Nykyri* [2002]. The example in Figure 1.3 shows magnetic field and plasma velocity of a KH simulation, projected into the x, y plane at time=358 seconds. B_z and plasma density are shown as color scale plots in a and current density and reconnection electric field are plotted in b. The two vertical lines indicates the slices along which plasma parameters will

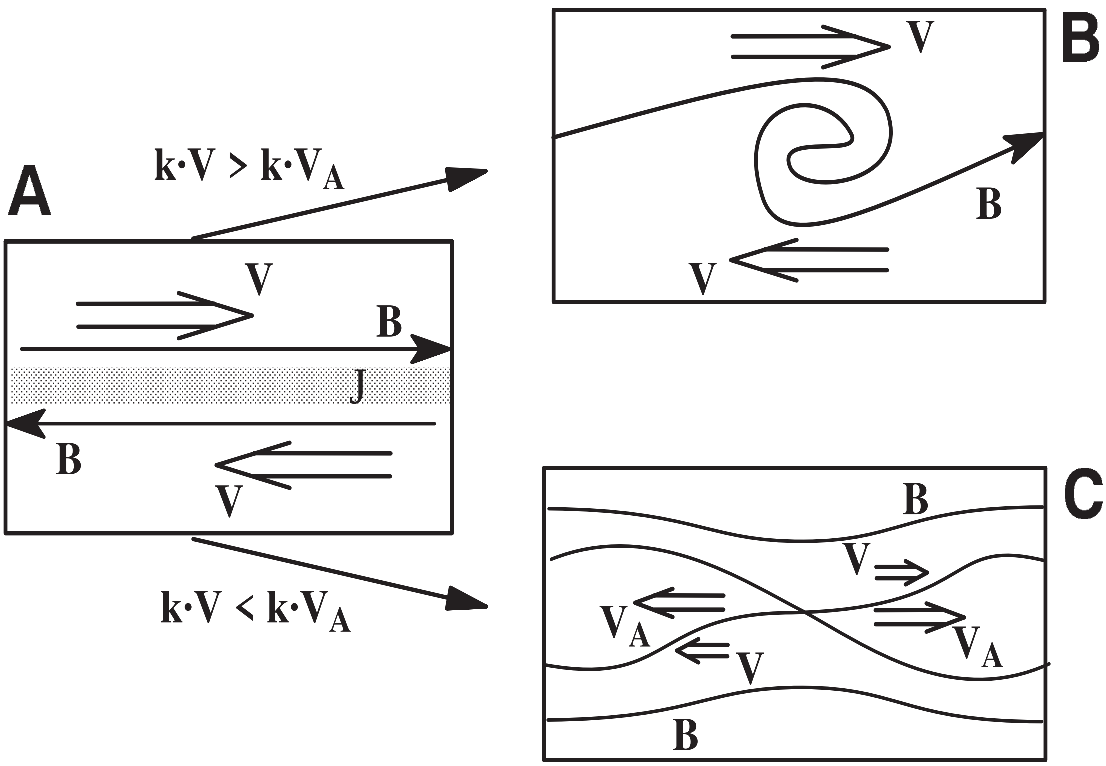

Figure 1.2. A) represents velocity shear layer with anti-parallel magnetic field components. When $\mathbf{k}\cdot\mathbf{B} > \mathbf{k}\cdot\mathbf{V}_{\mathbf{Alfvén}}$ KH mode becomes unstable (B). When $\mathbf{k}\cdot\mathbf{B} < \mathbf{k}\cdot\mathbf{V}_{\mathbf{Alfvén}}$ the tearing mode becomes unstable (C).

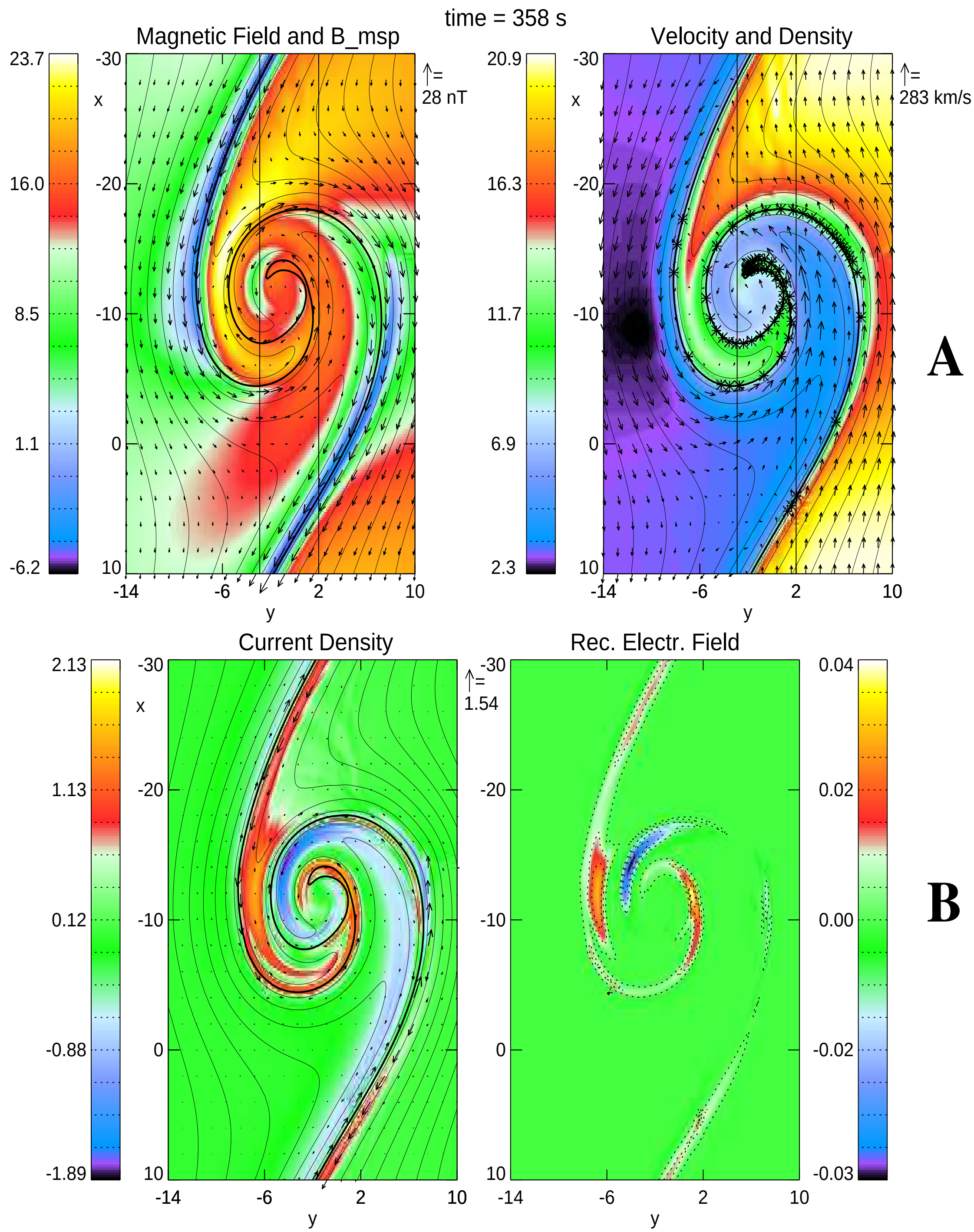

Figure 1.3. A) shows snapshot of magnetic field lines, field vectors, and B_z (color code) on the left and plasma velocity (arrows), field lines, and plasma density (color scale) on the right at 358 seconds into the evolution of the KH mode. B) represents current density (left) and reconnection electric field (right).

be studied.

In the plots of Figure 1.3 the magnetosheath is on the right and the vortex is moving in the negative x direction. A satellite at rest with the magnetosphere would move through the KH wave from the top in a time of approximately 2 minutes. The wave is changing sufficiently slow such that a slice through the wave for instance along the vertical line in Figure 1.3 is a reasonable representation of the typical signatures. The data which would be recorded are presented in Figure 1.4.

Upper panel of Figure 1.4 is a cut at $y = 2$ (1200 km), i.e., close to the path of the probe, and the lower panel of Figure 1.4 is a cut at $y = -3$ (-1800 km). Different shadings in Figure 1.4 indicate regions with different characteristic properties. The lighter shading indicates a region with high sheath-like density, the darker shading indicates a region of high temperature and low density, and the vertical lines indicate an additional boundary. Both cuts show similar properties, with some slightly more pronounced in lower panel of Figure 1.4 such that we labeled distinct intervals using lettering from a to e.

Region a represents the core of the KH vortex and is characterized by strong fluctuations in all plasma and field properties. The region can show high-density spikes somewhat resembling sheath-like properties (higher B_z, etc.). Often visible in this region are reversals of V_y which can be accompanied by changes in V_x.

Region b shows fairly steady plasma and field properties, with magnetospheric-like high temperatures and relatively low densities. Characteristic of this region is also a fairly steady decrease of the V_y component.

Region c represents the outbound transition just prior to the high-density intervals. Typical of region c are the decrease in temperature and increase in density, a high total magnetic field magnitude, a pronounced minimum in B_z, and extrema in the B_x and B_y components. The local maxima and minima in B_x and B_y are often accompanied by a minimum of B_z prior to the sheath-like intervals with larger and steady B_z. The outbound pass is often easy to identify in the Geotail data (Figure 7b of *Fairfield et al.* [2000]).

Region d shows the already mentioned high number density and low temperature, large B_z, and steady plasma and field properties, i.e., magnetosheath-like properties. The length of high-density intervals decreases with distance from the magnetosheath.

Finally, region e marks the inbound pass into a region of generally lower number density

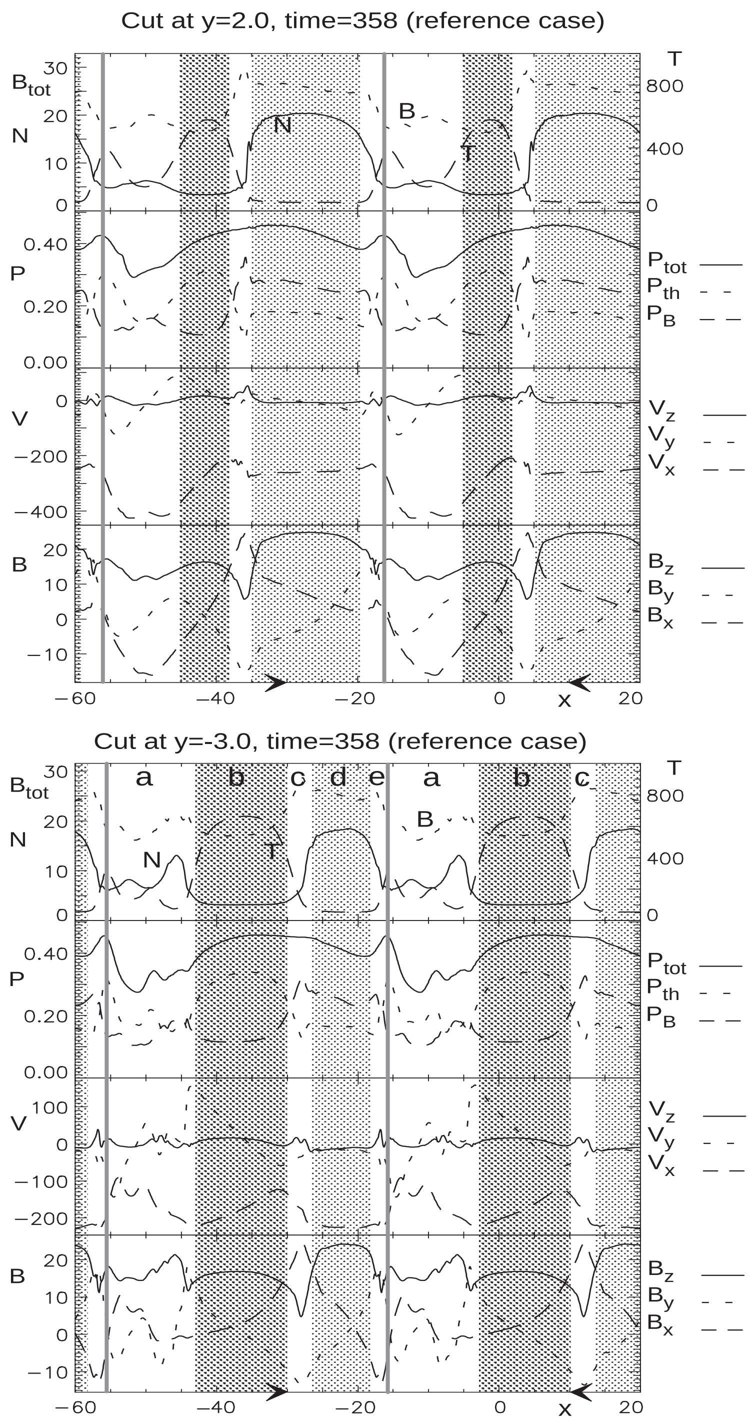

Figure 1.4. Data along the slices at $y = 2$ and $y = -3$ of the configurations shown in Figure 1.3.

and intermediate or high temperature. It shows a less pronounced minimum in B_z and frequently an extremum in B_y (sometimes in B_x depending on the normal direction of this boundary).

Figure 1.3 illustrates a strong depletion of B_z outside the vortex close to the original boundary. We will address this region as the spine of the KH wave. A rotation back into GSM coordinates often shows negative B_z values in the center of this spine. Typical are also large B_x and B_y components in the spine region and it extends partially into the vortex. Such a region can also been identified in prior work [*Miura*, 1984, 1987; *Wu*, 1986]. An outbound pass has to cross this spine and would show typical extrema in B_x and B_y (with opposite polarity on the dusk side flank). The KH vortex motion leads to a twisting of the magnetic field, which accounts for the strong variations of the field in the vortex (region a). Figure 1.4 shows high-density plasma in the vortex explaining the spikes of high number density in region a.

The large magnetic field magnitude along the spine and the depletion of the B_z component in the same region is explained as follows. During the early evolution the KH vortex region develops a strong depletion of the static total pressure due to centrifugal forces of the vortex motion. Plasma is swept into the vortex along the spine region as illustrated by the large number of plasma elements (asterisks) in the vortex in Figure 1.3. The resulting plasma depletion along the spine region (outside the vortex) leads to the increase of the magnetic flux aligned with this boundary (B_x and B_y). The B_z component along the spine decreases at the same time because the frozen-in condition implies that B_z flux is swept into the vortex together with the plasma elements.

This evolution eventually leads to a stabilization of the vortex motion because the increasing field along the spine requires a larger energy in order to twist the magnetic field. It is expected and indicated by these results that the stabilization occurs when the magnetic field energy density (based on the B_x and B_y components) approaches the energy density of the shear velocity in the boundary region. This leads locally to an approximate equipartition between kinetic energy of the bulk flow and the magnetic energy, which may be relevant for astrophysical systems [*Birk et al.*, 1999]. The similarity of the simulation results and the actual Geotail observations is noteworthy and leaves little doubt that the quasi-periodic Geotail events on March 24, 1995 [*Fairfield et al.*, 2000] are caused by nonlinear KH waves moving across the spacecraft.

1.4 Motivation of the Thesis

Plasma entry into the magnetosphere during quiet geomagnetic conditions with primarily northward IMF has been an unsolved mystery for long time. While some of this transport can be understood by high latitude reconnection [*Song and Russell*, 1992] and diffusive processes such as ion mixing due to the Kelvin-Helmholtz instability [*Fujimoto and Terasawa*, 1994], these models can hardly explain why a substantial part of the Earth's magnetotail is efficiently filled with cold, dense solar wind material, especially when the high latitude entry is said to become less efficient for periods of strongly northward IMF [*Fujimoto et al.*, 1998a]. In addition, present theoretical diffusion models cannot account for low latitude boundary layer thickness greater than $\approx 0.5\ R_E$.

Northward IMF conditions have long been associated with a cold and dense plasma sheet [*Fairfield and et al.*, 1981; *Lennartsson*, 1992]. *Borovsky et al.* [1998] demonstrated that the plasma sheet temperature and density are correlated to solar wind properties on a time scale of 1 to 2 hours. A top panel of Figure 1.5 represents 225 measured values of the plasma sheet density by ISEE-2 satellite as a function of the simultaneously measured values of the solar wind density (by ISEE-3 satellite) by *Borovsky et al.* [1998]. For these data the linear correlation coefficient is 0.74, which indicates strong correlation between the solar wind density and the magnetotail central plasma sheet density. The bottom panel of Figure 1.5 shows correlation between near Earth plasma sheet density (measured by three geosynchronous satellites) and solar wind density *Borovsky et al.* [1998]. *Borovsky et al.* [1998] also illustrate (Figure 11 in *Borovsky et al.* [1998]) that these correlation coefficients can be increased if a time lag between the solar wind measurements and plasma sheet measurements is introduced. The maximum correlations occur for time lags of 0-2.5 hours, which indicates that solar wind material reaches plasma sheet within this time scale[*Borovsky et al.*, 1998].

Recently *Terasawa et al.* [1997] and *Fujimoto et al.* [1998a,b] reported a strong correlation between a high density, cold plasma sheet and a strongly northward IMF orientation during the hours prior to the plasma sheet observations. Figure 1.6a and b show the plasma sheet temperature versus the solar wind kinetic energy and the plasma sheet density versus the solar wind density, respectively [*Fujimoto et al.*, 1998a]. Color of data point depicts IMF latitudinal angle, blue corresponding to a northward IMF and red to a southward IMF orientation. While both of the panels show positive correlations for all IMF orientations (in agreement with results by *Borovsky et al.* [1998]), blue dots have less scatter. Figure 1.6c presents normalized plasma sheet density versus IMF orientation, which shows clearly that highest densities occur during northward IMF conditions. *Fujimoto et al.* [1998a] concludes that cold-dense plasma sheet appears when IMF is northward, but very unlikely when IMF is southward.

Except for cusp magnetic reconnection [*Song and Russell*, 1992] and anomalous diffusion [*Fujimoto and Terasawa*, 1994] no specific mechanisms are suggested to generate the cold dense plasma sheet.

Simulation results of *Otto and Fairfield* [2000] indicate that when the background magnetic field has a small component along the Kelvin-Helmholtz wave vector, the instability can twist the magnetic field in the plane of the k-vector (see Figure 1.3a). This leads to the formation of strong current layers embedded in the vortex motion. When these current layers get further intensified, reconnection detaches a high density, cold temperature magnetic island from the magnetosheath. It is worth mentioning here that this is not contradicting the results of *Chen et al.* [1997] (KH and tearing mode cannot operate in the same plane simultaneously), since in these narrow current layers the shear flow is reduced and becomes sub-Alfvénic, which allows reconnection to operate.

The goal of this thesis is to quantify reconnection inside Kelvin-Helmholtz vortices in two dimensions and to determine whether this process is efficient enough to transport cold, dense magnetosheath material into the Earth's plasma sheet during periods of northward IMF. Since the filamentary current sheets can become thinner than the ion inertia length, the ion dynamics can decouple from the electron motion. I will study this transport, first assuming that electron and ion motion is coupled, and then allow their motion to separate in scales defined by the local ion inertia length scale, c/ω_{pi}. Since the dynamical evolution of the magnetosphere depends on the physical processes at the magnetospheric boundary, it is crucial to distinguish these different mechanisms operating at the boundary from the satellite data. I have analyzed in detail Equator-S and Cluster satellite data as a goal to distinguish signatures of reconnection inside Kelvin-Helmholtz vortices and compared these results with MHD simulations.

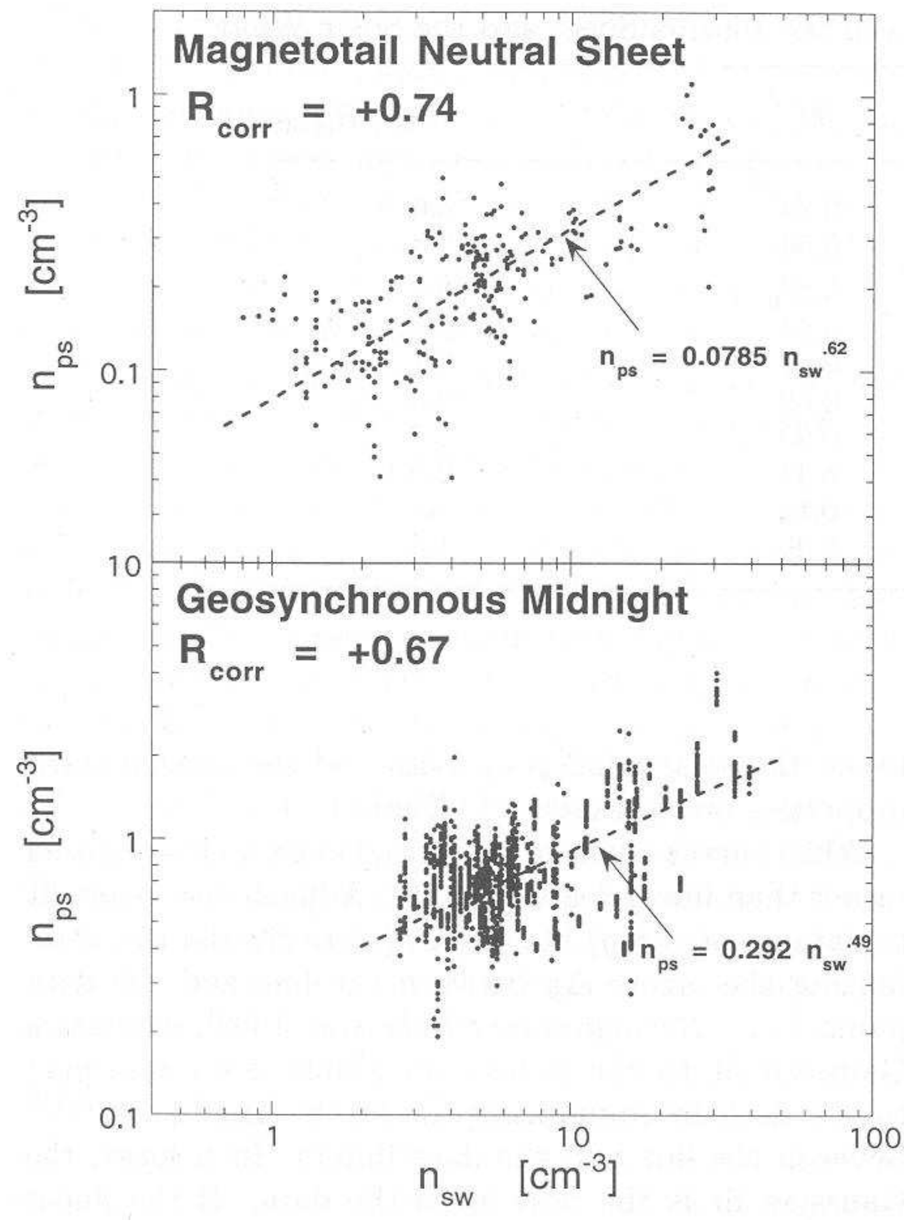

Figure 1.5. Neutral sheet density versus solar wind density [*Borovsky et al.*, 1998].

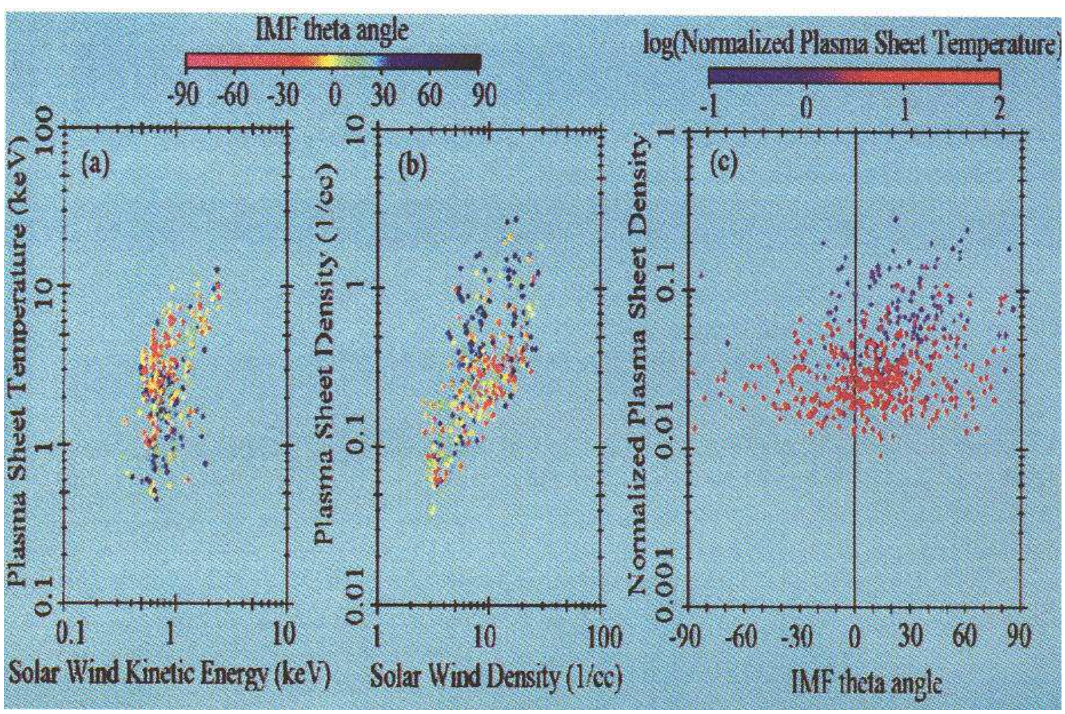

Figure 1.6. Neutral sheet temperature and density versus solar wind conditions [*Fujimoto et al.*, 1998a].

1.5 Outline of the Thesis

In this thesis, I use two-dimensional MHD and Hall-MHD simulations and satellite data analysis methods to investigate plasma transport associated with Kelvin-Helmholtz modes. The main emphasis is a quantitative study of reconnection inside Kelvin-Helmholtz vortices both for MHD and Hall-MHD approximations. I have analyzed in detail Equator-S and Cluster satellite data with the goal to distinguish signatures of reconnection inside Kelvin-Helmholtz vortices and compared these results with MHD simulations. I have studied the differences between signatures of flux transfer events, FTE's and those of reconnection inside Kelvin-Helmholtz vortices. Understanding the 3-D structure of the Earth's magnetosphere from the data of four satellites is a challenging and a relatively new task. This thesis presents examples of how the data from the four Cluster satellites can be analyzed, and how the process of reconnection inside Kelvin-Helmholtz vortices can be identified. I have also discussed ground observations associated with Kelvin-Helmholtz modes and estimated from the simulation results what should be the typical ionospheric signatures due to the Kelvin-Helmholtz instability. The thesis is divided into chapters in the following way:

Chapter 2 introduces numerical simulation codes used in this thesis.

Chapter 3 presents a two-dimensional quantitative MHD simulation study of reconnection and mass transport in KH vortices depending on magnetosheath and magnetospheric plasma properties and discusses the influence of resistivity on reconnection process inside KH vortices.

In Chapter 4, I include the Hall-term in the system of MHD equations and study qualitatively and quantitatively the effect of the ion inertia term on reconnection inside Kelvin-Helmholtz vortices and plasma transport for several magnetosheath and magnetospheric plasma and magnetic field configurations. I also study the influence of the wavelength on the instability, basic properties of the Hall-MHD Kelvin-Helmholtz instability, and ion inertia scale turbulence caused by the Hall effect. The Hall-MHD simulation results are compared with MHD simulation results and I discuss their role in the Earth's magnetosphere.

Chapter 5 presents MHD simulations of the KH instability in a magnetospheric inertial frame. Magnetic field and velocity perturbations caused by the KH instability in the magnetosphere are mapped into the ionosphere. I compare these predicted ionospheric signatures with radar, optical, and ground observations discussed in literature.

In Chapter 6, Equator-S satellite data on March 10th 1998 at the dawn side low latitude boundary layer is analyzed and these observations are compared with 2-D MHD simulations. I determine whether these signatures are caused by flux transfer events, FTE's, or reconnection inside Kelvin-Helmholtz vortices and compare typical properties of these processes.

In Chapter 7 I analyze data from the four Cluster satellites on July 3rd 2001 at the dawn side magnetospheric flank. I illustrate satellite trajectories, boundary normal directions and de Hoffman Teller frame velocities in three dimensions during intervals with reconnection signatures and current sheet crossings. I study in detail plasma acceleration events observed by two of the Cluster satellites and compare this analysis with MHD simulations of the Kelvin-Helmholtz instability.

In last chapter I summarize the research done in this thesis and discuss possible future topics to be studied.

Chapter 2

Numerical Method

Plasmas are most accurately described by the evolution of the exact phase space density in the Klimontovich-Dupree equation, which contains exact microscopic fields caused by each particle. Solving such a equation is a difficult task. One can define the plasma distribution function, $f(\mathbf{r}, \mathbf{v}, \mathrm{t})$, by averaging over a large number of particles, considering them as statistically correlated in time, space, and velocity by their mutual interactions [*Baumjohann and Treumann*, 1997].

The Boltzmann equation (Equation 2.1) describes the dynamical evolution of the distribution function for species α after the corrections between the fields have been neglected and correlations between the particles have been included via collisions.

$$\frac{\partial f_\alpha}{\partial t} + \mathbf{v} \cdot \frac{\partial f_\alpha}{\partial \mathbf{r}} + \frac{q_\alpha}{m_\alpha}(\mathbf{E} + \mathbf{v} \times \mathbf{B}) \cdot \frac{\partial f_\alpha}{\partial \mathbf{v}} = (\frac{\partial f_\alpha}{\partial t})_c \tag{2.1}$$

In the collisionless case we can neglect the right-hand side of Eq. 2.1 and obtain the Vlasov equation. There are several types of distribution functions in plasmas but the most general is the Maxwellian distribution. Computationally it is still a time and computer resources demanding task to try to solve the time evolution of the exact distribution function. If the temporal changes of the plasma system are slow, it is sufficient to know the dynamical evolution of the macroscopic quantities of the plasma, such as densities, velocities and temperatures.

We obtain the fluid description of collisionless plasma by taking moment integrals of

Eq. (2.1) and neglecting the collision term on the right-hand side (see Appendix A).

Magnetohydrodynamic theory, MHD, describes plasma as a one-fluid medium, where macroscopic quantities such as plasma density, pressure and velocity are defined as averages over all particle species. MHD assumes long temporal and spatial scales of the system.

2.1 MHD Simulations

MHD simulations are a computational technique to replace the governing partial differential equations with systems of algebraic equations, so that a computer can be used to obtain the solution. The most common methods are the finite difference, finite element, finite volume and spectral methods. In this thesis I solve the full set of resistive MHD equations [*Otto*, 1990a] with a finite differences leap frog scheme [*Potter*, 1973]:

$$\frac{\partial \rho}{\partial t} = -\nabla \cdot (\rho \mathbf{v}) \tag{2.2}$$

$$\frac{\partial \rho \mathbf{v}}{\partial t} = -\nabla \cdot \left[\rho \mathbf{v}\mathbf{v} + \left(\frac{1}{2}\right) \left(p + \mathbf{b}^2\right) \mathbf{I} - \mathbf{b}\mathbf{b} \right] \tag{2.3}$$

$$\frac{\partial \mathbf{b}}{\partial t} = \nabla \times (\mathbf{v} \times \mathbf{b} - \eta \mathbf{j}) \tag{2.4}$$

$$\frac{\partial h}{\partial t} = -\nabla \cdot (h\mathbf{v}) + \left[\frac{(\gamma - 1)}{\gamma}\right] h^{1-\gamma} \eta \mathbf{j}^2 \tag{2.5}$$

$$\mathbf{j} = \nabla \times \mathbf{b} \tag{2.6}$$

with $h = (p/2)^{1/\gamma}$. Here ρ is the plasma mass density, $\mathbf{v}$ is the plasma velocity, p is the plasma pressure, $\mathbf{b}$ is the magnetic field, $\mathbf{j}$ is the current density, η is the resistivity, $\mathbf{I}$ is the unit tensor, and γ is the ratio of specific heats (γ =1.667). All quantities are normalized to characteristic values for the system, i.e., length scales l to a typical length L_0; density ρ to $\rho_0 = n_0 m_0$ with the number density n_0 and the ion mass m_0; magnetic field $\mathbf{b}$ to B_0; velocity $\mathbf{v}$ to the typical Alfvén velocity $v_A = B_0/\sqrt{4\pi\rho_0}$; pressure to $P_0 = B_0^2/(8\pi)$; current density to $J_0 = cB_0/(4\pi L_0)$; and time t to a characteristic Alfvén transit time $\tau_A = L_0/v_A$.

Figure 2.1 shows an example of numerical integration of the continuity equation, Eq. 2.2 in 2-D using a finite differences leapfrog scheme. The discretized continuity equation becomes with $\rho\mathbf{v} = \mathbf{s}$

$$\rho^{n+1}_{i,j} - \rho^{n-1}{}_{i,j} = -2\Delta t \left[\frac{sx^n_{i+1,j} - sx^n_{i-1,j}}{x(i+1,j) - x(i-1,j)} + \frac{sy^n_{i,j+1} - sy^n_{i,j-1}}{y(i,j+1) - y(i,j-1)} \right] \tag{2.7}$$

so the update at time $t = t_{n+1}$ uses information from surrounding gridpoints at $t = t_n$ and the same gridpoint at $t = t_{n-1}$.

2.2 Hall-MHD Simulations

When typical system scale sizes approach ion inertia length, c/ω_{pi}, the Hall-term in Generalized Ohm's law (Appendix A) must be included in system of equations. Ohm's law in resistive Hall-MHD simulations is $\mathbf{E} = -\mathbf{v} \times \mathbf{b} + \eta\mathbf{j} - \frac{\mathbf{1}}{\mathbf{ne}}(\mathbf{j} \times \mathbf{b})$. The normalized set of Hall-MHD equations used in this thesis is:

$$\frac{\partial \rho}{\partial t} = -\nabla \cdot (\rho \mathbf{v}) \tag{2.8}$$

$$\frac{(\partial \rho \mathbf{v})}{\partial t} = -\nabla \cdot \left[\rho \mathbf{v}\mathbf{v} + \left(\frac{1}{2}\right) \left(p + \mathbf{b}^2\right) \mathbf{I} - \mathbf{b}\mathbf{b} \right] \tag{2.9}$$

$$\frac{\partial \mathbf{b}}{\partial t} = \nabla \times \left(\mathbf{v} \times \mathbf{b} - \eta \mathbf{j} + \frac{1}{ne}(\mathbf{j} \times \mathbf{b}) \right) \tag{2.10}$$

$$\frac{\partial h}{\partial t} = -\nabla \cdot (h\mathbf{v}) + \left[\frac{(\gamma - 1)}{\gamma} \right] h^{1-\gamma} \eta \mathbf{j}^2 \tag{2.11}$$

$$\mathbf{j} = \nabla \times \mathbf{b} \tag{2.12}$$

Simulations assume one-dimensional initial equilibrium, such that $\partial/\partial z, \partial/\partial y = 0$. In the equilibrium $\frac{\partial \mathbf{B}}{\partial t} = 0$, so one has to be careful that $\partial_x E_z$ =0 and $\partial_x E_y$ =0.

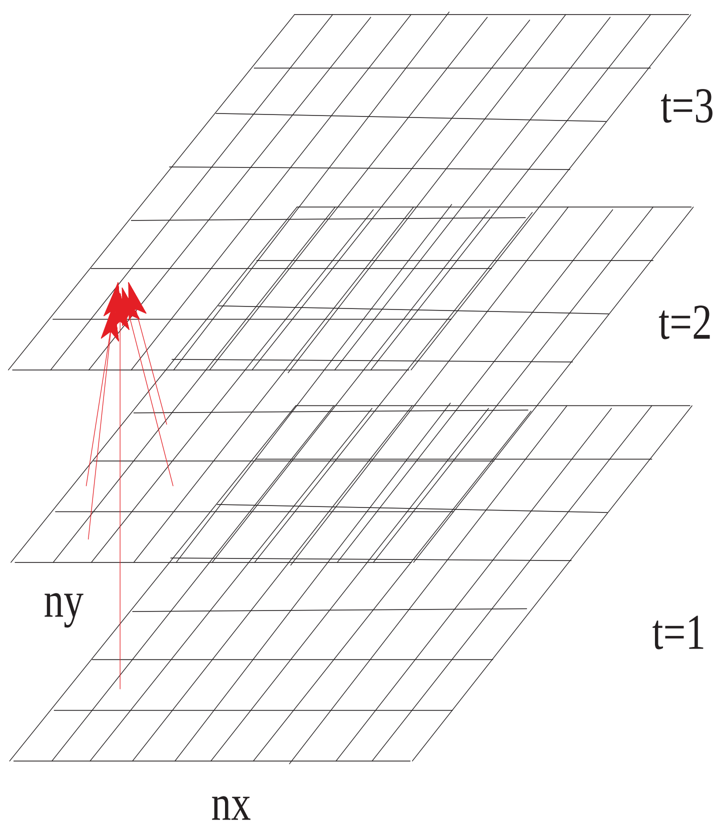

Figure 2.1. Task at time $t = t_{n+1}$ uses information from surrounding gridpoints at $t = t_n$ and it's value at the same gridpoint at $t = t_{n-1}$.

Chapter 3

Plasma Transport at the Magnetospheric Boundary due to Reconnection in Kelvin-Helmholtz Vortices: MHD approximation

The results in this chapter are published in the Geophysical Research Letters [*Nykyri and Otto*, 2001].

3.1 Introduction

The momentum transport by Kelvin-Helmholtz waves into the magnetosphere has long been suggested as a mechanism for the formation of the low latitude boundary layer (LLBL). *Miura* [1984] estimated the momentum transport to be consistent with the transport required to form the LLBL. However, the KH mode is an ideal plasma instability and has therefore not been expected to produce a significant mass transport. Hybrid and full particle simulations indicate that fast anomalous diffusion is possible for sufficiently thin boundaries in the KH vortex [*Fujimoto and Terasawa*, 1994, 1995; *Thomas and Winske*, 1993].

Recent studies [*Keller and Lysak*, 1999; *Otto and Fairfield*, 2000] of the evolution and signatures of KH waves show that KH instability can cause mass transport during periods of strongly northward IMF. The study by *Otto and Fairfield* [2000] has been motivated by Geotail observations in the LLBL at the duskside flank [*Fairfield et al.*, 2000] which showed very large and rapid magnetic field changes in which the B_z component could assume negative values despite the fact that the field on both sides of the LLBL (magnetosheath and plasma sheet) is strongly northward. The simulations demonstrated many detailed properties of the quasi-periodic signatures observed by the Geotail spacecraft by assuming a small magnetic field component along the $\mathbf{k}$ vector of the KH mode. Surprisingly the high resolution two-dimensional simulations also demonstrated that magnetic reconnection occurs in the twisted magnetic field of the KH vortices. However, other than a rough estimate of the expected plasma transport, *Otto and Fairfield* [2000] did not study the transport in detail.

This work presents a detailed parameter study to quantify the plasma transport in two dimensions. The reconnection process in KH filaments is sketched in Figure 3.1 The twisting of the magnetic field leads to anti-parallel magnetic field components generating strong and thin current layers. Finally high density magnetic islands (flux ropes) are detached from the magnetosheath by magnetic reconnection.

This process is not related to so-called vortex induced reconnection which addresses the coupling of KH and tearing mode. Here the magnetic field can be parallel on the two side of the boundary and anti-parallel magnetic field is generated through the KH vortex motion.

3.2 Numerical Method

The mass transport calculations in this study are obtained with two-dimensional MHD simulations (Chapter 2) [*Otto*, 1990a] in the x, y-plane (approximately the equatorial plane for strongly northward IMF). The basic equations are solved with a finite differences leapfrog scheme [*Potter*, 1973; *Birn*, 1980], which is of second-order accuracy in space and time. The initial configuration for the simulation in the boundary coordinates uses a magnetic field of $b_{x0}(x) = b_0(x)\sin\varphi$, $b_{y0}(x) = 0$, and $b_{z0}(x) = b_0(x)\cos\varphi$ such that $90° - \varphi$ is the angle between the unperturbed magnetic field direction and the $\mathbf{k}$ vector of the KH mode. The initial density, pressure,velocity, and magnetic field on the magnetospheric and magnetosheath sides are chosen according to Geotail 1995 event [*Otto and Fairfield*, 2000;

Fairfield et al., 2000]. The velocity is given by $v_{x0}(x) = v_0(x)$, $v_{y0}(x) = 0$, and $v_{z0}(x) = 0$. Initial density, pressure, velocity, and magnetic field magnitudes are

$$\begin{aligned}
\rho_0(x) &= \frac{1}{2}(\rho_{sh} + \rho_{sp}) + \frac{1}{2}(\rho_{sh} - \rho_{sp}) \tanh(\frac{y}{L_0}) \\
p_0(x) &= \frac{1}{2}(p_{sh} + p_{sp}) + \frac{1}{2}(p_{sh} - p_{sp}) \tanh(\frac{y}{L_0}) \\
v_0(x) &= -\frac{1}{2}v_{sh}(\tanh(\frac{y}{L_0}) + 1) \\
b_0(x) &= \frac{1}{2}(b_{sh} + b_{sp}) + \frac{1}{2}(b_{sh} - b_{sp}) \tanh(\frac{y}{L_0}),
\end{aligned}$$

where the indices sp and sh correspond to the average values on the magnetospheric and magnetosheath sides of the magnetopause boundary. $v_{sh} = 315$ km/s; $v_{msp} = 0$ km/s;$\rho_{sh} = 19.2$ 1/cm^3; $\rho_{msp} = 2.8$ 1/cm^3;$\beta_{sh} = 0.69$; $\beta_{msp} = 2.8$. The two-dimensional simulations are performed in the plane determined by the direction normal to the magnetospheric boundary y and the $\mathbf{k}$ vector of the instability. For the configuration illustrated in Figure 3.2a this corresponds to a boundary normal system with x generally pointing sunward along the magnetospheric boundary, y being normal to the average magnetopause, and z being northward along the tail boundary.The initial state of the simulation uses a Galilei transformation for the velocity such that the simulation frame is moving with half the magnetosheath velocity. In this manner the KH vortex is moving slower in the simulation frame, with the advantage that the time step limit for the integration of the MHD equation is larger than in a frame which is at rest with the magnetosphere. In other words the simulation frame illustrated in the sketch in Figure 3.2c is sliding with half the magnetosheath plasma velocity tailward. Boundary conditions for the simulations are periodic along the x direction, and boundary conditions in y are open to inflow and outflow of plasma. The values for φ, and the magnetic field magnitude are listed in Table 3.1 for different simulation runs. All quantities are normalized to characteristic values for the system, i.e., length scales l to a typical length L_0; density ρ to $\rho_0 = n_0 m_0$ with the number density n_0 and the ion mass m_0; magnetic field $\mathbf{b}$ to B_0; velocity $\mathbf{v}$ to the typical Alfvén velocity $v_A = B_0/\sqrt{4\pi\rho_0}$; pressure to $P_0 = B_0^2/(8\pi)$; current density to $J_0 = cB_0/(4\pi L_0)$; and time t to a characteristic Alfvén transit time $\tau_A = L_0/v_A$. The values for the normalization of the simulation units are summarized in Table 3.2.

The system size is 40 units in x, corresponding to a wavelength of about 4 R_E. The

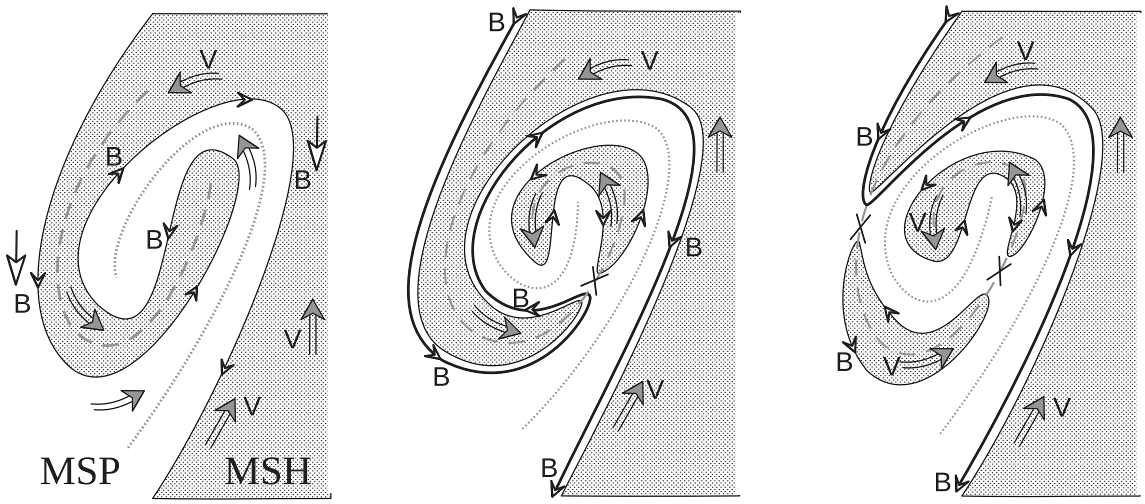

Figure 3.1. Sketch of the evolution of magnetic reconnection in the Kelvin-Helmholtz vortex.

Table 3.1. Simulation Runs

	φ	B in MSP	B in MSH
CASE 1	3°	16 nT	24 nT
CASE 2	3°	24 nT	16 nT
CASE 3	5°	16 nT	24 nT
CASE 4	5°	24 nT	16 nT
CASE 5	10°	16 nT	24 nT
CASE 6	10°	24 nT	16 nT
CASE 7	15°	16 nT	24 nT
CASE 8	15°	24 nT	16 nT
CASE 9	25°	16 nT	24 nT
CASE 10	25°	24 nT	16 nT
CASE 11	35°	16 nT	24 nT
CASE 12	35°	24 nT	16 nT

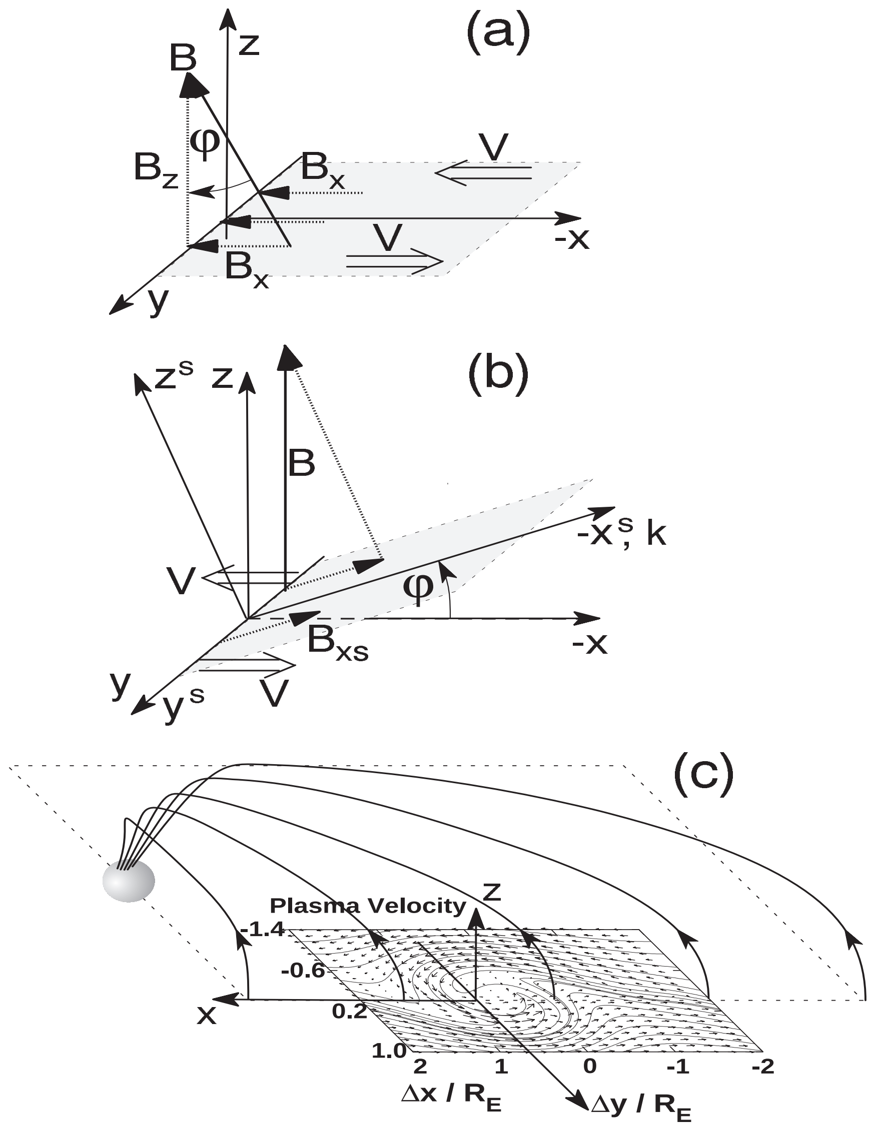

Figure 3.2. Illustration of basic geometries for the occurrence of KH instabilities on the magnetospheric flank: (a) The **k** vector of the KH mode is in the equatorial plane and the magnetospheric and the magnetosheath fields have a small x component; (b) the magnetospheric and magnetosheath fields are along the z direction and the **k** vector has a component out of the equatorial plane (the upper index s denotes simulation coordinates); (c) illustration of the KH mode at the magnetospheric boundary. In the cases (a) and (b) the angle between the **k** vector and the magnetic field is $90^\circ - \varphi$.

Table 3.2. Simulation Normalization

Magnetic field B_0	16 nT
Number density n_0	11 cm^{-3}
Current density	22 nA m^{-2}
Length scale L_0	600 km
Velocity v_A	105 km s^{-1}
Time τ_A	5.7 s

simulation employs 403 $\times$ 203 gridpoints in the x and y-directions. The choice of the resistivity does not appear to be important for the results as long as the resistivity is chosen to avoid fast large scale diffusion. The following four resistivity models are used to demonstrate the influence of the resistivity.

$$\begin{aligned}
\eta(j) &= \kappa\sqrt{(j^2 - {J_c}^2)}S(j^2 - {J_c}^2) && (\mathit{model}\ 1)\\
\eta(j) &= \kappa(j - J_c)S(j - J_c) && (\mathit{model}\ 2)\\
\eta(j) &= \kappa(j^2 - {J_c}^2)S(j^2 - {J_c}^2) && (\mathit{model}\ 3)\\
\eta(j) &= 0 && (\mathit{model}\ 4)
\end{aligned}$$

Here $\kappa = 0.005$ and S is a step function equal to unity for arguments greater than 0 and equal to 0 otherwise. All cases in Table 3.1 use the current dependent model 1 with a critical current density of $J_c = 1.1J_0 = 24$ nA m^{-2} (model 1a). In addition to cases 1-12 we present results with the parameters of CASE 5 and the resistivity models 1b, 2, 3, and 4. The model 1b is same as 1a but with the $J_c = 2.1J_0$. Models 2 and 3 use $J_c = 1.1J_0$, and model 4 uses a zero resistivity.

The mass transport is calculated by integrating the plasma density over magnetic islands (flux ropes) captured from the magnetosheath. These islands are defined by plasma elements which are used as tracers for the initial boundary. During the simulation, the location of these elements is determined by integrating the plasma velocity. Ideally the plasma elements stay on the same field line if the magnetic field is frozen into the plasma flow. However, reconnection and numerical dissipation can break this condition.

In two dimensions Ohm's law can be written as

$$\frac{\partial A_z(t)}{\partial t} + (\mathbf{V} \cdot \nabla) A_z(t) = -\eta J_z. \tag{3.1}$$

A_z is the z-component of the magnetic vector potential and changes along the path of a fluid element only due to the resistive term on the right side of (1) if the initial gauge of A_z is maintained. If this is the case a fixed value of A_z determines the magnetic boundary. Since A_z is determined by integrating the magnetic field, we use the plasma elements to determine the proper gauge and to test the frozen-in condition.

Figures 3.2a to 3.2c present velocity and density plots for CASE 5, and Figure 3.3 d) shows a plot of the time integral $-\int_0^t \eta J_z dt$ versus the value A_z for each plasma element. The scatter is due to numerical dissipation and the gauge is determined by the value of A_z where the regression line of slope 1 crosses the abscissa. The yellow line in the plots of Figure 3.3 shows the boundary and its deformation as determined by this method.

3.3 Results

We will describe here the analysis of the CASE 5, with φ =10° for the magnetic field orientation, yielding a positive B_x component of 2.8-4.2 nT on the two sides of the boundary. Figures 3.3a to c illustrate the time evolution of the Kelvin-Helmholtz wave for this case. The plasma density is color coded, lines represent magnetic field lines projected onto the simulation plane, and arrows illustrate the orientation and magnitude of the plasma velocity. The asterisks represent plasma elements which were originally at the boundary $y = 0$.

At time $\sim$55.5 τ_A, the KH velocity vortex is twisting the magnetic field, and filamentary current layers are developing fast inside the vortex. No reconnection has occurred up to this time. At time $\sim$ 74.5 τ_A (panel B) the KH vortex has further evolved, and a first filament of magnetosheath material (the island in the center of the vortex) is detached from the magnetosheath. Note the periodic boundary conditions in x. The corresponding boundary (yellow line) is determined from Figure 3.1 d). At time $\sim$ 89.4 τ_A, the main filament is detached similar to the illustration in Figure 3.1. Figure 3.4 represents magnetic field vectors (arrows), magnetic field lines, and the z-component of the current density (color code) for CASE 5 at time $\sim$ 74.5 τ_A (Figure 3.3b). The Kelvin-Helmholtz vortex motion

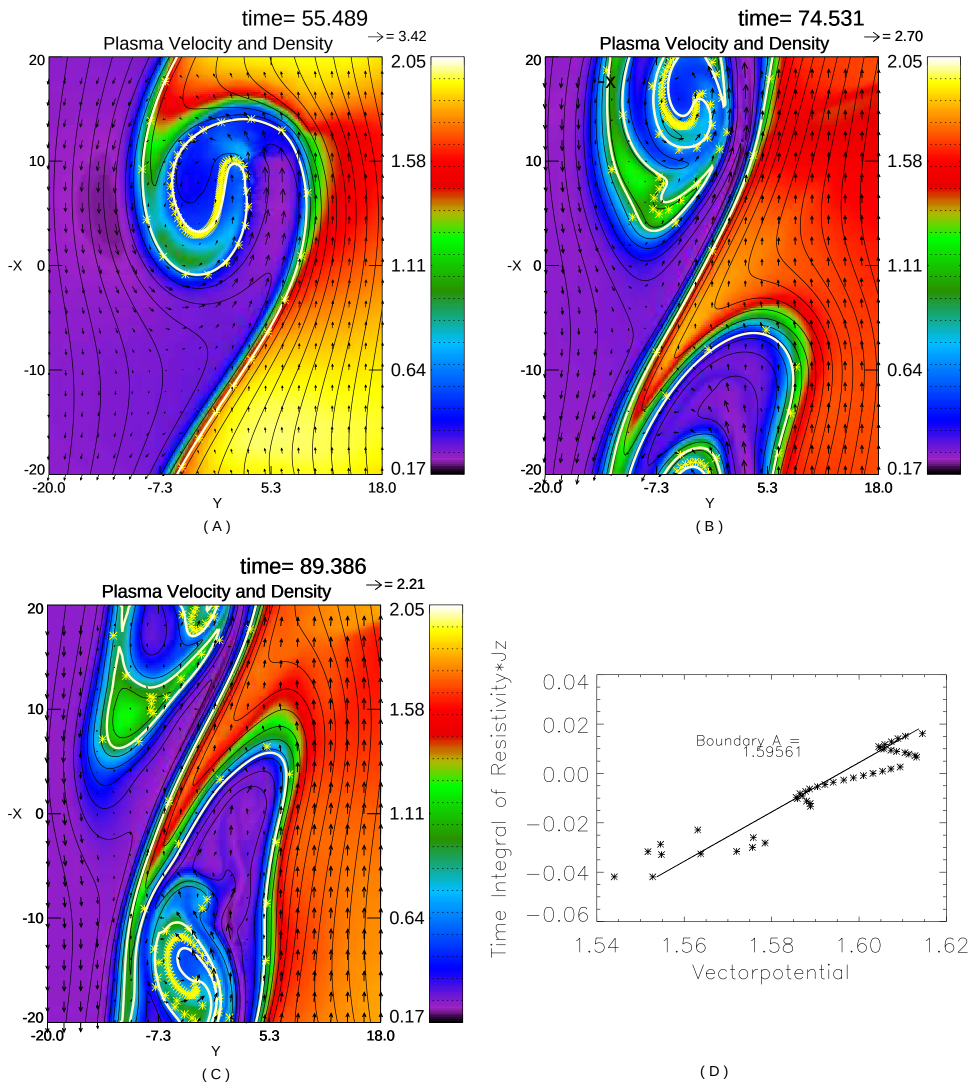

Figure 3.3. Panel (A) to (C) present the time evolution of Kelvin-Helmholtz wave for CASE 5. The yellow line is the marker for original boundary and yellow asterisks present plasma elements that mark the original boundary $y = 0$. The color measures plasma density, lines are magnetic field lines and arrows are velocity vectors. Panel (D) shows an example of $A_z(t_2)$ versus $-\int \eta J_z dt$ for plot (A) to determine the appropriate boundaries (yellow line in the color plots).

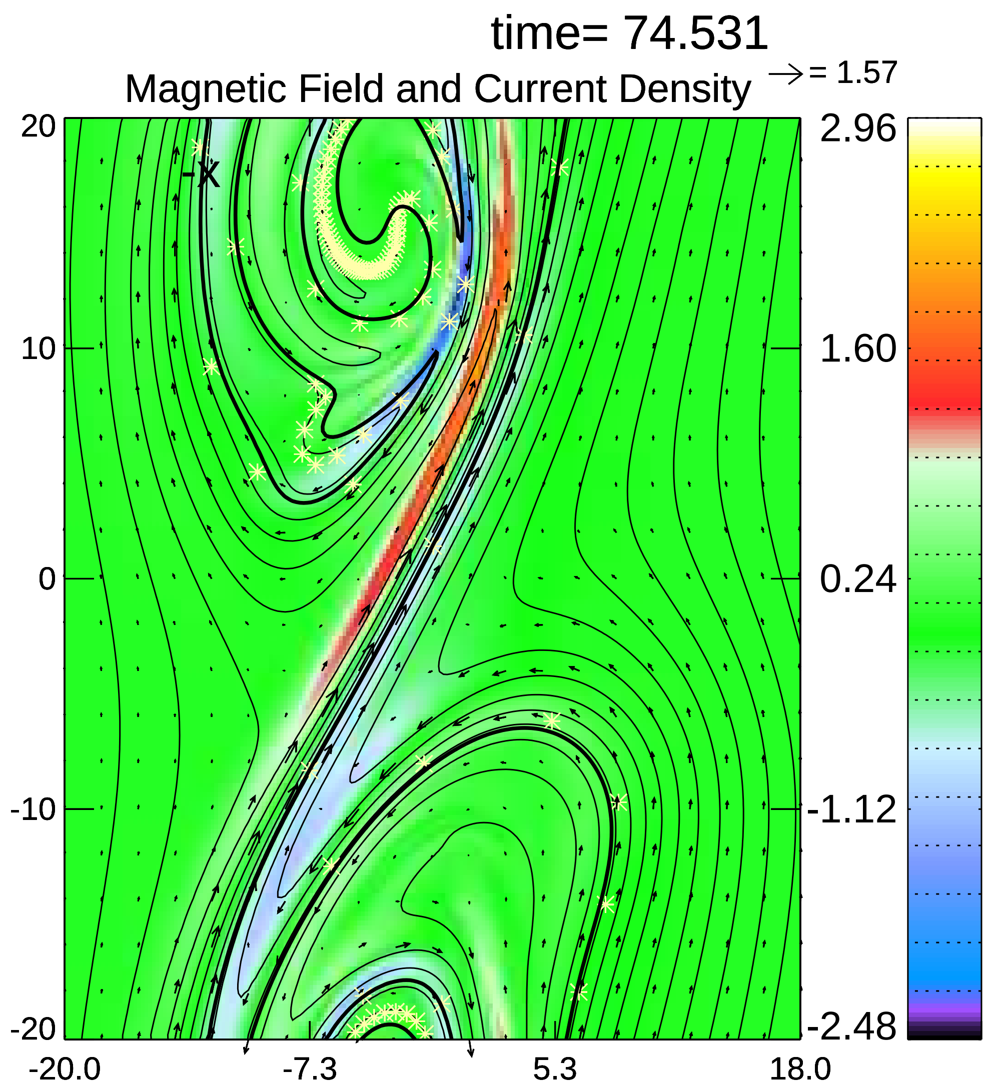

Figure 3.4. Magnetic field vectors (arrows), magnetic field lines and z-component of the current density (color code) for CASE 5 at time $\sim 74.5\ \tau_A$.

has twisted magnetic field in x, y-plane resulting in antiparallel magnetic field components. This leads to formation of strong negative and positive current layers adjacent to each other. Reconnection in the negative current layer at $x, y \approx$[13,-3] detaches a magnetic island from the magnetosheath.

The mass entry from the magnetosheath into the magnetosphere is calculated by integrating the density over the area of the detached magnetic islands. An averaged mass entry rate is determined by dividing the mass in the islands through a typical time (i.e. the time it takes to form a nonlinear wave). The results in Figure 3.5 are expressed in terms of an average entry velocity

$$v_{entry} = \frac{\Delta M}{\Delta t} \frac{1}{\rho_{sh} L_x} \tag{3.2}$$

where M is the mass of the magnetic island, Δt is the simulation time, L_x is the wavelength and ρ_{sh} is the magnetosheath density.

Figure 3.5 shows that mass entry starts at time $\sim$ 74.5, and the maximum rate is obtained at time $\sim$ 89.4 corresponding to the detached islands in Figure 3.3. Errors in the average velocity can be caused by the choice of Δt and inaccuracies of the island boundaries. The time Δt depends on the magnitude of the initial perturbation. In the simulation reconnection starts after about 8 growth times. A reduction of the initial perturbation by a factor of 10 would only change the derived entry velocity by $\sim$ 25 % because of the exponential growth of the mode.

Figure 3.6 shows the maximum mass entry rates of the 12 simulations and four additional cases with modified resistivity models 1b, 2, 3 and 4. The vertical bars present the error associated with the choice of the island boundary (numerical dissipation). In all cases the mass transport occurs from the magnetosheath into the magnetosphere. The mass entry velocities are of order several km s^{-1}. Assuming a magnetosheath density of 20 particles cm^{-3} and an entry velocity of 1.5 km s^{-1} it would take about an hour to replace the plasma in the plasma sheet with this process (for a plasma sheet density of 1 cm^{-3}) which is in good agreement with corresponding observations [*Borovsky et al.*, 1998]. The mass transport is lower for increasing angle φ, because of increasing stabilization of the KH instability. The scale on the right translates the average entry velocity into a diffusion coefficient for a boundary layer width of 1000 km.

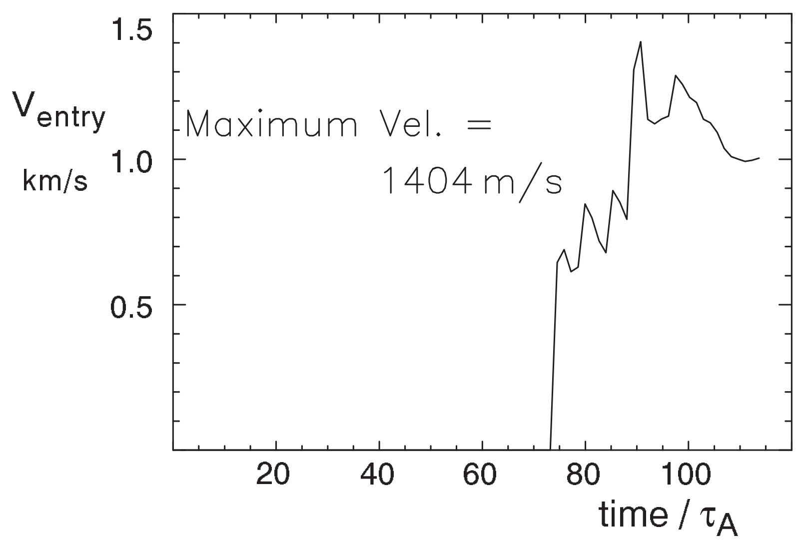

Figure 3.5. Mass entry velocity as a function of time for CASE 5 ($\varphi = 10$ ° and magnetosheath field strength 24 nT).

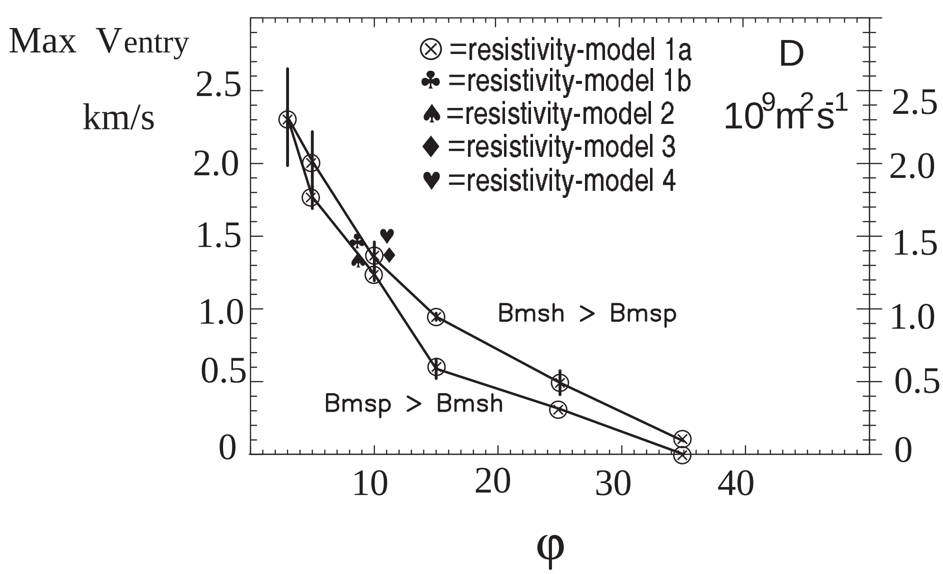

Figure 3.6. Maximum mass entry velocities with error bars as a function of φ for the cases of Table 3.1. The scale on the right axis presents the equivalent diffusion coefficient assuming a boundary layer width of 1000 km.

Figure 3.6 illustrates that magnetic field asymmetry does not have a major effect on average mass entry velocities. For increasing φ a larger asymmetry in the Alfvén speed contributes to the stabilization and may explain the larger relative difference for $\varphi > 15°$. In all cases reconnection always occurs first in the high density filament. We believe that this is caused by the higher inertial forces compared to magnetic forces in these regions of magnetosheath origin. The cases with the modified resistivity (including a 0 resistivity) yield the same mass entry rates within the error margin of the other cases. They demonstrate that the resistivity does not appear to alter the results significantly, and that the dynamics is strongly governed and driven by the ideal KH vortex evolution.

The average entry velocity should not depend much on the wavelength of the mode as long as inhomogeneities do not alter the growth significantly. In equation (2) the numerator scales with the square of the wavelength and the growth time is proportional to the wavelength such v_{entry} is to lowest order independent of the wavelength.

3.4 Discussion and Conclusions

Our 2-D MHD simulations indicate that during periods of northward IMF, magnetic reconnection inside Kelvin-Helmholtz vortices can provide a major mass transport mechanism from the solar wind into the magnetosphere. For single wave modes we obtain mass entry velocities of several km/s. This is in excellent agreement with observations [*Fujimoto et al.*, 1998a] which show the presence of high density and low temperature plasma blobs in plasma sheet, turbulent flow in a plasma sheet, and a 2-hour correlation in the plasma sheet density in response to changes in solar wind plasma [*Borovsky et al.*, 1998].

The mass entry is reduced for an increasing magnetic field in KH plane, because a larger parallel field stabilizes the KH wave. Our results indicate that considerable mass transport can be expected for magnetic field rotations of less than $\sim 50°$. An asymmetry of the magnetic field strength across the magnetopause does not have a significant influence on the plasma transport.

The presented two-dimensional results are a necessary first step to understand the plasma transport associated with KH modes. In two dimensions we have assumed that the magnetospheric boundary is represented by the initial shear flow boundary. A 2-D model does not provide any information on how magnetic field is connected in the third dimension which requires three-dimensional studies. In three dimensions we expect the process to produce a more complex magnetic connection with a portion of the LLBL on open field lines and a portion on closed field lines. While the precise quantitative transport may change in three dimensions, the basic mechanism and its properties will be present in three dimensions.

Another limitation of the present results is the assumption of MHD dynamics. In particular thin current sheets may require to include physics on the ion inertia scale. However, the presented results demonstrate that reconnection is strongly driven by the twisting of the magnetic field in the vortex motion. Changes caused by the resistivity are minor as long as the magnetic diffusion remains sufficiently small to permit the formation of the filamentary currents. Thus the net plasma transport might not be very sensitive to the details of the plasma approximation.

Chapter 4

Influence of the Hall Term on KH Instability and Reconnection inside KH Vortices

4.1 Introduction

In Chapter 3 we estimated plasma transport associated with Kelvin-Helmholtz modes using an MHD approximation. When the thickness of the boundary layer approaches the ion inertia scale, c/ω_{pi}, the Hall-term in generalized Ohm's law becomes important. By including the Hall term, $\mathbf{J} \times \mathbf{B}$, in the system of equations describing plasma dynamics, one can show that the magnetic field becomes frozen into the electron fluid: $\mathbf{E} = -\mathbf{v_e} \times \mathbf{B}$ (see Appendix B).

Newton's 1st law states that "an object at rest tends to stay at rest and an object in motion tends to stay in motion with the same speed and in the same direction unless acted upon by an unbalanced force." Inertia is a property of the mass to resist changes in their state of motion when a force is applied on it. When plasma is disturbed by some external force, electrons react faster to the changes due to their smaller inertia than ions. Electrons thus stay frozen into a magnetic field but the ions lose their magnetic connection due to their larger inertia. The inertia length, $c/\omega_p = \sqrt{\frac{c^2 m \epsilon_0}{ne^2}}$, is 43 times larger for ions than for electrons. If we assume plasma number densities between 5-11/cm^3, the ion inertia length varies between 68-100 km. Another important length scale is the gyroradius $r_L = v_\perp m/qB$, which for protons can be approximated from the formula $1.3{\cdot}10^3 \cdot \sqrt{T_i}/B$, where T_i is the proton temperature in 10^6 K and B is magnetic field strength in nT. If we assume proton temperatures of $T_i = 5 \cdot 10^6$ K and B =20 nT, $r_L = 145$ km which is close to ion inertia length scale at the magnetotail low latitude boundary layer. In the regions where plasma β is close to one, the inertia length scales of protons and electrons are close to their gyroradius (larmor radius).

Fujimoto and Terasawa [1991] included both the Hall term and electron pressure term in the generalized Ohm's law, linearized and numerically solved these extended MHD equations in parallel ($\mathbf{V_0} \parallel \mathbf{B_0}$) and perpendicular ($\mathbf{V_0} \perp \mathbf{B_0}$) configurations. Their simulation results indicate that ion inertia effect doesn't alter the growth rates significantly nor the fastest growing wave numbers of the KH instability compared to MHD cases. They found however, that the interior structure of the surface ripples seems to be more complicated than the corresponding results from the MHD analysis indicate, and that the ion inertia effect is most enhanced for the parallel configuration in a low β plasma.

Terasawa et al. [1992] observed fast anomalous ion mixing in a hybrid code simulation (particle ions and a massless electron fluid) in perpendicular configuration. Their simulation results show that the mixing occurs within a time scale comparable to roll-up time of the Kelvin-Helmholtz vortex. They consider this process to be responsible for generating the low latitude boundary layer.

Fujimoto and Terasawa [1994] further studied this anomalous mixing in a perpendicular configurations assuming a constant magnetic field across the initial shear flow layer. They conclude that the mixing layer formed by the KH instability is independent of the initial thickness of the boundary and that this mechanism could be in part responsible for generating the LLBL. In companion paper *Fujimoto and Terasawa* [1995] consider a more realistic configuration where the background magnetic field is inhomogeneous but still perpendicular to the initial shear flow layer. Their motivation was to solve whether KH mixing at the magnetopause alone can be efficient enough to produce the observed mixing layer at the LLBL. *Fujimoto and Terasawa* [1995] found that including the background inhomogeneity has a reduces ion mixing: 1) The KH vortex island area is smaller compared to homogeneous cases when the magnetosheath plasma beta and density ratio across the boundary is larger than one; 2) Magnetosheath ions are blocked out of the vortex island due to the electrostatic potential which becomes larger when the magnetic field inhomogenouity increases. *Fujimoto and Terasawa* [1995] also concluded that their initial [*Fujimoto and Terasawa*, 1994] estimate for ion mixing was too optimistic. When background plasma is nonuniform, the mixing efficiency becomes a function of the density ratio, the magnetic field ratio, plasma beta, the shear layer width and the wavelength of the growing mode.

Huba [1994] studied the effect of the Hall term on the Kelvin-Helmholtz Instability using a configuration where the ambient magnetic field is exactly perpendicular to the plasma and field dynamics. He found that the maximum velocities perpendicular to the initial shear flow layer are smaller than for ideal MHD cases, indicating that the Hall term acts to inhibit the vortex formation, as well as to relax sharp density and magnetic field gradients. He also studied the influence of positive ($\nabla \times \mathbf{V} > 0$) and negative ($\nabla \times \mathbf{V} < 0$) vorticity on the instability. His simulation results indicate that positive and negative vorticity cases are not mirror images of each other but that there is an asymmetry caused by magnetic drift mode waves, $\mathbf{B} \times \nabla \mathbf{n}$. For positive vorticity cases the boundary layer thickness grows from $a \approx 5$km to 140 km, whereas for cases with negative vorticity, the boundary layer broadens only from $a \approx 5$km to 90 km [*Huba*, 1994]. He also reported an enhanced diffusion of the magnetic field into the high density, low magnetic field region.

Huba [1996] used a 2-D finite larmor radius (FLR) MHD code to study the nonlinear evolution of the KH instability in a perpendicular ($\mathbf{V_0} \perp \mathbf{B_0}$), low plasma beta configuration. His simulation results indicate that the FLR effects arising from an anisotropic ion stress tensor in the momentum equation can either increase or decrease the growth rate of KH instability depending on the sign of $\mathbf{B} \cdot (\nabla \times \mathbf{V})$. A positive sign yields a larger growth rate than a negative sign which is opposite to the behavior of the real part of the frequency [*Huba*, 1996]. Similarly, like in his earlier paper [*Huba*, 1994], he suggests that the Kelvin-Helmholtz turbulence may be asymmetric with respect to the dawn and dusk flanks (vorticity changes sign at dawn and dusk) if the boundary layer is sufficiently thin; and that the high density plasma blobs can detach from the boundary layer and be transported into the low density region. *Huba* [1996] neglected the Hall term from his simulations in order to isolate and understand the FLR effects of the instability. His results [*Huba*, 1994, 1996] indicate that both the Hall term and the finite larmor radius effect may cause differences between the KH instability operating at dawn and dusk flanks at least in a perpendicular configuration.

In this chapter we study the effects of the Hall term on the evolution and dynamics of the KH instability for different initial configurations. We also complete our 2-D study of plasma transport associated with the KH instability by extending the MHD results to Hall-MHD regime and considering a realistic configuration where the magnetic field has a component along the **k**-vector of the instability. Our main motivation is to understand the ion inertia effect on reconnection inside Kelvin-Helmholtz vortices and whether this effect will alter the net plasma transport estimated with MHD approximation in Chapter 3.

4.2 Numerical Method

Most (except of *Thomas* [1995]) of the previous work [*Fujimoto and Terasawa*, 1991; *Terasawa et al.*, 1992; *Thomas and Winske*, 1993; *Fujimoto and Terasawa*, 1994, 1995; *Huba*, 1994, 1996], that include the ion inertia term or finite larmor radius effect on their simulations, use a perpendicular ($\mathbf{V_0} \perp \mathbf{B}$) configuration or a linearized set of extended MHD equations, or both.

Thomas [1995] studied KH instability with 3-D kinetic simulations using a uniform density embedded in the uniform magnetic field but let the relative angle of the magnetic field and the velocity vector vary. He found that when $\mathbf{V_0} \cdot \mathbf{B} = 0$ the ion mixing property in 2-D and 3-D simulations are almost the same. When $\mathbf{V_0} \cdot \mathbf{B} \neq 0$, the mixing is strongly reduced in 2-D but the 3-D results are not reduced by much.

The results in this chapter are obtained by solving a full set of resistive two-dimensional Hall-MHD equations (Chapter 2) in several magnetic field and plasma configurations (including realistic configurations with density and magnetic field asymmetry, and assuming that magnetic field has a component both perpendicular and parallel to the **k**-vector of the instability).

All quantities are normalized to characteristic values for the system, i.e., length scales l to a ion inertia length $L_0 = c/\omega_{pi}$; density ρ to $\rho_0 = n_0 m_0$ with the number density n_0 and the ion mass m_0; magnetic field $\mathbf{b}$ to B_0; velocity $\mathbf{v}$ to the typical Alfvén velocity $v_A = B_0/\sqrt{4\pi\rho_0}$; pressure to $P_0 = B_0^2/(8\pi)$; current density to $J_0 = cB_0/(4\pi L_0)$; and time

Table 4.1. Simulation Normalization

Magnetic field B_0	16 nT
Number density n_0	11 cm^{-3}
Current density	22 nA m^{-2}
Length scale L_0	100 km
Velocity v_A	105 km s^{-1}
Time τ_A	0.95 s

t to a characteristic Alfvén transit time $\tau_A = L_0/v_A$. The values for the normalization of the simulation units are summarized in Table 4.1.

The initial configuration for the simulation in the boundary coordinates uses a magnetic field of $b_{x0}(x) = b_0(x)\sin\varphi$, $b_{y0}(x) = 0$, and $b_{z0}(x) = b_0(x)\cos\varphi$. The velocity is given by $v_{x0}(x) = v_0(x)$, $v_{y0}(x) = 0$, and $v_{z0}(x) = 0$. Initial density, pressure, velocity, and magnetic field magnitudes are

$$\begin{aligned}
\rho_0(x) &= \frac{1}{2}(\rho_{sh} + \rho_{sp}) + \frac{1}{2}(\rho_{sh} - \rho_{sp})\tanh(\frac{y}{L_0}) \\
p_0(x) &= \frac{1}{2}(p_{sh} + p_{sp}) + \frac{1}{2}(p_{sh} - p_{sp})\tanh(\frac{y}{L_0}) \\
v_0(x) &= -\frac{1}{2}v_{sh}(\tanh(\frac{y}{L_0}) + 1) \\
b_0(x) &= \frac{1}{2}(b_{sh} + b_{sp}) + \frac{1}{2}(b_{sh} - b_{sp})\tanh(\frac{y}{L_0}),
\end{aligned}$$

The problem with the inclusion of the Hall-term is the increasing phase speed of the Whistler waves for short wavelengths. The Whistler phase speed, $v_{ph} = \omega/k$, is proportional to $\frac{\Delta x}{\Delta t}$ and increases since the higher resolution (small Δx) demands a very small integration time step, Δt. We were able to avoid the compressional effects due to Whistler waves by choosing $\Delta t = 0.02$ and making the system large enough in y-direction.

We study the effect of the Hall term in two different system sizes. The smaller system uses a simulation box of 25.2 units in x, corresponding to a wavelength of about 0.4 R_E or $ka = 0.25$, where a is the thickness of the velocity shear layer and k is the wave number. A large size of the simulation domain in y of 45.2 (approximately 0.7 R_E) is used to minimize the influence of the boundary conditions on the evolution of the KH waves, for instance, by reflection of waves from these boundaries (and effects of the Whistler waves). We use a nonuniform grid in y with maximum resolution of 0.1 in the center of the initial shear flow layer and a uniform grid in x with resolution of 0.12. The time step used in the simulation is $\Delta t = 0.02$. The larger system uses a simulation box of 51.2 units in x, corresponding to a wavelength of about 0.8 R_E or $ka = 0.12$. The simulation domain in y is 102.4 (approximately 1.6 R_E). The spatial and temporal resolution are same as for the smaller system size.

We study the influence of the Hall term with 17 different plasma and magnetic field configurations. The first two simulation sets have a magnetic field only along the **k**-vector of the instability and the remaining 15 simulation sets have magnetic field in both z-direction and along the **k**-vector. Simulation runs are listed in Table 4.2 in simulation units and indices 1,2 refer to magnetosheath and magnetospheric side respectively. Empty blocks indicate no change in parameter from the line above.

Simulation runs 1-7 have same parameters as the MHD simulations in Chapter 3 except for larger simulation domain in x-direction. In addition to the simulation runs listed in Table 4.2, we have simulated cases 8-12 with the MHD code (with exactly same parameters) for comparison. Runs 13-17 are shorter wavelength runs that are compared with longer wavelength cases 8-12. We use the following two resistivity models in these simulations:

$$\begin{aligned} \eta(j) &= \kappa\sqrt{(j^2 - {J_c}^2)}S(j^2 - {J_c}^2) \qquad (model\,1) \\ \eta(j) &= \kappa(j^2 - {J_c}^2)^2 S(j^2 - {J_c}^2) \qquad (model\,2) \end{aligned} \tag{4.1}$$

Here $\kappa = 0.005$ and $J_c = 1.1J_0$ for model 1 which corresponds to model 1a) in MHD simulations of Chapter 3. Model 2 uses $\kappa = 0.001$ and $J_c = 2.5J_0$. S is a step function equal to unity for arguments greater than 0 and equal to 0 otherwise.

Table 4.2. Simulation Runs

	ka	φ	B_1	B_2	n_1	n_2	$\frac{\Delta\rho}{\Delta y_\rho}$	Res. model	viscosity
CASE 1	0.25	90°	0.15	0.1	1.	1.	0	2	0.04
CASE 2	0.25	90°	0.15	0.1	1.65	0.35	0.59	2	0.04
CASE 3	0.12	3°	1.5	1.0	1.75	0.25	0.25	1	0.015
CASE 4		5°							
CASE 5		10°							
CASE 6		15°							
CASE 7		25°							
CASE 8	0.12	3°	1.5	1.0	1.65	0.35	0.59	2	0.04
CASE 9		5°							
CASE 10		10°							
CASE 11		15°							
CASE 12		25°							
CASE 13	0.25	3°	1.5	1.0	1.65	0.35	0.59	2	0.04
CASE 14		5°							
CASE 15		10°							
CASE 16		15°							
CASE 17		25°							

4.3 Demonstration of the Hall Effect (Simulation Results Without Background B_z)

4.3.1 Magnetic Field Asymmetry (CASE 1)

Figures 4.1 and 4.2 show evolution of the Kelvin-Helmholtz vortex for CASE 1 at $t/\tau_A \approx 60$ and at t/τ_A 82 In Figures 4.1 lines are magnetic field lines projected to x, y -plane and arrows are electron velocity vectors. Color coded is the electron current (left) and the z component of the magnetic field (right). Yellow asterisks are fluid elements that are located initially at the boundary $y = 0$. At $t/\tau_A \approx 60$ a vortex is clearly visible with narrow electron current layers of opposite polarity forming in the center of the simulation box. The Hall effect also starts generating an out-of-the-plane magnetic field component. At $t/\tau_A \approx 82$ a highly nonlinear vortex has formed with very strong electron current layers. Ongoing reconnection is observable in the positive electron current layer at $x, -y$ = [6.3, 2.0] and at negative electron current layer at $x, -y$ = [-6.3, -2.7]. Reconnection is not symmetric because the initial configuration had a magnetic field asymmetry. If the magnetic field is exactly the same on both sides of the initial shear flow layer, magnetic reconnection would happen at the same rate in both negative and positive current layers forming a symmetric structure. Strong quadrupolar, out-of-the-plane magnetic field structure is formed in the center of the simulation box. The strongest, negative B_z layer is located between the strong current layers of opposite polarity. The strongest, positive B_z layers are in the current sheet regions with the largest electron flow velocities (accelerated flow from reconnection region).

In Figure 4.2 arrows are plasma velocity vectors, the color code represents ion current (left) and total current (right). At $t/\tau_A \approx 60$ a vortex is clearly visible but there is no ion current. The total current is dominated by the electrons. At $t/\tau_A \approx 82$ the ion current increases in two regions where there is no electron current and where the plasma velocity is very slow. The total current which is mostly carried by electrons has a maximum in reconnection regions at $x, -y$ = [6.3, 2.0] and at $x, -y$ = [-6.3, -2.7].

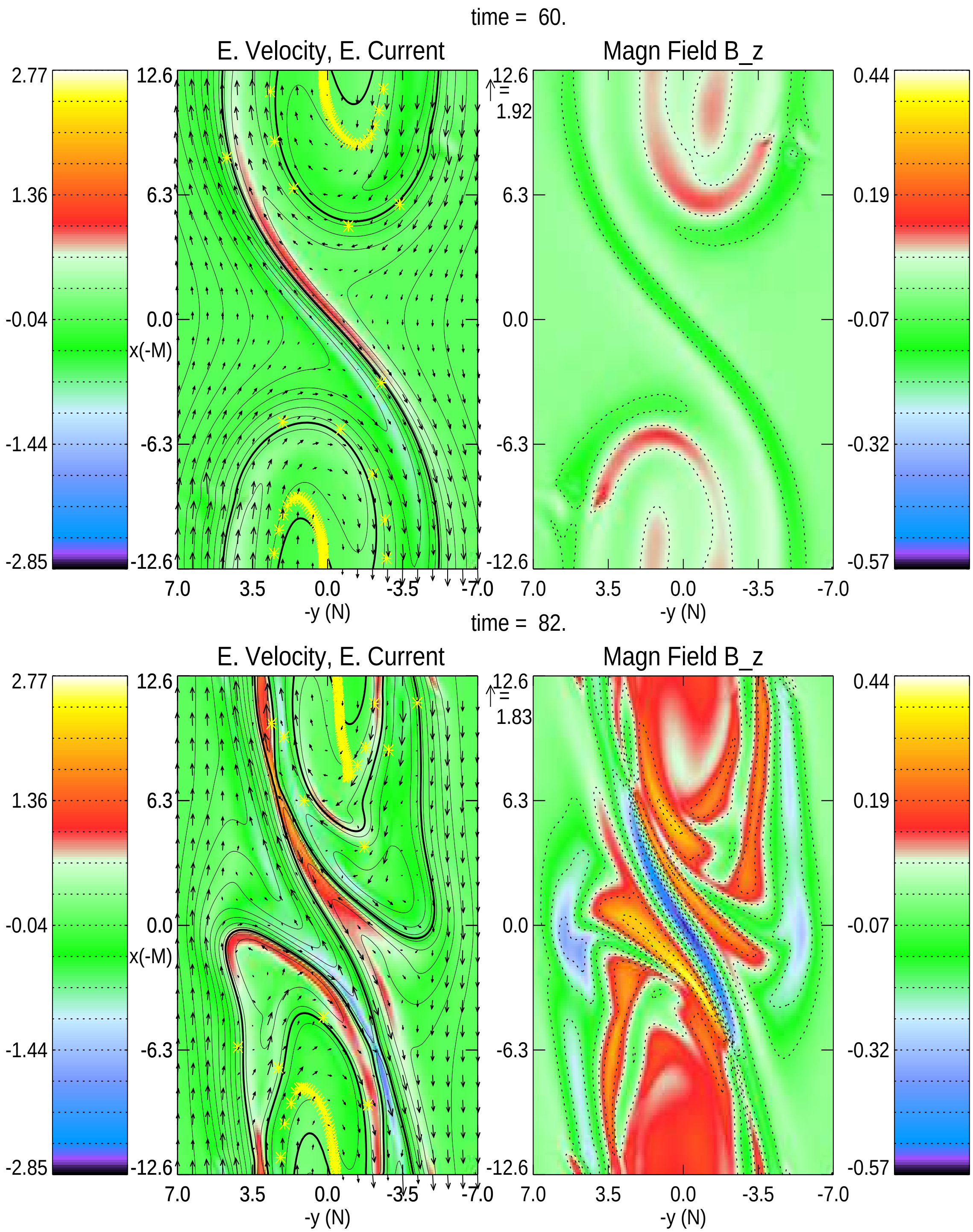

Figure 4.1. KH vortex at $t/\tau_A \approx 60$ and at $t/\tau_A \approx 82$. Lines are magnetic field lines projected to x, y -plane and arrows are electron velocity vectors. Color code represents electron current (left) and z component of the magnetic field (right).

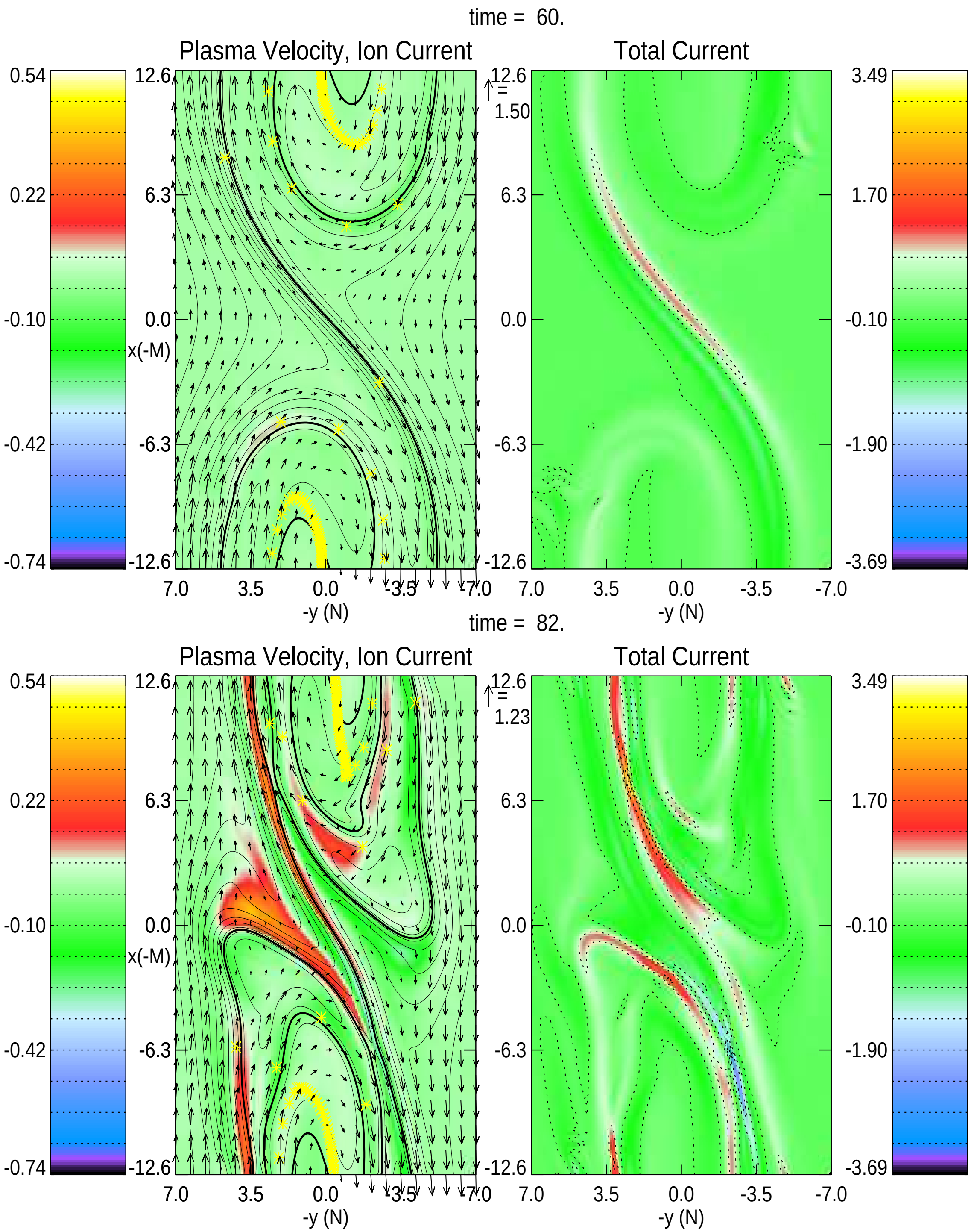

Figure 4.2. KH vortex at $t/\tau_A \approx 60$ and at $t/\tau_A \approx 82$. Lines are magnetic field lines projected to x, y -plane and arrows are plasma velocity vectors. Color code represents ion current (left) and total current (right).

4.3.2 Magnetic Field and Density Asymmetry (CASE 2)

Figures 4.3 depicts a KH vortex at $t/\tau_A \approx 63$ and at $t/\tau_A \approx 81$. Lines are magnetic field lines projected to x, y -plane and arrows are electron velocity vectors. The color code represents plasma density. Kelvin-Helmholtz instability twists the magnetic field in the x, y-plane which leads to anti-parallel magnetic field components. A high density magnetic island gets reconnected at $t/\tau_A \approx 63$, and a second island is detached at $t/\tau_A \approx 81$. Compared to CASE 1, the reconnection occurs 20 τ_A earlier for CASE 2. The density asymmetry across the shear flow boundary seems to increase the reconnection rate for Kelvin-Helmholtz instability.

Figure 4.4 shows magnetic field lines projected to the x, y -plane and arrows are electron velocity vectors. Color coded are electron current (left) and the z component of the magnetic field (right) at $t/\tau_A \approx 63$ (top) and at $t/\tau_A \approx 81$ (bottom). At $t/\tau_A \approx 63$ reconnection occurs at $x, -y$ = [3,0] in a region of negative electron current. A positive, elongated electron current layer is located adjacent to a strong magnetic field layer. A weak, negative B_z layer starts forming in the elongated regions of enhanced magnetic field. At $t/\tau_A \approx$ 81 a second magnetic island is detached at $x, -y$ = [-11,-5] and the negative B_z layers are intensified.

In Figure 4.5 arrows are plasma velocity vectors and the color code represents ion current (left) and total current (right) at $t/\tau_A \approx 63$ and at $t/\tau_A \approx 81$. At $t/\tau_A \approx 63$ (top) the first magnetic island is detached in the region where total current (top right) is negative. At $t/\tau_A \approx 81$ (bottom) a second magnetic island is detached at $x, -y$ = [-11,-5] in the negative current layer. The positive current has increased but it is not distributed along the elongated layer like at $t/\tau_A \approx 63$.

4.4 Results of the Plasma Transport

In Chapter 3 plasma transport associated with the Kelvin-Helmholtz instability was estimated using an MHD approximation. Here I study the influence of the Hall effect on plasma transport and compare the results with the MHD cases.

The mass transport is calculated by integrating the plasma density over magnetic islands (flux ropes) captured from the magnetosheath, i.e., islands of magnetosheath material which are entirely embedded in the magnetosphere. The method of defining the initial boundary

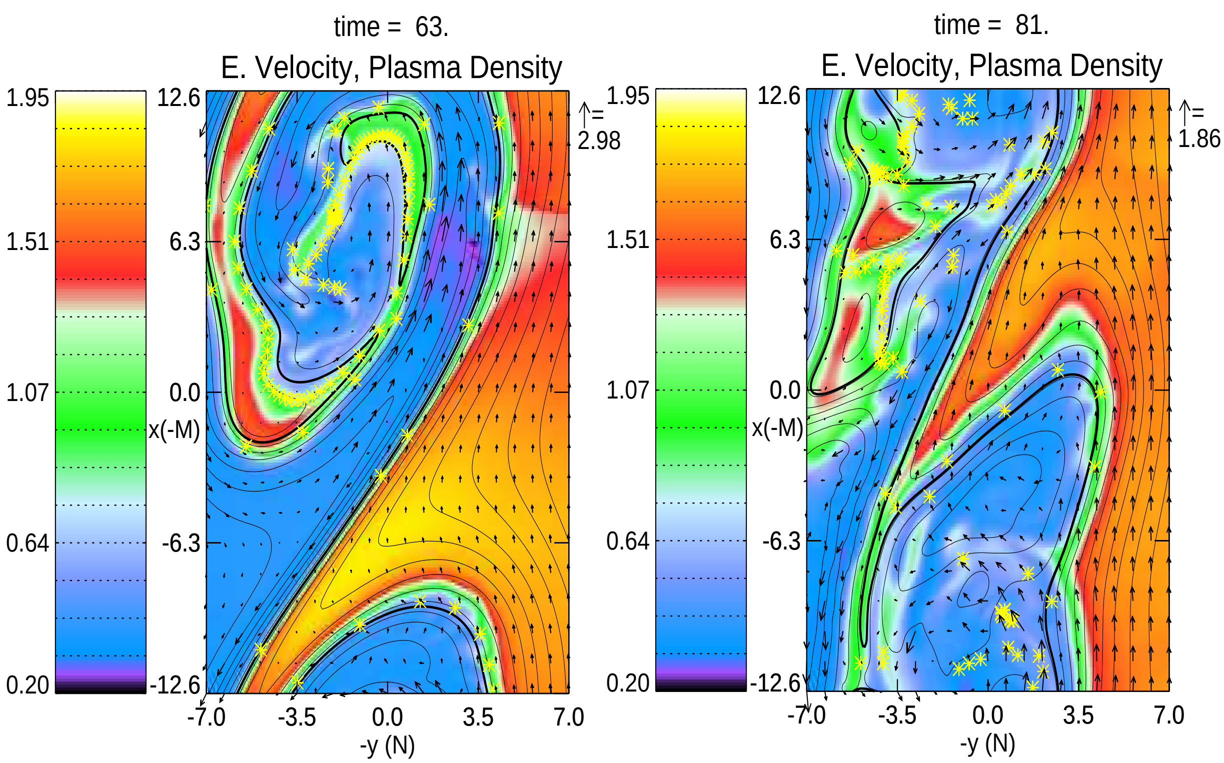

Figure 4.3. KH vortex at $t/\tau_A \approx 63$ and at $t/\tau_A \approx 81$. Lines are magnetic field lines projected to x, y -plane and arrows are electron velocity vectors. Color code represents plasma density.

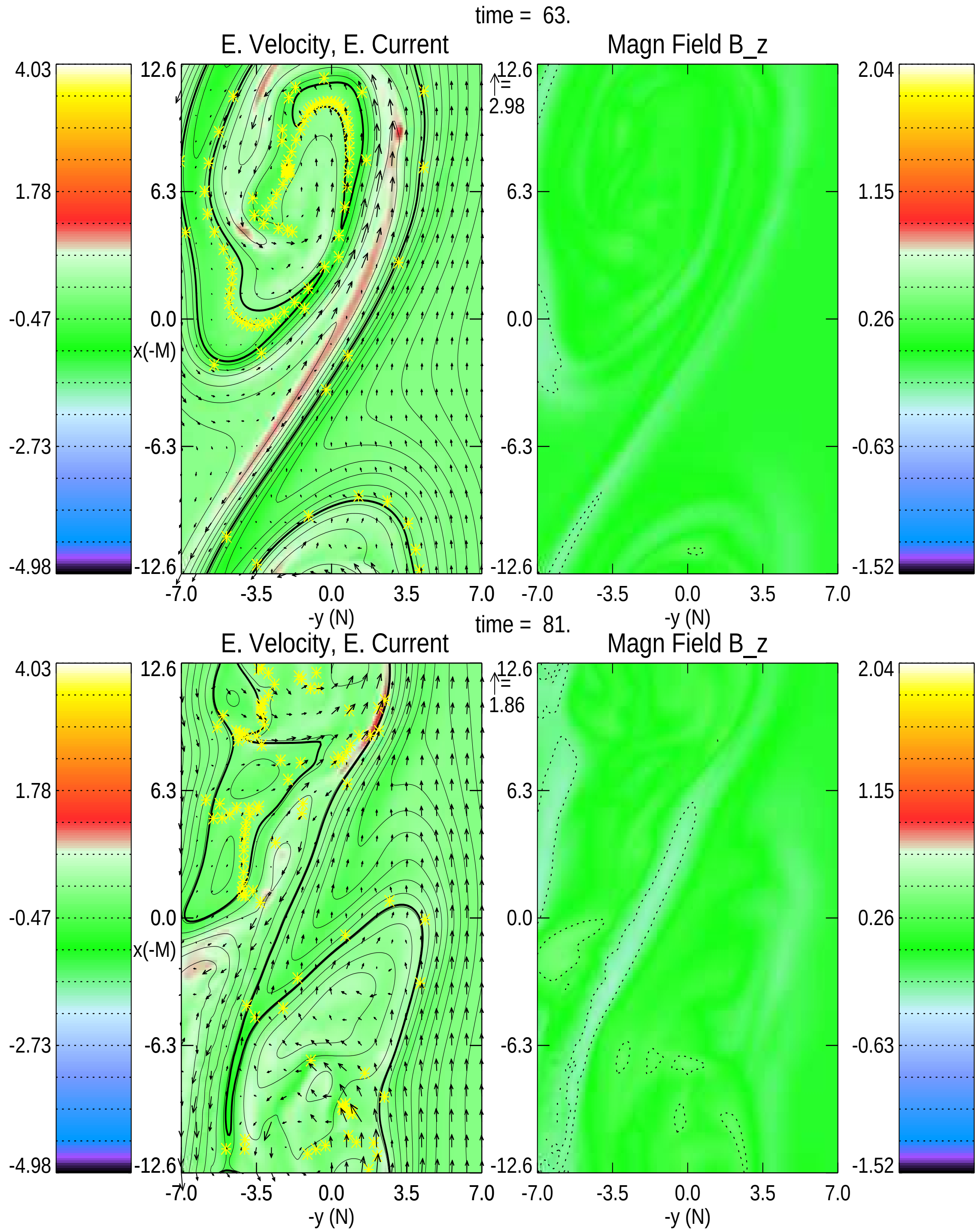

Figure 4.4. KH vortex at $t/\tau_A \approx 63$ and at $t/\tau_A \approx 81$. Lines are magnetic field lines projected to x, y -plane and arrows are electron velocity vectors. Color code represents electron current (left) and z component of the magnetic field (right).

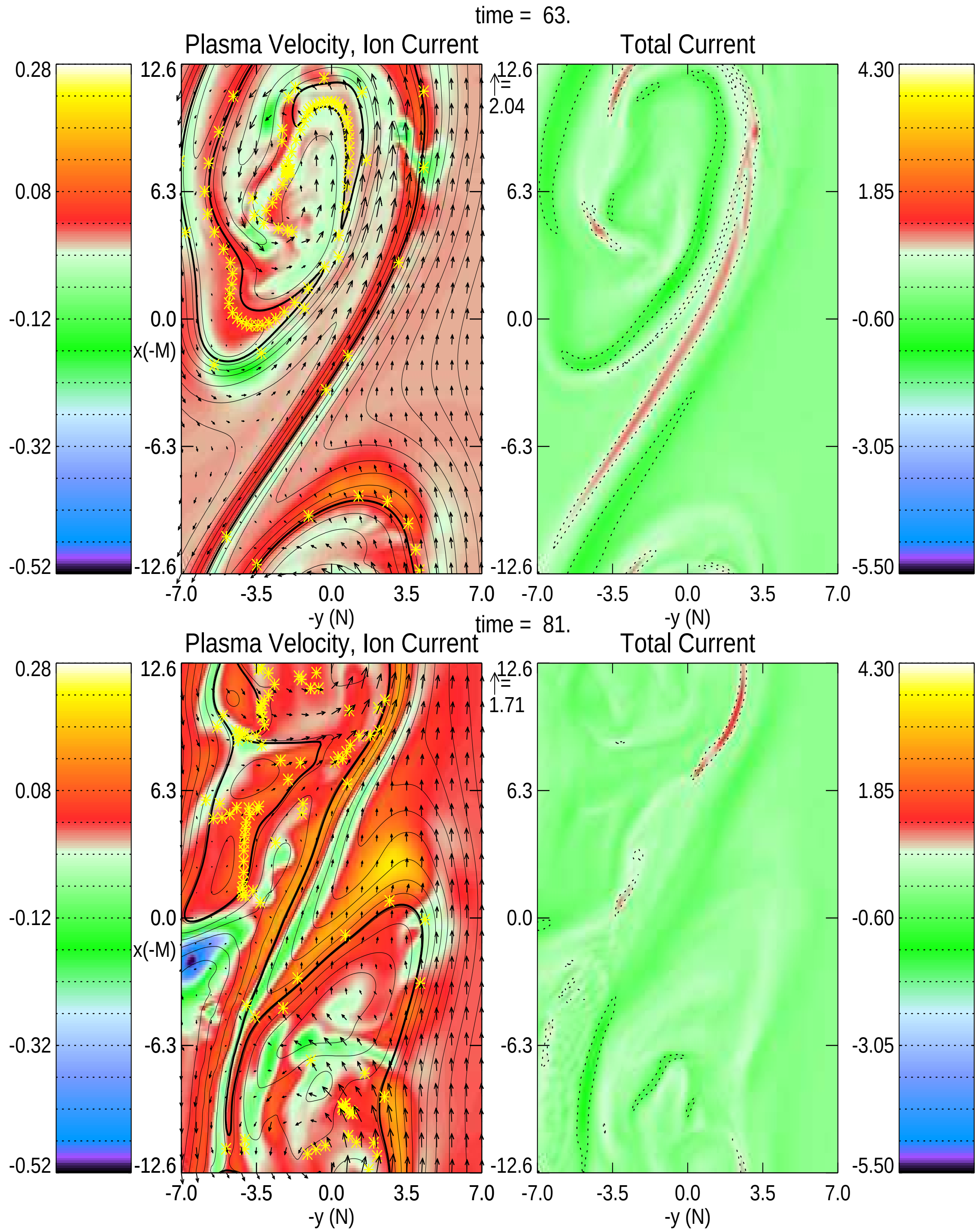

Figure 4.5. KH vortex at $t/\tau_A \approx 63$ and at $t/\tau_A \approx 81$. Lines are magnetic field lines projected to x, y -plane and arrows are plasma velocity vectors. Color code represents ion current (left) and total current (right).

is similar to the one discussed in Chapter 3 but here the magnetic islands are defined by electron fluid elements. During the simulation, the location of these elements is determined by integrating the electron fluid velocity. Ideally the electron fluid elements stay on the same field line if the magnetic field is frozen into the electron fluid flow (see Appendix B). However, reconnection and numerical dissipation can break this condition.

In two dimensions Ohm's law (including the Hall term) can be written as

$$\frac{\partial A_z(t)}{\partial t} + (\mathbf{V_e} \cdot \nabla) A_z(t) = -\eta J_z. \tag{4.2}$$

A_z is the z-component of the magnetic vector potential and changes along the path of a fluid element are only due to the resistive term on the right side of (1) if the initial gauge of A_z is maintained. If this is the case, a fixed value of A_z determines the magnetic boundary. Since A_z is determined by integrating the magnetic field, we use the electron fluid elements to determine the proper gauge and to test the frozen-in condition.

The mass entry from the magnetosheath into the magnetosphere is calculated by integrating the density over the area of the detached magnetic islands. An averaged mass entry rate is determined by dividing the mass in the islands through a typical time (i.e. the time it takes to form a nonlinear wave). The results in Figure 4.7, 4.8, and 4.9 are expressed in terms of an average entry velocity

$$v_{entry} = \frac{\Delta M}{\Delta t} \frac{1}{\rho_{sh} L_x} \tag{4.3}$$

where M is the mass of the magnetic island, Δt is the simulation time, L_x is the wavelength and ρ_{sh} is the magnetosheath density.

4.4.1 Demonstration of Plasma Transport and Growth Rates (CASES 3-7)

Figure 4.6 shows evolution of the Kelvin-Helmholtz wave for CASE 5 at $t/\tau_A \approx 62$ and at $t/\tau_A \approx 107$. Lines are magnetic field lines projected to x, y -plane and arrows are electron velocity vectors. Color represents plasma density (upper panel) and the z-component of the magnetic field (lower panel). The first magnetic island is detached at $t/\tau_A \approx 62$ and there is a depletion of B_z-component surrounding the reconnected island. Formation of this first island corresponds to the first peak in mass transport velocity in the Figure 4.7a. At

$t/\tau_A \approx 107$ the main magnetic island is detached by reconnection from the magnetosheath corresponding to the maximum mass diffusion velocity of 1.2 km/s in the Figure 4.7a.

Figure 4.7b illustrates the effect of the magnetic field along the $\mathbf{k}$ -vector of the KH instability for CASES 3-7. Plasma transport velocities are reduced for increasing φ ($B_x = B_0 \sin(\varphi)$) due to the stabilization of the KH instability by the magnetic field. Errors in the average velocity can be caused by the choice of Δt and inaccuracies of the island boundaries.

Figure 4.7c depicts the growth of the Kelvin-Helmholtz instability as a function of t/τ_A for $\varphi = 3°$, $5°$, $10°$, $15°$ and $25°$. Naturally, the largest growth rate, $q = 0.1$, is obtained for $\varphi = 3°$ and the smallest growth rate, $q = 0.09$, is obtained for $\varphi = 25°$. So the maximum linear growth rate is only about 10% larger than the minimum growth rate, but the corresponding maximum mass transport velocities for $\varphi = 3°$ and $25°$ differ by about 88%.

4.4.2 Comparison of Plasma Transport and Growth Rates Between MHD and Hall-MHD Simulations (CASES 8-12)

Figure 4.8a represents mass transport velocities as a function of φ for simulation runs 8-12. For comparison we also simulated these cases with the MHD code. Both plasma approximations give the same results within the limits of the error bars. The maximum plasma transport velocity, $V_{diff} = 1.8$ km/s is obtained for $\varphi = 3°$. The plasma transport is reduced for large φ due to the stabilization by the magnetic field.

Figure 4.8b and 4.8c show growth of the Kelvin-Helmholtz instability for the Hall-MHD and MHD approximations as a function of t/τ_A.

The largest growth rate, $q = 0.1$, is obtained for the Hall-MHD case with $\varphi = 3°$ and the smallest growth rate, $q = 0.07$, is obtained for the MHD case with $\varphi = 25°$.

For the Hall-MHD approximation the maximum linear growth rate is 24% larger than the minimum growth rate. For MHD simulations the maximum growth rate is only 13 % larger than the minimum growth rate. The Hall-MHD growth rates for $\varphi = 3°$, $5°$, $10°$, $15°$, and $25°$ are 21%, 17%, 13%, 13% and 7% larger than the corresponding MHD growth rates, respectively. The growth rates are larger for all the Hall-MHD cases compared to the corresponding MHD cases because in the Hall-MHD the magnetic field is frozen into the electrons and thus it doesn't stabilize the ion motion. This difference between MHD

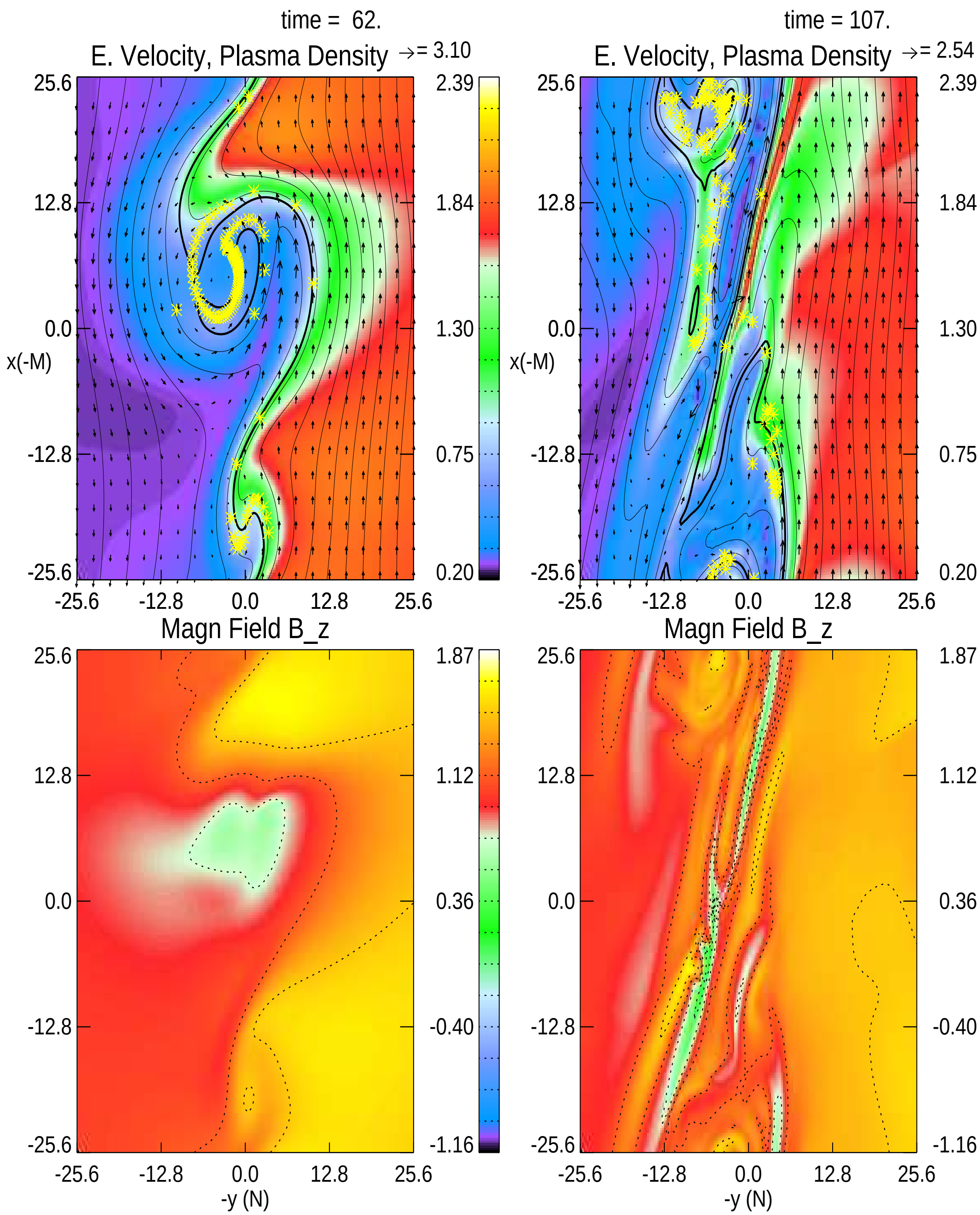

Figure 4.6. KH vortex at $t/\tau_A \approx 62$ and at $t/\tau_A \approx 107$ for CASE 5. Lines are magnetic field lines projected to x, y -plane and arrows are electron velocity vectors. Color code represents plasma density (upper panel) and z-component of the magnetic field (lower panel).

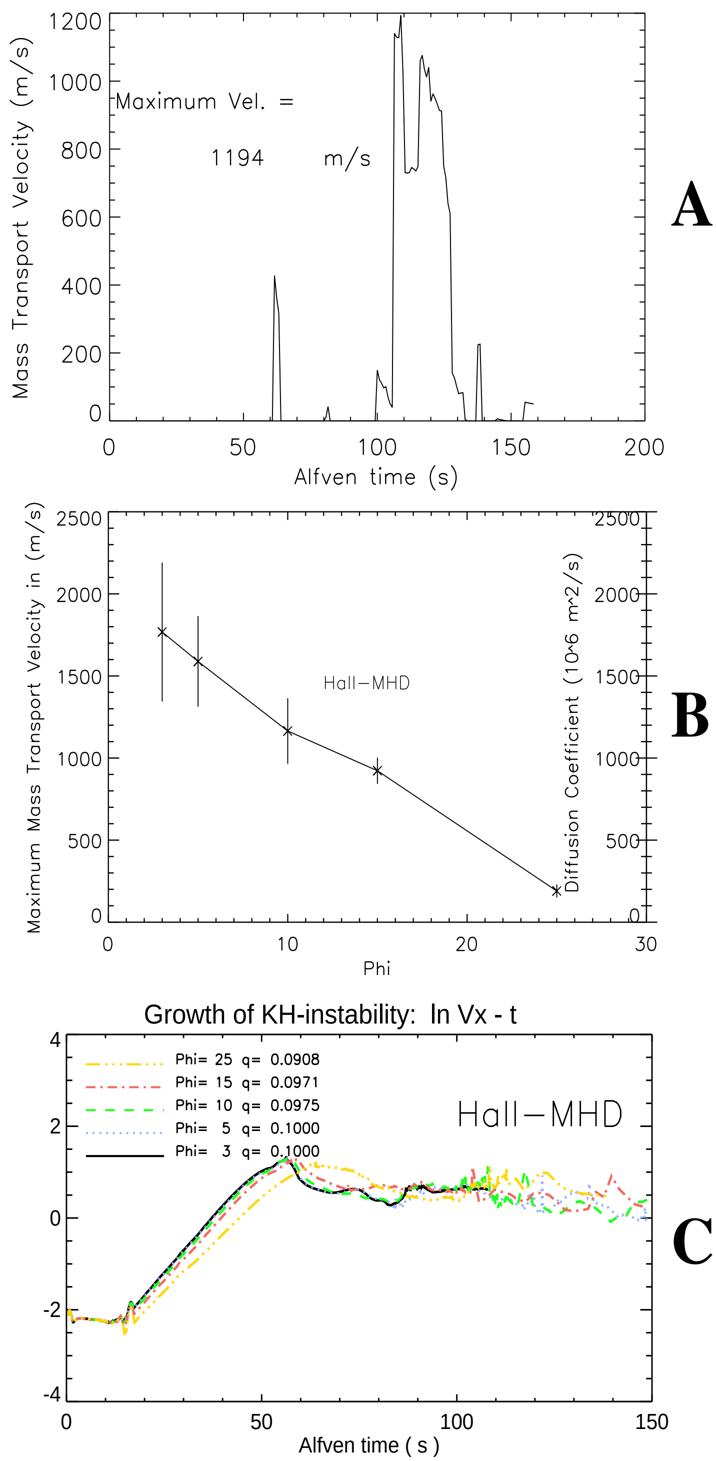

Figure 4.7. A) Mass transport velocity as a function of time for $\varphi = 10°$. B) Mass transport velocity as a function of φ. C) Growth of KH instability for $\varphi = 3°, 5°, 10°, 15°$ and $25°$.

and Hall MHD KH growth becomes smaller for larger magnetic field values along the **k**-vector of the KH mode. This appears counterintuitive at first glance because the smaller magnetization of ions due to the Hall physics should be more important for larger magnetic fields along the **k**-vector. However, the Hall effect also generates a perpendicular (out of the plane) magnetic field which is not present in MHD. The energy for this magnetic field generation must come from the kinetic flow energy such that this effect should act to reduce the growth rate for Hall dynamics in particular for larger magnetic field values along the **k**-vector. Thus the combined effect of the of the demagnetized ions and of the perpendicular magnetic field generation may account for the smaller difference of Hall MHD and MHD growth rates for larger magnetic field along the **k**-vector.

Except for the case with $\varphi = 3°$, the Hall-MHD growth rates are slightly larger for simulations runs 3-7 than for cases 8-12. This is probably due to the lower viscosity and smaller density gradient used in runs 3-7. Hall-MHD mass transport velocities agree for small φ, between cases 3-4 and 8-9, but are smaller for cases 10-12 than for cases 5-7. In Chapter 3 it was shown that reconnection inside Kelvin-Helmholtz vortices is independent of the resistivity model since the reconnection is strongly driven by the vortex motion. I assume that the discrepancy between plasma transport velocities for large φ is due to the increased stabilization of the KH mode both by larger viscosity used in runs 8-12 and by large magnetic field.

4.4.3 Demonstration of the Wavelength Effect on the Plasma Transport (CASES 13-17)

Figure 4.9a represents mass transport velocities for the small wavelength ($ka = 0.25$) cases 13-17. These results agree (within error bars) with mass transport velocities obtained for large wavelength cases 8-12 ($ka = 0.12$). Figure 4.9b shows KH growth for $\varphi = 3°$, $5°$, $10°$, $15°$, and $25°$. The short wavelength growth rates are about 40% larger than the large wavelength growth rates. The maximum linear growth rate is 25% larger than the minimum growth rate for $ka = 0.25$. At $t/\tau_A \approx 60$ this fast growing, small wavelength mode is clearly observable in Figure 4.6. It grows faster into a non-linear stage and decays before reconnection occurs at the vortex of the larger wavelength.

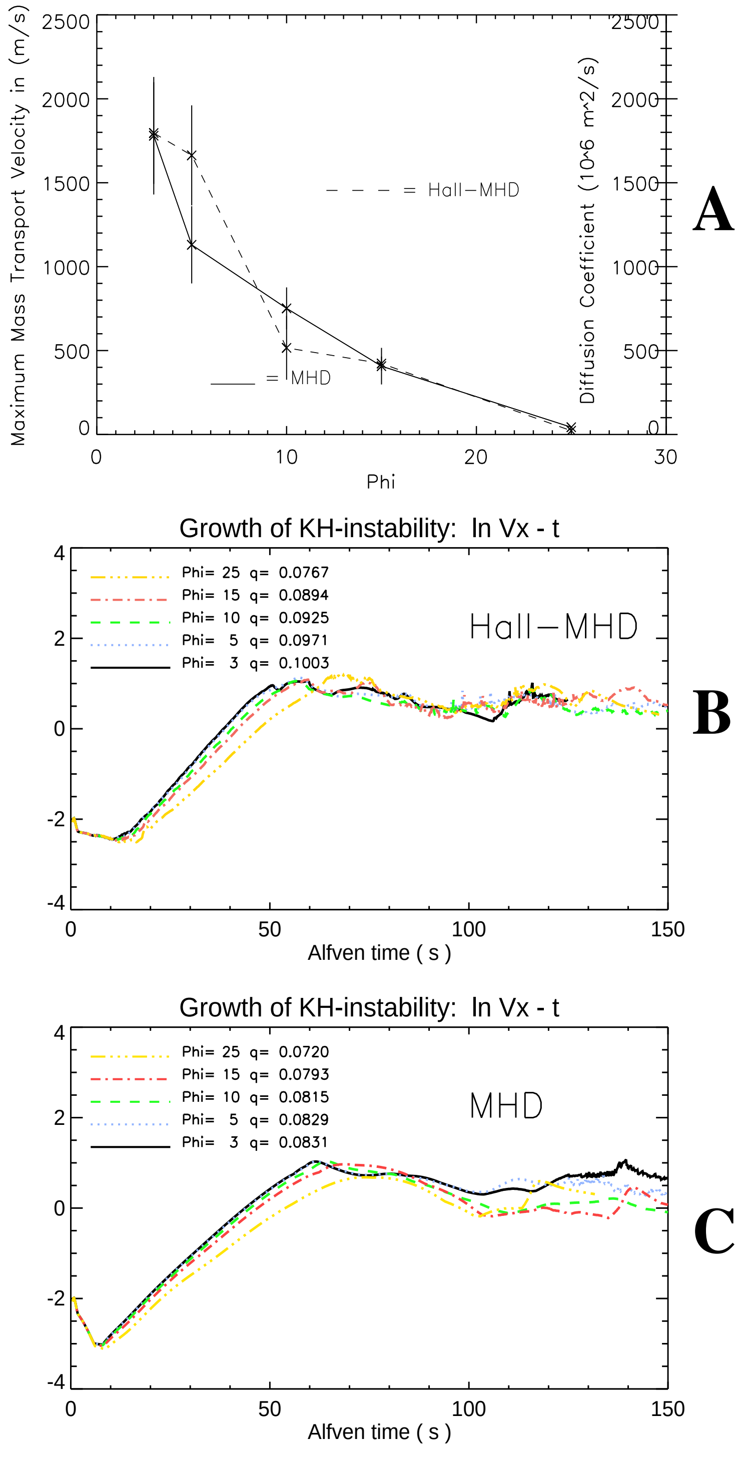

Figure 4.8. A) Mass transport velocity as a function of φ for MHD and Hall-MHD. B) Growth of KH instability for $\varphi = 3°, 5°, 10°, 15°$ and $25°$. for Hall-MHD approximation. C) Growth of KH instability for MHD approximation.

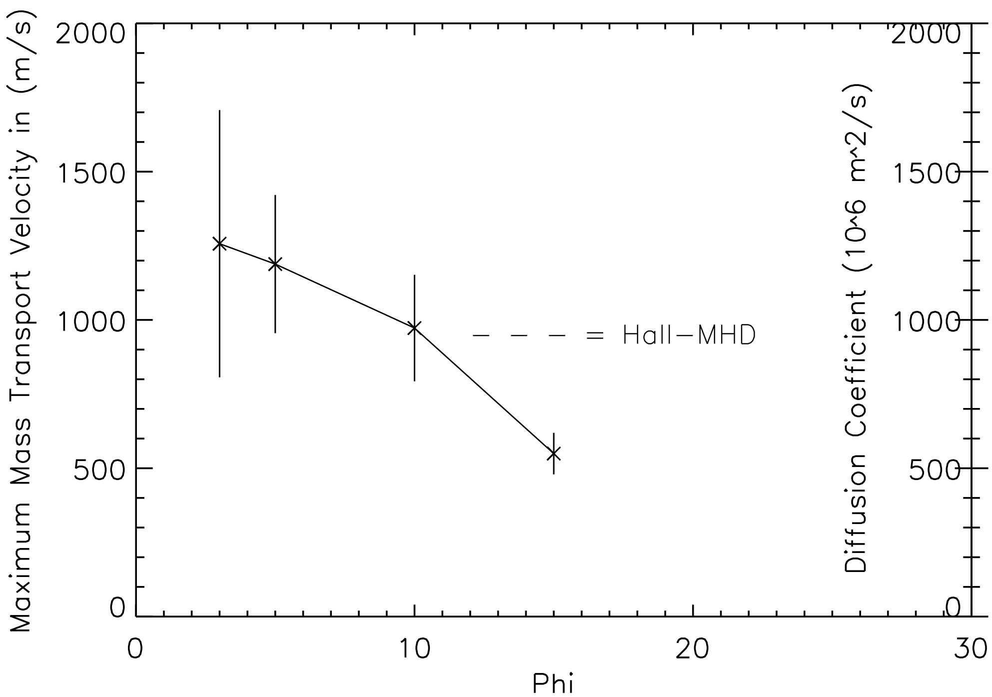

A

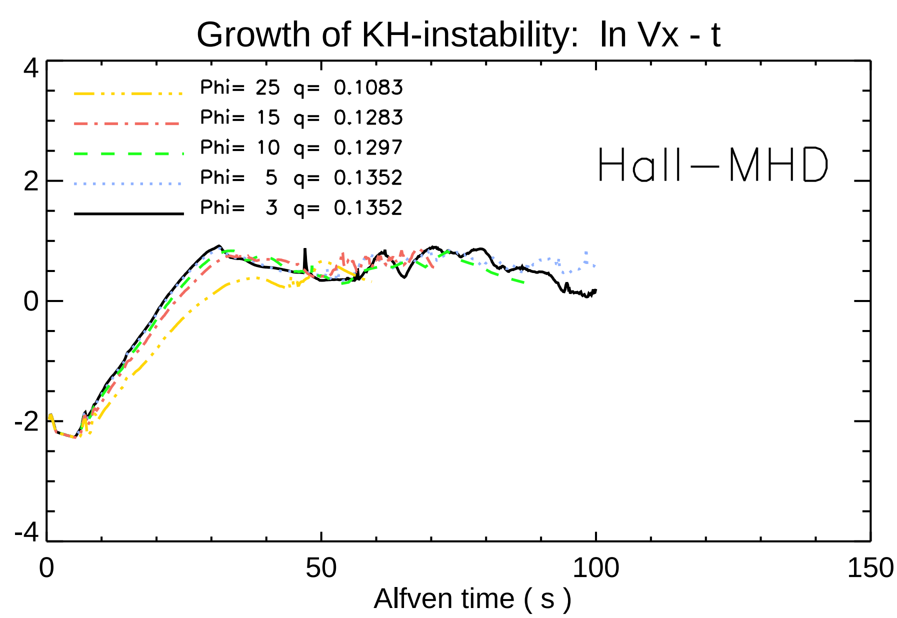

B

Figure 4.9. A) Mass transport velocity as a function of φ for short wavelength ($ka = 0.25$, $\lambda = 0.4R_E$) Hall-MHD. B) Growth rates of KH instability for $\varphi = 3°$, $5°$, $10°$, $15°$ for Hall-MHD approximation.

Huba [1994] got growth rates of $q \approx 0.04V_0/a$ for both MHD and Hall-MHD approximations for $ka = 0.26$. For the values of $V_0 = 315$km/s and $a = 100$km used in the simulation study of this Chapter, the growth rate obtained by *Huba* [1994] becomes $q \sim 0.126$, which is comparable to the values presented in Figure 4.9b. *Fujimoto and Terasawa* [1991] report little affect of Hall dynamics on the linear growth rate of the Kelvin-Helmholtz instability for $ka < 0.4$.

4.5 Turbulence in the Ion Inertia Scale

Huba [1994] reported Hall effect to cause small-level turbulence (ka >1) that inhibits vortex formation. We also found this small-level, ion inertia scale turbulence in our simulations. The most clearly structured, small scale vortices we found for $\varphi = 5°$ (CASE 4). Figure 4.10a represents electron velocity (arrows) and plasma density (color code) at $t/\tau_A \approx 93$. and Figure 4.10b shows the B_z component of the magnetic field. Magnetic field lines are not plotted on these figures in order to distinguish the small scale structure better. One can see two vortices in figure 4.10a, one corresponding to a $ka = 0.12$ and the other $ka = 0.25$. Figure 4.10c represents a magnified region of Figure 4.10a revealing a chain of small scale vortices with a wavelength of approximately 1 to 1.5 c/ω_{pi}. Turbulence appeared first in the smaller wavelength (ka >0.25) vortex at $t/\tau_A \approx 90$. This structure existed for 9 τ_A before the vortex decayed. Small scale turbulence is observed for all cases 3-8, but the longest lasting structures are obtained for small angles $\varphi = 3°, 5°$. In these cases the turbulence "attacks" the high density, small wavelength ($ka = 0.25$) vortex resulting in vortex decay. The dynamical evolution of the larger vortex is not altered by this ion inertia length turbulence. For larger angles ($\varphi = 10°$ and $15°$) the turbulence doesn't cause a decay of the smaller, high density vortex but works mostly in the "edges" of the higher density region, mixing "intermediate" density plasma with the lowest density plasma. For $\varphi = 25°$, the small scale turbulence was strongly reduced. We also studied the effect of zero magnetic field in the simulation plane using a perpendicular configuration ($\mathbf{k} \perp \mathbf{B}$) to see whether this small scale turbulence is further enhanced from cases with $\varphi = 3°$ and $5°$. For $\varphi = 0°$, the growth rate of KH is larger and overall dynamics is more turbulent due to the lack of magnetic field stabilization, so the system was already in the saturation stage when the small scale turbulence started affecting a narrow high density layer. It's also worth mentioning that, while *Huba* [1994] observed this small scale turbulence to inhibit vortex formation, in our simulation the main vortices were already fully developed before the small scale turbulence started decaying the smaller vortex.

Figure 4.11 shows magnification of Figure 4.10a for different plasma and field properties. Figure 4.11a represents electron velocity (arrows) and plasma density (color code) on the left, and the z-component of the magnetic field on the right. Figure 4.11b depicts plasma velocity (arrows) and ion current (color code) on the left, and total current on the right. Magnetic field (arrows) and electron current (color code) are plotted on the left of Figure 4.11c and z-component of the velocity is plotted on the right. A comparison between Figures 4.11a and 4.11b indicates that regions of high plasma density correspond to regions of negative ion current. Similarly, the positive ion current regions correspond to the regions of low plasma density. Positive ion current regions correlate also with regions of positive plasma velocity. The magnetic field reverses sign across the positive electron current layer. Since the magnetic field is frozen into the electron fluid, a depletion in B_z is formed in the regions of strong positive electron current (electrons traveling into the -z -direction). In the regions of negative ion current, there is a large positive electron current, so in these regions the electrons and protons are traveling into same direction reducing the total current in these regions.

4.6 Discussion and Conclusions

In this Chapter it has been demonstrated that the net plasma transport due to reconnection inside Kelvin-Helmholtz vortices is unaltered in a Hall-MHD approximation for the considered cases. For small φ cases (corresponding to strongly northward interplanetary magnetic field) we estimate the mass diffusion velocities to be about 1.5 km/s. If we assume a solar wind density of 11/cm^3 and plasma sheet density of 1/cm^3, it would take about 2 hours to replace all the mass in the plasma sheet with this process. This is in excellent agreement with observations by *Borovsky et al.* [1998] and *Fujimoto et al.* [1998a] which indicate that during periods of strongly northward IMF the cold dense plasma sheet is formed in a time scale of about two hours.

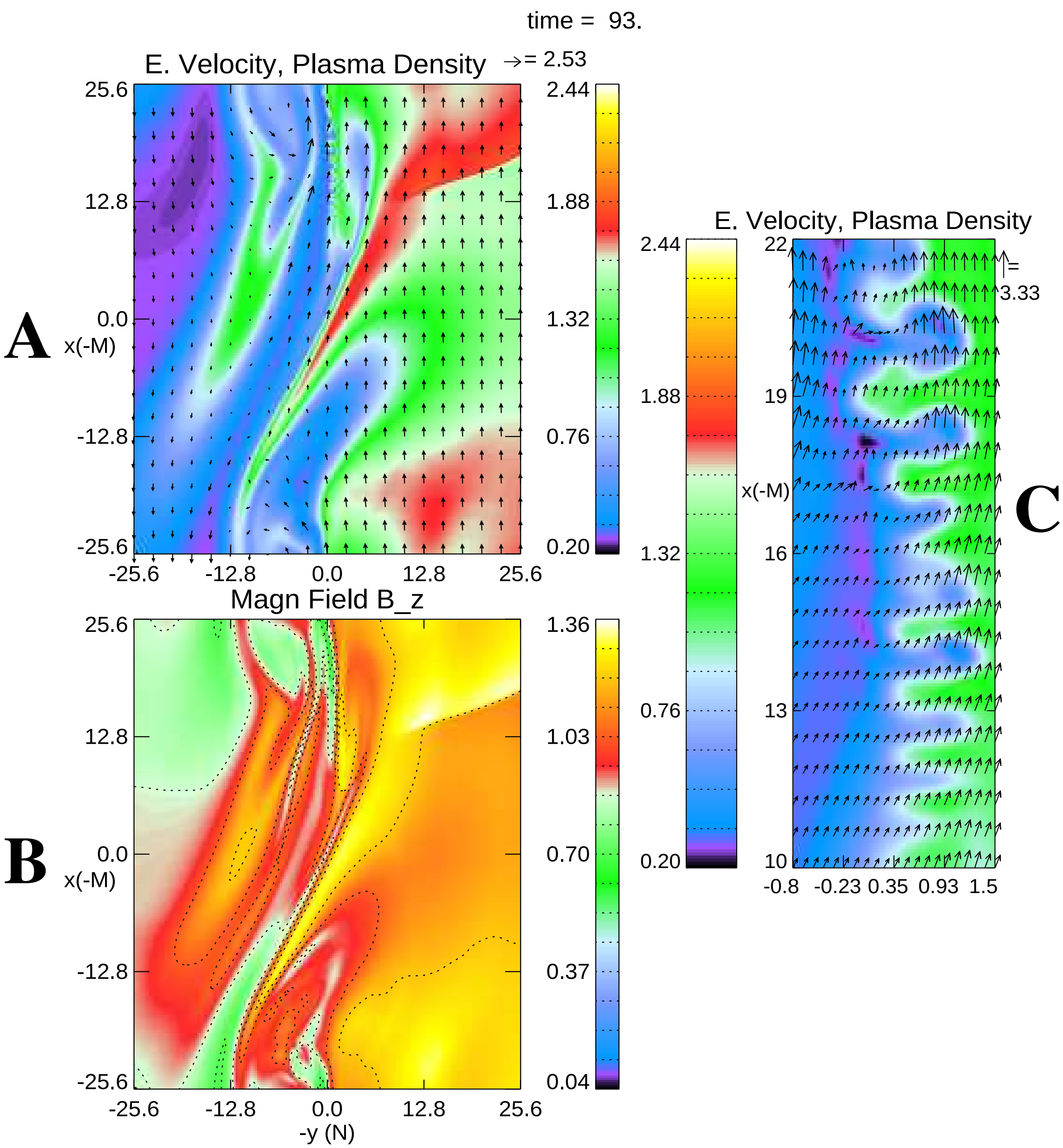

Figure 4.10. KH vortex for $\varphi = 5$ at $t/\tau_A \approx 93$. A) shows electron velocity (arrows) and plasma density (color code). B) represents z-component of the magnetic field. C) is a magnified domain of figure A).

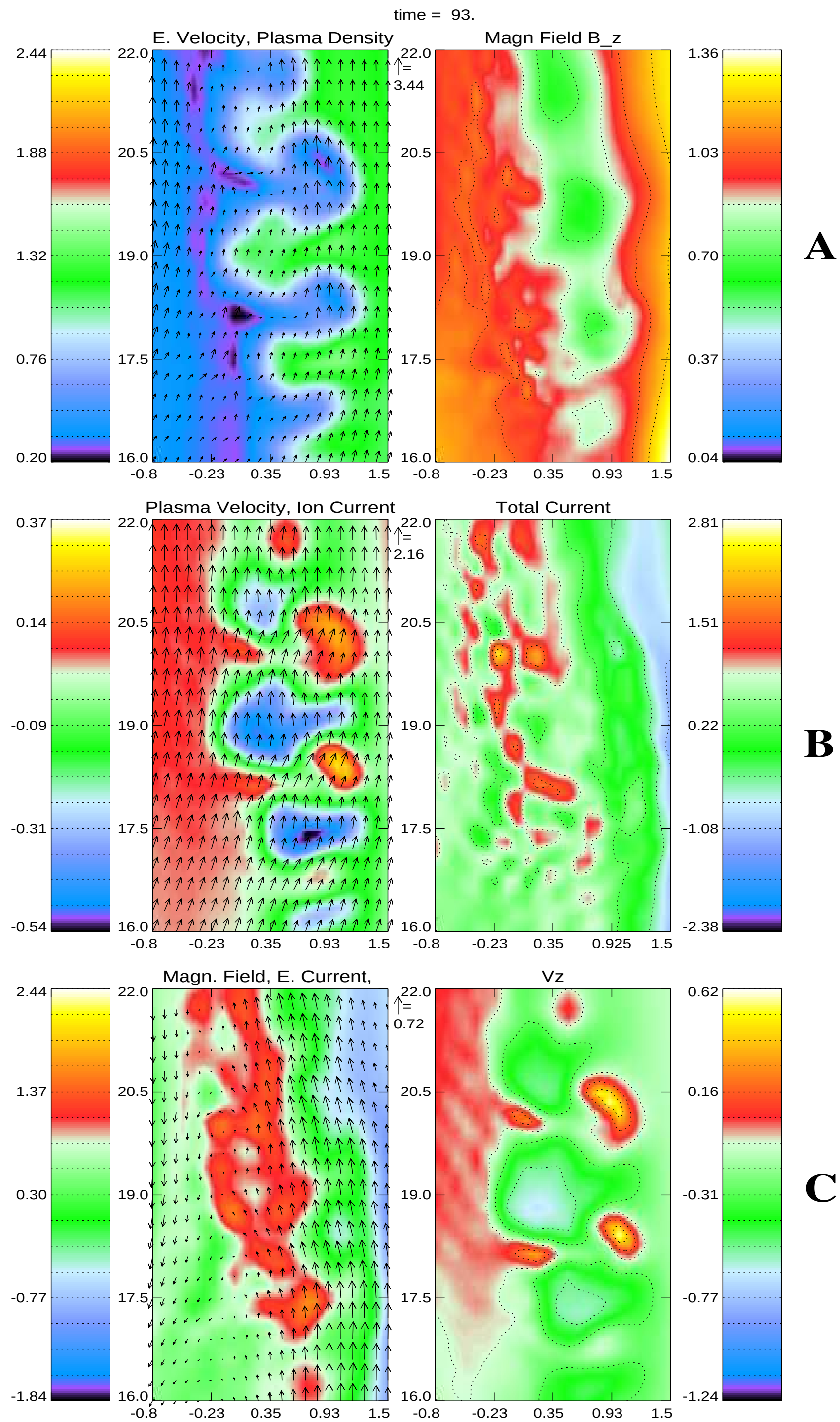

Figure 4.11. A) is a magnified domain of figure 4.10 A). B) shows plasma velocity vectors (arrows), and ion current (color code) on left and total current on right. C) depicts magnetic field vectors (arrows) and electron current (color code) on left, and z-component of the plasma velocity on right.

For small φ, Hall-MHD growth rates are about 20% larger than MHD growth rates, and for cases with large magnetic field along the **k**-vector of the instability (large φ), the Hall-MHD growth rates are about 7% larger. The growth rates are larger for all the Hall-MHD cases compared to the corresponding MHD cases because in the Hall-MHD the magnetic field is frozen into the electrons and thus it doesn't stabilize the ion motion. Figure 4.12 shows a comparison between linear MHD theory and our simulation results. Figure 4.12a indicates that the growth rates predicted from the linear, incompressible ($\nabla \cdot \mathbf{v} = 0$) theory are about 50 percent larger than from the simulations for longer wavelength ($ka >$ 0.12) cases. This difference is even larger (100%) for shorter wavelength cases ($ka > 0.25$) in Figure 4.12b. Theory assumes that the velocity shear layer thickness a, is infinitesimal, that plasma is incompressible, and that the world is linear. When the wavelength approaches the shear flow layer thickness, the growth of the wave is not possible in reality (and simulations), but for linear theory there is not such a limit.

Huba [1994] concluded that the Hall term acts to inhibit vortex formation implying that the growth rate for the Kelvin-Helmholtz mode is reduced by ion inertia effects. However, results in this chapter indicate that Hall-MHD growth rates are about 20% larger than the corresponding MHD growth rates. *Huba* [1994] comes to his conclusion by evaluating only the maximum value of the perpendicular velocity component across the initial shear flow layer such that the one maximum value of the whole simulation represents the growth. In MHD approximation *Huba* [1994] reported the maximum v_y to be 40 km/s, and in Hall-MHD 20 km/s (for negative vorticity case) and 14 km/s (for positive vorticity case). Growth rates in this chapter are obtained by plotting (in log-scale) the maximum values of perpendicular velocity components during the whole simulation as a function of time and calculating the slope of the growth graph (slope of the graph $\ln(v_y)$ vs t in Figures 4.7, 4.8, 4.9).

Similarly, like *Thomas and Winske* [1993] we find that short wavelength perturbations grow initially, evolve into vortex structures, and eventually decay or coalesce to longer wavelength structure. We observe the ion inertia scale turbulence to be the cause for decaying of the small wavelength vortices for cases with small φ. For larger φ, mixing is also observed, but it operates mostly in the lower density regions.

Simulations without B_z indicate that reconnection rates are strongly enhanced by density asymmetry across the initial shear flow layer. In addition, the Hall effect generates

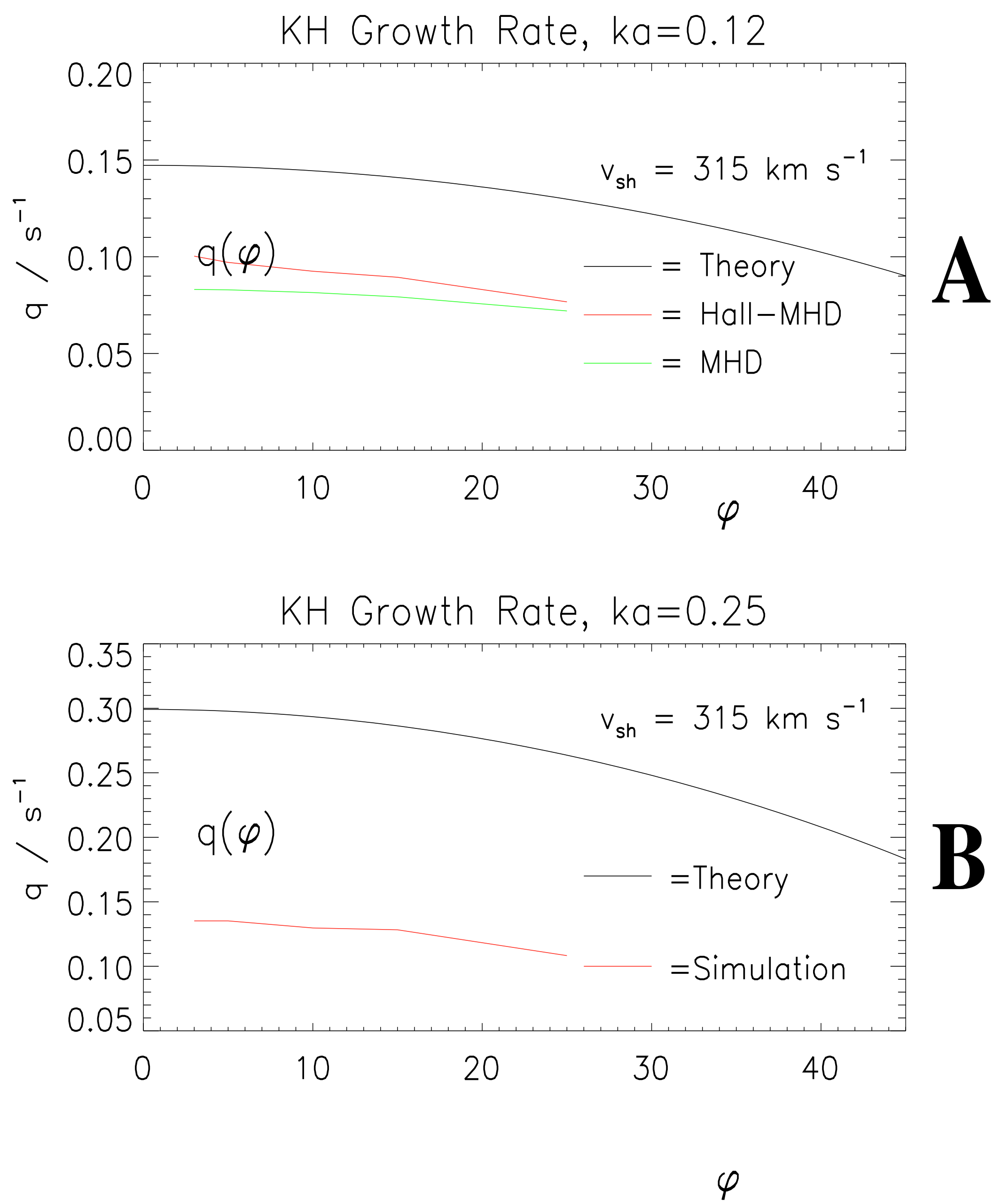

Figure 4.12. A) represents comparison of KH growth rates between theory and Hall-MHD and MHD simulations for $ka = 2\pi/a\lambda = 0.12$. B) shows comparison between KH growth rates between theory and Hall-MHD simulations for $ka = 0.25$.

positive and negative B_z components and these reach their maximum values between reconnection regions forming an intense quadrupolar structure for symmetric density case. When density asymmetry is included, the bipolar B_z layers become more elongated.

While the net plasma transport due to the reconnection inside Kelvin-Helmholtz vortices is not changed in the Hall-MHD approximation, the dynamical fine structure (arising from the finite ion inertia length) of the Kelvin-Helmholtz instability showed highly interesting results. Observed ion inertia scale turbulence might become very important in regions such as Earth's magnetospheric cusps. The magnetic field in the immediate vicinity of the cusp is rather small and in the larger vicinity the geomagnetic field converges towards the cusp location such that the field close to the magnetopause rotates by 360 degrees around the cusp. Thus there are always two regions in which the IMF is parallel or anti-parallel to the geomagnetic field allowing reconnection to operate, and a region where the velocity component is perpendicular to the magnetic field allowing Kelvin-Helmholtz instability to operate. *Chen* [1997] showed that in three dimensions a Kelvin-Helmholtz vortex can get filamentary structure by magnetic reconnection such that the ion inertia scale becomes important.

Chapter 5

Ionospheric Signatures of the Kelvin-Helmholtz Instability

5.1 Introduction

There are several ionospheric and ground observations associated with the KH instability at the magnetospheric boundary layer. *Lui et al.* [1989] used global auroral images from the ultraviolet imager on the Viking spacecraft to investigate spatially periodic bright spots on the dayside auroral oval that resemble beads on the string. *Wei and Lee* [1993] reported observations of these bright spots by several authors concluding that dimension of these spots typically ranges from 50 km to 200 km and the separation between two successive spots is about 100-500 km. *Lui et al.* [1989] suggested that these bright spots are related to the small scale field aligned currents resulting from the dynamic change of vorticity associated with the Kelvin-Helmholtz Instability.

Dawn/dusk auroras can also be generated by solar wind ram pressure changes: Pressure pulses compress magnetosphere which may lead to particle precipitation via the loss-cone instability. *Zhou et al.* [2002] studied auroral events during intense solar wind ram pressure pulse on June 27th, 1997 with spacecraft data, all-sky images, and magnetometers. On June 27th, 1997, from 08:00 to 09:30 UT, the solar wind pressure increased from 4.5 to 11 nPa enhancing the auroral intensities by a factor of 5 near 06:00 MLT and by factor of 3 near 18:00 MLT. Both diffuse and discrete auroras were observed at 05:00-06:00 MLT [*Zhou* *et al.*, 2002].

Several authors have studied geomagnetic pulsations in the ULF range using ground magnetometer observations [*Lee and Olson*, 1980; *Olson and Rostoker*, 1978; *Olson*, 1986; *Ohtani et al.*, 1999]. *Ohtani et al.* [1999] examined a morningside Pc5 event on April 29, 1993, by using satellite and magnetometer data. They found that the magnetic field oscillated at the same 5 min period at Geotail in the boundary region and at geosynchronous altitude, and also the ground stations observed the corresponding oscillations. *Ohtani et al.* [1999] suggested that the most plausible excitation mechanism for this event is the KH instability at the magnetopause since the polarization of the rotation of the plasma flow velocity at Geotail and that of ground magnetic variations are consistent. *Olson and Rostoker* [1978] found that high latitude observations of geomagnetic pulsations on the morning side are more sinusoidal compared to more irregular afternoon events. *Lee and Olson* [1980] attribute dawn/dusk asymmetries to the significant differences in the magnetosheath magnetic field strength. Draping of the typical parker spiral IMF configuration around the magnetosphere generates a larger magnetic field component along the dusk side magnetospheric flank which makes the KH instability more stable along this boundary.

The traveling ionospheric convection vortices may also be associated with the KH instability in the LLBL [*McHenry et al.*, 1990; *McHenry and Clauer*, 1990; *Bristow et al.*, 1995; *Clauer and Ridley*, 1995; *Clauer et al.*, 1990, 1997; *Ridley and Clauer*, 1996]. Using Greenland magnetometer chain, *McHenry et al.* [1990] showed that many dayside, continuous, long period pulsations are caused by steady, traveling ionospheric current systems. They found that these events have multiple traveling vortices in a chain and that the rotation direction of neighboring vortices alternates in a regular pattern. *McHenry et al.* [1990] believe that their observations can be explained by the KH instability for following reasons: 1) the radar observations show that ionospheric vortices are located at the convection reversal boundary, 2) vortices exist for many cycles and rotation direction of neighbouring vortices alternates, 3) there are no upstream solar wind pressure changes to drive these events. In a companion paper*McHenry and Clauer* [1990] present results of a statistical study of the occurrence of these vortices and the upstream solar wind parameters observed by the IMP 8 spacecraft, and they survey fifty days of Greenland magnetometer data. They claim that the regular nature of the vortices is different from the impulsive, sporadic FTE behaviour and thus exclude FTE's and reconnection as a possible cause for these multiple vortices. *McHenry and Clauer* [1990] also demonstrate that these vortices are mostly found in the post-noon sector which contradicts the results by *Olson and Rostoker* [1978] and *Lee and Olson* [1980]. *McHenry and Clauer* [1990] suggest that the possible vortices can be identified with ground observations only when the boundary layer is not overly turbulent: the dawn side boundary layer is more unstable with smaller, broken and/or unsteady vortices which are much more difficult to identify on ground. *Clauer et al.* [1990] found that under quiet conditions the continuous, irregular magnetic pulsations in the high latitude ionosphere, are caused by trains of steady, alternately directed, field aligned currents. These currents produce ionospheric flow vortices that travel anti-sunward and are located at the convection reversal boundary. *Clauer et al.* [1990] also observed a solar wind speed dependence of these vortices to be related to the vortex identification process. The clearest vortex patterns are found at low solar wind speeds at afternoon hours. *Clauer and Ridley* [1995] reported an occurrence of very long lived, 15 min vortices, but unlike the usual Kelvin-Helmholtz generation mechanism, these vortices appeared close to local noon. *Clauer and Ridley* [1995] suggest that perhaps the combination of the strong solar wind velocity and the strong IMF B_y component may produce high latitude magnetospheric flows and shear boundaries in the noon and prenoon region which can become Kelvin-Helmholtz unstable. *Ridley and Clauer* [1996] have investigated convection reversal boundaries using incoherent back scatter radar, magnetometers, and satellite data. Similarly, like *Clauer and Ridley* [1995], they attribute the turbulence at local noon to the the KH instability which occurs between antisunward moving reconnected (B_y driven reconnection) plasma and the plasma which is convected sunward (different from the typical notion of the the KH instability at the LLBL). *Clauer et al.* [1997] find that equatorward of the convection reversal boundary there is power in the pulsation spectra in bands with 34,17,12, and 8 min. They further analyze the northward components of these pulsations and suggest that the source of the resonance is the turbulence generated at the shear convection reversal boundary which then produces resonances equatorward on nearby closed field lines.

In this chapter we map magnetospheric perturbations caused by KH instability at the duskside magnetospheric flank boundary into the ionosphere and compare the simulation results with SuperDARN radar signatures and with optical observations of bright auroral spots. We find relatively good agreement between our 2-D MHD simulations and SuperDARN radar observations if we assume larger initial perturbation level than the one used in our simulations and consider a finite Alfvén wave travel time.

5.2 Numerical Method

The magnetosperic velocity and magnetic field perturbation levels due to the KH instability in the magnetosphere are obtained using 2-D MHD simulations [*Otto*, 1990a] in the x, y-plane (approximately the equatorial plane for strongly northward IMF). For simplicity the initial configuration for the simulation in the boundary coordinates uses a magnetic field configuration perpendicular to the equatorial plane on both sides of the magnetopause. Initial density, pressure, velocity, and magnetic field on magnetospheric and magnetosheath side are chosen according to the Geotail 1995 event [*Otto and Fairfield*, 2000], [*Fairfield et al.*, 2000]. Length is measured in units of $L_0 = 600$ km and the simulation box is 40 units in x corresponding to a wavelength of about 4 R_E. The time unit for the simulation is expressed in Alfvén time $\tau_A = 5.7$ seconds.

The simulation is done in the non-moving magnetospheric inertial frame in order to observe whether the vortex structure is indeed formed: several rows of fluid elements are added onto the simulation box, and for each time step of the simulation their location is integrated from the plasma velocity. Flow velocities of the fluid elements forming the tip of the vortex are used to estimate the average velocity perturbance in the magnetosphere $\delta\mathbf{V_m}$. The magnetic field perturbation level in the magnetosphere, δB_m, is obtained using the following formula:

$$\delta B_m = \frac{\delta V_m B_{0_{msp}}}{V_{A_{msp}}} \tag{5.1}$$

Where $B_{0_{msp}}$ is the unperturbed magnetic field in magnetosphere and $V_{A_{msp}}$ is the Alfvén speed in the magnetosphere.

We can map the magnetospheric velocity perturbation into the ionosphere easily if we assume that the potential drop, $\Delta\Phi$, in the magnetosphere equals the potential drop in the ionosphere and assume ideal MHD:

$$\Delta\Phi_{msp} = \delta\Phi_{ion} \tag{5.2}$$

$$E_{msp}\Delta s_{msp} = E_{ion}\Delta s_{ion} \tag{5.3}$$

$$V_{msp}B_{msp}\Delta s_{msp} = V_{ion}B_{ion}\Delta s_{ion} \tag{5.4}$$

$$V_{ion} = V_{msp}\sqrt{\frac{B_{msp}}{B_{ion}}} \tag{5.5}$$

$$\tag{5.6}$$

Where E is the electric field, s is the distance, and indices refer to the magnetosphere and ionosphere. Similarly we can derive the vortex speed in the ionosphere:

$$V_{ion_{vortex}} = V_{msp_{vortex}}\sqrt{\frac{B_{msp}}{B_{ion}}} \tag{5.7}$$

We get the corresponding area of the vortex in the ionosphere from the conservation of the magnetic flux:

$$\Phi_{msp} = \Phi_{ion} \tag{5.8}$$

$$A_{ion} = \frac{B_{msp}A_{msp}}{B_{ion}} \tag{5.9}$$

The corresponding current can be calculated from Ampére's law and using Stoke's theorem:

$$I = \frac{\oint \mathbf{B}\cdot d\mathbf{l}}{\mu_0} \tag{5.10}$$

5.2.1 Magnetic field line tracing

The *Tsyganenko* [1996] magnetic field model is used to map magnetic field lines from the location of the Geotail spacecraft on March 24 1995 at 062830 UT. Also, the magnetic field lines surrounding the Geotail (corresponding the boundaries of the simulation box) were traced into the ionosphere. Input parameters used by the magnetic field model during that date are listed in Table 5.1.

Table 5.1. Input for magnetic field line tracing

Quantity	Input values
Pressure	3 nPa
D_{st}-index	6 nT
B_y	-4 nT
B_z	8 nT
Geotail location	(-14, 20, 0) R_E
year,day,hour,minute,second	(1995, 83, 6, 28, 30)

5.3 Results

After following several rows of fluid elements in the magnetospheric equatorial plane, there are a few plasma elements that generate a closed vortex structure. Figure 5.1 shows the time evolution of the vortex. The background color is plasma density, indicating higher density on the magnetosheath (right) side. Asterisks are fluid elements that were initially located at $y = -1$. Their location is integrated from the plasma velocity for each simulation time step. Arrows are velocity vectors. The fluid elements that best show the vortex are marked with orange and their velocity perturbation is used to calculate δV in the magnetosphere. This vortex motion in the duskside flank is counter-clockwise, generating a clockwise magnetic field perturbation at the equatorial magnetospheric plane, and thus a converging current at the equatorial plane. There is thus an upward field-aligned current from both ionospheres indicating precipitating electrons into the ionosphere. This can be the reason why the auroral bright spots are most often observed in the post-noon sector ionosphere corresponding to the KH-instability at the duskside magnetospheric flank.

Magnetic field lines from the Geotail location on March 24, 1995, and surrounding field lines (corresponding to the boundaries of the simulation box) map into the post-noon sector approximately from 13 MLT to 16 MLT in the latitudes of 75°-80°.

Table 5.2 lists simulation results. The first three rows show the initial unperturbed velocity and magnetic field values, used in equations 5.1-5.10 to calculate the corresponding perturbed values in ionosphere. Perturbed velocity values in the magnetosphere are obtained from the simulation, and using equation 5.1 the corresponding magnetic field per-

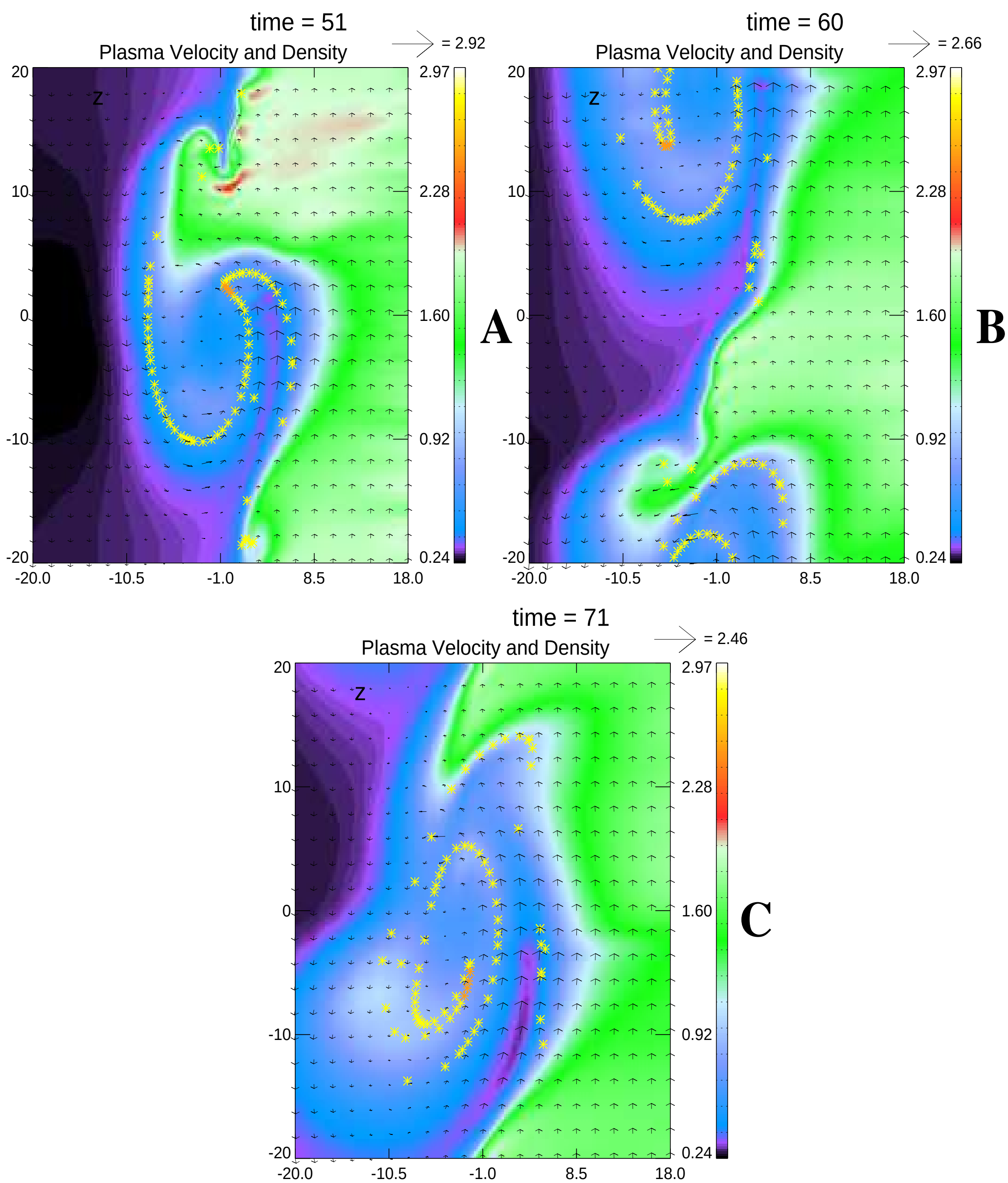

Figure 5.1. KH-vortex at the magnetospheric inertial frame at $\tau_A = 51$ (A), at $\tau_A = 60$ (B), and at $\tau_A = 71$ (C).

Table 5.2. Simulation Results

	Magnetosphere	Ionosphere
B	16 nT	50000 nT
V_{SW}	315 km/s	
$V_{Alfvén}$	209 km/s	
δV	74 km/s	1.3 km/s
δB	7 nT	200 nT
V_{vortex}	158 km/s	2.8 km/s
A_{vortex}	1 R_E x 1.3 R_E	70 km x 220 km
I	22000 A	22000 A
J	0.4 nA/m^2	1.4 μA/m^2

turbation is obtained. In Table 5.2 I is the calculated current (which is further used to calculate magnetic field disturbance in the ionosphere) and J is the corresponding current density. It is difficult to estimate light generated with this process because it involves nonlinear physics. One possibility would be to estimate the energy and flux of the newly captured plasma which is put into the loss cone by reconnection in KH vortices. A rough estimate could be done if one assumes particle energies of 1 keV. Using our calculated current density in the ionosphere, $J = 1.4$ μ A/m^2, we get a flux of 1.4 mW/m^2 which is corresponding to the brightness that is in visual range.

5.3.1 Comparison of Auroral Bright Spots with MHD Simulation results

Lui et al. [1989] reported spatially periodic bright spots on the dayside auroral oval that resemble beads on a string. These bright spots are typically seen in the 1400-1600 MLT sector. They occur typically during substorm activity but are also observed during northward IMF conditions [*Lui et al.*, 1989]. *Lui et al.* [1989] report an example in which these bright spots occur without substorm activity on July 26, 1986 (Viking orbit 849). During this day the Viking satellite observed two very intense auroral bright spots located at (73.3°, 1324 MLT) and (74.1°, 1506 MLT). The spatial dimension of these spots is typically 50-200 km and some spots are reported also on pre-noon sector. The fact that these spots are observed during periods of strongly southward (substorm intervals) and also during northward IMF conditions are in agreement with the KH-instability. Our simulation results indicate a energy flux of 1.4 mW/m^2 into the ionosphere, which would give visual aurora. According to our simulation results this flux is occupying an area of 70 km x 220 km in the afternoon ionosphere. This result is in agreement with the observations of these bright auroral spots [*Lui et al.*, 1989]. The KH-instability at the dawn-side magnetospheric flank could be the source of these bright spots in pre-noon sector. We studied Polar satellite UVI images and noticed these bright structures in pre- and post-noon sectors. Unfortunately for year 1995 there are no images from Polar satellite. Figure 5.2 presents a Polar UVI picture on March 10, 1998 at 14:12:28 UT. During that time the IMF was mostly northward having short southward intervals with substorm activity on the nightside, and with a large negative B_y component. Equator-S observations and comparison with 2-D MHD simulations [*Nykyri et al.*, 2002] at the dawnside magnetospheric flank of that time indicate KH-waves. Unfortunately, the pre-noon sector is not in the field of view of the satellite. A bright structure in the post-noon sector could be corresponding to a KH-instability at the dusk-side flank during that day.

5.3.2 Comparison of Super DARN radar observations with MHD Simulation results

During March 24th 1995 at 06:28:28 UT, the SuperDARN radar was monitoring the midnight section, and thus could not have observed estimated vortex structures. However, we found another date with mostly northward IMF conditions where SuperDARN HF radars were monitoring the afternoon sector of October 22, 1993.

Radar observations showed two convection vortices evolving within the field of view of two radars at about 21:20 UT and the second at about 21:45 UT: 14:46 MLT and 1512 MLT, respectively [*Bristow et al.*, 1995]. The vortices were roughly 900 km in diameter and moved tailward with a velocity of about 600 m/s. The local flow velocities were about 1 km/s and the vortex velocities gradually increased from 500 m/s to 1 km/s.

During the time interval of 21:10-21:39 UT the IMF was northward with B_z of about 6-9 nT and B_y of about -5 nT. The solar wind V_x component was about -400 km/s. After 21:39 UT the solar wind turned southward for about 5 minutes, after which it stayed northward for about 12 minutes. For the period 21:10-21:39 UT our simulations are suitable using

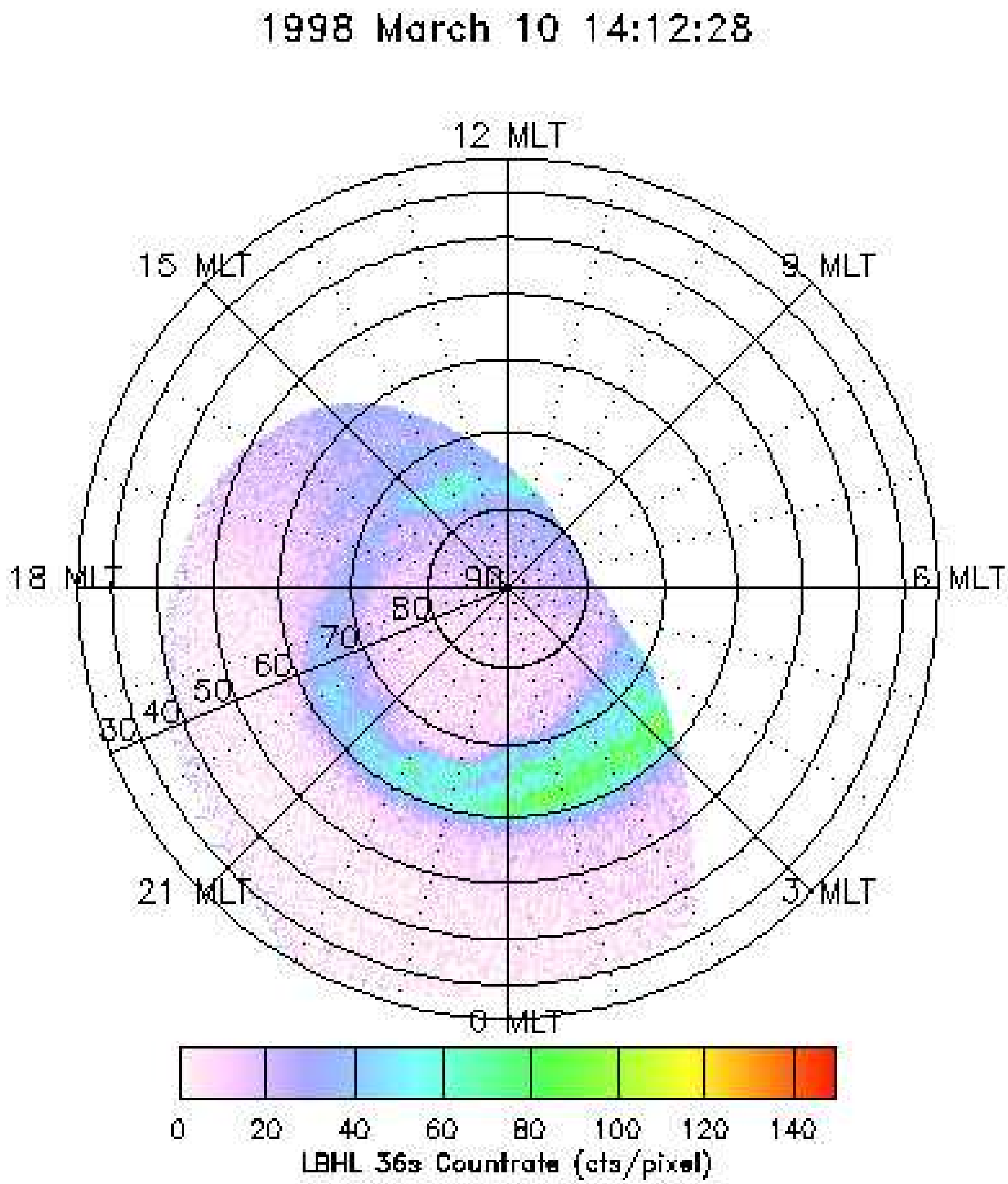

Figure 5.2. Polar UVI image of auroral luminosity on March 10 1998 at 14:12:28 UT.

initial values from Geotail observations. The velocity disturbance level should be larger in our simulations due to the higher IMF perturbance level and solar wind speed. The north-south oscillations of the magnetic field prior to 21:10 UT and after the 21:39 UT also increase the disturbance level in the ionosphere. With higher initial velocity perturbations, which can be expected for changing solar wind conditions, the KH-mode reaches the non linear-state faster resulting also in a larger vortex size in magnetosphere.

Without taking into account a higher initial perturbance level and finite Alfvén wave travel time, our estimated vortex size from MHD simulations is about 4 times smaller, our flow velocities are slightly larger and our vortex velocity in the ionosphere is about 4 times larger.

5.4 Discussion and Conclusions

Our 2-D MHD simulation results of KH-instability are in good agreement with the size, intensity, and location of the auroral bright spots observed often in afternoon ionosphere. Comparison with SuperDARN radar observations agree if we would assume a higher initial perturbation level in our simulations. Starting with a higher velocity perturbation we would reach a non-linear vortex faster, and the size can be comparable to those of SuperDARN radar measurements.

Our estimated tailward velocity of the vortex in the ionosphere is faster than observed, which is in agreement with simulation results of *Wei and Lee* [1993]. This is due to the fact that Alfvén waves have finite velocity, and from the initial location of the KH-vortex in the magnetosphere it takes a few minutes for a wave to travel into the ionosphere. When the wave travels back into the equatorial plane, the magnetospheric point has already moved further tailward and this feedback time between ionosphere and magnetosphere is increasing until the Alfvén wave travel time becomes so long that the structures further down the tail don't cause any signatures in the ionosphere. So the finite Alfvén wave travel time can explain why the structures move slower in the ionosphere. A better coupling model would be needed in order to understand how much slower at any particular time this motion occurs. This finite Alfvén wave travel time may also explain why there typically is only one or two convection vortices: it takes time to reach a nonlinear state, which corresponds to the time when a vortex is first observed in the ionosphere. Then it gradually vanishes, as the KH wave has moved so far in the tail that the Alfvén wave travel time becomes too long to cause any effects in the ionosphere.

Chapter 6

Equator-S Observations at the LLBL on March 10th 1998: FTE's or Kelvin-Helmholtz waves?

The results in this chapter are published in the AGU Monograph on the Low Latitude Boundary Layer [*Nykyri et al.*, 2002].

6.1 Introduction

On March 10th, 1998, the Equator-S satellite observed three intervals with strongly perturbed magnetic signatures on the dawnside equatorial magnetospheric flank. Detailed descriptions of the experiment are given by *Baumjohann et al.* [1999] and *Kistler et al.* [1999]. The plotted plasma and magnetic field parameters are spin averaged values (1.5 s). *Nikutowski et al.* [2000] calculated the power spectra of the magnetic field components for this date and found that the poloidal part of the Pc5 oscillations indicates surface waves driven by KHI. Here we analyze the magnetic field and plasma data (Figure 6.1a) from 13:00 to 13:36 UT on March 10th and study whether these oscillations are caused by flux transfer events (FTE's) or by Kelvin-Helmholtz waves. Equator-S was located at $\mathbf{r} = [\ 0.54, -10.33, 4.93\ ]\ \mathrm{R}_E$ and moved about 1 R_E sunward during this interval.

FTE's are characterized by a bipolar variation of the magnetic field component normal to the magnetopause and the intermittent appearance of particles of presumably magnetospheric origin in the magnetosheath and vice versa [*Elphic*, 1995]. *Russel and Elphic* [1978] explained the bipolar variation by a bending of field lines around the magnetic flux tubes (formed by reconnection) and the magnetic connection allows the leakage of particles through the magnetopause along the magnetic field.

Variations of the solar wind dynamic pressure can generate a wavelike motion along the magnetospheric boundary [*Kaufmann and Konradi*, 1969; *Elphic*, 1988] and cause bipolar signatures [*Sibeck and et. al.*, 1989; *Sibeck*, 1992]. *Otto et al.* [1995] studied systematically the interaction of a current sheet with strong pressure perturbations and compared these results with the typical properties of the magnetic reconnection by using 2-D MHD simulations.

Similar to pressure pulses the deformation of the magnetospheric boundary by Kelvin-Helmholtz (KH) modes can also cause bipolar B_N signatures. An additional difficulty to distinguish between FTE's and KH waves arises when reconnection is embedded in the motion of KH surface waves. However, our 2-D MHD simulations of KHI and FTE's show that these processes can be distinguished by evaluating the satellite data using the Walen relation, testing for a de Hoffmann-Teller (HT) frame, and performing a vector variance analysis.

Magnetic reconnection, pressure pulses, and KH waves transport momentum and energy into the magnetosphere, but only reconnection (also reconnection in KH vortices [*Otto and Fairfield*, 2000; *Nykyri and Otto*, 2001]) can transport plasma across the magnetopause. Therefore it is important to distinguish between these different processes in the satellite data to be able to predict the dynamics of the magnetosphere as a result of the processes at the magnetospheric boundary.

6.2 Numerical Method

Observations and results of the numerical simulations of this study are analyzed with the Walen relation, variance analysis, and de Hoffman Teller (HT) system.

6.2.1 Data analysis

The Walen relation $\Delta \mathbf{v} = \pm \Delta \mathbf{v_A}$ implies that the change of the plasma flow velocity equals to the change of Alfvén speed [*Sonnerup et al.*, 1995]. The Walen relation is satisfied for Alfvén waves, rotational discontinuities, but also approximately for intermediate and switch-off slow shocks. The latter two are often associated with magnetic reconnection. *Sonnerup et al.* [1995] studied dayside magnetopause AMPTE/IRM crossings on Sept. 4, 1984 and found that the likelyhood for existence of a good Walen relation without presence of a normal magnetic field component to the magnetopause surface is small. A good Walen relation is thus an indication for magnetic reconnection.

The HT frame is a frame where the electric field vanishes on both sides of the current layer, thus indicating an approximately steady state plasma configuration. The HT velocity, $\mathbf{v_{HT}}$ is determined by minimizing $|(\mathbf{v} - \mathbf{v_{obs}}) \times \mathbf{B_{obs}}|^2$ in terms of the constant transformation velocity $\mathbf{v}$ for a given dataset *Sonnerup et al.* [1995]. *Sonnerup et al.* [1995] showed that for a simple, locally one-dimensional magnetopause structure, the existence of an HT frame is a necessary but not a sufficient condition for ongoing reconnection.

The boundary normal directions in Equator-S observations are calculated using the minimum variance of the magnetic field and the maximum variance of the electric field [*Sonnerup and Scheible*, 1998]. Sometimes the minimum variance eigenvalue for $\mathbf{B}$ is close to the intermediate value and therefore fails to produce a reliable normal direction. Therefore we have also determined the boundary normal directions using the maximum variance of $\mathbf{E}$. Typically the dominant magnetic field and the dominant plasma velocity are tangential to the boundary layer such that the maximum variance for the convection electric field should be normal to the layer.

6.2.2 2-D MHD models

The simulation results of this study are obtained by solving the full set of resistive MHD equations [*Otto*, 1990a]. Plasma density ρ, velocity $\mathbf{v}$, pressure, and magnetic field are integrated with a finite differences leapfrog scheme which is of second order accuracy in space and time [*Birn*, 1980]. All the quantities are normalized to characteristic values of the system, i.e., length scales l to a typical length l_0, density ρ to $\rho_0 = n_0 m_0$ with the number density n_0 and the proton mass m_0, magnetic field $\mathbf{b}$ to B_0, velocity $\mathbf{v}$ to the typical Alfvén velocity $v_A = B_0/\sqrt{(\mu_0 \rho_0)}$, pressure to $P_0 = {B_0}^2/(2\mu_0)$, and time t to a characteristic Alfvén transit time $\tau_A = l_0/v_A$.

The initial configuration for the KH simulation in the boundary coordinates (y is boundary normal direction, x points sunward along the magnetospheric boundary and z is northward completing the coordinate system) uses a magnetic field of $b_{x0}(x) = b_0(x)\sin\varphi$, $b_{y0}(x) = 0$, and $b_{z0}(x) = b_0(x)\cos\varphi$ such that $90° - \varphi$ is the angle between the unperturbed magnetic field direction and the $\mathbf{k}$ vector of the KH mode. The velocity is given by $v_{x0}(x) = v_0(x)$, $v_{y0}(x) = 0$, and $v_{z0}(x) = 0$. Initial density, pressure, velocity, and magnetic field magnitudes are

$$
\begin{aligned}
\rho_0(x) &= \frac{1}{2}(\rho_{sh} + \rho_{sp}) + \frac{1}{2}(\rho_{sh} - \rho_{sp})\tanh(\frac{y}{L_0}) \\
p_0(x) &= \frac{1}{2}(p_{sh} + p_{sp}) + \frac{1}{2}(p_{sh} - p_{sp})\tanh(\frac{y}{L_0}) \\
v_0(x) &= -\frac{1}{2}v_{sh}(\tanh(\frac{y}{L_0}) + 1) \\
b_0(x) &= \frac{1}{2}(b_{sh} + b_{sp}) + \frac{1}{2}(b_{sh} - b_{sp})\tanh(\frac{y}{L_0}),
\end{aligned}
$$

where the indices sp and sh correspond to the average values on the magnetospheric and magnetosheath sides of the magnetopause boundary. The initial density, pressure,velocity, and magnetic field on the magnetospheric and magnetosheath sides are chosen according to Equator-S 1998 event and are normalized using $B_0 = 50$ nT, $n_0 = 18.0$ cm^{-3}, $L_0 = 900$ km which yields $v_A = 260$ km/s and $\tau_A = 3.5$ s.

In contrast to the previously discussed configuration for the KH simulation, the reconnection simulation uses a one-dimensional initial equilibrium configuration with x normal to the current layer (into the magnetosheath), z is along the direction with maximum anti-parallel fields, i.e., northward for exactly anti-parallel fields, and y completes the coordinate system. The equilibrium equations are given by *Otto et al.* [1995]. The equilibrium is determined by:

$$
\begin{aligned}
b_{x0}(x) &= 0 && (6.1)\\
b_{y0}(x) &= \sqrt{b_{yc}^2 + \lambda b_{zc}^2 \cosh^{-2} x} && (6.2)\\
b_{z0}(x) &= -b_{zc} \tanh x && (6.3)\\
p_0(x) &= \beta + (1-\lambda) b_{zc}^2 \cosh^{-2} x && (6.4)\\
\rho_0(x) &= 1 + \Delta_\rho \tanh(x/2) \\
&\quad +25\left[1 - \tanh((x+45)/7)\right] && (6.5)
\end{aligned}
$$

with $b_{zc} = \sin(\alpha/2)$ and $b_{yc} = \cos(\alpha/2)$. The subscript 0 indicates equilibrium quantities, λ determines the magnitude of the magnetic field in the current layer ($\lambda = 1$ corresponds to a force free field), α is the angle between the directions of the asymptotic magnetic field across the current layer, and Δ_ρ is half the density jump across the current layer, such that the density ratio between the MSH and the MSP is $(1 + \Delta_\rho)/(1 - \Delta_\rho)$. The parameters are chosen to be $\lambda = 0.9$, $\alpha = 150°$, $\beta = 1$, and $\Delta_\rho = 0.6$ for most of the presented results. This choice yields $b_{zc} \approx 0.96$, $b_{yc} \approx 0.26$, a plasma β (p/b^2 in our units) of 1 in the MSH and the MSP, a density ratio of 4, and a corresponding ratio for the Alfvén velocities of 1 : 2 in the MSH and the MSP. For quantitative evaluation we have chosen $B_0 = 50$ nT, $n_0 = 7.5$ cm^{-3}, $L_0 = 400$ km [*Sonnerup et al.*, 1981] which yields $v_A = 400$ km/s and $\tau_A = 1$ s.

6.3 Observations

Equator-S data (Figure 6.1a) shows strong variations of all plasma properties (from typical magnetospheric values to magnetosheath values) indicating multiple traversals of the dawnside magnetospheric boundary. Wind spacecraft data shifted by one hour show B_z ($\sim$ + 10 nT), B_x ($\sim \pm$ 4 nT) and B_y turning from small ($\sim \pm$ 2 nT) to ($\sim$ -15 nT). The observed strong negative B_x is consistent with draping of the IMF magnetic field or of cusp reconnected magnetic field lines. Figure 6.1b shows corresponding plots for Walen relation and the HT velocities. During this 36 minute interval the Walen relation is not well satisfied (slope is 0.615) and the HT system obtained with approximately half of the solar wind speed is poor. The boundary normal directions are obtained with 1289 data points and both the

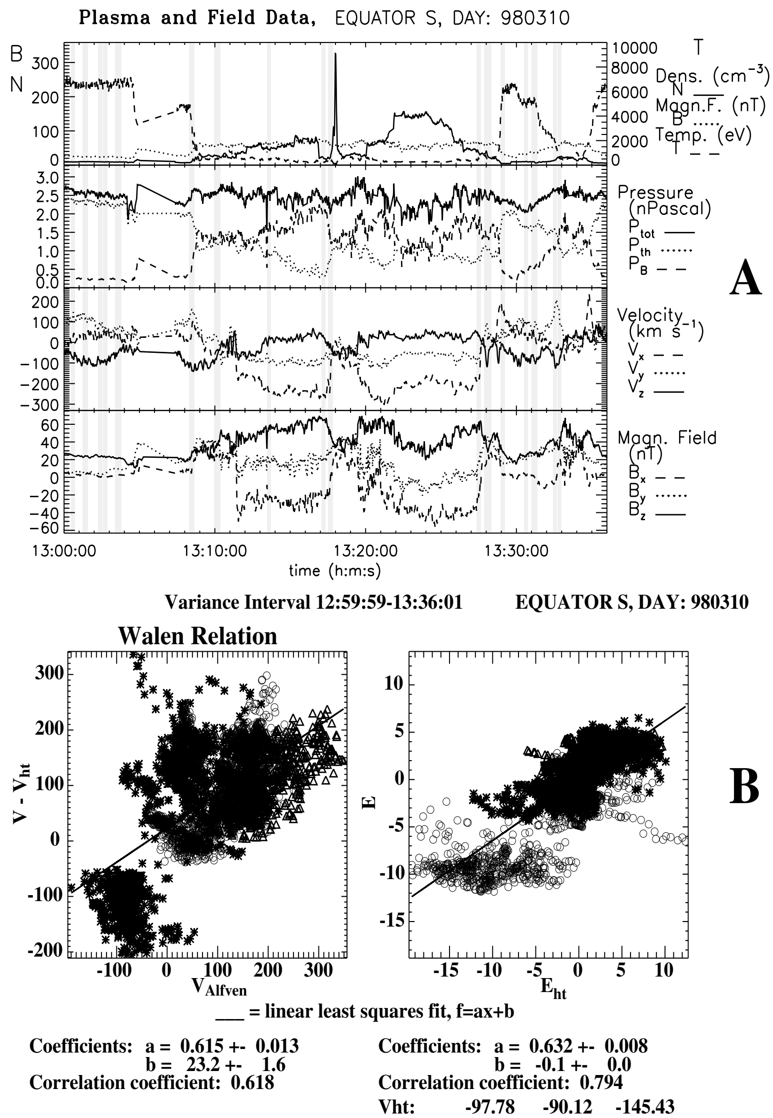

Figure 6.1. Plasma and magnetic field observations in GSE coordinates on March 10, 1998 from 13:00 to 13:36 UT. Shading illustrates regions with excellent Walen relation and de HT frame. Figure 6.1b has test of the Walen relation (left) and HT frame (right) during the same time interval as in Figure 6.1a.

minimum and maximum variance analysis agree with 0.5° of the average boundary normal direction of [-0.49, 0.80, 0.38].

Figure 6.2 shows a 19 second subinterval, where both the Walen relation and the HT frame are extremely well satisfied. The slope of Walen relation is 0.970 (left), which indicates almost a perfect correlation between a change of the plasma flow velocity and a change of Alfvén velocity indicative of reconnection, where the change of magnetic topology in to an x-line accelerates plasma to the outflow region. A good HT frame (right) with slope of 0.945 is obtained with a velocity almost twice as large as that of the 36 minute interval indicating plasma acceleration embedded in the large scale motion. The boundary normal direction for this interval ([-0.18, 0.83, 0.53]) is excellent (eigenvalue ratio = 40) and is different from the overall boundary normal direction. In addition to the case presented in Figure 6.2., we have analyzed several other 15-30 second subintervals between 13:00 - 13:36 UT. All the shaded short intervals (Figure 6.1a) satisfy the Walen relation and a good de Hoffman-Teller frame is obtained with significantly larger transformation velocity than that of the 36 minute interval. In addition the boundary normal direction of the interval from 13:32:43 - 13:33:10 UT has rotated 90 degrees from the overall boundary normal direction.

6.4 Simulations

6.4.1 Kelvin-Helmholtz Instability, KHI

Figure 6.3 illustrates 2-D MHD simulation results of the nonlinear evolution of the KHI at t= 116. The initial configuration (densities, temperatures, flow velocities) for the simulation was chosen according to Equator-S observations. The righthand side of Figure 6.3 depicts plasma density and velocity and the lefthand side shows current density and magnetic field. Black lines represent magnetic field lines projected into the x, y plane. The simulation box is 40 units in x corresponding to a wave length about 6 R_E. Twisting of the magnetic field inside KH-vortices generates strong and thin current layers, which leads to reconnection at $x = -14$, $y = -3.8$ and $x = 5$, $y = -13.4$ and a high density magnetic island is detached from the magnetosheath.

The simulation data were diagnosed along a cut at $y = -13.6$ (Figure 6.4a) representing a virtual spacecraft trajectory through the simulation box. This is justified because the

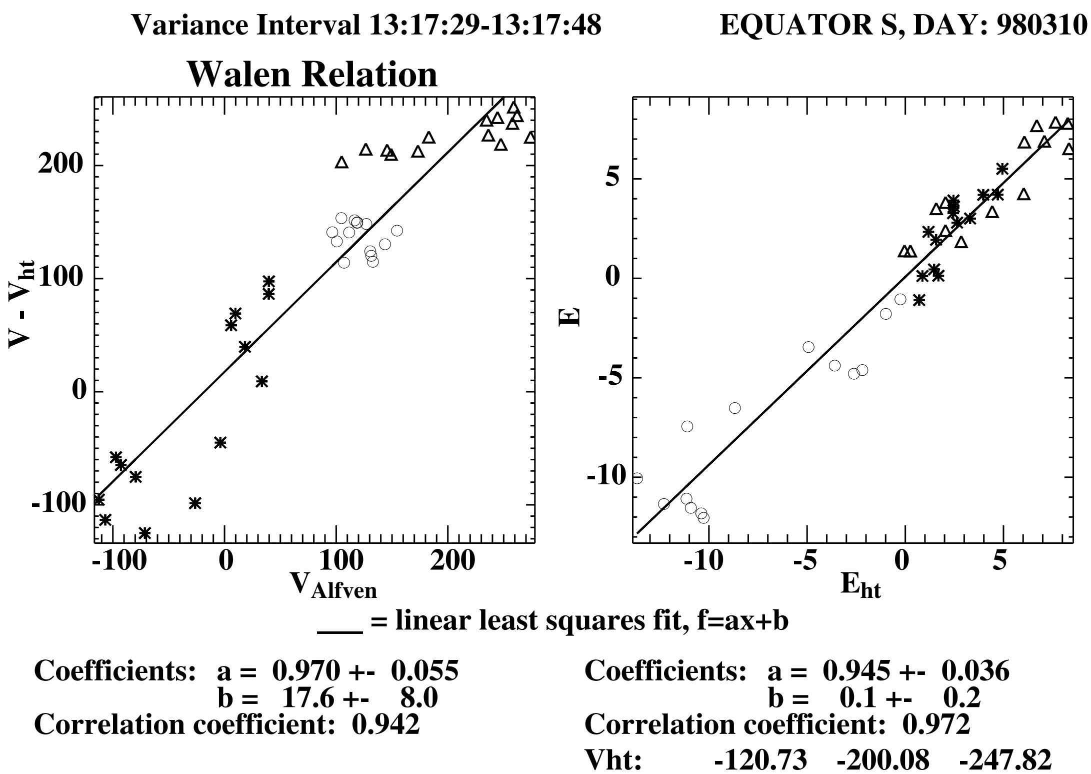

Figure 6.2. Tests of the Walen relation (left) and HT frame (right) during the interval from 13:17:29 UT to 13:17:48 UT on March 10, 1998

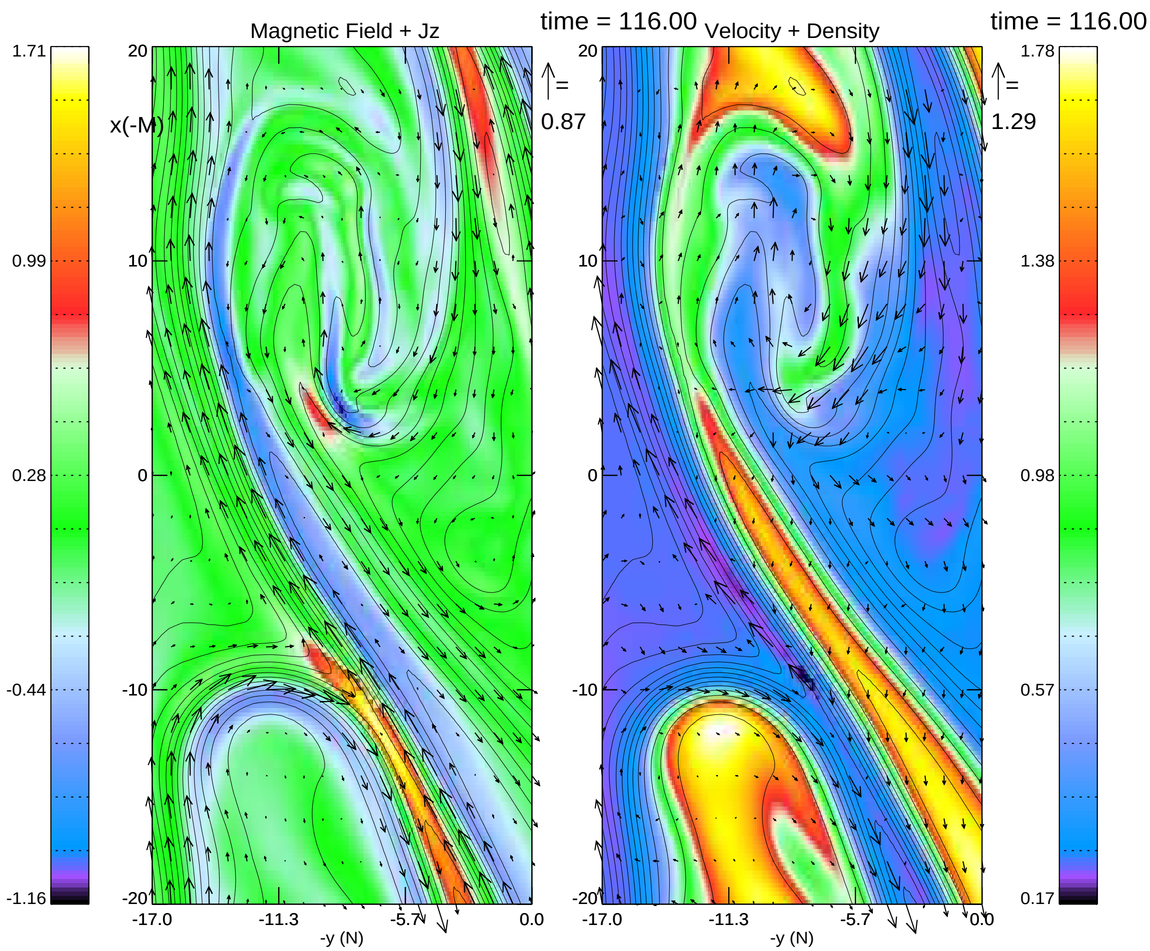

Figure 6.3. Results from the MHD simulation at t = 116. The left hand side shows magnetic field vectors and the z-component of the current density (color code). The right hand side depicts plasma velocity and plasma density (color code). Black lines represent magnetic field lines projected into x, y -plane.

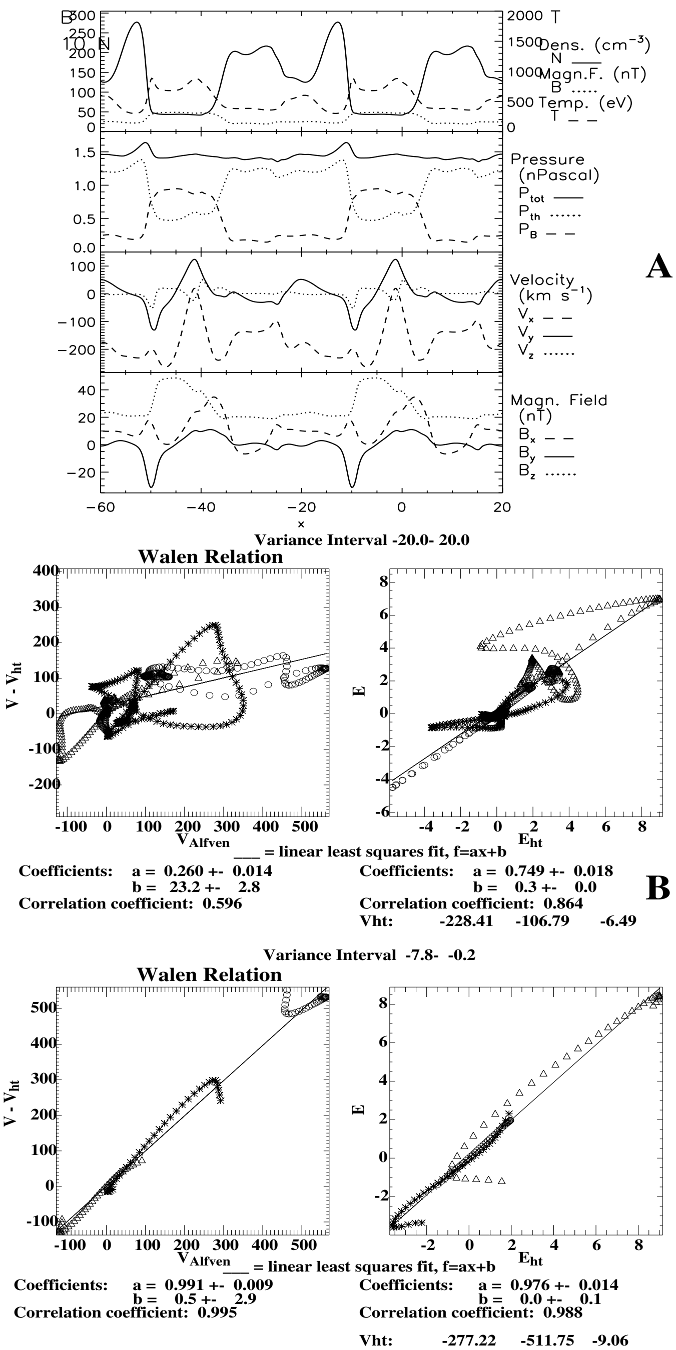

Figure 6.4. A) has plasma and magnetic field properties in cut through simulation box at y = -13.6 at t = 406 s. The upper panel panel of B) has the test for the Walen relation (left) and HT frame (right) from x = -20.0 to x = 20.0. The lower panel in B) has the test for the Walen relation (left) and HT frame (right) from x = -7.8 to x = -0.2.

configuration changes slowly on the timescale on which a spacecraft crosses the vortex and reconnection structures. The results (Figure 6.4b) show the properties of a surface wave.

In the upper panel of Figure 6.4b the whole wave length ($x = -20$ to $x = 20$) is analyzed indicating that the Walen relation is not well satisfied (slope=0.260) for this long interval. There is a reasonable HT frame (slope=0.749) indicating existence of a boundary wave. The lower panel of Figure 6.4b analyzes the shorter interval from $x = -7.8$ to $x = -0.2$. Strong field reversals of the B_y and B_x indicate crossing of a current sheet, which is clearly observable in Figure 6.4a. The lower panel of Figure 6.4a shows that the B_y is increasing (peak to peak magnitude is about 85 % of the B_{tot}) from $x = -7.8$ to $x = -0.2$. The satellite located on the magnetosheath side for this interval would observe a decreasing B_y component. The Walen relation for this shorter interval is excellent (slope=0.991), which is consistent with the presence of reconnection. Also the excellent HT frame (slope=0.976) with a much larger transformation velocity is consistent with plasma acceleration due to reconnection. Assuming the KH vortex velocities between 200-300 km/s, the virtual spacecraft travels through the interval from $x = -7.8$ to $x = -0.2$ in about 20-35 seconds. The source region for these waves can be estimated from the time required to form a non-linear wave (406 s) and from the vortex velocity (220 km/s) to be 14 R_E upstream from the Equator-S location close to the subsolar point. The IMF magnetic field configuration in x, y plane was closely perpendicular to the dayside magnetopause (and thus closely perpendicular to the **k** vector of the instability) so that the linear onset condition for the KH instability [*Chandrasekhar*, 1961] was well satisfied.

6.4.2 Flux Transfer Event, FTE

Figure 6.5 shows the time evolution of the density, B_y, and magnetic field lines of the 2-D magnetic reconnection in boundary normal coordinates. Boundary conditions are chosen mirror symmetric at $z = 0$ which implies that a symmetric reconnection bulge is traveling into the negative z-direction. The bipolar magnetic field behavior of the flux transfer events is clear from the Figure 6.5: a satellite in the northern hemisphere (same signature both in MSP and in MSH) will first observe a positive normal component of the magnetic field followed by a negative component and a satellite in southern hemisphere will first measure a negative normal component followed by a positive normal component [*Scholer*, 1988].

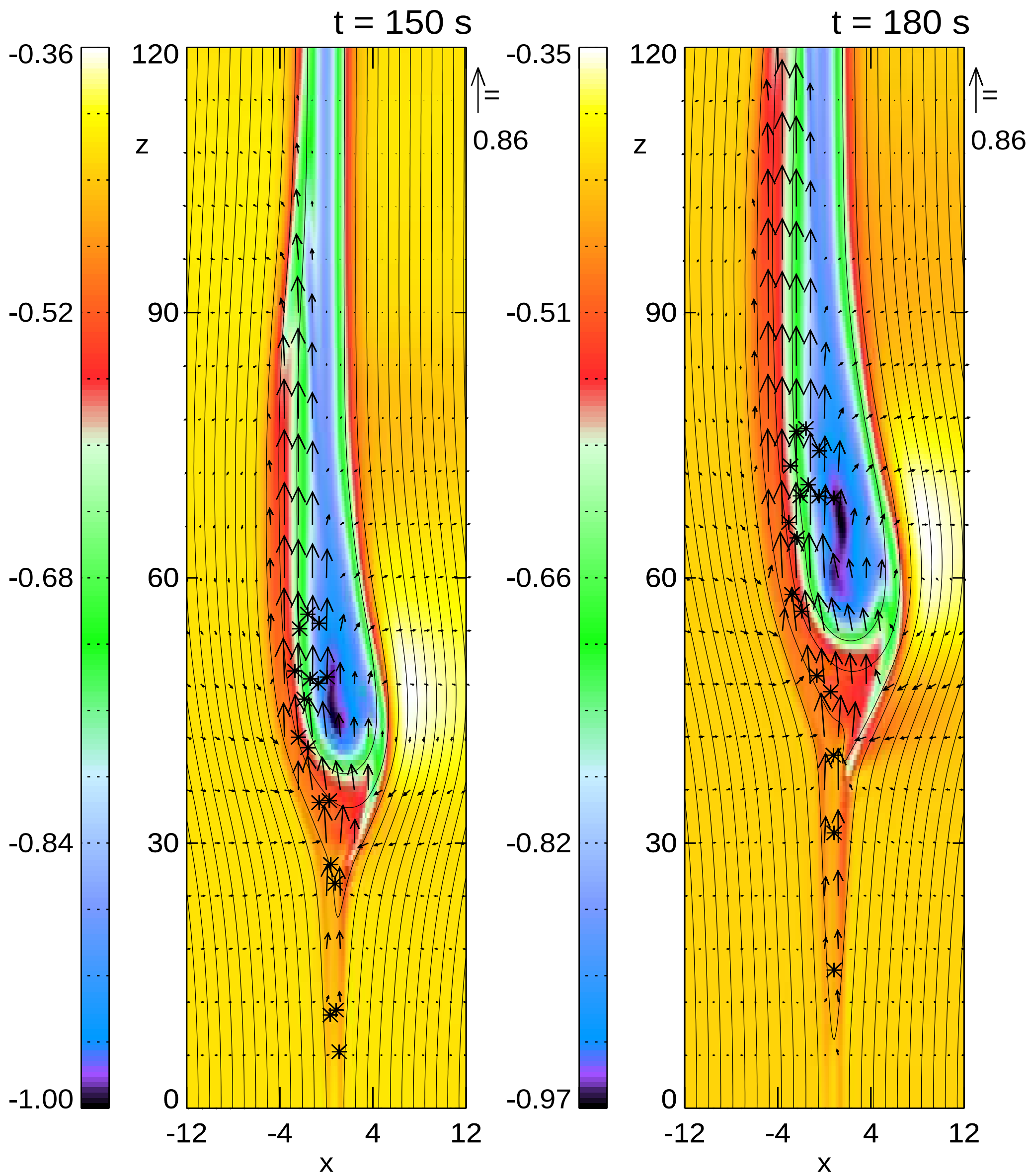

Figure 6.5. Time evolution of the 2-D magnetic reconnection. Arrows represent plasma velocity, black lines are magnetic field lines and the background color is B_y- component of the magnetic field.

Table 6.1. Properties of reconnection and the KH instability.

Property	Kelvin-Helmholtz Mode	Magnetic Reconnection
B_N peak to peak amplitude	50-90 % of B_{tot} for a nonlinear wave	50-90 % of B_{tot} for nonlinear reconnection.
B_N signature	Bipolar, or monopolar, opposite polarity in MSH and MSP.	Bipolar, same polarity in MSH and MSP.
Electric field	HT frame moving approximately with the wave. Accelerated HT velocity when reconnection in KH-vortices.	HT frame moving approximately with the reconnection structure.
Walen relation (RD, slow shocks)	No. Satisfied only for brief intervals if reconnection present.	Usually good Walen relation.
Duration	Depending on wavelength 20 s to few minutes.	1-3 minutes.

Figure 6.6a presents measurements in simulation box at x =6.0, y = 2.0 and z = 65.0 as a function of time. The bipolar signature of the normal component, B_x, is noticeable in lower panel. The peak to peak amplitude of B_x is about 80% of the total magnetic field. In Figure 6.6b the Walen relation is well satisfied (slope = 0.824) for 1 minute 20 second interval, and a good HT frame is obtained with the transformation velocity equivalent to the reconnection bulge velocity. The time scale satisfying the Walen relation and the HT frame is much larger than that of the KHI case. Table 6.1 lists the properties which we expect for KH modes and reconnection based on the numerical simulations.

6.5 Discussion and Conclusions

Our 2-D MHD simulations and comparison with Equator-S observations indicate that fluctuations in the data from 13:00 UT to 13:36 UT were due to the multiple crossings of the current sheet twisted by the KH instability.

Variance analysis shows that the boundary normal directions changed drastically during

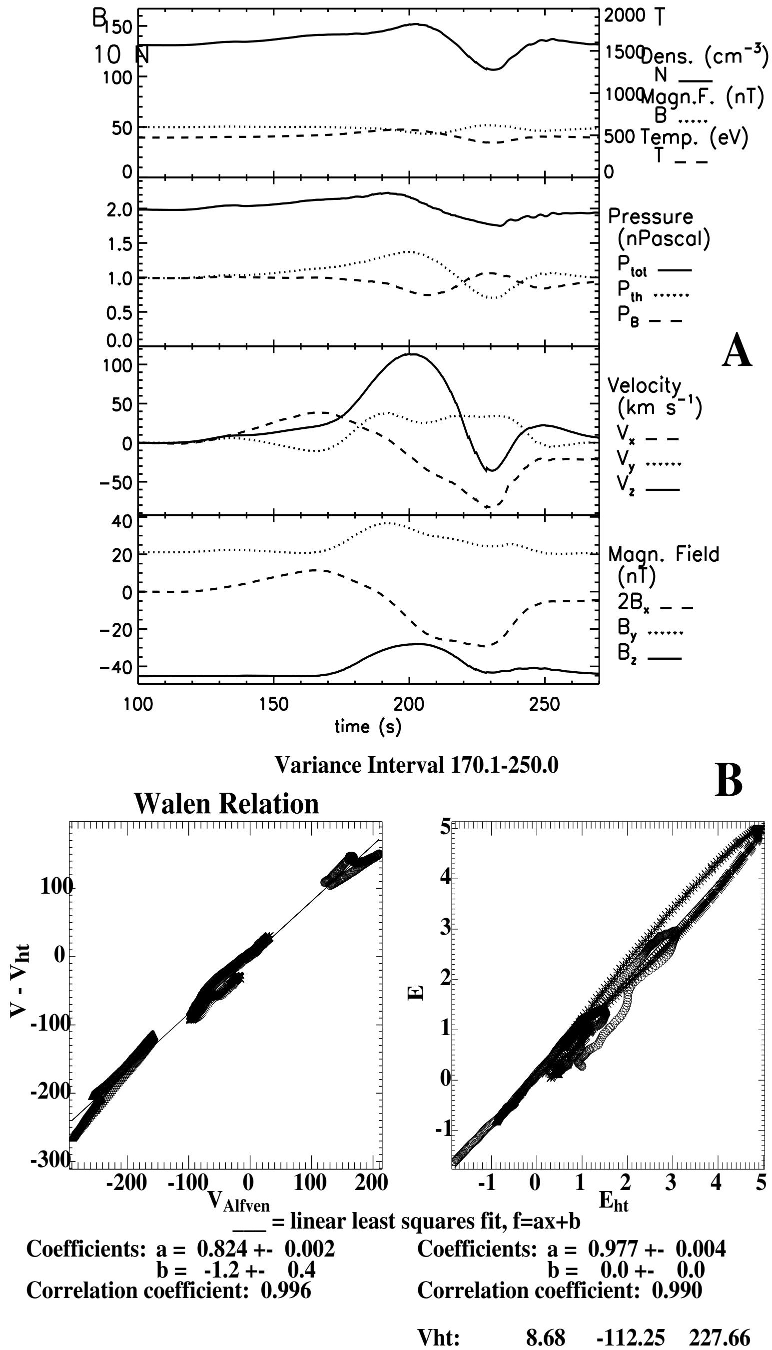

Figure 6.6. A) represents measurements of the magnetic field and plasma properties in simulation box at x=6.0, y = 2.0 and z = 65.0 as a function of time. B) has corresponding tests for the Walen relation and HT frame.

this interval indicating the presence of the boundary waves. The Walen relation was satisfied only for very brief 20-30 second periods and HT velocities for these periods were much higher than for the longer interval. This analysis indicates that Equator-S observed reconnection regions embedded in the motion of the boundary waves.

Our 2-D MHD simulations of reconnection in KH waves and single x-line reconnection support this interpretation. For the reconnection case the Walen relation is satisfied for 80 seconds, whereas, for the case with reconnection in KH vortices the Walen relation holds only for 10-25 s. Also the HT velocity is much larger for the brief intervals during which the Walen relation is satisfied, i.e. reconnection operates. In the case of a pure KH wave the electric field will minimize in the frame in which the KH vortices are approximately at rest yielding velocity v_{ht} close to the magnetosheath velocity. With reconnection present within the KH wave the reconnection electric field is superimposed yielding much higher HT velocities. For KH modes without reconnection neither the Walen relation would be satisfied nor would the large HT velocities be expected.

Chapter 7

Cluster Observations of the Kelvin-Helmholtz Instability on 3rd of July 2001 and Comparison with MHD Simulations

7.1 Introduction

The Cluster mission is one of ESA's first cornerstone projects dating back to first proposals in 1982, and was finally launched in the summer of 2000. Cluster I was initially launched in 1996, but the launch failure of the Ariane 5 destroyed all Cluster satellites. Luckily in 1997 ESA's Science Program Committee agreed to rebuild the entire mission [*Escoubet et al.*, 2001]. Cluster II consists of four identical spacecraft flying in tetrahedron formation. Each of the four Cluster satellites carries the same set of eleven instruments that allow for simultaneous measurements of electric and magnetic fields, and the detection of electron and ion distribution functions. For the first time in the history of space exploration, the four Cluster satellites are able to make a detailed, three dimensional study of changes and processes in near Earth space and distinguish between temporal and spatial structures. For this reason, the Cluster mission provides a fantastic opportunity to study also the Kelvin-

Helmholtz instability at the magnetotail and to identify signatures of reconnection inside Kelvin-Helmholtz vortices with help of four satellites. In this chapter I use the data of two Cluster instruments, the fluxgate magnetometers (FGM) and Cluster ion spectrometries (CIS).

The FGM instrument onboard each of the four Cluster spacecraft consists of two triaxial fluxgate sensors on a 5 m radial boom measuring the three components of the ambient magnetic field. The FGM has 5 different operational ranges and resolutions, that are automatically adjusted according to the surrounding magnetic field strength. The primary sensor samples magnetic field vectors at the rate of 201.793 vectors/s [*Balogh et al.*, 2001]. The CIS instruments analyze the composition, mass, and distribution functions of the ions during a four second spin of the spacecraft. It consists of two different instruments, a hot ion analyzer (HIA) and a "time-of-flight" ion composition and distribution function analyzer (CODIF) [*Rème et al.*, 2001]. The HIA instrument completes a full 4π scan during each 4 second spin of the spacecraft obtaining a full, 3-D distribution of the ions in the energy range of 5 eV/e to 32 keV/e. The CODIF instrument is a high-sensitivity, mass resolving spectrometer with an instantaneous $360^\circ \times 8^\circ$ field of view. It measures a complete 3-D distribution function of major ions (H^+, He^+, He^{++}, and O^+) during one spin of the spacecraft. The energy coverage is between 0.02-38keV/charge [*Rème et al.*, 2001].

Figure 7.1 represents Cluster orbits during polar cusp crossings (right) and tail crossings (left). During a two-year mission, Cluster will cross the dayside bow shock and magnetopause several hundred times. As Cluster satellites travel through particular regions in space, the constellation will be optimized accordingly: a perfect tetrahedron constellation has a resolution of 600 km in the cusps and 2000 km in the magnetotail [*Escoubet et al.*, 2001]. In this Chapter I have analyzed Cluster FGM and CIS data from three of the Cluster satellites SC1, SC3, SC4 on 3rd of July 2001 as a goal to find reconnection signatures embedded in the Kelvin-Helmholtz vortices. The data analysis tools used here are same as discussed in Chapter 6 and consists of: variance analysis [*Sonnerup and Scheible*, 1998], de Hoffman Teller frame system and Walen relation [*Sonnerup et al.*, 1995]. In addition we have included a few other methods (discussed later) in order to improve the automated search for reconnection intervals in satellite data. Data of SC4 is not used for calculations of the Walen relation, since the density measurements of HIA instrument onboard of SC4 were too low.

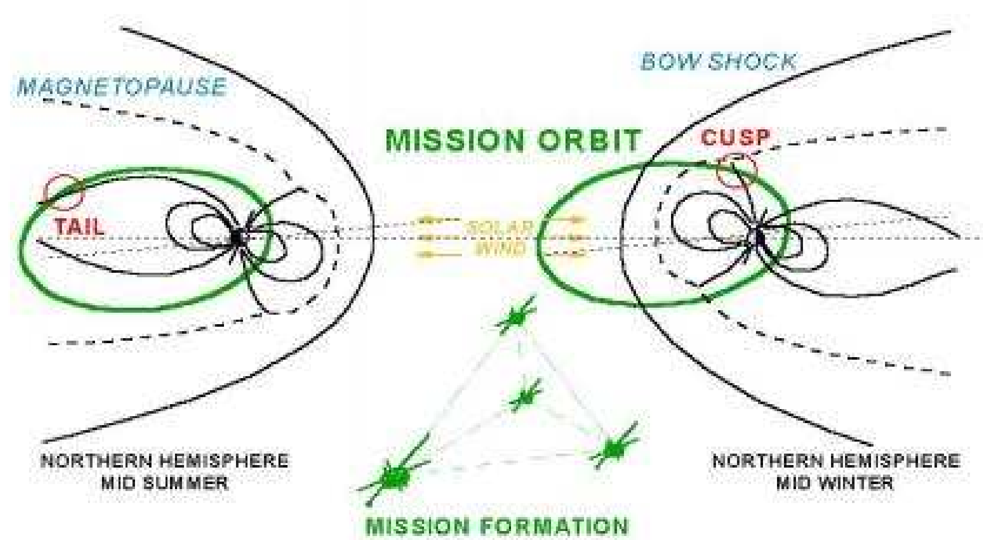

Figure 7.1. Cluster orbits during polar cusp crossings (right) and tail crossings (left). The size of the perfect tetrahedron in the cusp is 600 km and in the tail, 2000 km [*European Space Agency*, 2001].

7.2 Observations

On July 3rd 2001, between 0:00-12:00 UT the Cluster satellites located at the dawnside magnetospheric flank moving from $r \sim$ [-7.5, -17.2, 3.2] R_E to $r \sim$ [-10, -16.0, 4.5] R_E. These observations are about 8 R_E further downstream than Equator-S observations of the KH instability discussed in Chapter 6. The solar wind magnetic field, monitored by the ACE spacecraft at L1, remained northward with $B_z \sim 4$ nT from $\sim$ 20:00 UT of July 2nd to $\sim$ 2:45 UT of July 3rd, after which it decreased to $\sim$ -1 nT for 1.5 hours. It turned back northward again for $\sim$ 2.5 hours from $\sim$ 4:15 UT to $\sim$ 6:45 UT with $B_z \sim 2$ nT. The solar Wind B_x was fairly steady, varying slowly between 4-6 nT during an 11 hour period, until up to 7:00 UT when it rotated to -2nT. The solar wind B_y fluctuated in about two hour periods between from $\sim$ -5 nT to $\sim$ -3.5 nT except for a larger change from $\sim$ -4 nT to $\sim$ -7 nT during the same time interval when the IMF B_z rotated from northward to -1 nT. The IMF components formed thus a typical Parker-spiral configuration in the x, y -plane, such that the magnetic field is mostly parallel to the average magnetopause boundary normal direction. This configuration is most Kelvin-Helmholtz unstable, since there is little magnetic field along the **k**-vector of the instability to stabilize the KH modes. In addition to northward IMF conditions with Parker-spiral configuration, the flank boundaries are also Kelvin-Helmholtz unstable during very southward IMF orientations. However, during southward conditions merging at the subsolar point and resulting convection and substorm activity makes it more challenging to clearly distinguish between signatures caused by reconnection and FTE's and those caused by reconnection inside Kelvin-Helmholtz vortices. In addition, motivation for this thesis were the observations of the cold, dense plasma sheet that typically forms during periods of northward IMF [*Fujimoto et al.*, 1998a]. Therefore I selected this date in the Cluster data with northward IMF conditions to find clear signatures of reconnection inside Kelvin-Helmholtz vortices. It is also worth mentioning here that the draping of the initially Parker-spiral orientated magnetic field generates a negative tailward magnetic field component along the magnetospheric boundary, and depending on the thickness of this draping layer the boundary may become Kelvin-Helmholtz unstable or not. The cusp reconnection due to the negative B_y could also generate such a layer. In the simulation (last section of this chapter) we have taken this effect into account by including a normal component of the magnetic field with respect to the initial shear flow layer, which will generate a layer of tailward magnetic field components.

In the following sections I have first identified all current sheet crossings by the three Cluster spacecraft, SC1, SC3 and SC4 between 0:00-12:00 UT. I have analyzed boundary normal directions and de Hoffman Teller frame velocities obtained by each Cluster spacecraft and plotted them on their trajectories, respectively. Then I have identified all the brief 18-30 second intervals with reconnection signatures and corresponding boundary normal directions and HT velocities during these intervals along trajectories of each spacecraft between 5:00 UT to 8:30 UT. I will study in detail several of these brief intervals and determine whether the signatures are reconnection inside Kelvin-Helmholtz vortices. In this detailed analysis I have concentrated on cases between 5:30-6:02 UT since during this interval the 1-hour time shifted ACE data of the solar wind measurements showed steady IMF with northward B_z, solar wind speed of 400-410 km/s and proton number density of $\sim 9/\text{cm}^3$.

7.2.1 Current Sheet Crossings

Figure 7.2a represents plasma (left panel) and magnetic field (right panel) observations by four Cluster satellites between 00:00-12:00 UT on 3rd of July 2001. The top right panel shows the Cluster constellation in x, y- and x, z-planes in relative (trajectories presented relative to spacecraft 3, SC3) and absolute coordinates. The color of the observed data corresponds to different spacecraft: black corresponds to spacecraft 1, SC1; yellow to spacecraft 2, SC2; green to spacecraft 3, SC3; and red to spacecraft 4, SC4. The top panel of the plasma data shows the plasma density. The bottom panel shows the plasma temperature and the middle panels from top to bottom represent the plasma velocity components, v_x, v_y, and v_z respectively. Magnetic field data shows b_x (top panel), b_y, and b_z. The bottom panel shows current density which is calculated from $\mathbf{J} = \frac{1}{\mu_0}\nabla \times \mathbf{B}$, where $\mathbf{B}$ is interpolated between four Cluster satellites. Thus the current layers that are smaller than spacecraft separation are not plotted. Shaded regions indicate intervals when SC1 observed current sheets for more than 50 seconds and with magnetic field variance of more than 7 nT. Current sheets are determined from rotation of the magnetic field. This magnetic field rotation is defined by how much the variance of the measured magnetic field values differs from the average of the measured values during the 50 second interval. All the plasma and magnetic field components show fluctuations. Comparing the top and bottom panel in the plasma data one can see that the groups of high density peaks correspond to the low temperature regions. The v_x component goes strongly negative $\sim$ -400 km/s in these regions and the spacecraft observe the strongest current layers. In these regions spacecraft are close to the dawn side flank magnetopause, sometimes crossing the boundary observing the fast, tailward magnetosheath flow with colder and denser sheath-type plasma. The velocity oscillations are more rapid than the density oscillations indicating fine structure embedded in large scale motion. Figure 7.2b represents the trajectory of spacecraft 1 between 0:00-12:00 UT. Black vectors are boundary normal directions and red vectors are de Hoffman Teller velocities determined with the maximum variance of electric field during the intervals when SC1 observed magnetic field rotations illustrated as shaded regions in Figure 7.2. Projections of these vectors and satellite trajectory are plotted on the walls of the 3-D box.

Shaded regions in Figure 7.3a and in Figure 7.4a represent current sheet crossings observed by spacecraft 3 and 4, respectively. Figure 7.3b and Figure 7.4b show boundary normal directions (black vectors) and de HT frame velocities (red vectors) during the shaded intervals in Figure 7.3a and Figure 7.4a. These are plotted along the trajectory of SC3 and SC4 between 0:00-12:00 UT.

When comparing Figures 7.2, 7.3, and 7.4, one can see that all of the 3 satellites observe more or less the same current sheets. Since SC4 was located furthest in the magnetosheath direction it seemed to observe more frequent current sheet crossings than SC1 and SC3. Looking at satellite trajectory projections in the x, y -plane one can see that satellites are moving perpendicular towards the average magnetopause boundary direction. The average de HT velocities during these over 50 s intervals with current sheet crossings are perpendicular to the boundary normals at the x, y-plane, indicating the direction of the average tailward flowing magnetosheath plasma tangential to the magnetopause. During this 12 hour period the satellites are first moving out from the equatorial plane to the positive z-direction and in the end they start moving back towards the equatorial plane again. Whereas the boundary normals don't vary much in x, y plane during these "large" current sheet crossings, they seem to vary in y, z-plane indicating waves propagating to positive and negative z-direction.

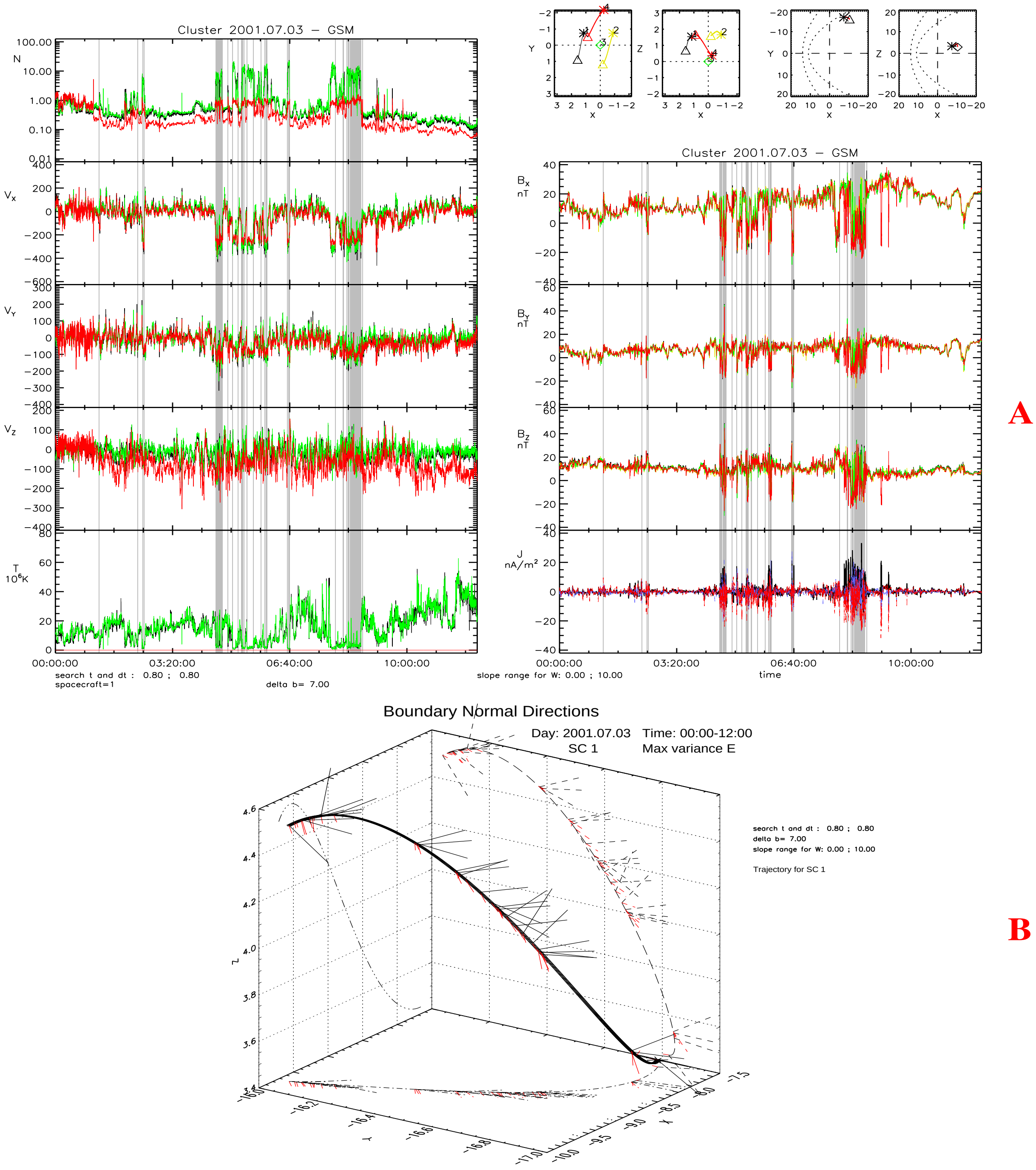

Figure 7.2. A) represents plasma (left) and magnetic field (right) observations along Cluster orbit on 3rd of July 2001 between 00:00-12:00 UT. The shaded regions indicate intervals when SC1 observed current sheets. The upper right box shows the Cluster constellation. B) shows boundary normal directions (black vectors) and de HT velocities (red vectors) during shaded intervals.

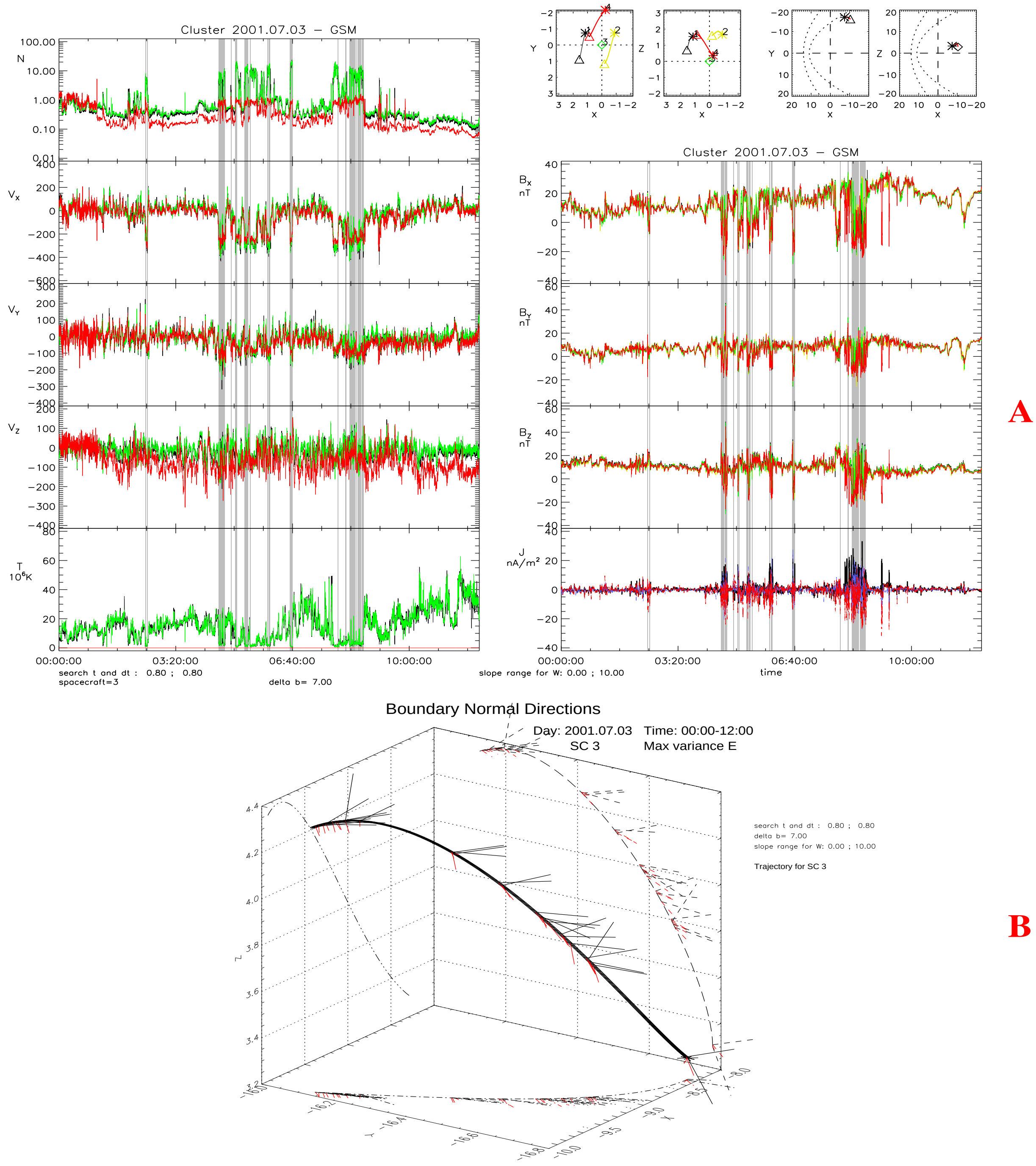

Figure 7.3. A) represents plasma (left) and magnetic field (right) observations along Cluster orbit on 3rd of July 2001 between 00:00-12:00 UT. The shaded regions indicate intervals when SC3 observed current sheets. The upper right box shows the Cluster constellation. B) shows boundary normal directions and de HT velocities during the shaded intervals.

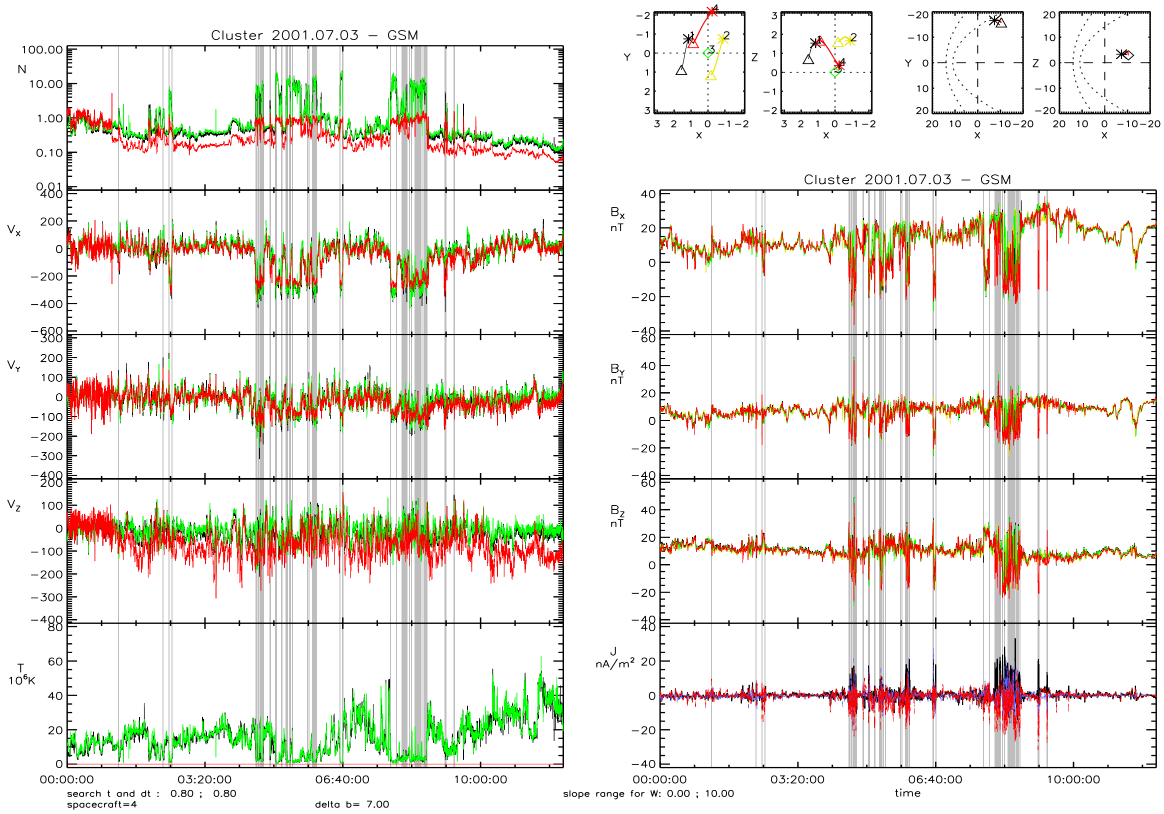

A

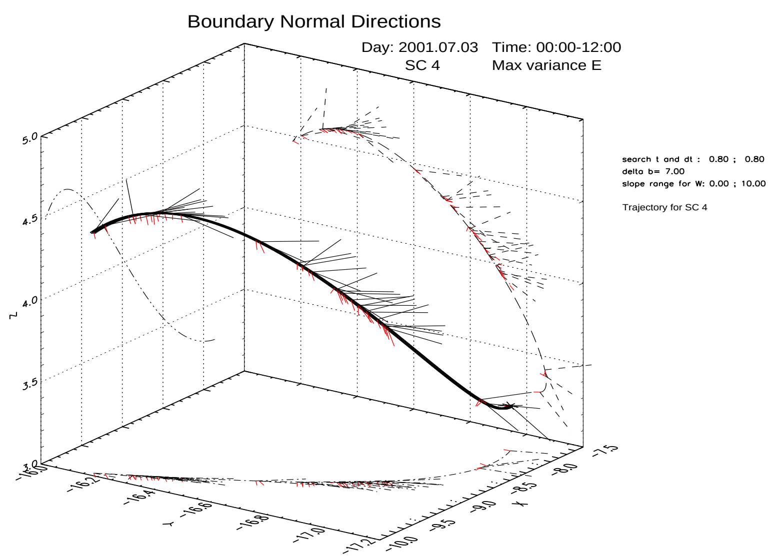

B

Figure 7.4. A) represents plasma (left) and magnetic field (right) observations along Cluster orbit on 3rd of July 2001 between 00:00-12:00 UT. The shaded regions indicate intervals when SC4 observed current sheets. The upper right box shows the Cluster constellation. B) shows boundary normal directions and de HT velocities during the shaded intervals.

7.2.2 Intervals with Reconnection Signatures: Accelerated Flow or Alfvén Waves?

Intervals chosen with SC1

Figure 7.5 shows a sub-domain of Figure 7.2 with magnetic field and plasma observations between 5:00-8:30 UT. The shaded regions indicate 20-35 s intervals with reconnection signatures observed by spacecraft 1. Reconnection intervals are chosen by the following conditions: i) the slope for Walen relation is between 0.65-1.35 and ii) the slope for de HT frame is between 0.9-1.1. SC1 observes several brief intervals satisfying the reconnection condition during this 3.5 hour period. These reconnection intervals are adjacent to or are embedded in the larger current sheet regions. There are more frequent boundary layer crossings between 5:00-6:40 UT after which Cluster goes deeper into the magnetosphere. After 8:00 UT boundary crossings become more frequent again.

Figure 7.6 represents trajectories, boundary normal directions, and de HT velocities of SC1, SC3, and SC4 between 5:00-8:30 UT during the intervals with reconnection signatures observed by SC1 illustrated in Figure 7.5. The boundary normals oscillate more than for larger intervals in Figures 7.2, 7.3 and 7.4. Very large de HT frame vectors are observed along the trajectory of SC1 and SC3. It is worth noting here that since the scaling of each box is different one cannot compare the sizes of the vectors between different boxes but only compare vectors within the same box.

Figure 7.7 shows plasma and magnetic field observations for the brief 20 s period between 06:40-06:40:22 UT in variance E coordinates chosen by SC1. The upper right box shows the Cluster constellation and de HT frame velocity in GSM and in variance E coordinates observed by SC1. This interval corresponds to the largest de Hoffmann Teller velocity vector observed by SC1 in Figure 7.51). The de HT velocity is $\mathbf{v_{HT}} = [667, 293, 640]$ km/s in GSM coordinates and $\mathbf{v_{HT_{VarE}}} = [958, 53, 137]$ km/s in variance E coordinates. The largest de Hoffmann Teller velocity of 958 km/s is into the direction of the tangent (L) measured by SC1. The de HT velocity along the normal direction (N) is 137 km/s and only 53 km/s into the intermediate direction (M). The velocity and magnetic field components use following notation: i corresponds to normal direction, j intermediate direction and k tangential direction.

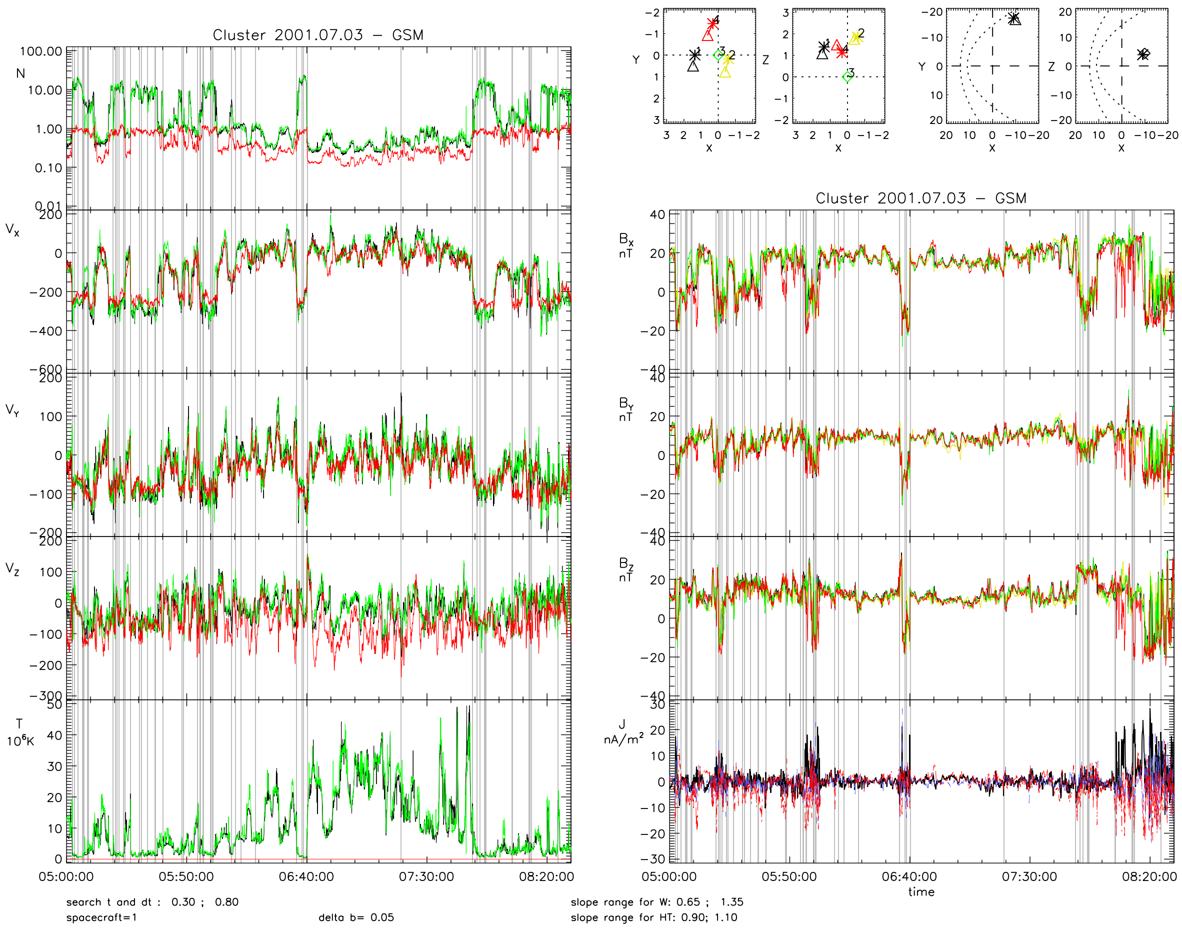

Figure 7.5. Plasma (left) and magnetic field (right) observations along Cluster orbit on 3rd of July 2001 between 05:00-8:30 UT. The shaded regions indicate intervals when SC1 observed reconnection signatures. The upper right box shows the Cluster constellation.

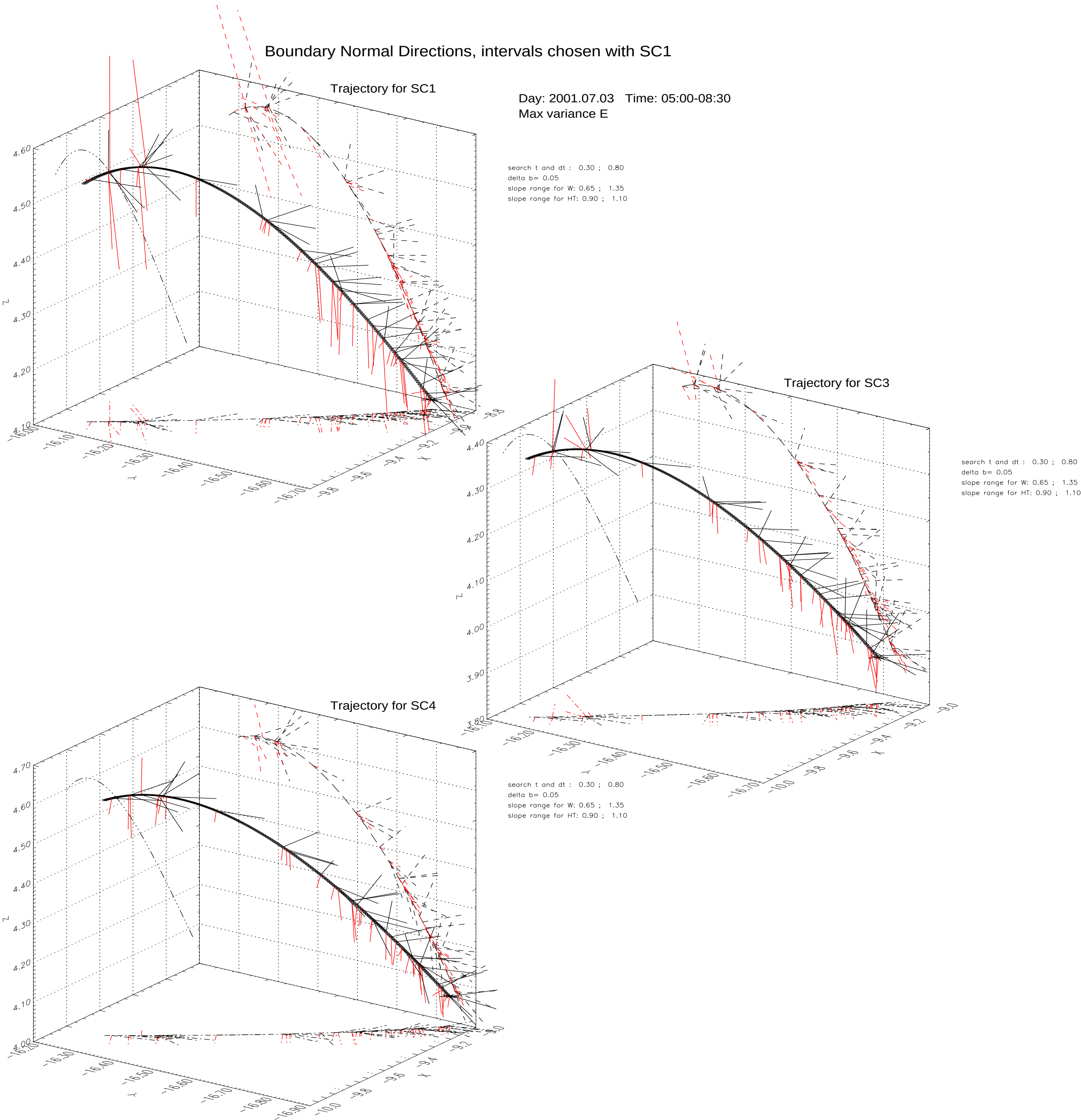

Figure 7.6. Boundary normal directions (black vectors) and de HT velocities (red vectors) during the intervals (illustrated in Figure 7.5) with reconnection signatures observed by SC1 between 05:00-8:30 UT and plotted along the trajectory of SC3, SC1, and SC4.

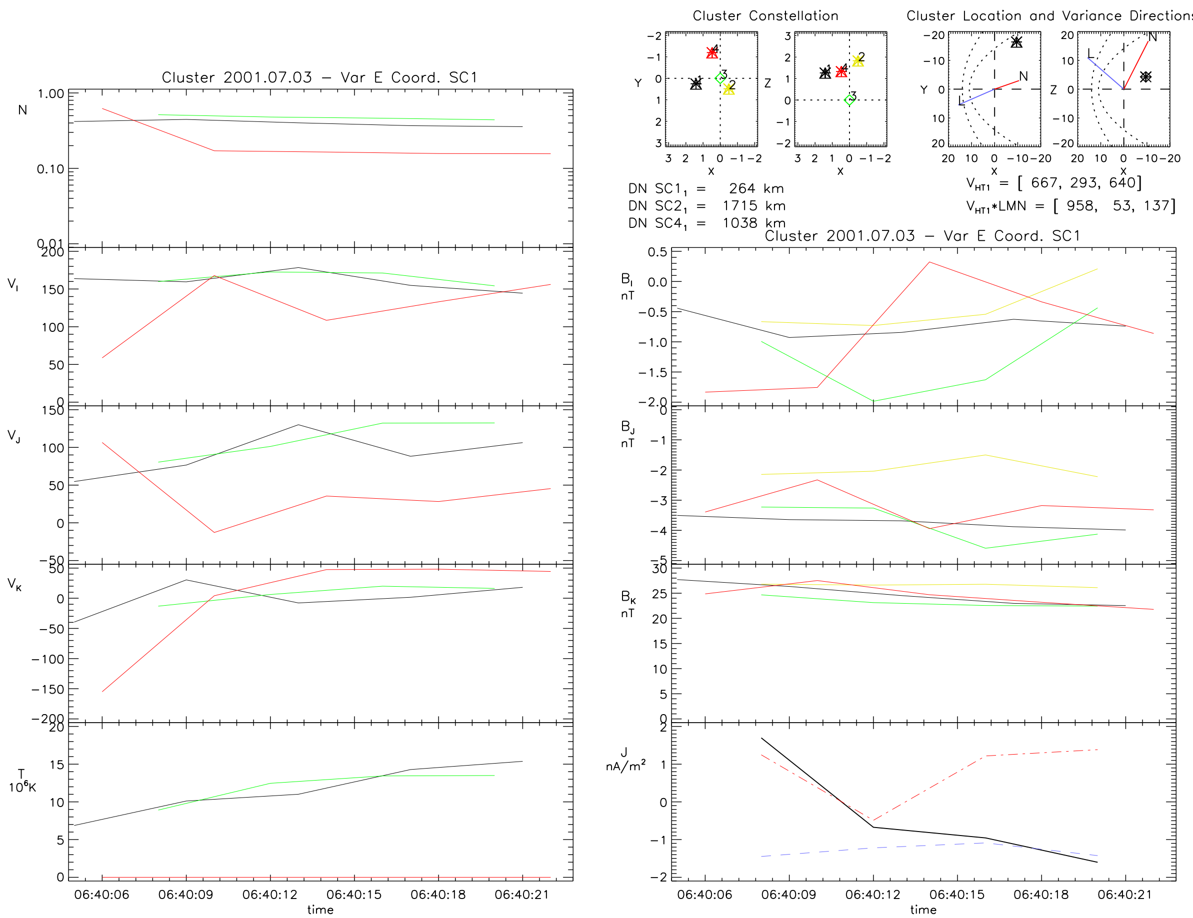

Figure 7.7. Plasma (left) and magnetic field (right) observations along Cluster orbit on 3rd of July 2001 for brief 20 s period between 06:40-06:40:22 UT in variance E coordinates chosen by SC1. The upper right box shows the Cluster constellation and de HT frame velocity in GSM and in variance E coordinates observed by SC1.

Figure 7.8a shows the Walen relation s (left) and de HT frames (right) observed by SC1 for a 6.5 minute period between 6:36-06:42:30 UT in a and for a brief 20 second period in b. For the 6.5 minute period the Walen relation is not satisfied. The de HT frame velocity for this interval is $\mathbf{v_{HT}}$ = [-239, -125, -64] km/s, which is about 70 % of the magnetosheath velocity on 3rd of July 2001. The boundary normal direction for this 6.5 minute period measured by SC1 is mostly in the x, y-plane pointing to the average magnetopause direction at the dawnside flank. For the brief 20 s interval (Figure 7.8b the Walen relation is satisfied and de HT frame is obtained with much larger transformation velocity,$\mathbf{v_{HT}}$ = [667, 293, 640] km/s. So the de HT Frame velocity for this 20 second period is about 690 km/s larger than for the surrounding 6.5 minute period. The boundary normal for this 20 s period points mostly into the z-direction and has drastically changed from the overall 6.5 minute period. If SC1 really went through the reconnection region, this large change in de HT frame velocity should correspond to the plasma acceleration out from the reconnection region. However, the plasma velocity components measured by SC1 (black traces) in Figure 7.7 show plasma acceleration of only $\sim$ 90km/s, and also the magnetic field doesn't change direction. This indicates that determining the "reconnection" intervals from satellite data just by using an excellent Walen relation and an excellent de HT frame with an enhanced velocity is not a sufficient test for reconnection. However, this high de HT frame velocity could correspond to an Alfvén wave passing by the satellite. The cluster constellation, and boundary normal (red vector) and tangent (blue vector) orientation at the upper right panel of Figure 7.7 indicate that SC3 is located in the tangent direction of the SC1. The electric field was minimized at the SC1 location with the tangential transformation velocity of 958 km/s, so SC3 should also see an accelerated de HT velocity in this direction.

SC3 observations of large de HT frame velocity during intervals chosen with SC1

Figure 7.9 shows plasma and magnetic field observations for brief 20 s period between 06:40-06:40:22 UT in variance E coordinates chosen by SC3. The upper right box shows the Cluster constellation and de HT frame velocity in GSM and in variance E coordinates observed by SC3. The de HT velocity is $\mathbf{v_{HT}}$ = [411, 137, 439] km/s in GSM coordinates and $\mathbf{v_{HT_{VarE}}}$ = [358, 501, 43] km/s in variance E coordinates. The largest de Hoffmann

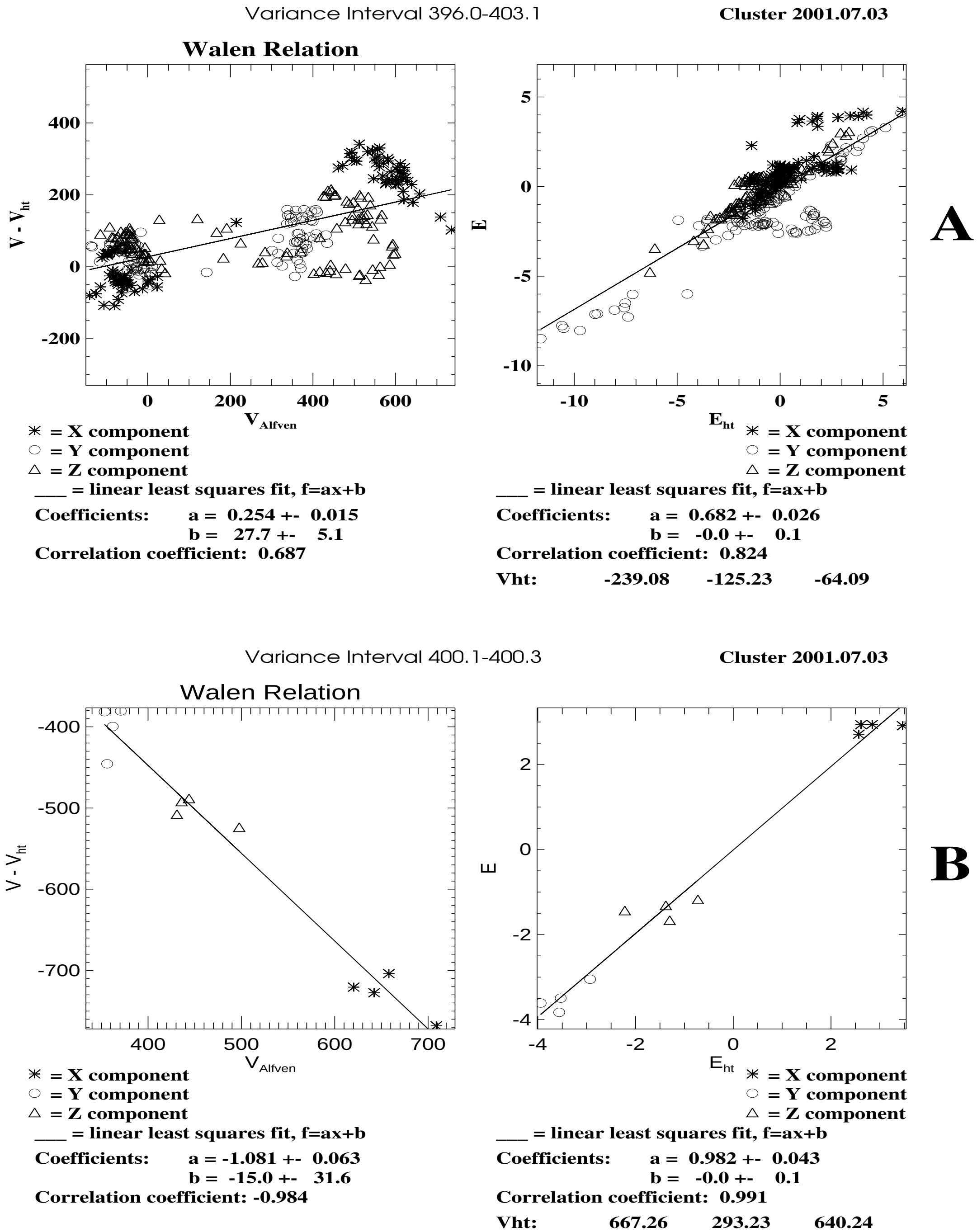

Figure 7.8. Walen relations (left) and de HT frames (right) observed by SC1 for a 6.5 minute period between 6:36-06:42:30 UT in A) and for a brief 20 second period in B).

Teller velocity of 501 km/s is into the intermediate direction measured by SC3. The de HT velocity along the normal direction is 43 km/s and 358 km/s in the tangent direction. The boundary normal direction measured by SC3 is same as measured by SC1 and mostly into the z-direction and very different from the overall 6,5 minute boundary normal direction (same for SC1, SC3, and SC4) which is mostly in the x, y-plane pointing into the average magnetopause direction.

Figure 7.10a shows the Walen relation s (left) and de HT frames (right) observed by SC3 for a 6.5 minute period between 6:36-06:42:30 UT and for a brief 20 second period in b. For the longer 6 minute period the Walen relation is not satisfied. The de HT frame velocity for this interval is $\mathbf{v_{HT}}$ = [-236, -124, -53] km/s, which is approximately 60 % of the solar wind speed for that time interval on 3rd of July 2001 and almost the same as measured by SC1. For the shorter 20 s interval the Walen relation is satisfied and de HT frame is obtained with much larger transformation velocity, $\mathbf{v_{HT}}$ = [412, 137, 440] km/s. Like SC1, SC3 sees the accelerated de HT frame velocity even though the velocity components (green trace) to the normal (v_i) and intermediate (v_j) direction do not change. Also, the velocity component in the tangent direction (v_k) only changes about 80 km/s disagreeing with the estimated velocity change of 618 km/s. SC1 is closer to the source region of this Alfvén wave observing a higher velocity than the SC3.

SC4 observations of large de HT frame velocity during intervals chosen with SC1

Figure 7.11 shows plasma and magnetic field observations for brief 20 s period between 06:40-06:40:22 UT in variance E coordinates chosen by SC4. The upper right box shows the Cluster constellation and de HT frame velocity in GSM and in variance E coordinates observed by SC4. The de HT velocity is $\mathbf{v_{HT}}$ = [164, 61, 242] km/s in GSM coordinates and $\mathbf{v_{HT_{VarE}}}$ = [108, 264, -87] km/s in variance E coordinates. The largest de Hoffmann Teller velocity of 264 km/s is to the intermediate direction measured by SC4. The de HT velocity along the normal direction is -87 km/s and 108 km/s in the tangent direction.

Figure 7.12a shows the Walen relation s (left) and de HT frames (right) observed by SC4 for a 6.5 minute period between 6:36-06:42:30 UT and for a brief 20 second period in b. The de HT frame velocity for this interval is $\mathbf{v_{HT}}$ = [-222, -109, -75] km/s, which is

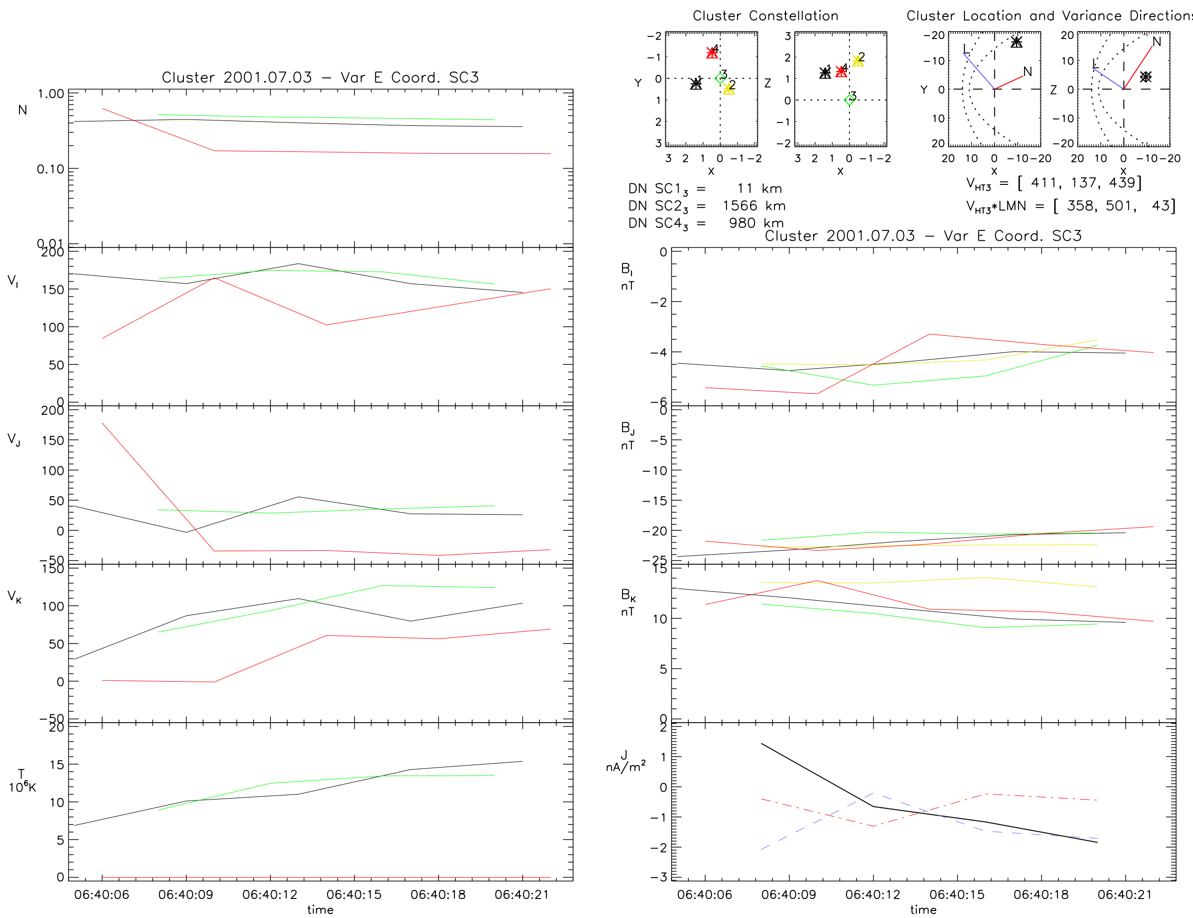

Figure 7.9. Plasma (left) and magnetic field (right) observations along Cluster orbit on 3rd of July 2001 for brief 20 s period between 06:40-06:40:22 UT in variance E coordinates chosen by SC3. The upper right box shows the Cluster constellation and de HT frame velocity in GSM and in variance E coordinates observed by SC3.

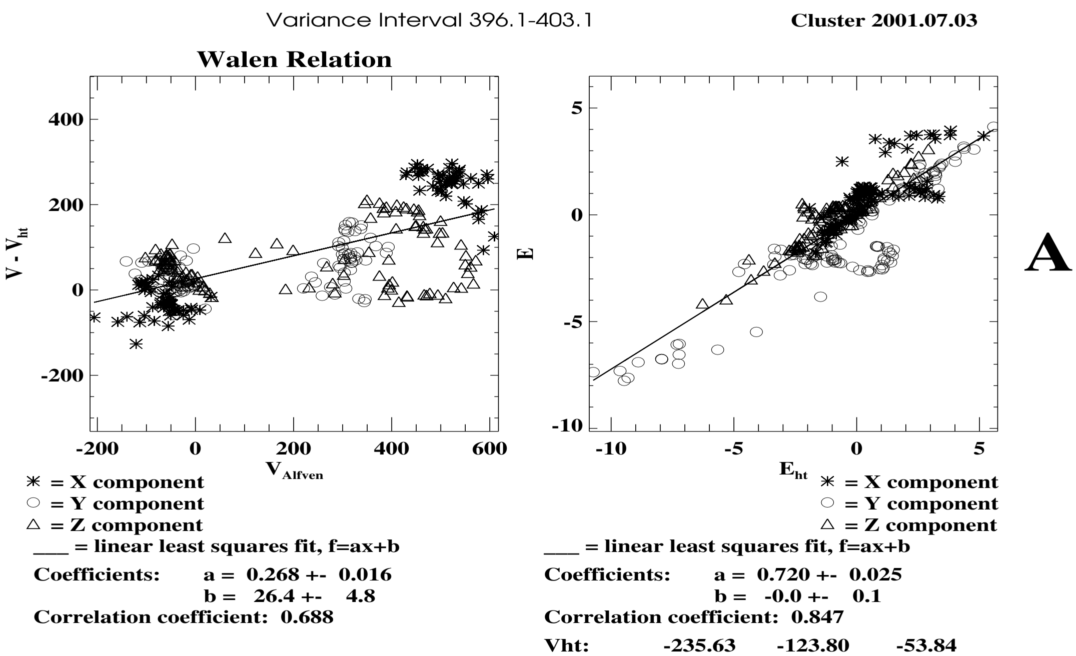

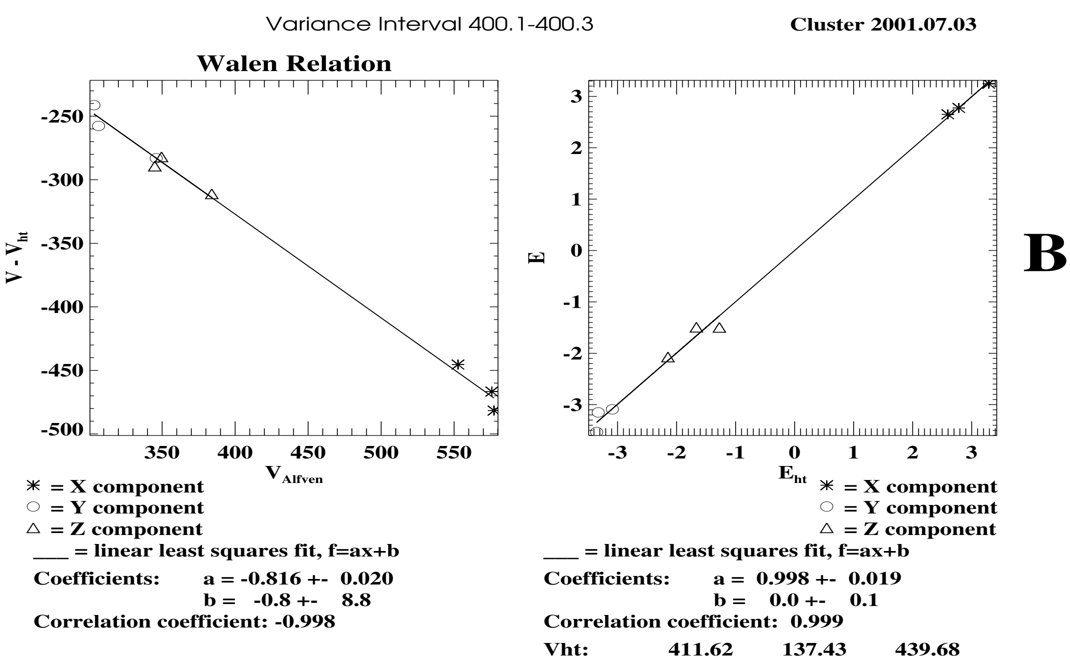

Figure 7.10. Walen relations (left) and de HT frames (right) observed by SC3 for a 6.5 minute period between 6:36-06:42:30 UT in A) and for a brief 20 second period in B).

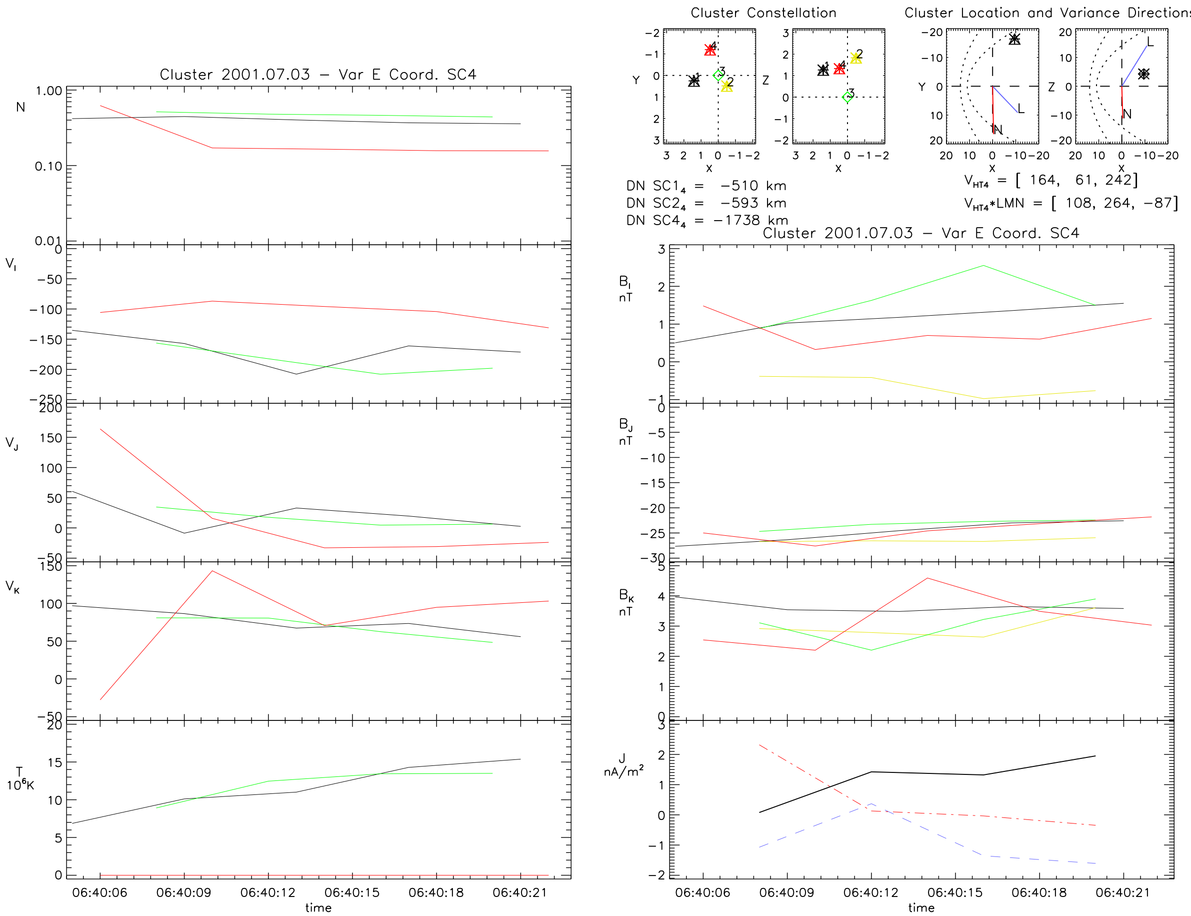

Figure 7.11. Plasma (left) and magnetic field (right) observations along Cluster orbit on 3rd of July 2001 for brief 20 s period between 06:40-06:40:22 UT in variance E coordinates chosen by SC4. The upper right box shows the Cluster constellation and de HT frame velocity in GSM and in variance E coordinates observed by SC4.

approximately 70% of the solar wind speed for that time interval on the 3rd of July 2001 and almost the same as measured by SC1. For the brief 20 s interval the de HT frame velocity is different from the overall velocity of the boundary motion, $\mathbf{v_{HT}} = [164, 61, 242]$ km/s. Unfortunately, the value for the Walen relation can not be used here since the HIA instrument in SC4 measured too low density values (due to a calibration problem). SC4 is the only satellite during this interval that actually measures reasonable change of 270 km/s in flow velocity. The absolute value of the de HT frame velocity doesn't differ much from the value of the overall interval, but it has rotated (all the components have changed direction) having the largest velocity component in the z-direction.

The observations of the accelerated de HT frame velocity by SC1 and SC3 are not signatures of accelerated flow from the reconnection region. However, the facts that SC1 and SC3 are located in the tangent direction of each other and both of these satellites observed this accelerated de HT frame velocity might be indicative that reconnection took place further upstream along the tangent direction of the SC1. In this scenario the reconnection could have launched an Alfvén wave with a group velocity of $\sim$ 900km/s, and SC1 would observe this. As the wave travels it loses energy and by the time it reaches SC3 its group velocity is only $\sim$ 600km/s. Such a high group velocity for a Alfvén wave would be possible if the magnetic field would change about 40 nT and plasma density would change by 10/cm^3. Figure 7.13 shows Cluster plasma (left) and magnetic field (right) observations between 6:36-06:42:30 UT illustrating that prior to the SC1 and SC3 observations of the high de HT frame velocities the Cluster satellites are crossing a strong current sheet. Spacecraft move from the high density, low-temperature magnetosheath-type region to the hot and tenuous magnetospheric plasma. The x-component of the magnetic field changes $\sim$ 40 nT, and B_y and B_z change $\sim$ 20 nT. The density changes more than 10/cm^3 indicating that these changes in plasma and magnetic field could provide the source for the observed disturbance launched as an Alfvén wave. Another interesting feature in this 6.5 minute interval is that in the magnetosheath region, the magnetic field has a strong negative z-component ($B_z \sim$ -10 nT), even though the time shifted magnetic field data of the ACE satellite indicates a positive $B_z \sim$ 2 nT at the Cluster location. The v_y and v_z components measured by SC4 (red trace) in Figure 7.13 show a big change during the $\sim$ 20 second interval when SC1 and SC3 observed high de HT frame velocities. This could be outflow from the reconnection

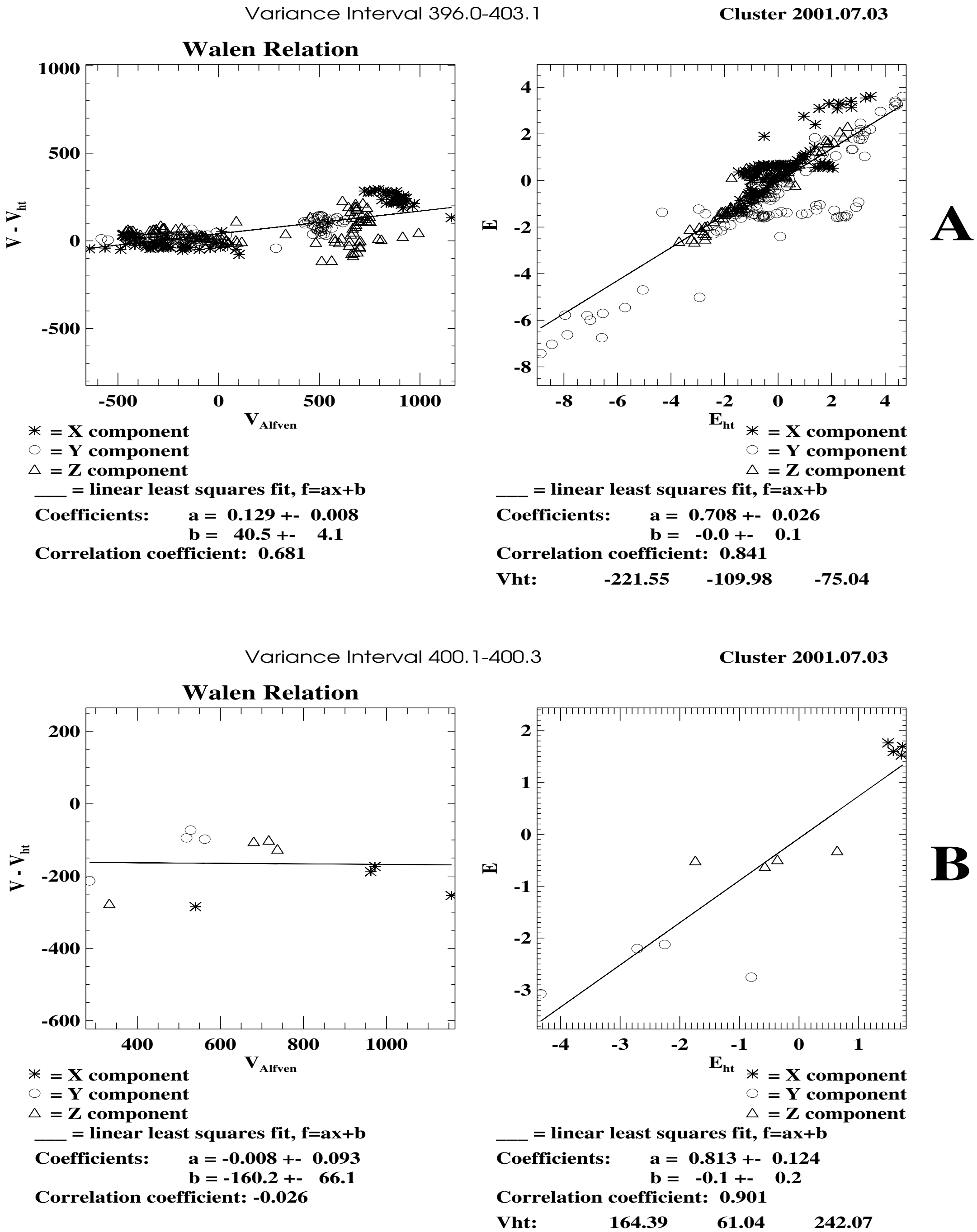

Figure 7.12. Walen relations (left) and de HT frames (right) observed by SC4 for a 6.5 minute period between 6:36-06:42:30 UT in A) and for a brief 20 second period in B).

region since the previous analysis for SC4 indicated that the de HT Frame velocity was rotated form the larger 6.5 minute interval, but (like discussed before) unfortunately for SC4 we cannot test for the Walen relation. SC1 and SC3 observe this jump in v_y and v_z about 15 second earlier than SC4 but the Walen relation is not satisfied during this change. The other two shaded regions in Figure 7.13 are also just Alfvén waves since none of the spacecraft observe changes in plasma velocity components.

Intervals chosen with SC3

Figure 7.14 shows a sub-domain of Figure 7.4 with magnetic field and plasma observations between 5:00-8:30 UT. The shaded regions indicate 20-35 s intervals with reconnection signatures observed by SC3. Reconnection intervals are chosen with the same conditions as in Figure 7.5. While some of the intervals are same as observed by SC1 or partly overlapping with those chosen by SC1, there are also additional intervals that were not found in the SC1 data as well as intervals that were found in the SC1 data but that are not present here.

Figure 7.15 represents spacecraft trajectories, boundary normal directions and de HT velocities between 5:00-8:30 UT during the intervals with reconnection signatures observed by SC3 illustrated in Figure 7.7. Also in this case the boundary normals oscillate more than for cases with large magnetic field rotations. The large de HT frame vectors are observed along the trajectory of SC1, SC3, and SC4.

Plasma and magnetic field observations of SC1 and SC3 between 06:40:00-06:40:22 UT show that–even though the Walen relation is satisfied and the de HT frame is obtained with much higher transformation velocity than for the overall interval–no plasma acceleration corresponding to the large HT velocity is observed. Our goal was to find intervals with reconnection signatures in the Cluster data. If a satellite travels through the reconnection outflow region, the Walen relation should be satisfied, and the de HT frame should be obtained with a velocity larger or smaller than that of the overall interval (also a rotation of the HT velocity from the overall interval could be consistent with reconnection). We found several brief 20-30 second intervals on the 3rd of July 2001 between 5:00-8:30 UT which satisfied this criteria for reconnection. However, the observed de HT velocities should be consistent with the plasma outflow from the reconnection region embedded in the large scale motion of the boundary. This was not the case for the numerous intervals observed between

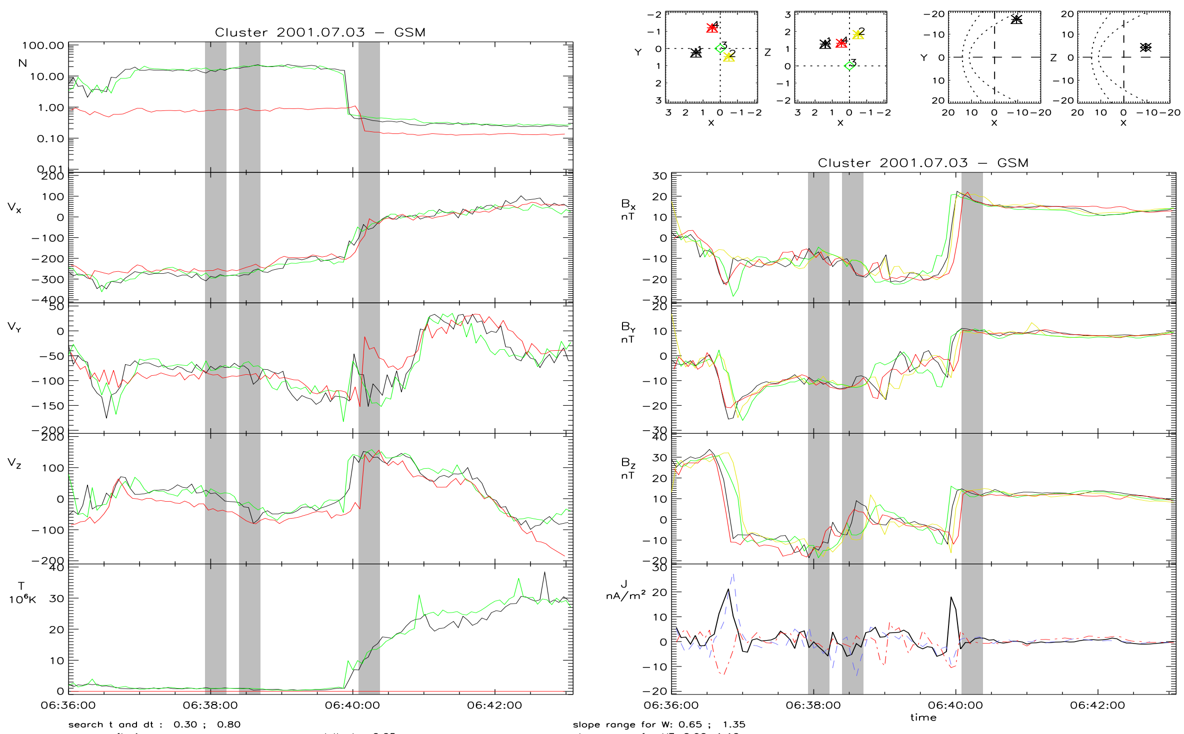

Figure 7.13. Cluster plasma (left) and magnetic field (right) observations between 6:36-06:42:30 UT. The shaded regions indicate regions with reconnection signatures.

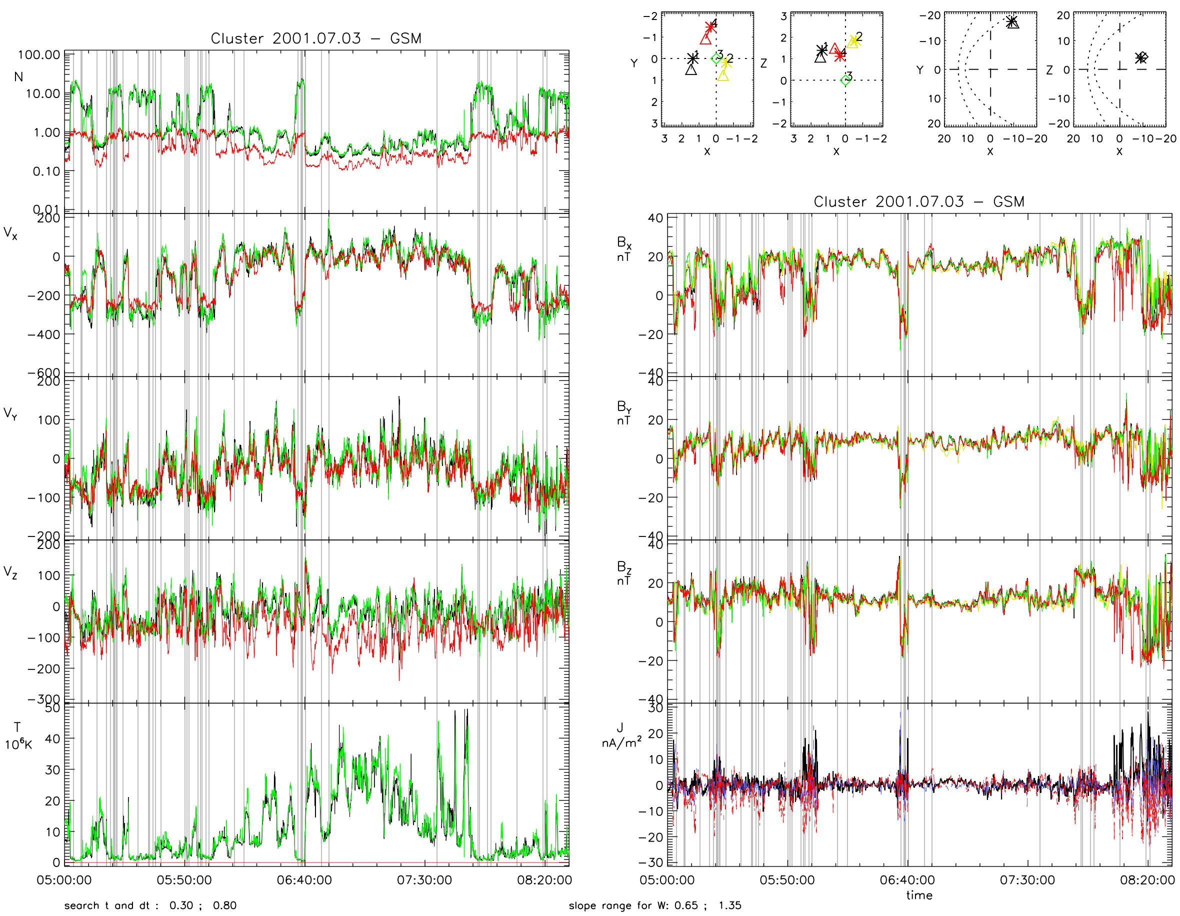

Figure 7.14. The data shown in this figure are the same as in Figure 7.4 but the shaded intervals that indicate reconnection signatures are here based on SC3 data.

5:00-8:30 UT, as illustrated by observations of SC1 and SC3 between 06:40:00-06:40:22 UT. The Cluster spacecraft 1 and 3 most likely observed an Alfvén wave propagating into the boundary tangent direction (boundary tangent direction measured with both spacecraft was the same during 06:40:00-06:40:22 UT). An Alfvén wave would also satisfy the Walen relation, and the de HT frame with a different velocity than that of the overall interval. Results in this section indicate that satisfying the Walen relation and de HT frame is a necessary but not sufficient condition for ongoing reconnection. Thus the additional criteria of plasma acceleration must be included in the automated search for reconnection intervals. However, detection of the same Alfvén wave by both spacecraft might be important, as a reconnection event could have occurred further upstream of the location of SC1, which could have launched a perturbation along the magnetic field line.

7.2.3 Intervals with Accelerated Flow

It was discussed above that satisfying the Walen relation and de HT frame is a necessary but not a sufficient condition for defining intervals with accelerated outflow from the reconnection region. In the following we have further developed this automated search for reconnection signatures by including the condition for the variance of the plasma velocity and magnetic field. Figure 7.16a represents Cluster plasma (left) and magnetic field (right) observations between 04:54:00-06:06:00 UT. The shaded regions indicate regions with reconnection signatures and accelerated flow observed by SC1. Reconnection intervals were chosen with same criteria as before but in addition the variances of the magnetic field and velocity are required to be larger than 2 nT and 60 km/s, respectively. Between 04:54:00-06:06:00 UT SC1 observes 6 brief ~ 20 s intervals that satisfy the above mentioned reconnection conditions. Figure 7.16b represents Boundary normal directions and de HT frame velocities during the shaded intervals along the trajectory of SC1. In the following I will analyze these brief intervals in detail by transforming observations to the boundary normal coordinates defined by the maximum variance of electric field, E.

Accelerated flow between 05:40:06-05:40:27 UT

Figure 7.17a shows Cluster plasma (left) and magnetic field (right) observations between 05:40:06-05:40:27 UT in variance E coordinates determined by SC1 and b represents the

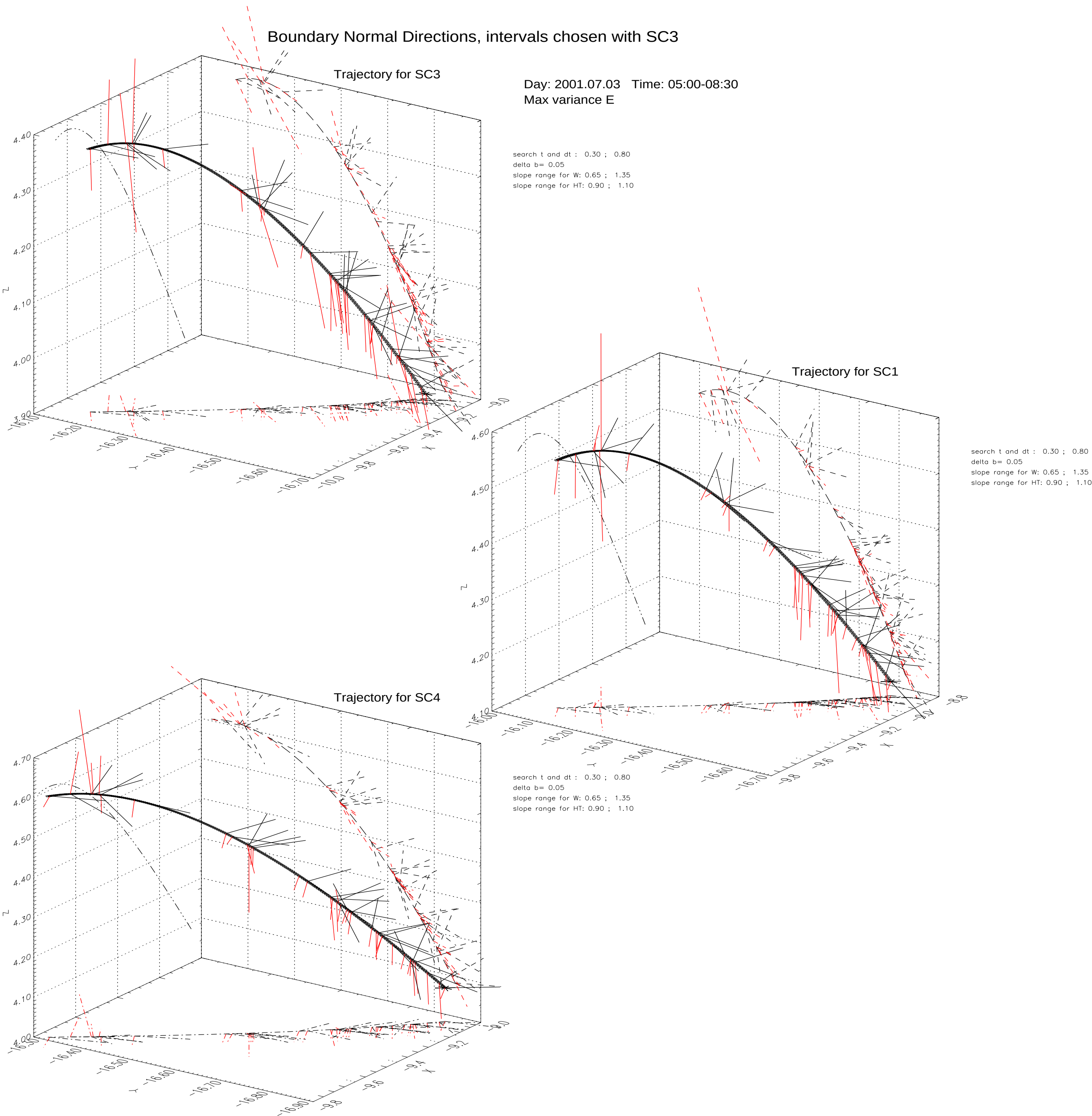

Figure 7.15. Boundary normal directions (black vectors) and de HT velocities (red vectors) during the intervals (illustrated in Figure 7.7) with reconnection signatures observed by SC3 between 05:00-8:30 UT and plotted along the trajectory of SC3, SC1 and SC4.

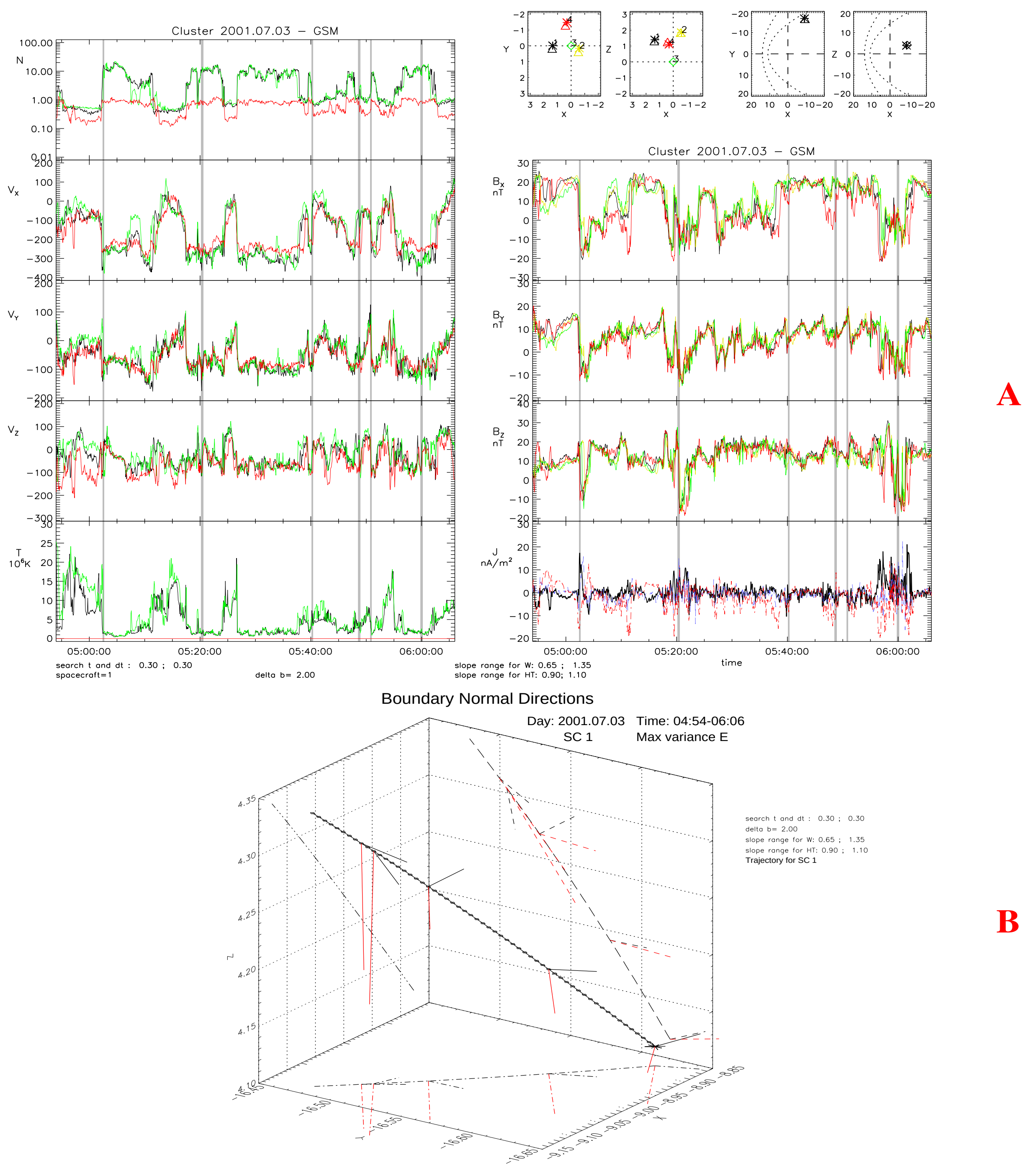

Figure 7.16. A) Represents Cluster plasma (left) and magnetic field (right) observations between 04:54:00-06:06:00 UT. The shaded regions indicate regions with reconnection signatures and accelerated flow observed by SC1. B) represents boundary normal directions and de HT frame velocities during shaded intervals along the trajectory of SC1.

Walen relation (left) and de HT frame (right) for this interval. The de Hoffmann Teller velocity, $\mathbf{v_{HT}}$, is [-434, -165, -292] km/s in GSM coordinates, and v_{HT} = [-548, 29, 2] km/s in variance E coordinates indicating the maximum transformation velocity along the tangent direction. The boundary tangent is mostly in the x, z -plane with a smaller y-component. The slope for the Walen relation and de HT frame are 0.77 and 0.98, respectively. From the density profile it is easy to notice that SC1 and SC3 are not in the high density magnetosheath-like region nor in very low density magnetospheric region, but in the region with intermediate values of these plasmas. During this interval the normal component of the plasma velocity changes from positive 20 km/s to negative -90 km/s simultaneously as the normal magnetic field component changes from zero to negative 4 nT. The intermediate component of the velocity changes by 40 km/s and the tangential velocity component changes by 300 km/s. Figure 7.18a shows Cluster plasma (left) and magnetic field (right) observations between 05:36-05:42 UT in variance E coordinates determined by SC1 and b represents the Walen relation and de HT frame for this 6 minute interval, enclosing the brief 20 second interval discussed above. The de Hoffmann Teller velocity, $\mathbf{v_{HT}}$, is [-289, -122, -147] km/s in GSM coordinates, and v_{HT} = [-345, 2, -15] km/s in variance E coordinates indicating the maximum transformation velocity along the tangent direction. Tangent and normal have nearly the same orientation as for the enclosed brief 20 second interval. The slope for the Walen relation and de HT frame during the longer interval are 0.48 and 0.95 respectively. The de HT frame velocity during 05:40:06-05:40:27 UT has increased by $\sim$ 200 km/s in the tangent direction compared to the average HT frame velocity. Corresponding plasma acceleration is observable in the tangential velocity component. Since the Walen relation was also satisfied during 05:40:06-05:40:27 UT, this could indicate that SC1 traveled through the reconnection region observing fast outflow into the same direction where the overall boundary wave was moving. It is now worth-while to study what SC3 and SC4 observed during this interval.

Figure 7.19a shows Cluster plasma (left) and magnetic field (right) observations between 05:40:06-05:40:27 UT in variance E coordinates determined by SC3 and b represents the Walen relation (left) and de HT frame (right) for this interval. The de Hoffmann Teller velocity, $\mathbf{v_{HT}}$, is [-327, -150, -226] km/s in GSM coordinates, and v_{HT} = [-422, 37, -14] km/s in variance E coordinates indicating the maximum transformation velocity along the tangent

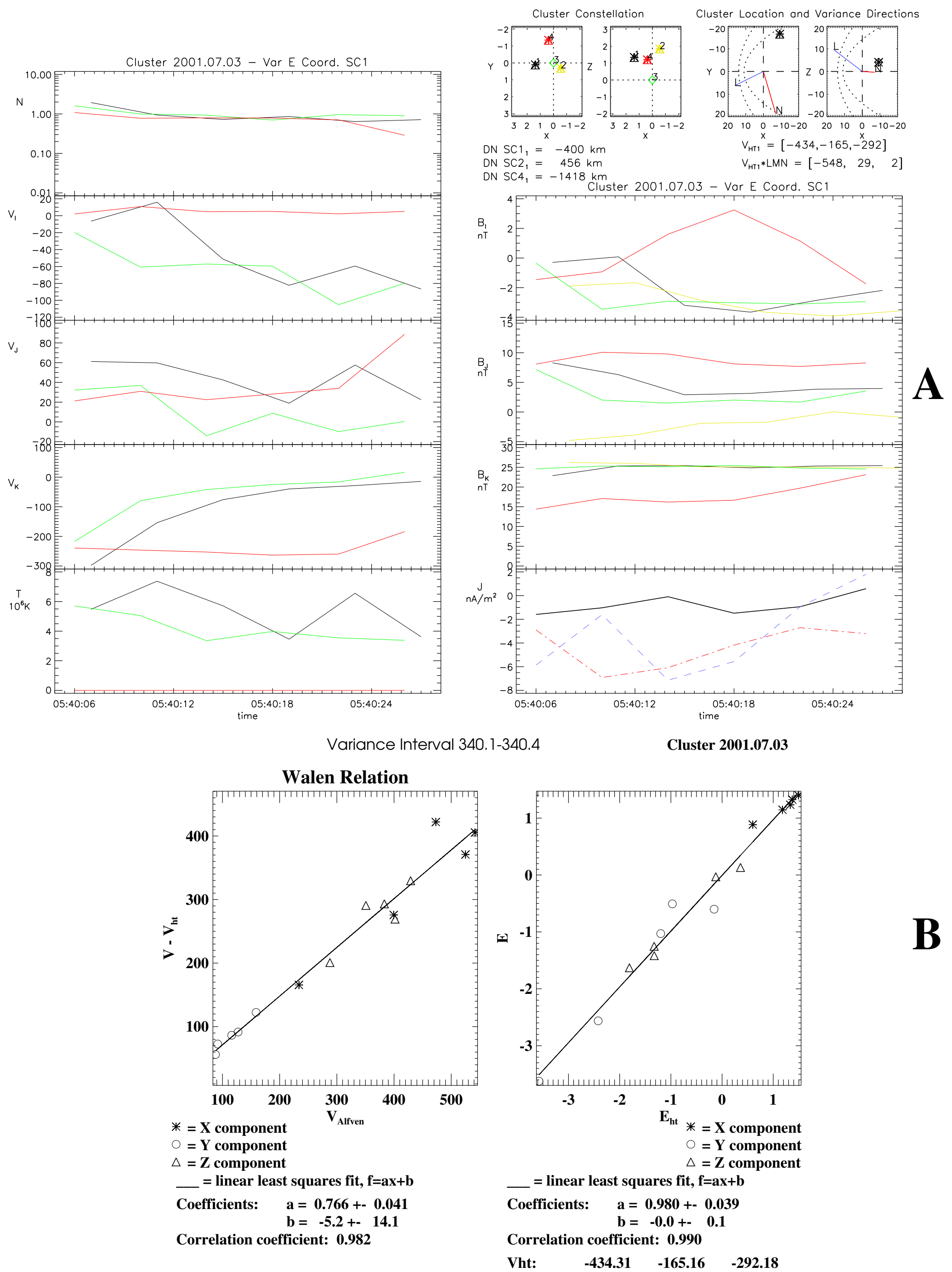

Figure 7.17. A) Represents Cluster plasma (left) and magnetic field (right) observations between 05:40:06-05:40:27 UT in variance E coordinates determined by SC1. The top right boxes show the Cluster constellation and de HT frame velocities in GSM and in variance E coordinates. B) represents the Walen relation (left) and de HT frame (right) for this interval.

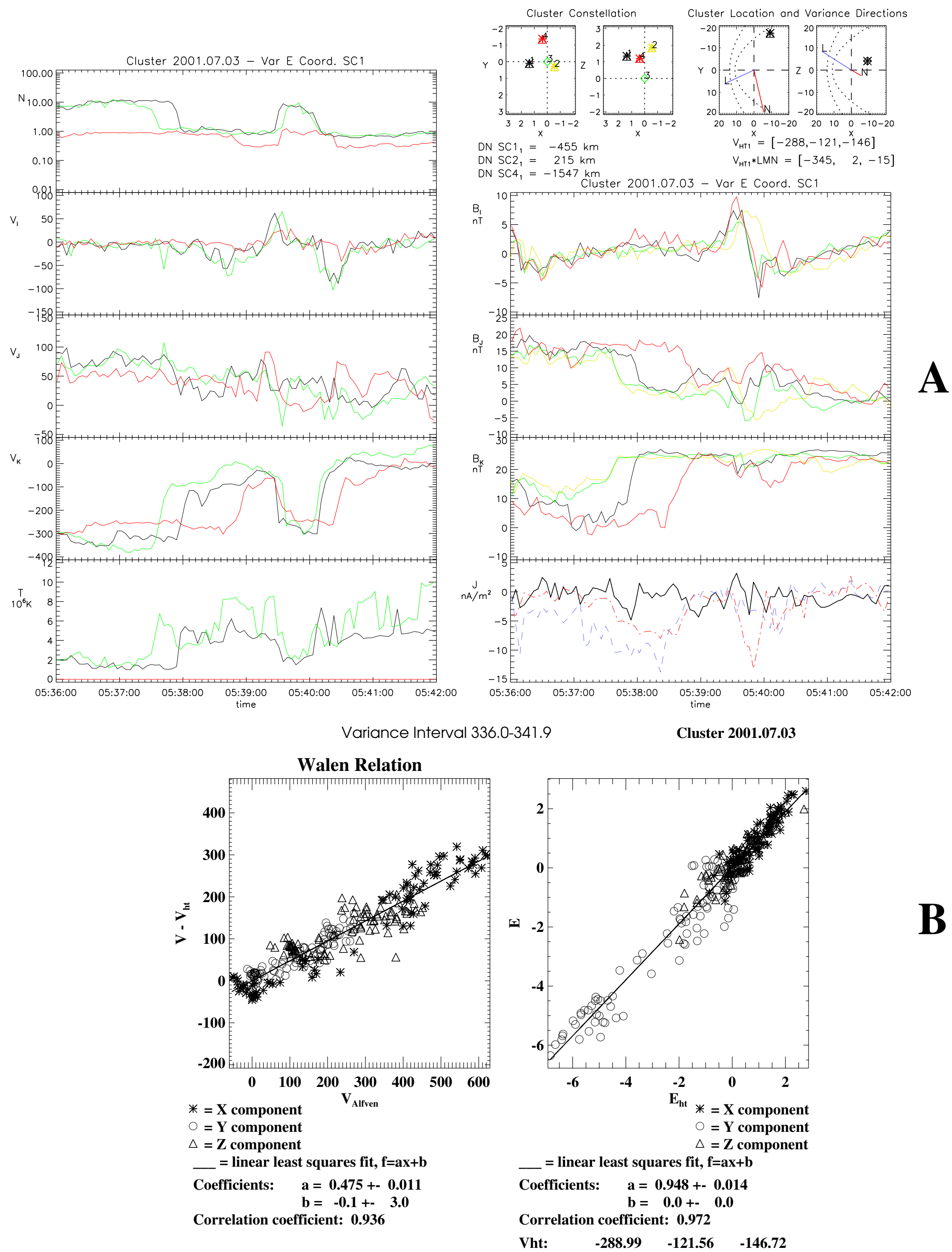

Figure 7.18. A) Represents Cluster plasma (left) and magnetic field (right) observations between 05:36-05:42 UT in variance E coordinates determined by SC1. The top right boxes show the Cluster constellation and de HT frame velocities in GSM and in variance E coordinates. B) represents the Walen relation (left) and de HT frame (right) for this interval.

direction. Again, the tangent is mostly in the x, z -plane with a smaller y-component. The slope for the Walen relation and de HT frame are 0.65 and 0.92, respectively. Figure 7.19b represents Cluster plasma and magnetic field observations between 05:36-05:42 UT in variance E coordinates determined by SC3. Figure 7.19d represents the Walen relation (left) and de HT frame (right) for this interval. The HT velocity, $\mathbf{v_{HT}}$, is [-317, -138, -143] km/s in GSM coordinates, and v_{HT} = [-371, -34, -27] km/s in variance E coordinates. The slopes for the Walen relation and de HT frame are nearly the same as for the brief interval discussed above, but the HT velocity is reduced by about 51 km/s in tangent direction, 71 km/s in intermediate direction and increased 13 km/s in the normal direction. Comparing HT-velocity components in GSM coordinates indicates that the velocity changes mostly in the z-direction. The tangential velocity component of SC3, v_k, shows a large change of 200 km/s. Velocity components measured with SC1 change more in the tangent and normal direction than those of SC3, and thus the HT-velocity measured by SC1 is also $\sim$ 120 km/s larger than that of the SC3. Based on the facts that SC1 and SC3 are located in the tangent direction of each other, SC1 observed a good Walen relation, SC3 observed a reasonable Walen relation, both SC1 and SC3 observed accelerated flow, and flow measured by SC1 is larger than measured by SC3, it is tempting to interpret that reconnection took place upstream in the tangent direction of the SC1.

Figure 7.20a shows Cluster plasma (left) and magnetic field (right) observations between 05:40:06-05:40:27 UT in variance E coordinates determined by SC4 and b shows corresponding observations between 05:36-05:42 UT. The de Hoffmann Teller velocity, $\mathbf{v_{HT}}$, is [-204, -70, -71] km/s in GSM coordinates for the brief interval, and v_{HT} = [-226, -23, 17] km/s in variance E coordinates indicating the maximum transformation velocity along the tangent direction. Again, the tangent is mostly in the x, z -plane with a smaller y-component. For the larger interval between 05:36-05:42 UT, the HT frames are (in GSM and variance E coordinates) v_{HT} = [-233, -91, -112] and [-274, 8, -3] km/s, respectively. The tangential HT velocity has decreased for the brief $\sim$ 20 second interval by 48 km/s compared to the larger interval. While the boundary tangent direction has remained the same during the brief interval, the boundary normal direction has rotated 90 degrees. The normal component of the plasma velocity changes $\sim$ 80 km/s but other velocity components remain quite constant. The slopes for the HT frames for 20 second and 6 minute period are both 0.98.

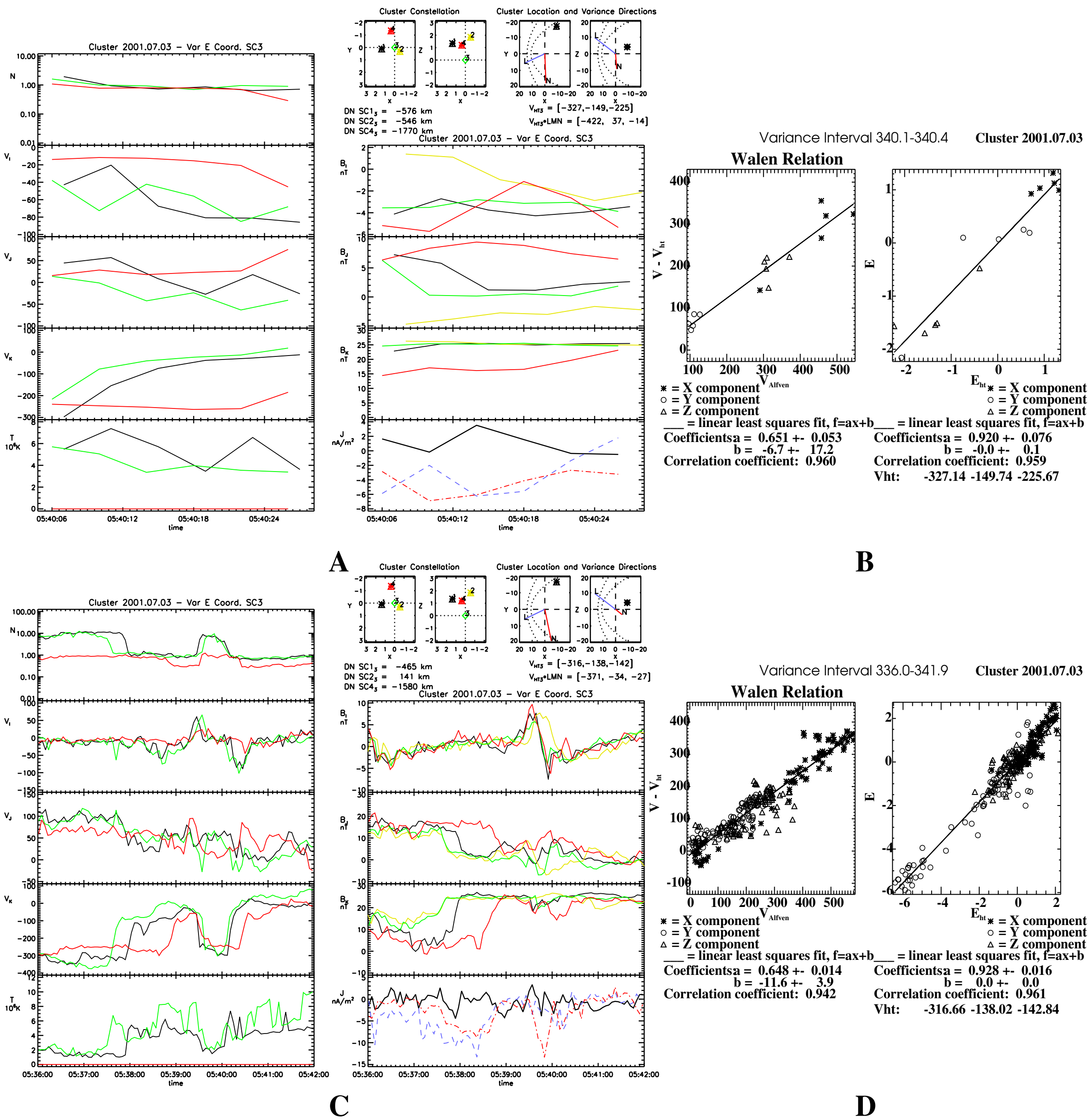

Figure 7.19. A) Represents Cluster plasma (left) and magnetic field (right) observations between 05:40:06-05:40:27 UT in variance E coordinates determined by SC3. The top right boxes show the Cluster constellation and de HT frame velocities in GSM and in variance E coordinates. B) shows the Walen relation (left) and de HT frame (right) for this interval. C) Represents Cluster plasma and magnetic field observations between 05:36-05:42 UT in variance E coordinates determined by SC3. D) represents the Walen relation (left) and de HT frame (right) for this interval.

Like before, the Walen relation cannot be tested for SC4. So it seems that SC4, located furthest in the magnetosheath, didn't observe the same event as SC1 and SC3 during this time interval.

Accelerated flow between 05:48:34-05:48:54 UT

Figure 7.21a shows Cluster plasma (left) and magnetic field (right) observations between 05:48:34-05:48:54 UT in variance E coordinates determined by SC1 and b represents the Walen relation (left) and de HT frame (right) for this interval. The de Hoffmann Teller velocity, $\mathbf{v_{HT}}$, is [-385, -159, -233] km/s in GSM coordinates, and v_{HT} = [-476, -36, 13] km/s in variance E coordinates indicating the maximum transformation velocity along the tangent direction. The tangent is mostly in x, z -plane with a smaller y-component. The boundary normal has a significant z-component. The slope for the Walen relation and de HT frame are 0.79 and 0.93, respectively. During this interval the intermediate component of the velocity rotates from 90 km/s to -40 km/s, and the intermediate component of the magnetic field rotates from +2 nT to -7 nT, which is consistent with the magnetic reconnection. The tangential velocity component changes by $\sim$ 150 km/s, corresponding to a transition to a magnetosheath type plasma region with higher density (top panel of Figure 7.21a, while the tangential magnetic field remains constant. The normal component of the velocity changes by 80 km/s. It is worthwhile to remember here that the normal component is mostly in the z-direction so that this acceleration is in the z-component of the plasma velocity. Figure 7.22a shows Cluster plasma (left) and magnetic field (right) observations between 05:45-05:51 UT in variance E coordinates determined by SC1 and b represents the Walen relation and de HT frame for this 6 minute interval enclosing the brief 20 second interval discussed above. The de Hoffmann Teller velocity, $\mathbf{v_{HT}}$, is [-301, -131, -122] km/s in GSM coordinates, and v_{HT} = [-332, -104, -33] km/s in variance E coordinates indicating the maximum transformation velocity along the tangent direction. Boundary tangents have the same orientation during the brief 20 second interval and during the longer 6 minute interval, but the boundary normal has changed almost 90 degrees. The slope for the Walen relation and de HT frame during the longer interval are 0.54 and 0.91 respectively. The de HT frame velocity during 05:48:34-05:48:54 UT has increased by $\sim$ 150 km/s in the tangent direction compared to the average HT frame velocity. Plasma

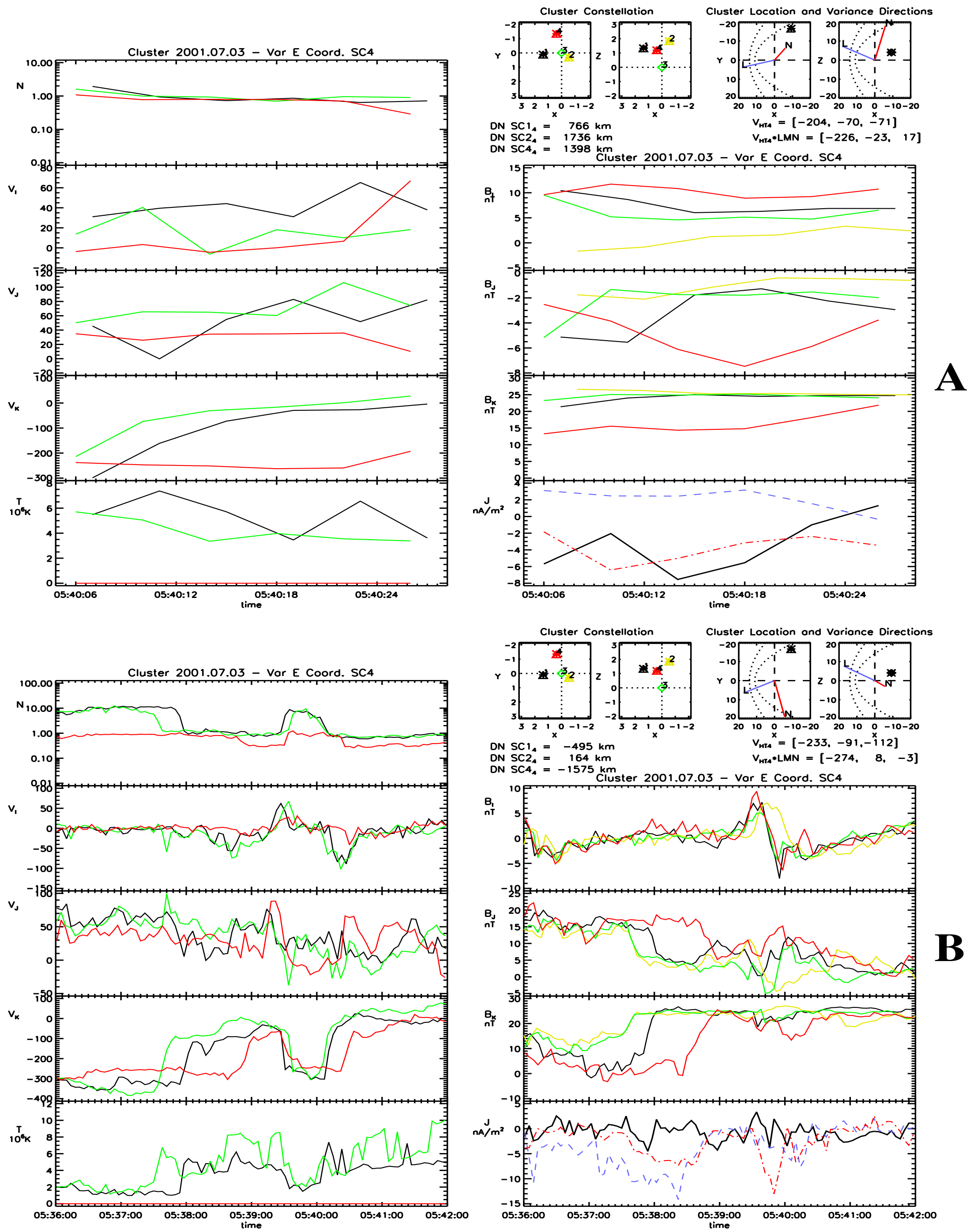

Figure 7.20. A) Represents Cluster plasma (left) and magnetic field (right) observations between 05:40:06-05:40:27 UT in variance E coordinates determined by SC4. The top right boxes show the Cluster constellation and de HT frame velocities in GSM and in variance E coordinates. B) Represents Cluster plasma and magnetic field observations between 05:36-05:42 UT in variance E coordinates determined by SC4.

acceleration is observable in all velocity components. Since the Walen relation was also satisfied during 05:48:34-05:48:54 UT, this could indicate that also during this interval SC1 traveled through the reconnection region observing fast outflow into the same direction where the overall boundary wave was moving. Let us examine next what SC3 and SC4 observed during this interval.

Figure 7.23a shows Cluster plasma (left) and magnetic field (right) observations between 05:48:34-05:48:54 UT in variance E coordinates determined by SC3 and b represents the Walen relation (left) and de HT frame (right) for this interval. The de Hoffmann Teller velocity, $\mathbf{v_{HT}}$, is [-362, -144, -205] km/s in GSM coordinates, and v_{HT} = [-438, -46, 5] km/s in variance E coordinates indicating the maximum transformation velocity along the tangent direction. The tangent is again mostly in the x, z -plane with a smaller y-component. SC3 measured a boundary normal with a significant z-component. The slope for the Walen relation and de HT frame are 0.78 and 0.89, respectively. During this interval the normal component of the plasma velocity (green trace) changes from positive 60 km/s to negative -10 km/s simultaneously as the normal magnetic field component changes from +2 nT to negative -2 nT. The intermediate component of the velocity rotates from +70 km/s to -20 km/s, and the intermediate component of the magnetic field rotates from +2 nT to -8 nT. The tangential velocity component changes by $\sim$ 150 km/s corresponding to a transition to a magnetosheath type plasma region with higher density (top panel of Figure 7.23a). Figure 7.24a shows Cluster plasma (left) and magnetic field (right) observations between 05:45-05:51 UT in variance E coordinates determined by SC3 and b represents the Walen relation and de HT frame for this 6 minute interval enclosing the brief 20 second interval discussed above. The de Hoffmann Teller velocity, $\mathbf{v_{HT}}$, is [-300, -134, -122] km/s in GSM coordinates, and v_{HT} = [-332, -103, -37] km/s in variance E coordinates indicating the maximum transformation velocity along the tangent direction. Boundary tangents have the same orientation during the brief 20 second interval as during the longer 6 minute interval, but, like observed by SC1, the normal direction has changed almost 90 degrees during this smaller interval. Based on the similar behavior of boundary tangents and normals during this plasma acceleration event embedded in the large scale motion, one can collude that SC1 and SC3 both observe a similar deformation of the boundary. The slope for the Walen relation and de HT frame during the longer interval are 0.59 and 0.90 respectively. The de

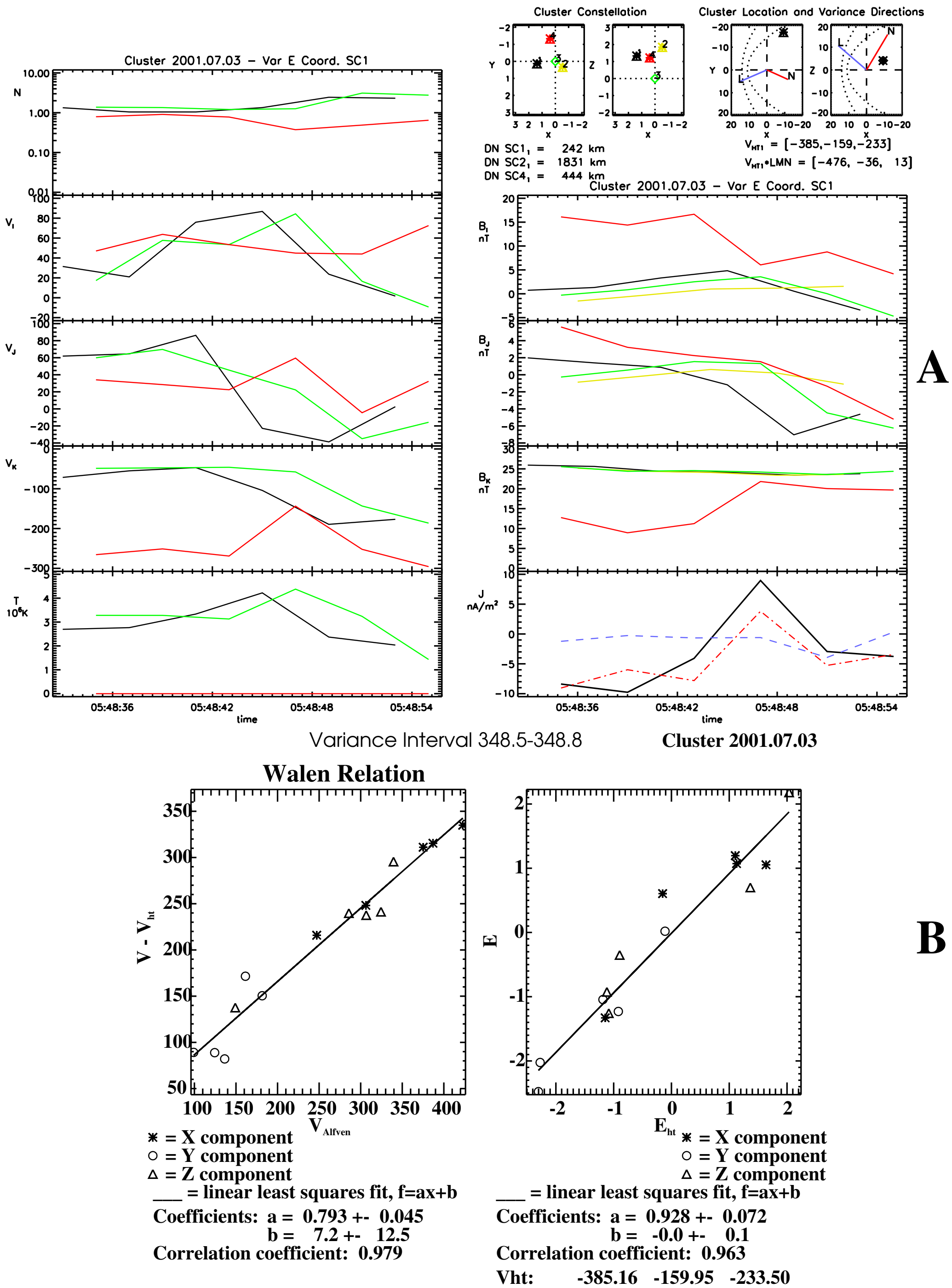

Figure 7.21. A) Represents Cluster plasma (left) and magnetic field (right) observations between 05:48:34-05:48:54 UT in variance E coordinates determined by SC1. The top right boxes show the Cluster constellation and de HT frame velocities in GSM and in variance E coordinates. B) represents the Walen relation (left) and de HT frame (right) for this interval.

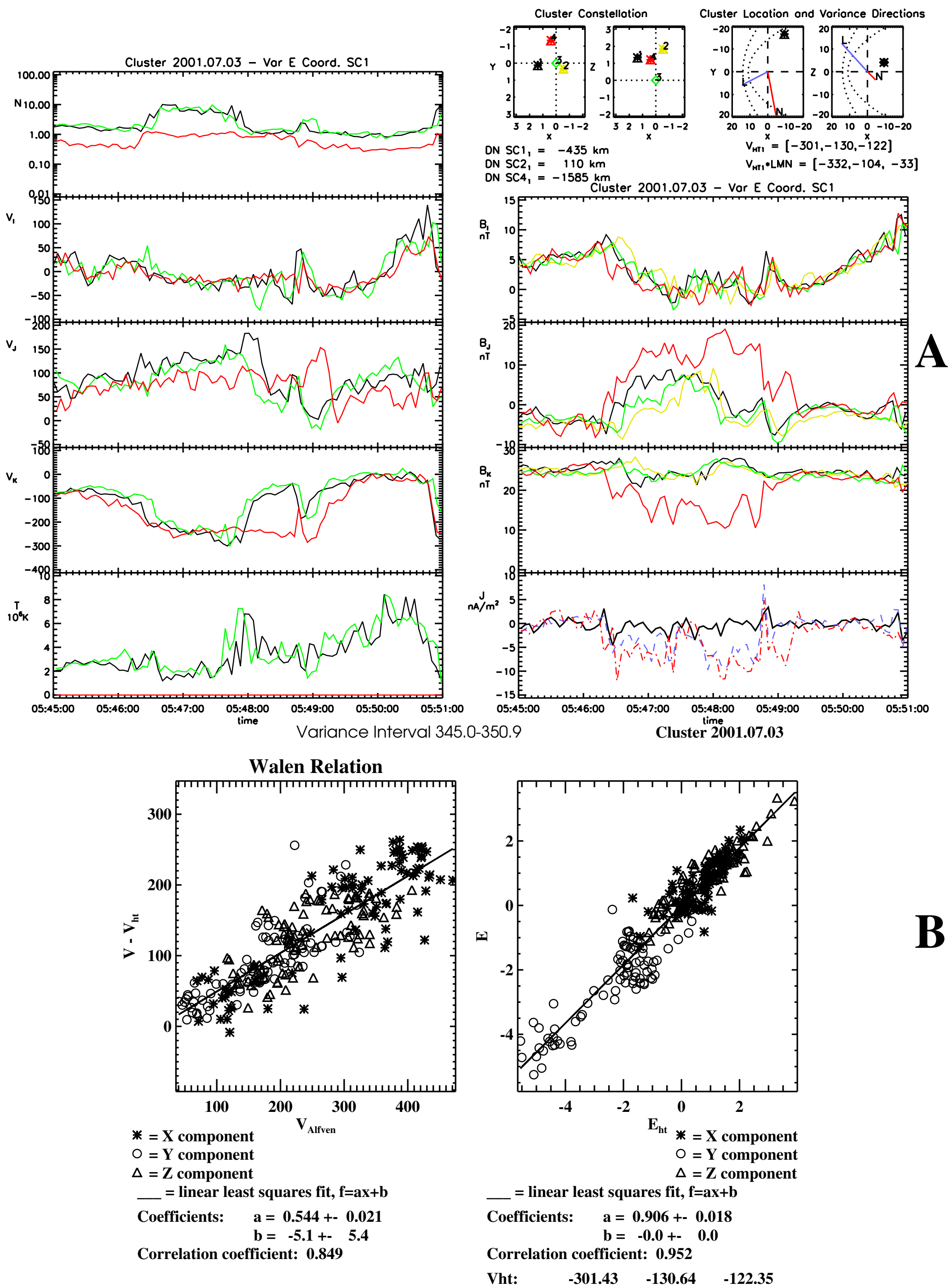

Figure 7.22. A) Represents Cluster plasma (left) and magnetic field (right) observations between 05:45-05:51 UT in variance E coordinates determined by SC1. The top right boxes show the Cluster constellation and de HT frame velocities in GSM and in variance E coordinates. B) represents the Walen relation (left) and de HT frame (right) for this interval.

HT frame velocity during 05:48:34-05:48:54 UT has increased $\sim$ 106 km/s in the tangent direction compared to the average HT frame velocity. Since the Walen relation was satisfied during 05:48:34-05:48:54 UT, plasma acceleration was observed, and SC3 was located in the tangent direction downstream from SC1, this could indicate that SC3 also observed outflow from the reconnection region into the same direction where the overall boundary wave was moving.

Figure 7.25a shows Cluster plasma (left) and magnetic field (right) observations between 05:48:34-05:48:54 UT in variance E coordinates determined by SC4 and b shows corresponding observations between 05:45-05:51 UT. The de Hoffmann Teller velocity, $\mathbf{v_{HT}}$, is [-241, -97, -143] km/s in GSM coordinates for the brief interval, and v_{HT} = [-293, -48, -11] km/s in variance E coordinates indicating the maximum transformation velocity along the tangent direction. Again, the tangent is mostly in the x, z -plane with a smaller y-component and the normal is mostly in y-direction, both for brief 20 s interval and the longer 6 minute interval. For the larger interval between 05:45-05:51 UT, the HT frames are (in GSM and variance E coordinates) v_{HT} = [-227, -99, -97] and [-254, -75, -24] km/s, and the slopes for the HT frames for 20 second and 6 minute period are 0.97 and 0.95, respectively. SC4 observes neither accelerated HT velocity nor accelerated flow. Also the structure of the boundary remains the same during the brief interval. This analysis indicates that SC4 doesn't see the same structure and accelerated flow as SC1 and SC3.

Accelerated flow between 05:50:38-05:51:02 UT

Previous examples of the large de HT frame velocities illustrate plasma acceleration into the same direction where the overall boundary wave is moving. If this data set includes signatures of reconnection inside Kelvin-Helmholtz vortices (and if the satellites happen to travel through such a region), acceleration into the opposite direction should also be observed. This means that there should exist frames in this data set where the electric field is minimized with the de HT velocity smaller than the average velocity of the Kelvin-Helmholtz vortex. In the following I will show an example of such a case.

Figure 7.26a shows Cluster plasma (left) and magnetic field (right) observations between 05:50:38-05:51:02 UT in variance E coordinates determined by SC1 and b represents the Walen relation (left) and de HT frame (right) for this interval. The de Hoffmann Teller

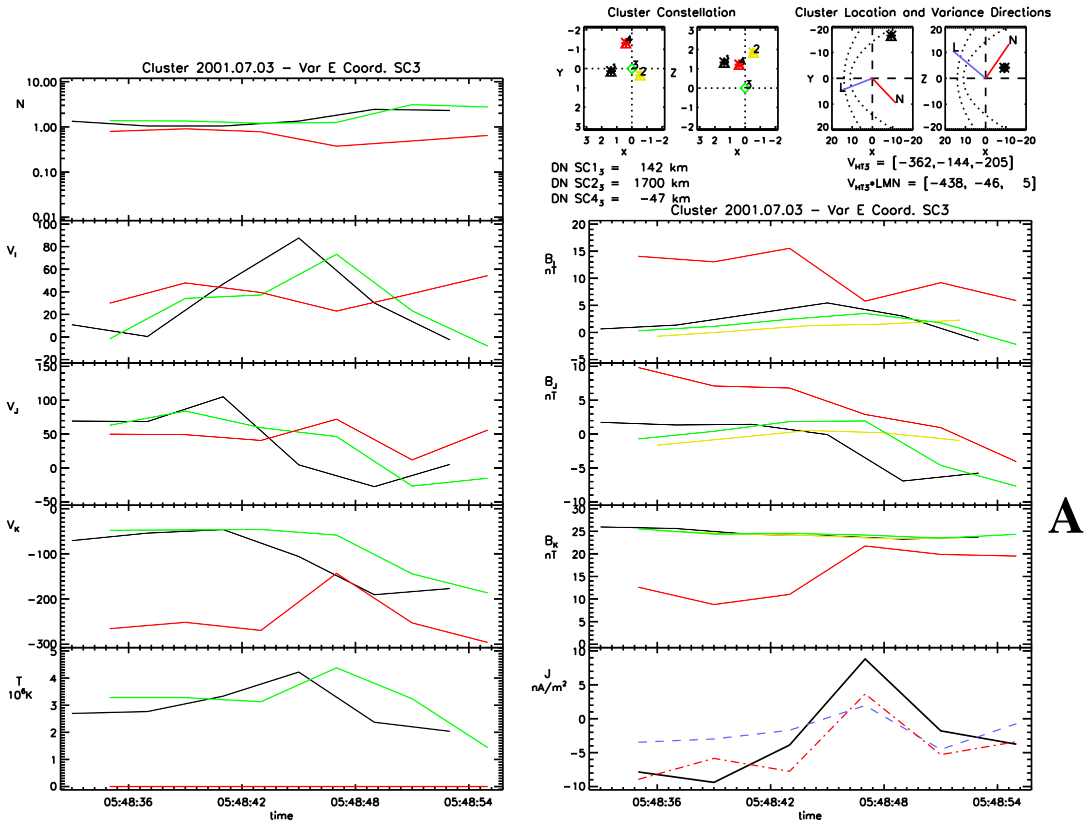

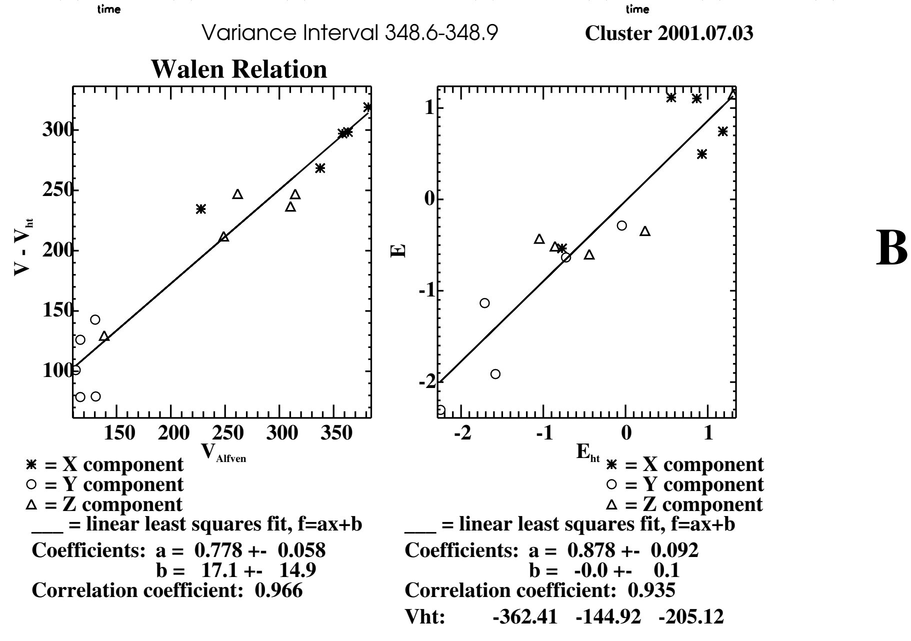

Figure 7.23. A) Represents Cluster plasma (left) and magnetic field (right) observations between 05:48:34-05:48:54 UT in variance E coordinates determined by SC3. The top right boxes show the Cluster constellation and de HT frame velocities in GSM and in variance E coordinates. B) represents the Walen relation (left) and de HT frame (right) for this interval.

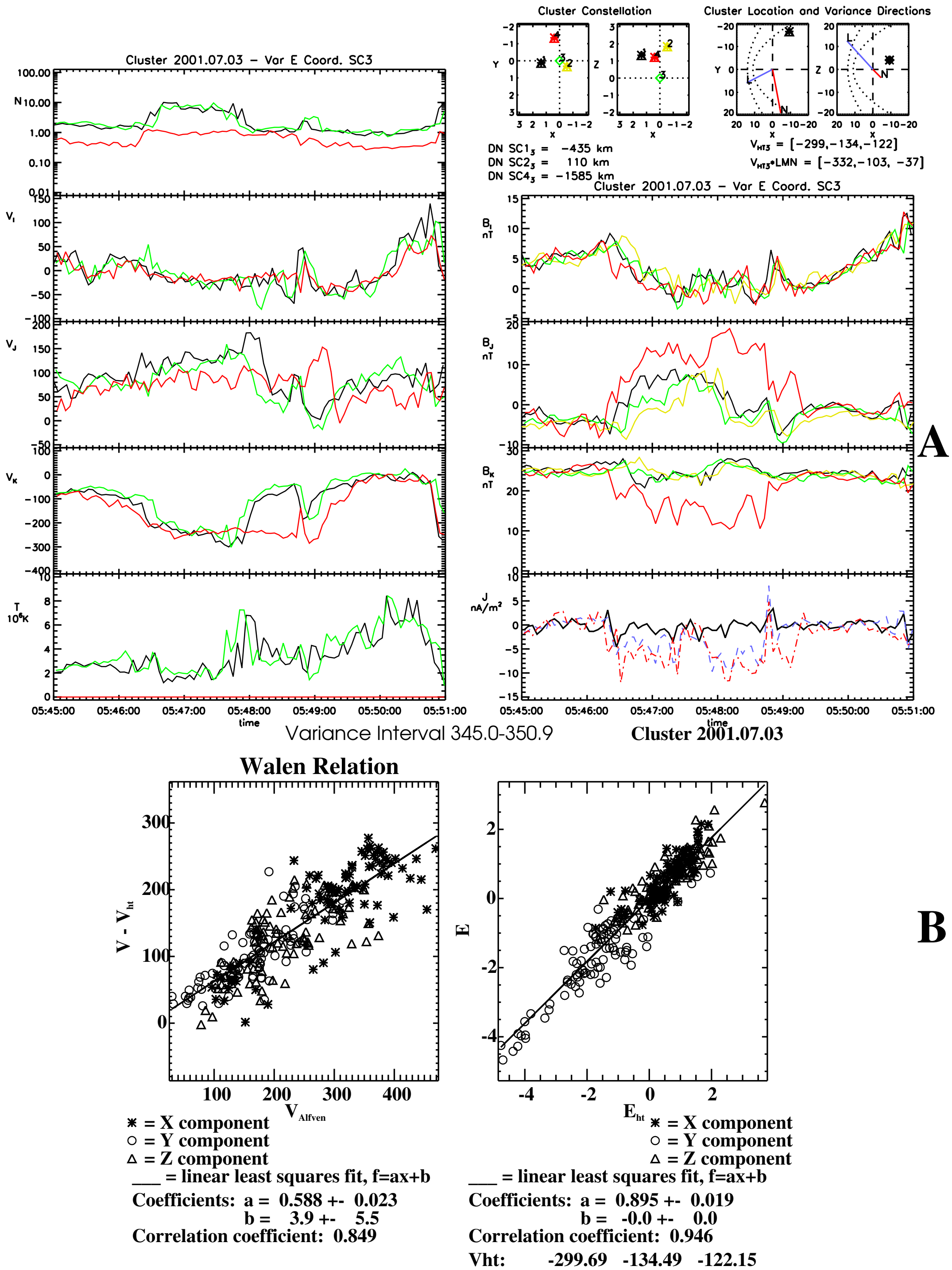

Figure 7.24. A) Represents Cluster plasma (left) and magnetic field (right) observations between 05:45-05:51 UT in variance E coordinates determined by SC3. The top right boxes show the Cluster constellation and de HT frame velocities in GSM and in variance E coordinates. B) represents the Walen relation (left) and de HT frame (right) for this interval.

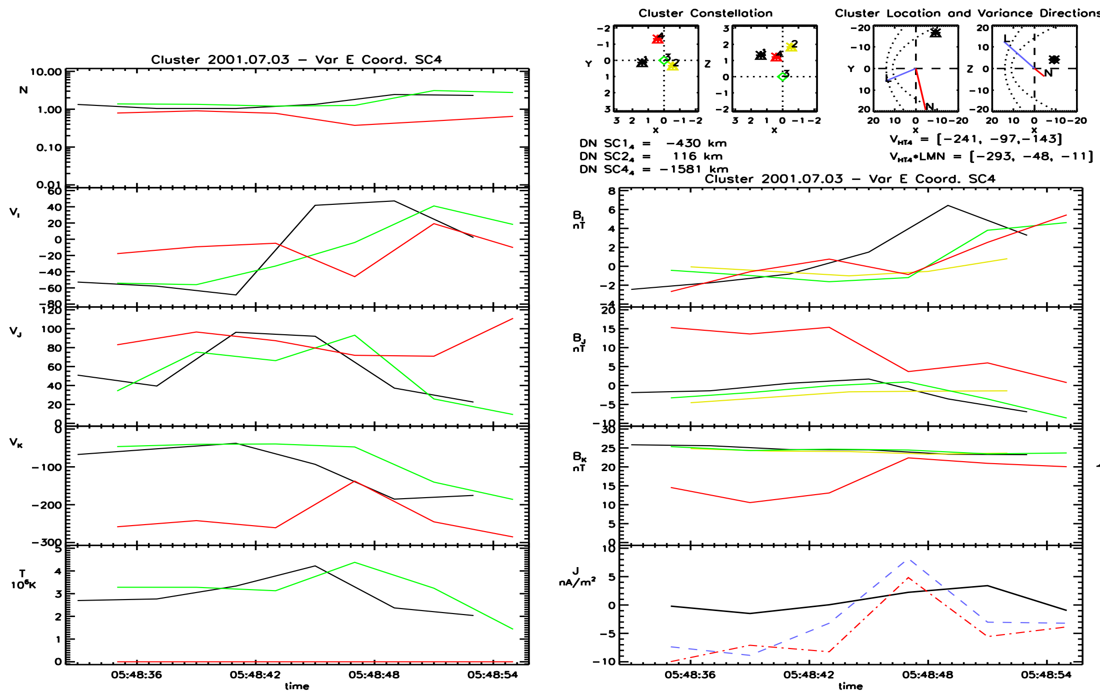

A

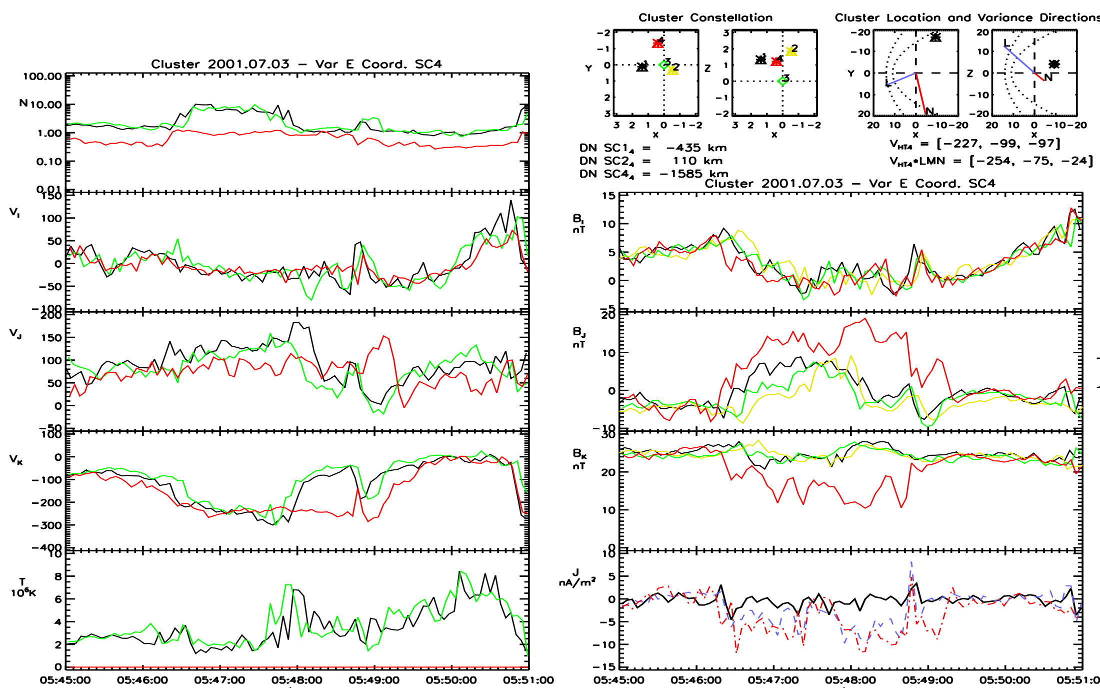

B

Figure 7.25. A) Represents Cluster plasma (left) and magnetic field (right) observations between 05:48:34-05:48:54 UT in variance E coordinates determined by SC4. The top right boxes show the Cluster constellation and de HT frame velocities in GSM and in variance E coordinates. B) Represents Cluster plasma and magnetic field observations between 05:45-05:51 UT in variance E coordinates determined by SC4.

velocity, $\mathbf{v_{HT}}$, is [-236, -42, -85] km/s in GSM coordinates, and v_{HT} = [-50, -242, 5] km/s in variance E coordinates indicating the maximum transformation velocity along the intermediate direction. The tangent is mostly in the y, z -plane with a large z-component. During this interval the normal component of the plasma velocity (black line for SC1) changes from 140 km/s to 40 km/s whereas the normal magnetic field decreases by 4 nT. The intermediate component of the velocity rotates from + 30 km/s to 300 km/s, and the intermediate component of the magnetic field doesn't vary much. The tangential velocity component rotates from $\sim$ 30 km/s to -50 km/s, simultaneously as the tangential magnetic field component rotates from +6 nT to -2 nT. Figure 7.26b shows the Walen relation (slope is 0.72) and de HT frame (slope is 0.95) for this interval. This interval is within the larger 6 minute interval (discussed above), but since the boundary structure is different during this brief interval, instead of comparing the HT velocities in boundary normal coordinates, I will compare those in GSM coordinates. During the larger interval the HT velocity had a maximum component along the negative x-direction (tailward), but also significant y and z components. During this brief interval, the tailward component of the HT velocity was reduced by 65 km/s, the y -component by 90 km/s and the z-component by 40 km/s. The boundary structure shows that the intermediate direction is mostly aligned with the tailward direction, and that the change in the intermediate velocity component corresponds to SC1 moving into the magnetosheath plasma. The reconnection-like acceleration is clearly observable in tangential velocity component: the velocity changes sign simultaneously with the corresponding magnetic field component. Figure 7.27a shows Cluster plasma and magnetic field observations between 05:50:38-05:51:02 UT in variance E coordinates determined by SC3 and b represents the Walen relation (slope is 0.26) and de HT frame (slope is 0.85) for this interval. The de Hoffmann Teller velocity, $\mathbf{v_{HT}}$, is [-174, -25, -60] km/s in GSM coordinates, and v_{HT} = [-170, -36, -65] km/s in variance E coordinates indicating the maximum transformation velocity along the tangent direction. The HT velocity is further reduced from the measurements of SC1 in the tailward (tangent direction in the boundary coordinates of SC3) direction. The boundary structure measured by SC3 differs from that measured by SC1, ie. the intermediate direction for SC3 corresponds to tangent direction measured by SC1. The Walen relation is not satisfied and the HT frame is reasonably good (slope is 0.85). The de HT frame velocity measured by SC4 during this interval is $\mathbf{v_{HT}}$ =

[-272, -142, -152] km/s in GSM coordinates, and v_{HT} = [-329, 91, -31] km/s in variance E coordinates indicating increase of 75 km/s in velocity in the tangential direction from the surrounding 6 minute interval (Figure 7.25b). Also the intermediate component of the HT velocity changes from 91 km/s (of the longer interval) to -75 km/s. Some of this change is also observable in the intermediate component of the plasma velocity in Figure 7.27a (red trace in v_j for SC4). SC3 and SC4 measured the same boundary tangent and normal directions for this interval, so it is justified to compare here a plot of SC4 observations in boundary coordinates of SC3 with HT velocities measured by SC4. Unfortunately, the Walen relation cannot be tested for SC4, and thus it cannot be verified whether SC4, located, in the tangent direction of SC1, would see the outflow from the reconnection region tailward, to the opposite direction with respect to SC1.

7.2.4 Flux Transfer Events or Reconnection inside the KH Vortices?

Figure 7.28 represents an interval between 5:00-6.00 UT in boundary normal coordinates and reveals distinctive bipolar variations in normal component of the magnetic field (b_i), which is typical for flux transfer events and the Kelvin-Helmholtz instability. In Chapter 6 we concluded that the Walen relation and HT frames should be satisfied for 1-3 minute periods during FTE's. When keeping the reconnection requirements the same as before but with the additional constraint that these conditions must be satisfied for at least 80 seconds, no intervals were picked between 5:00-6.00 UT. In addition, the flux transfer events are isolated events with the same polarity in the same hemisphere. But here the bipolar variation was very rapid with about two minute period with a very sharp $+/-$ signature when moving from magnetospheric region into the magnetosheath type of region which is consistent with observations by *Fairfield et al.* [2000] of the Kelvin-Helmholtz instability.

7.3 Simulations

Since two of the Cluster satellites, SC1 and SC4 were located in the same plane (same z-coordinate) and SC4 was located in the tangent direction of the SC1 in the x, y-plane, it is justified to use two-dimensional simulations in order to interpret their data.

The simulation results of this study are obtained by solving the full set of resistive

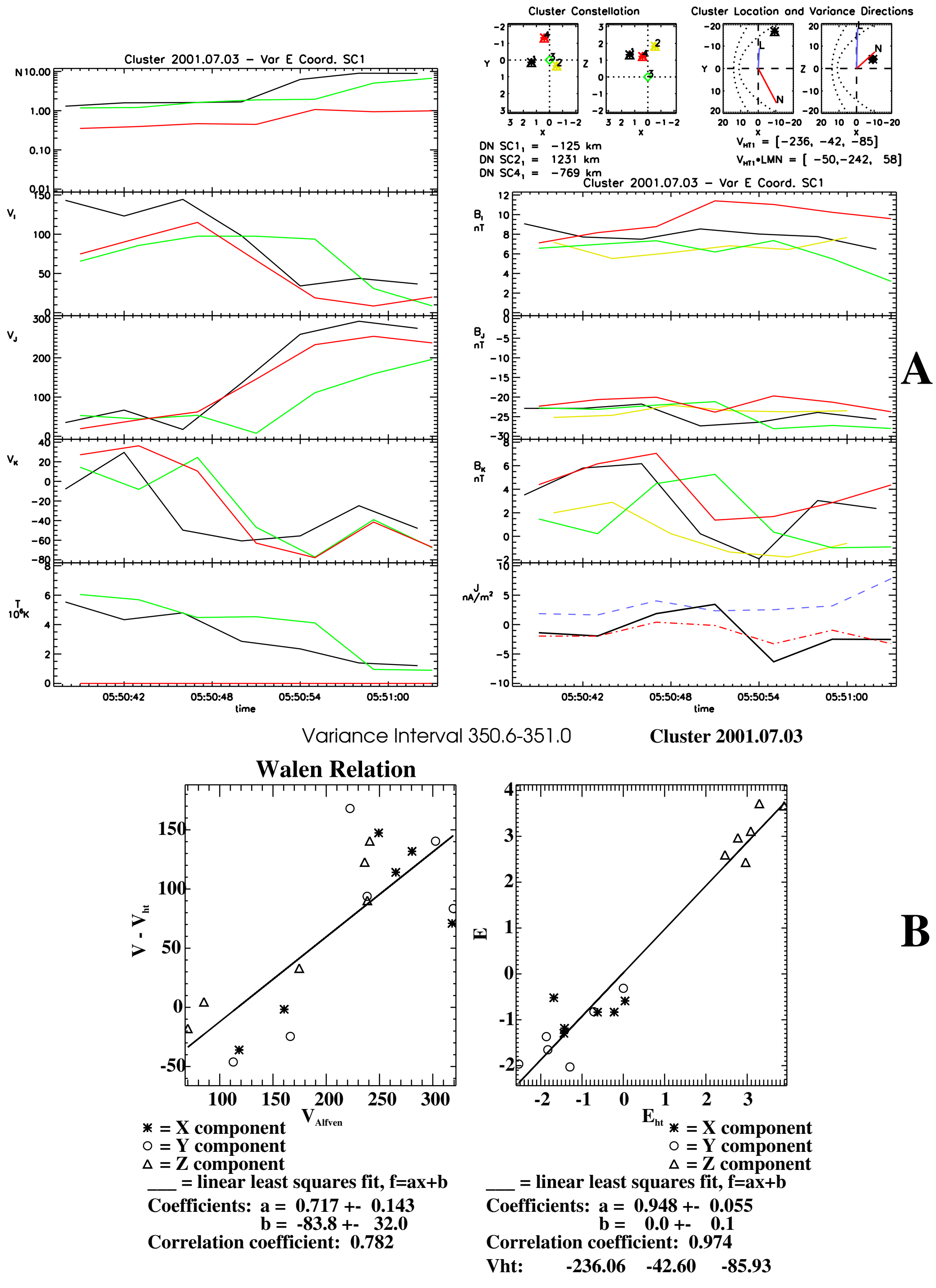

Figure 7.26. A) Represents Cluster plasma (left) and magnetic field (right) observations between 05:50:38-05:51:02 UT in variance E coordinates determined by SC1. The top right boxes show the Cluster constellation and de HT frame velocities in GSM and in variance E coordinates. B) represents the Walen relation (left) and de HT frame (right) for this interval.

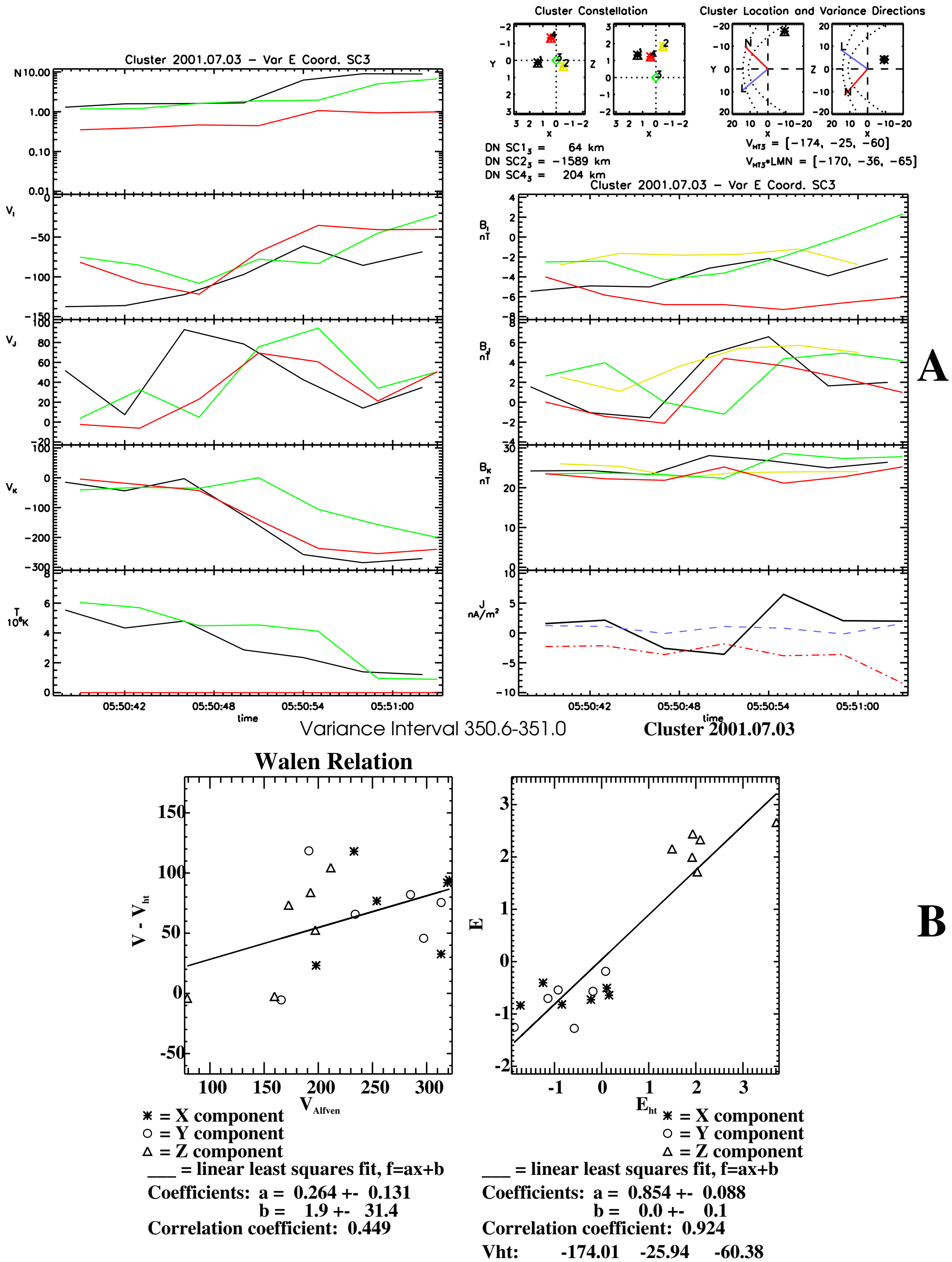

Figure 7.27. A) Represents Cluster plasma (left) and magnetic field (right) observations between 05:50:38-05:51:02 UT in variance E coordinates determined by SC3. The top right boxes show the Cluster constellation and de HT frame velocities in GSM and in variance E coordinates. B) represents the Walen relation (left) and de HT frame (right) for this interval.

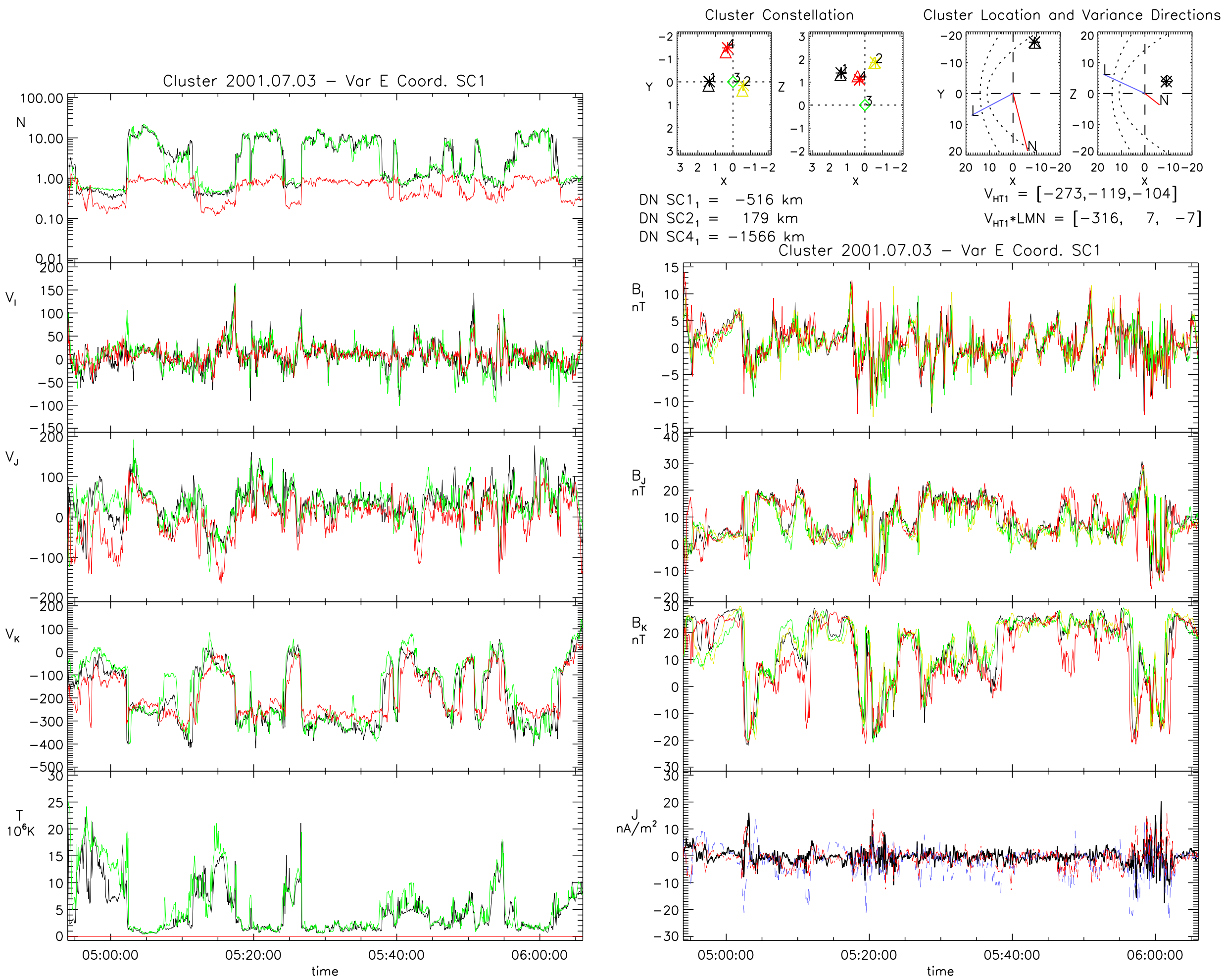

Figure 7.28. Represents Cluster plasma (left) and magnetic field (right) observations between 04:54-06:06 UT in variance E coordinates determined by SC1. Note the bipolar signatures in normal components of the magnetic field, b_i.

MHD equations [*Otto*, 1990a]. Plasma density ρ, velocity $\mathbf{v}$, pressure, and magnetic field are integrated with a finite differences leapfrog scheme which is of second order accuracy in space and time [*Birn*, 1980]. All quantities are normalized to characteristic values of the system, i.e., length scales l to a typical length l_0, density ρ to $\rho_0 = n_0 m_0$ with the number density n_0 and the proton mass m_0, magnetic field $\mathbf{b}$ to B_0, velocity $\mathbf{v}$ to the typical Alfvén velocity $v_A = B_0/\sqrt{(\mu_0 \rho_0)}$, pressure to $P_0 = {B_0}^2/(2\mu_0)$, and time t to a characteristic Alfvén transit time $\tau_A = l_0/v_A$.

Figure 7.29 illustrates the geometry in boundary normal coordinates used in Kelvin-Helmholtz simulations, such that negative y is normal to the boundary, positive x is sunward, and z completes the coordinate system.

The initial configuration for the KH simulation in the boundary coordinates uses a magnetic field of $b_{x0}(x) = b_0(x)\sin\varphi$, $b_{y0}(x) = 0.02$, and $b_{z0}(x) = b_0(x)\cos\varphi$ such that $90^\circ - \varphi$ is the angle between the unperturbed magnetic field direction and the $\mathbf{k}$ vector of the KH mode. The velocity is given by $v_{x0}(x) = v_0(x)$, $v_{y0}(x) = 0$, and $v_{z0}(x) = 0$. Initial density, pressure, velocity, and magnetic field magnitudes are

$$
\begin{aligned}
\rho_0(x) &= \frac{1}{2}(\rho_{sh} + \rho_{sp}) + \frac{1}{2}(\rho_{sh} - \rho_{sp})\tanh(\frac{y}{L_0}) \\
p_0(x) &= \frac{1}{2}(p_{sh} + p_{sp}) + \frac{1}{2}(p_{sh} - p_{sp})\tanh(\frac{y}{L_0}) \\
v_0(x) &= -\frac{1}{2}v_{sh}(\tanh(\frac{y}{L_0}) + 1) \\
b_0(x) &= \frac{1}{2}(b_{sh} + b_{sp}) + \frac{1}{2}(b_{sh} - b_{sp})\tanh(\frac{y}{L_0}),
\end{aligned}
$$

where the indices sp and sh correspond to the average values on the magnetospheric and magnetosheath sides of the magnetopause boundary. $v_{sh} = 432$ km/s; $v_{msp} = 0$ km/s; $b_{sh} = 10$ nT; $b_{sp} = 50$ nT; $\rho_{sh} = 11/\text{cm}^3$; $\rho_{msp} = 1/\text{cm}^3$;$\beta_{sh} = 15$; $\beta_{msp} = 0.5$; $\varphi = 15^\circ$. The initial density, pressure,velocity, and magnetic field on the magnetospheric and magnetosheath sides are chosen according to ACE and Cluster data and are normalized using $B_0 = 30$ nT, $n_0 = 6.0$ cm^{-3}, $L_0 = 1000$ km which yields $v_A = 270$ km/s and $\tau_A = 3.7$ s.

Figure 7.30 represents the Kelvin-Helmholtz vortex at $t = 110\ \tau_A$. The magnetic field (arrows) and the z-component of the current density (color code) are plotted on left and plasma velocity (arrows) and density (color code) are represented on the right. The magnetic field has been twisted by the velocity shear resulting in anti-parallel magnetic field

Kelvin-Helmholtz Simulations

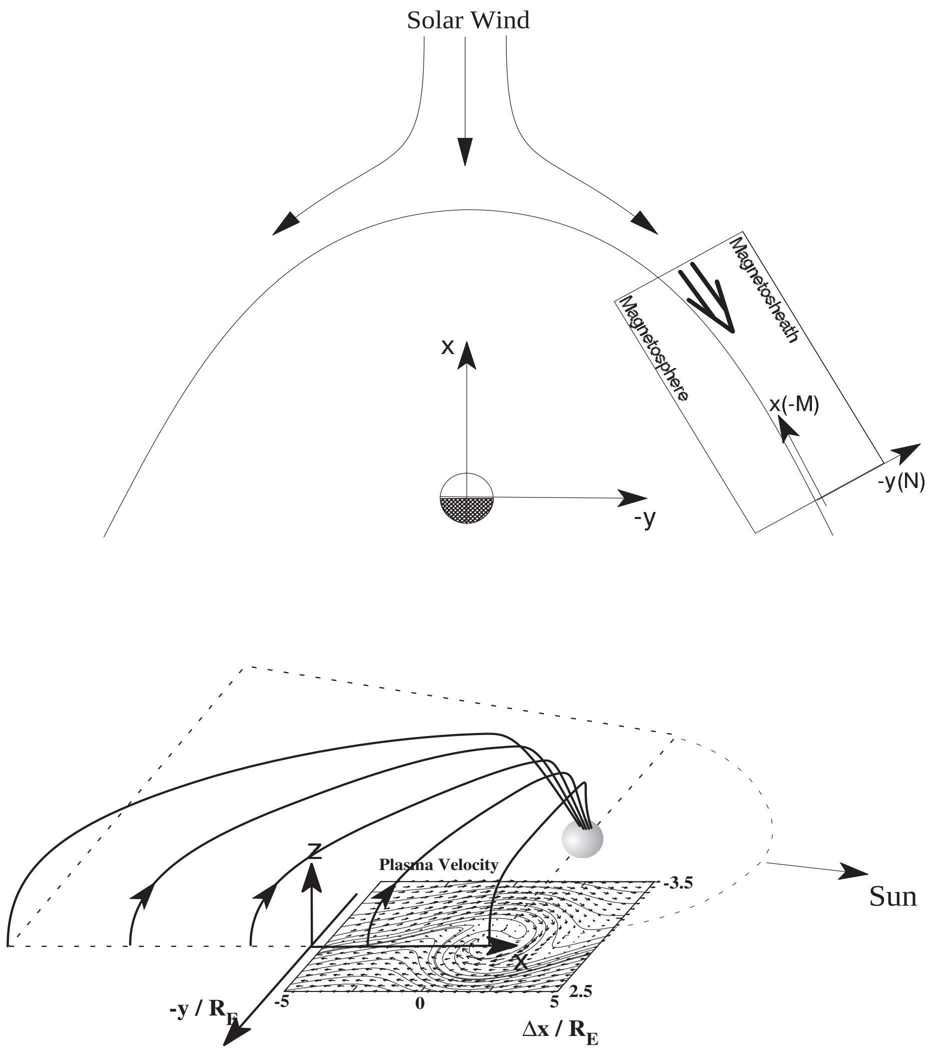

Figure 7.29. Simulation geometry.

components and strong current layers in the simulation plane. Reconnection occurs in the positive current region at x, y= [-17,-2.8] and fast plasma outflow is observable out from the reconnection region to the same direction as the KH-wave is moving. In the following I will simulate SC1 and SC4 trajectories in Cluster observations with cuts through the simulation box at y=1.2 corresponding to the path of SC1 and at y=3.2 corresponding to the path of SC4.

Figure 7.31a represents plasma and magnetic field measurements observed by virtual spacecraft (imitating SC1 in the Cluster constellation) traveling through the simulation box at constant $y = 1.2$. Note that the coordinates are rotated here with respect to the coordinates in Figure 7.30 so that the z component corresponds to -y, and x corresponds to -x. Figure 7.31b shows the Walen relation and de HT for this whole wave length period. Walen relation is not satisfied but de HT frame velocity is obtained approximately with the magnetosheath velocity with the slope of 0.922. Comparison to Cluster observations in Figures 7.18 and 7.22 shows many similarities: Good HT frames are obtained approximately with the magnetosheath velocity, magnetic field and velocity components rotate in intermediate or tangent directions, and magnetosheath type of plasma changes into the magnetospheric type plasma. In the observation there is, however, a significant HT velocity component in the z direction which is not present in our 2-D simulation.

Figure 7.32a represents plasma and magnetic field measurements observed by a virtual spacecraft imitating SC4 in Cluster constellation in Figures 7.20b and 7.25b traveling through the simulation box at constant $y = 3.2$. Figure 7.32b shows the Walen relation and de HT for this whole wave length period. The Walen relation is not satisfied and the de HT frame velocity is obtained approximately with the magnetosheath velocity with an excellent slope of 0.98.

Figure 7.33a represents the Walen relation (left) and de HT frame (right) at $y = 1.2$, $x =$ [14.2, 15.8], which is the flight through the reconnection outflow region for SC1. Both the Walen relation and de HT frame are satisfied. The de HT frame is obtained with a velocity about twice the magnetosheath velocity. This is in agreement with the Cluster observations of SC1 of the accelerated flow with enhanced HT frame velocities in Figure 7.17 and 7.21. Figure 7.33b shows the virtual spacecraft measurements of the Walen relation and de HT frame through $y = 3.2$, $x =$ [11.2, 12.8], which is approximately in the tangent direction

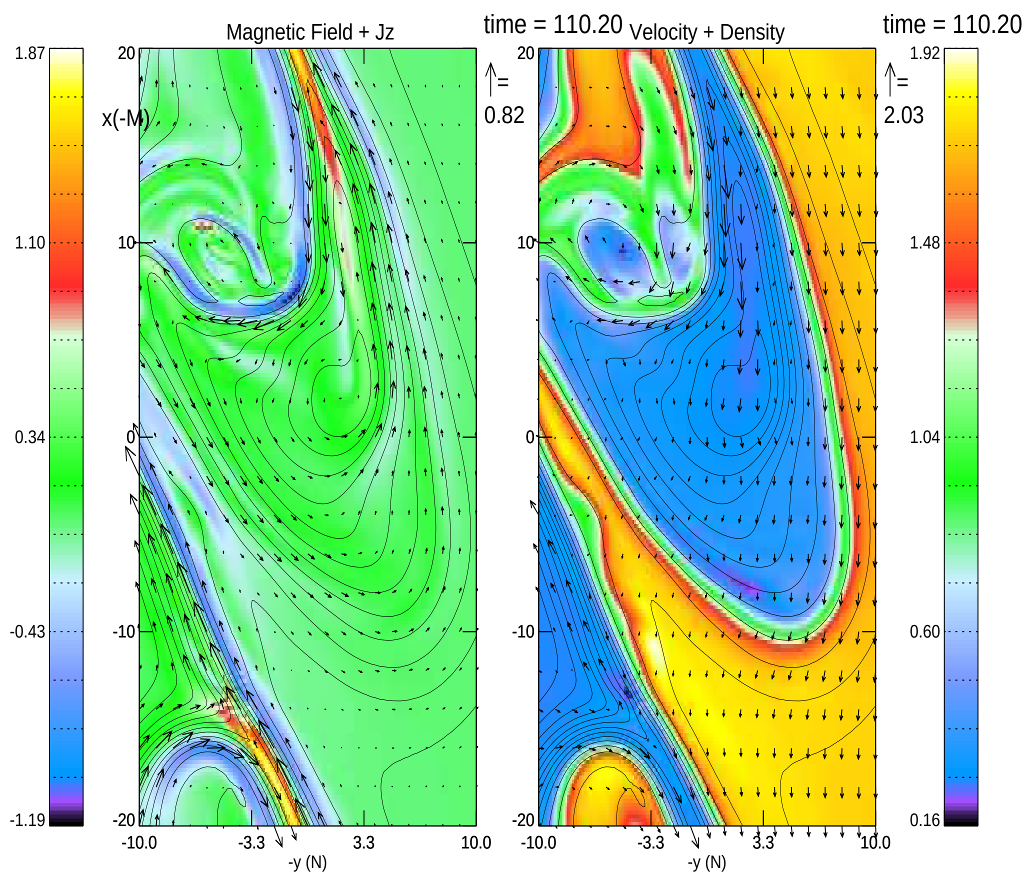

Figure 7.30. Kelvin-Helmholtz vortex at $t \sim 110$. Magnetic field (arrows) and z-component of the current density (color code) are plotted on left and plasma velocity (arrows) and density (color code) are represented on the right.

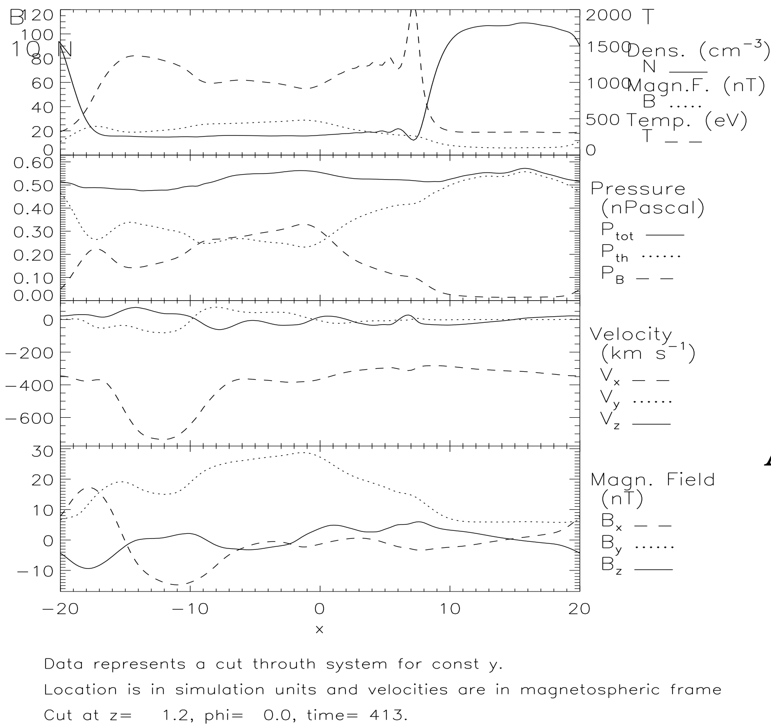

A

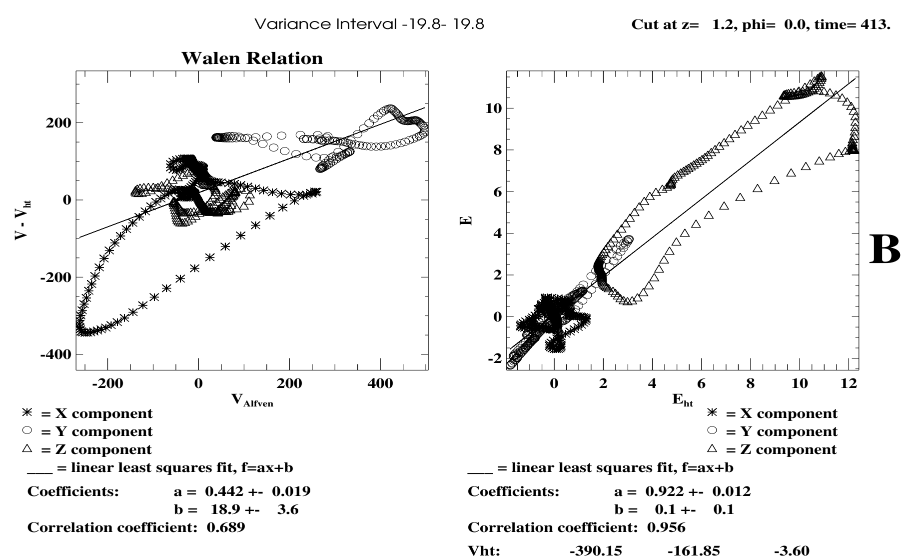

B

Figure 7.31. A) represents plasma and magnetic field measurements observed by virtual spacecraft traveling through the simulation box (Figure 7.22) from x = -20 to x = 20 at y = 1.2. Walen relation and de Hoffman teller frame for this interval are plotted in B).

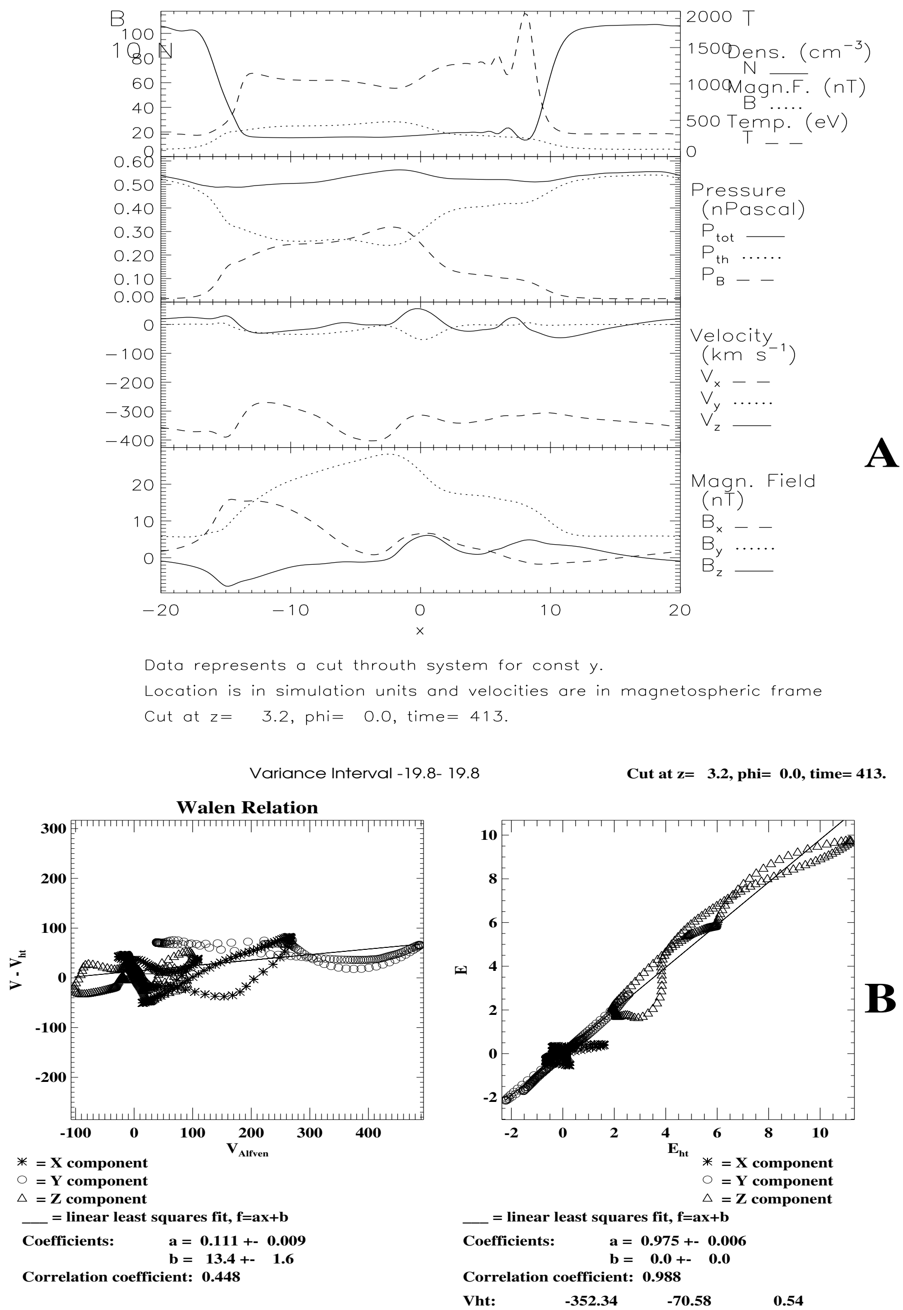

Figure 7.32. A) represents plasma and magnetic field measurements observed by virtual spacecraft traveling through the simulation box (Figure 7.30) from x = -20 to x = 20 at y = 3.2. The Walen relation (left) and de HT frame (right) for this interval are plotted in B).

from the location of SC1. The Walen relation is not satisfied since virtual SC4 doesn't see the rapid outflow from the reconnection region. The de HT frame velocity is about half of the magnetosheath velocity. We cannot compare the Walen relation of the Cluster SC4, but the de Hoffman teller frame velocities measured by SC4 in Figures 7.20a and 7.25a agree with the measurements of virtual SC4, which is further away from the reconnection region and thus doesn't see the accelerated flow nor measures accelerated HT frame.

If we would take a cut through the simulation box (Figure 7.30) at the opposite side of the reconnection region from x, y = [-12.0, -7.0] to x, y = [-5.0, -7.0], the flow from the reconnection region would be to the opposite direction than the overall motion of the Kelvin-Helmholtz vortex and the measured HT frame would be lower than the HT frame of the whole wavelength. This corresponds to the situation in Cluster observations of SC1 in Figure 7.26.

7.4 Discussion and Conclusions

Results in this Chapter indicate that on the 3rd of July, 2001 four Cluster satellites had several quasi-periodic encounters of low density, high temperature magnetospheric -like plasma and high density, low temperature magnetosheath-like plasma with a period ≈ 5 minutes. The velocity and magnetic field components show more rapid oscillations with period ≈ 2 minutes, which indicates sub-structure embedded in the large scale motion. The boundary normals didn't change much in the x, y -plane but showed significant fluctuations in the z-direction. In addition, the satellites observed several brief intervals satisfying the Walen relation and de HT frame, often with much higher or lower transformation velocity than that of the overall boundary wave. While several of these reconnection signatures can be caused just by Alfvén waves, intervals with significant plasma acceleration were also observed. Between 5:00 and 6:00 UT SC1 observed three intervals with excellent Walen relation, excellent HT frame with significantly different HT velocity than that of the overall motion, and with plasma acceleration. In two of these cases the plasma acceleration was into the same direction as the motion of the overall boundary wave, and in the third case the plasma acceleration was into the opposite direction from the overall motion. SC1 and SC3 had the same boundary tangent direction during these first two intervals with accelerated

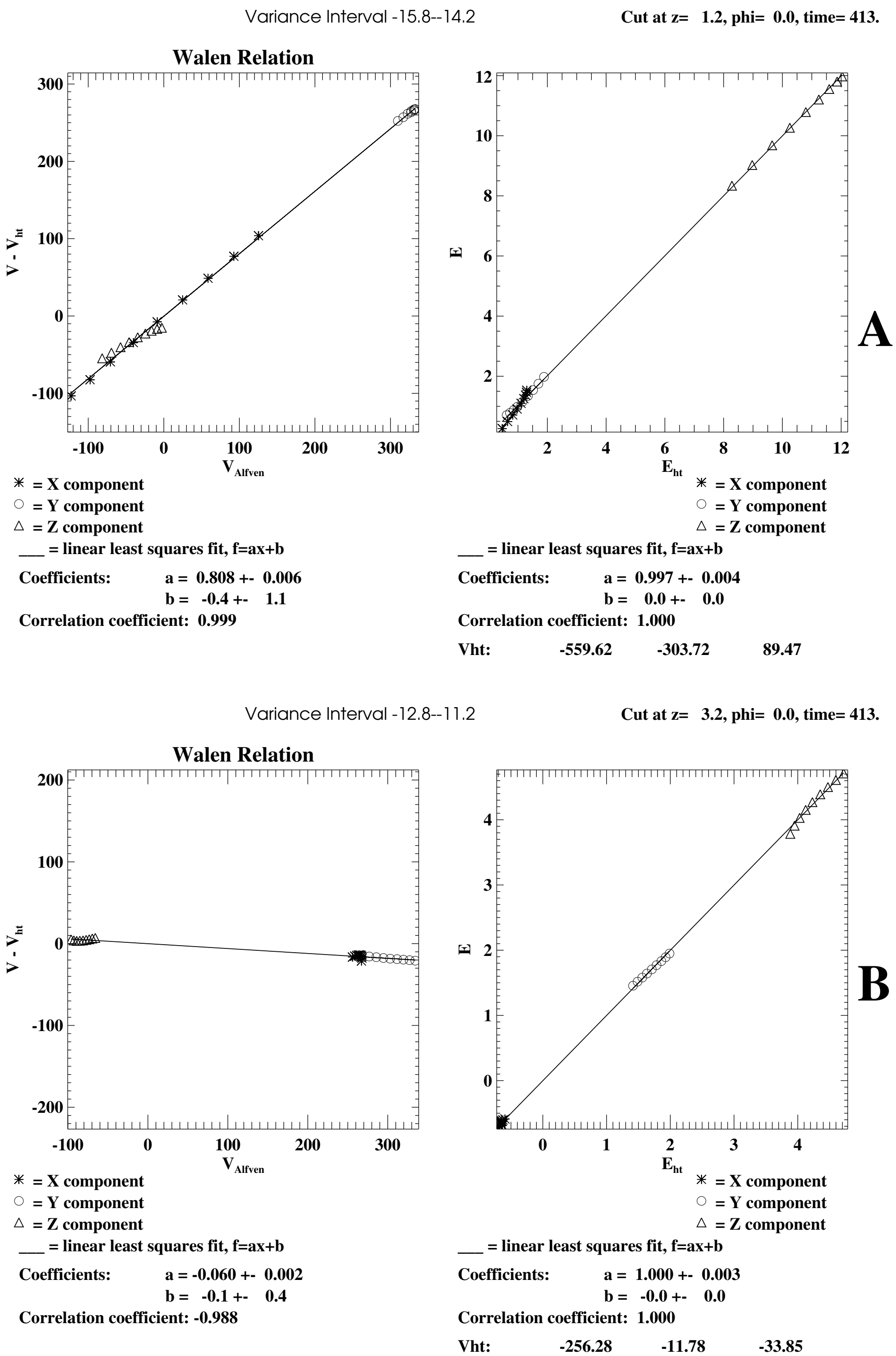

Figure 7.33. A) shows Walen relation and de HT frame measured by virtual spacecraft at $y = 1.2$ from $x = 14.2$ to $x = 15.8$. B) shows Walen relation and de HT frame measured by virtual spacecraft at $y = 3.2$ from $x = 11.2$ to $x = 12.8$.

HT velocity. SC3 was located downstream from SC1 along the tangent direction, observing the same outflow from the reconnection region as SC1, but with slightly reduced velocity. SC4 was located furthest in the negative y direction $\sim$ 1400 km from SC1 and SC3 and didn't observe these acceleration events. In the third case, SC1 observed a reduced HT frame with plasma acceleration into the opposite direction from the overall motion.

Since SC1 and SC4 were located approximately in same plane (same z-coordinate), I have compared their observations with 2-D MHD simulations. These simulation results agree with Cluster observations showing that the Walen relation is satisfied and the HT frame is obtained with a much higher transformation velocity when spacecraft see the outflow from the reconnection region into the same direction as where the overall boundary wave motion. The HT frame velocity is reduced from the overall velocity when the outflow from the reconnection region is to the opposite direction from the overall motion.

The ongoing reconnection in our simulation is observable at $t = 110\ \tau_A$, which corresponds to 407 seconds in physical units. If we assume that the KH-vortex velocity is $\sim$ 300 km/s, the wave has had to travel $\sim 19\ R_E$ downstream to grow nonlinear. This means that the source region for this wave is 19 R_E upstream from the Cluster location, close to the subsolar point at the dawnside magnetopause. The wavelength in the simulation is $\sim$ 6 R_E, so that the wave has undergone 3 oscillations before arriving to Cluster location. A wavelength of 6 R_E corresponds to a period of $\sim$ 2 minutes if we assume that KH-vortex moves with 300 km/s. This two minute period is observable in the Cluster magnetic field and velocity observations most clearly from 5:40 to 6:00 UT (Figure 7.16 and 7.28).

The rapid bipolar variation of the normal component of the magnetic field observable in Figure 7.28 is consistent with the Kelvin-Helmholtz instability [*Fairfield et al.*, 2000]. The flux transfer events, FTE's, are isolated events also with bipolar signatures of the magnetic field, but here the bipolar variations occurred between 5:00-6:00 UT in constant manner. In addition, the Walen relation and HT frame were not satisfied for 80 second periods which is typical for FTE's.

The large oscillations of boundary normals in z-direction indicate that the Kelvin-Helmholtz wave has a component of the **k**-vector along the z direction. This can be understood from the Parker-spiral IMF configuration, which is draped along the dawnside magnetospheric flank generating a negative B_x component which in turn might stabilize

KH modes in this direction, so that the fastest growing KH mode has a component of the **k** vector in z-direction.

Chapter 8

Summary and Discussion

During southward interplanetary magnetic field the plasma, momentum, and energy transport from the solar wind into the Earth's magnetosphere is well understood as reconnection at the subsolar point opens Earth's magnetic field. For northward IMF the mass transport into the Earth's plasma sheet has been a longstanding problem. The observations show that the plasma sheet gets filled with cold, dense solar wind material in about two hours during northward IMF conditions. While high latitude reconnection might provide some of this transport, no other processes efficient enough to provide diffusion coefficients of order of $\sim 10^9$ m^2/s has been suggested. The results in this thesis demonstrate that reconnection inside Kelvin-Helmholtz vortices can be the major plasma transport mechanism during northward IMF providing diffusion coefficients and plasma transport velocities consistent with the formation time of the cold, dense plasma sheet. In this chapter I will summarize the main results in this thesis and discuss the future work to be studied.

8.1 Results

The Kelvin-Helmholtz instability can be a major plasma transport mechanism from the solar wind into the magnetosphere during periods of northward IMF conditions. This plasma transport becomes possible when the KH vortex motion twists the magnetic field in the plane of the **k**-vector of the instability, which leads to the formation of strong current layers. The flow velocity in these narrow current layers is slower than the Alfvén speed, so that reconnection can detach a high density magnetic island from the solar wind. In this thesis I have quantified the associated plasma transport due to this process in two dimensions using MHD and Hall-MHD approximations. In addition I have analyzed Equator- S and Cluster satellite data in order to distinguish signatures of reconnection inside Kelvin-Helmholtz vortices and compared these results with MHD simulations. Ionospheric signatures due to the Kelvin-Helmholtz instability are also discussed.

8.1.1 Plasma Transport in KH Vortices in MHD Approximation

Mass entry velocities of $\sim$ 1.5 km/s

In Chapter 3 the plasma transport due to reconnection inside Kelvin-Helmholtz vortices was quantified in two dimensions. The influence of the different magnetic field strengths and resistivity was studied in 15 different simulations. For single wave modes the mass entry velocities were determined to be few km/s, starting from $\sim$ 2.5 km/s for small magnetic field values along the **k**-vector of the instability, and decreasing to zero km/s for very large magnetic field values due to the stabilization of the instability by the large magnetic field. The choice of resistivity didn't have influence on results since the reconnection inside KH vortices is strongly driven by the inertia of the vortex motion. Also the magnetic field asymmetry didn't have much effect on the net plasma transport.

Formation of the low latitude boundary layer, LLBL

The plasma transport velocities transformed to the corresponding diffusion coefficients of order $D = 10^9 \mathrm{m}^2\mathrm{s}^{-1}$ when a boundary layer thickness of 1000 km was assumed. A diffusion coefficient of this order is sufficient to generate the low latitude boundary layer. None of the previous models suggested for generating the LLBL could produce such a efficient mass transport as reconnection inside Kelvin-Helmholtz vortices. The Kelvin-Helmholtz instability should be almost entirely switched off or expect only small amplitude waves if any other processes cause strong diffusion and generate the LLBL. Therefore the presence of nonlinear KH waves with only slightly reduced growth rates indicates that for such times the KH is likely to be the dominant process for generating the LLBL.

Formation of the cold, dense plasma sheet during northward IMF

Assuming a mass diffusion velocity of 1.2 km/s, plasma sheet density of 1 cm^{-3}, solar wind density of 11 cm^{-3} and distance from the flank magnetopause to the plasma sheet of 15 R_E, the derived transport rates produce a plasma flux that is sufficient to re-populate the entire plasma sheet with magnetosheath material in about two hours if plasma enters from the dusk and dawn sides. This is consistent with observations of a typical correlation time between solar wind and plasma sheet properties.

8.1.2 Reconnection Inside KH Vortices in the Hall-MHD Approximation

In Chapter 4 the influence of the Hall term on reconnection inside Kelvin-Helmholtz vortices was studied using 17 different simulations. These were compared with corresponding MHD results.

Plasma transport

The net plasma transport remained unchanged from the MHD results, providing mass transport velocities of a few km/s. I studied this plasma transport also with a reduced system size, finding essentially no difference in plasma transport rates. In addition it was found that the density asymmetry across the initial shear flow boundary increases reconnection rates from the symmetric density case. However, the fine structure of the evolution of the Kelvin-Helmholtz vortex differed in an interesting way from the MHD dynamics.

Growth rates

The growth rates of the Kelvin-Helmholtz instability were found to be larger for the Hall-MHD approximation than for the MHD cases. This difference was the largest, ~ 20 %, for the most perpendicular ($\varphi = 3°$) configuration and approached those of the MHD results in the strongly parallel case. Naturally, for the small wave length case the growth rate was larger than for a longer wavelength case. The growth rates are larger for all the Hall-MHD cases compared to the corresponding MHD cases because in the Hall-MHD the magnetic field is frozen into the electrons and thus it doesn't stabilize the ion motion.

Formation of the B_z component

As the Kelvin-Helmholtz vortex evolves it generates narrow layers (with thickness close to ion inertia scale) with oppositely directed magnetic fields. In these narrow layers electrons react faster to the twisting of the magnetic field forming a strong electron current. Since the magnetic field is frozen into the electron fluid, the electrons will pull the magnetic field with them as they move generating an out-of-the-plane magnetic field component. If initially the out-of-the-plane magnetic field is zero and the density across the boundary is same, these electron motions generate a quadrupolar magnetic field structure between two reconnection reconnection points within the KH wave. While the influence of the Hall-term in magnetic reconnection has been studied widely, and compared with the MHD and particle simulations [*Birn and Hesse*, 2001; *Ma and Bhattacharjee*, 2001; *Pritchett*, 2001; *Otto*, 2001; *Birn et al.*, 2001], the results presented in this thesis are the first results of a small scale reconnection in a turbulent plasma.

Small scale turbulence

Small wave length turbulence with $\lambda \sim c/\omega_{pi}$ was observed for all φ, but the most clear, longest lasting structures were found for cases with $\varphi = 3°$ and $5°$. This turbulence didn't seem to inhibit the vortex formation but caused the decay of a smaller wavelength vortex in the larger system size ($ka = 0.12$) after the vortex was already fully formed. The small scale structure of this turbulence reveals that the ion current is negative in the regions of the higher density and positive in lower density regions. This small scale turbulence is formed in the regions where the electrons pull the magnetic field from the x, y-plane to the z-direction, such that this reduced magnetic field in the x, y-plane is destabilizing the KH instability on the scale of the ion inertia length.

8.1.3 Ionospheric Signatures of the Kelvin-Helmholtz Instability

Simulations of the KH instability in the magnetospheric inertial frame and mapping of the magnetospheric perturbations into the ionosphere indicate that during very northward IMF conditions the KH at the duskside magnetospheric flank will cause velocity perturbations in the ionosphere of order ~1.3 km/s. The corresponding magnetic field disturbances are of order ~ 200 nT corresponding to a field aligned current density of ~ 1.4 μA/m2. The vortex size of 1 $R_E \times 1.3$ R_E in the magnetosphere corresponds to a area of $\sim 70 \times 220$ km^2 in the ionosphere, which is in agreement with the size of the observed auroral bright spots. Also the location of these spots, in the post-noon sector from 13 to 16 MLT at latitudes of 75°-80°, is in agreement with magnetic field mapping of the KH instability from the Geotail location [*Fairfield et al.*, 2000; *Otto and Fairfield*, 2000] on March 24th, 1995, into the ionosphere. The estimated vortex speed in the ionosphere of 2.8 km/s is larger than observed, probably because the simulations don't take into account the finite travel time of the Alfvén waves.

8.1.4 Equator-S Observations of the Kelvin-Helmholtz Instability

Comparison of MHD simulations and Equator-S observations on March 10th, 1998, at the dawnside magnetospheric flank indicate that fluctuations in the data and boundary normal oscillations were due to multiple crossings of a current sheet twisted by the KH instability. Even though the signatures of flux transfer events and Kelvin-Helmholtz instability are similar it is possible to distinguish between these processes. The Walen relation is satisfied for ~ 80 seconds for reconnection cases whereas during reconnection inside Kelvin-Helmholtz vortices the Walen relation holds only for brief 10-35 seconds.

8.1.5 Cluster Observations of the Kelvin-Helmholtz Instability

On July 3rd, 2001, four Cluster satellites traversed along the dawnside magnetospheric flank and observed large variations in all plasma parameters. The boundary normals were oscillating in the z-direction and the Walen relation and de Hoffman Teller frames were satisfied only for brief 20-30 second intervals with different transformation velocities from the surrounding period. While some of these intervals satisfying the reconnection conditions were just Alfvén waves, intervals with plasma acceleration corresponding to the change in de Hoffman Teller frame velocity were also observed. Sometimes two of the Cluster setellites were able to see the same acceleration event when their boundary tangent directions were aligned. Plasma acceleration was observed both into the same direction of the overall motion of the boundary wave and into the opposite direction of the wave. This is consistent with two outflow streams from the reconnection regions embedded inside Kelvin-Helmholtz vortices.

Seeing plasma acceleration and the same deformation of the boundary with two satellites can hardly be a coincidence. Therefore I consider these Cluster observations of quasiperiodic plasma and field oscillations on 3rd of July, 2001 as a strong evidence of reconnection inside Kelvin-Helmholtz vortices. We also considered whether these signatures could be caused by flux transfer events, but they are more consistent with reconnection inside KH vortices, because the reconnection conditions were not satisfied for 80 seconds, which is a typical time scale for FTE's to satisfy the Walen relation. During this date the Geotail satellite traveled through the plasma sheet from the dusk side to the dawn side close to the equatorial plane. Geotail data should be studied in more detail for this date. An initial quick look seems to indicate a correlation of the ion temperature with the solar wind conditions, such that ion temperatures are decreased in few hours after the solar wind has turned northward. Unfortunately, the Geotail density data wasn't available.

8.2 Summary and Future Work

The Kelvin-Helmholtz instability is an ideal instability and as such not able to produce mass or magnetic flux transport across a plasma boundary. However, it has been shown that the Kelvin-Helmholtz instability can twist the magnetic field in the plane of the $\mathbf{k}$ -vector of the instability, leading to anti-parallel magnetic field components causing reconnection which will break this ideal picture. The 2-D MHD and Hall-MHD simulation results in this thesis indicate that during periods of northward IMF, the Kelvin-Helmholtz instability can be the major mass transport mechanism providing the source of plasma which is consistent with observations for both, the low latitude boundary layer and Earth's plasma sheet.

The presented two dimensional results are a necessary first step to understand the plasma transport associated with KH modes. In two dimensions we have assumed that the magnetospheric boundary is represented by the initial shear flow boundary. However, a 2-D model does not provide any information how magnetic field is connected in the third dimension which requires three-dimensional studies. In three dimension we expect the process to produce a more complex magnetic connection with a portion of the LLBL on open field lines and a portion on closed field lines.

Another interesting aspect for the KH mode is the stabilization of this mode by various conditions. First it is important to note that local criteria are generally not applicable because the KH mode is a convective instability and as such is modifying the very environment where it operates and where local stability analysis is considered. The stabilizing effects include magnetic field curvature, line tying to the ionosphere and formation of LLBL due to other processes which may cause diffusion, and the magnetic field component aligned with the magnetosheath flow. Any significant stabilization will lead to a lower growth rate and move the source region further upstream. Field line curvature would localize the region where the KH mode operates and three-dimensional effects will be significant if the transverse scale becomes comparable to the wavelength. The influence of the ionospheric line tying is unresolved. This has been considered in some 2D studies through an integration of the drag along field lines. However, the associated force is instantaneous while the real ionospheric feedback has a lag time.

It is interesting to consider the physical processes which can produce diffusion of the order of $D = 10^9\ \mathrm{m^2s^{-1}}$ to generate the LLBL. The simulation results in this thesis indicate that reconnection inside Kelvin-Helmholtz vortices is such a process providing a major source of plasma into the magnetosphere during northward interplanetary magnetic field. This is also an interesting consideration for numerical simulations. Numerical simulations depend on the presence of some diffusion to avoid large numerical dispersion errors when wavelengths approach the grid scale. This numerical diffusion is necessary to obtain physical results on scales larger than the grid scale. However, if the grid scale approaches the width of the boundary, numerical diffusion in global simulations can approach $D = 10^9 m^2 s^{-1}$ and can thus strongly damp the evolution of the KH mode. This is the likely reason why current global models rarely see the KH instability. High resolution simulations can overcome this problem and provide insight into the three-dimensional structure of the mode. Thus it would be an interesting task for global modelers to increase the resolution from their current resolution to 100 km/grid shell along the low latitude flanks as a goal to study the KH instability.

The highly interesting topic for future work is the mutual interaction of the Kelvin-Helmholtz instability and reconnection in the magnetospheric cusp regions. In view of the rich physics, it is surprising that there have been no self-consistent high resolution models of cusp physics. While the cusps are an intrinsic part of global simulations, the rather small-scale turbulence of these regions is not well represented by the global models, as they lack the required resolution. Global models focus mostly on the topological properties and the location of the cusps as a function of IMF orientation. The physics of the outer cusps require a proper understanding of several fundamental processes which control the transport at the magnetospheric boundary such as reconnection and Kelvin-Helmholtz instability. Cusps have been observed to be a considerable source for turbulence. The magnetic field in the immediate vicinity of the cusp is rather small. In a larger vicinity, the geomagnetic field converges to the cusp location such that the geomagnetic field close to the magnetopause rotates by 360 degrees in the vicinity of the cusp. Thus there are always two regions in which the IMF is parallel or anti-parallel to the geomagnetic field. In the general case, there is a velocity component perpendicular to the field in the two regions such that a KH wave with a **k**-vector approximately perpendicular to the magnetic field can be unstable in these regions. Flow vortex formation may also occur in the central cusp region, where the magnetic field is rather weak. In addition, tearing modes or magnetic reconnection may operate in the region with a large anti-parallel magnetic field components.

This thesis provides a necessary understanding of 2-D dynamics of the Kelvin-Helmholtz instability and reconnection inside Kelvin-Helmholtz vortices both in MHD and Hall -MHD approximations and these will be necessary tools for future studies of turbulence in the cusps. We have already started building of the axis-symmetric (i.e., symmetric with respect to the cusp axis) model used for the geomagnetic field of the initial configuration. The corresponding equation for the φ component of the vector potential is elliptic, and a two-dimensional elliptic solver is used to determine an appropriate solution. This initial state is two-dimensional in cylindrical and three-dimensional in Cartesian coordinates. Results in this thesis indicate that with help of four Cluster satellites it is possible to detect deformations of the boundary and find intervals with reconnection inside KH vortices. Our future cusp work will include the comparison between Cluster data of the cusp regions and compare these with the 3-D cusp magnetic field model. The automated search for intervals satisfying de Hoffman-Teller frames and the Walen relation saves an enormous amount of time to identify clear events, and in doing statistical analysis with the data. We expect also the Hall physics to play an important role in the cusp and will be considered in the future work.

The Kelvin-Helmholtz instability and reconnection are fundamental instabilities, so that understanding them well in the Earth's plasma environment will help us to understand their behavior everywhere in the universe where the ratios between magnetic field and plasma parameters are similar. In our solar system, differences in the intrinsic strengths of the planetary magnetic fields, different orientations of the dipole axes, and varying rotation periods of the planets generate vastly differing magnetospheric environments. Mercury's magnetosphere is very small compared to Earth's and the solar wind parameters at the location of Mercury are different from those at 1 AU. The study of the plasma transport into Mercury's magnetosphere can be carried out by choosing a proper length scale and magnetic field strength for its magnetopause. Jupiter's corotation velocity is about 1000 km/s and its magnetic moment is 20000 times larger than that of the Earth's! This high corotation speed would destabilize the Kelvin-Helmholtz instability at the dawn side flank. On the afternoon flank this could be a stabilizing effect by reducing the velocity shear. Thus the mass transport into the Jupiter's magnetosphere would be a highly asymmetric process with respect to the dawn and dusk side flanks of its magnetosphere. The reconnection inside the Kelvin-Helmholtz vortices could be a particularly important process for generating turbulence and transport at very large size astrophysical plasma boundaries. Here the large scale Kelvin-Helmholtz vortices can generate multiple current layers making magnetic reconnection more efficient compared to a reconnection at a single magnetic boundary. The reconnection inside the KH vortices may also be important in the heating of the solar corona, where the KH instability can generate thin current sheets in the regions where the shear flow is perpendicular to the coronal magnetic field. In addition, the reconnection inside in the KH vortices may be important in the applications of fusion plasmas by providing a source for efficient plasma mixing.

Appendix A

From Boltzmann Equation to MHD

The Boltzmann equation:

$$\frac{\partial f_\alpha}{\partial t} + \mathbf{v} \cdot \frac{\partial f_\alpha}{\partial \mathbf{r}} + \frac{q_\alpha}{m_\alpha}(\mathbf{E} + \mathbf{v} \times \mathbf{B}) \cdot \frac{\partial f_\alpha}{\partial \mathbf{v}} = (\frac{\partial f_\alpha}{\partial t})_c \tag{A.1}$$

The continuity equation:

$$\int (A.1) d^3v \rightarrow$$

$$\frac{\partial n_\alpha}{\partial t} + \nabla \cdot (n_\alpha \mathbf{V}_\alpha) = 0 \tag{A.2}$$

The momentum equation:

$$\int m_\alpha \mathbf{v} (A.1) d^3v \rightarrow$$

$$n_\alpha m_\alpha \frac{\partial \mathbf{V}_\alpha}{\partial t} + n_\alpha m_\alpha \mathbf{V}_\alpha \cdot \nabla \mathbf{V}_\alpha - n_\alpha q_\alpha (\mathbf{E} + \mathbf{V}_\alpha \times \mathbf{B}) + \nabla \cdot P_\alpha = m_\alpha \int \mathbf{v} (\frac{\partial f_\alpha}{\partial t})_c \tag{A.3}$$

The energy equation

$$\int \mathbf{vv}(A.1)d^3v \rightarrow$$

$$\frac{3}{2}n_\alpha k_B(\frac{\partial T_\alpha}{\partial t} + \mathbf{V}_\alpha \cdot \nabla T_\alpha) + p_\alpha \nabla \cdot \mathbf{V}_\alpha = -\nabla \cdot \mathbf{H}_\alpha - (P'_\alpha \cdot \nabla) \cdot \mathbf{V}_\alpha + \frac{\partial}{\partial t}(\frac{n_\alpha m_\alpha V_\alpha^2}{2})_c \quad (A.4)$$

Adding together the momentum equations of different species gives the total current transport equation, the generalized Ohm's law:

$$\sum_\alpha (\frac{q_\alpha}{m_\alpha}(A.3)) \rightarrow \qquad (A.5)$$

For electrons (e) and ions (i) this becomes:

$$\begin{aligned} \frac{\partial \mathbf{J}}{\partial t} + \nabla \cdot (\mathbf{VJ} + \mathbf{JV} + \mathbf{VV}\rho_\mathbf{q}) \quad &= \quad \sum_\alpha \frac{n_\alpha q_\alpha^2}{m_\alpha}\mathbf{E} + (\frac{\mathbf{e^2}}{\mathbf{m_e}} + \frac{\mathbf{e^2}}{\mathbf{m_i}})\frac{\rho_\mathbf{m}\mathbf{V} \times \mathbf{B}}{\mathbf{m_e} + \mathbf{m_i}} \\ &- \quad (\frac{em_i}{m_e} - \frac{em_e}{m_i})\frac{\mathbf{J} \times \mathbf{B}}{m_e + m_i} \\ &- \quad \frac{e}{m_e}\nabla \cdot (P_i^{CM}\frac{m_e}{m_i} - P_e^{CM}) \qquad (A.6) \\ &+ \quad \sum_\alpha \int q_\alpha \mathbf{v}(\frac{\partial f_\alpha}{\partial t})_c d^3v \end{aligned}$$

where

$$\rho_m(\mathbf{r}, \mathbf{t}) = \sum_\alpha \mathbf{n}_\alpha \mathbf{m}_\alpha \qquad (A.7)$$

$$\rho_m(\mathbf{r}, t) = \sum_\alpha n_\alpha q_\alpha = e(n_i - n_e) \qquad (A.8)$$

$$\mathbf{V}(\mathbf{r}, t) = \frac{\sum_\alpha n_\alpha m_\alpha \mathbf{V}_\alpha}{\sum_\alpha n_\alpha m_\alpha} \qquad (A.9)$$

$$\mathbf{J}(\mathbf{r}, t) = \sum_\alpha n_\alpha q_\alpha \mathbf{V}_\alpha \qquad (A.10)$$

$$P_\alpha^{CM}(\mathbf{r},t) = m_\alpha \int (\mathbf{v}-\mathbf{V})(\mathbf{v}-\mathbf{V}) f_\alpha d^3v \tag{A.11}$$

$$P_\alpha(\mathbf{r},t) = \sum_\alpha P_\alpha^{CM}(\mathbf{r},t) \tag{A.12}$$

MHD approximations

- assumption of average collision frequency $\sum_\alpha \int q_\alpha \mathbf{v}(\frac{\partial f_\alpha}{\partial t})_c d^3v = -\nu \mathbf{J}$

  where $\nu = \frac{ne^2}{\sigma m_e}$

- in macroscopic scales plasma is quasi neutral:

  $\nabla \cdot \mathbf{J} = 0$

- small perturbations in equilibrium:

  $\mathbf{VJ}, \mathbf{JV}, \mathbf{VV} \rightarrow 0$

- ions are much heavier than electrons:

  $\frac{m_e}{m_i} \rightarrow 0$

After these approximations we get the generalized Ohm's law into the form:

$$\mathbf{E} + \mathbf{V} \times \mathbf{B} = \frac{\mathbf{J}}{\sigma} + \frac{1}{ne}\mathbf{J} \times \mathbf{B} - \frac{1}{ne}\nabla \cdot P_e + \frac{m_e}{ne^2}\frac{\partial \mathbf{J}}{\partial t} \tag{A.13}$$

- As more terms are incorporated (progressing from left to right) more physics is included on smaller and smaller scales. The "frozen-in" condition of ideal MHD ($\mathbf{E} + \mathbf{V} \times \mathbf{B} = 0$) is broken at successively smaller scales.

- Terms from left to right are: resistive term, Hall term, electron pressure term, and electron inertial term.

Appendix B

Magnetic Field Frozen into the Electron Fluid

Far from the diffusion region we have $\eta = 0$, and Ohms' law for electrons and ions can be written:

$$\mathbf{E} + \mathbf{V} \times \mathbf{B} = \frac{1}{ne}\mathbf{J} \times \mathbf{B} \tag{B.1}$$

where $n = n_i = n_e$ and

$$\mathbf{V}(\mathbf{r}, t) = \frac{m_i \mathbf{v_i} + m_e \mathbf{v_e}}{m_i + m_e} \tag{B.2}$$

$$\mathbf{J}(\mathbf{r}, t) = ne(\mathbf{v_i} - \mathbf{v_e}) \tag{B.3}$$

Substituting these into Equation B.1 yields:

$$\mathbf{E} + (\frac{m_i}{m_i + m_e}\mathbf{v_i} + \frac{m_e}{m_e + m_i}\mathbf{v_e} - \mathbf{v_i} + \mathbf{v_e}) \times \mathbf{B} = \mathbf{0} \tag{B.4}$$

Ions are much heavier than electrons: $\frac{m_e}{m_i} \to 0$ and $m_e + m_i = m_i$, so that we get

$$\mathbf{E} + \mathbf{v_e} \times \mathbf{B} = \mathbf{0} \tag{B.5}$$

which indicates that the magnetic field is frozen into the electron fluid. This could have been done more elegantly starting from electron and ion momentum equations, adding them together and assuming same approximations as in Appendix A.

Bibliography

Axford, W. I., and C. O. Hines, A unifying theory of high latitude geophysical phenomena and geomagnetic storms, *Can. J. Phys.*, *39*, 1433, 1961.

Balogh, A., C. M. Carr, M. H. Acuna, M. W. Dunlop, T. J. Beek, P. Brown, and et. al., The Cluster magnetic field investigation: overview of in-flight perfomance and initial results, *Ann. Geophys.*, *19*, 1207, 2001.

Baumjohann, W., G. Haerendel, R. A. Treumann, T. M. Bauer, J. Rustenbach, E. Georgescu, U. Auster, K. H. Fornacon, K.-H. Glaßmeier, H. Lühr, J. Büchner, B. Nikutowski, A. Balogh, and S. W. H. Cowley, First ELF wave measurements with the EQUATOR-S magnetometer, *Adv. Space Res.*, *24*, 77, 1999.

Baumjohann, W. B., and R. A. Treumann, *Basic Space Plasma Physics*, Imperial College Press, London, 1997.

Birk, G. T., H. Wiechen, and A. Otto, Magnetic field amplification in M82 winds caused by Kelvin-Helmholtz modes, *Astrophys. J.*, *518*, 177, 1999.

Birn, J., Computer studies of the dynamical evolution of the geomagnetic tail, *J. Geophys. Res.*, *85*, 1214, 1980.

Birn, J., and M. Hesse, GEM magnetic reconnection challenge: Resistive tearing, anisotropic pressure and Hall effects, *J. Geophys. Res.*, *106*, 2001.

Birn, J., J. F. Drake, M. A. Shay, B. N. Rogers, R. E. Denton, M. Hesse, M. Kuznetsova, Z. W. Ma, A. Bhattacharjee, A. Otto, and P. L. Pritchett, Geospace Environment Modeling (GEM) magnetic reconnection challenge, *J. Geophys. Res.*, *106*, 3715, 2001.

Borovsky, J. E., M. F. Thomsen, and R. C. Elphic, The driving of the plasma sheet by the solar wind, *J. Geophys. Res.*, *103*, 17617, 1998.

Bristow, W. A., D. G. Sibeck, C. Jacquey, R. A. Greenwald, G. J. Sofko, T. Mukai, T. Yamamoto, S. Kokubun, T. J. Hughes, and M. J. Engebretson, Observations of convection vortices in the afternoon sector using the SuperDARN HF radars, *J. Geophys. Res.*, *100*, 19743, 1995.

Chandrasekhar, S., *Hydrodynamic and Hydromagnetic Stability*, Oxford Univ. Press, New York, 1961.

Chen, Q., Two- and three -dimensional study of the Kelvin-Helmholtz instability, magnetic reconnection and their mutual interaction at the magnetospheric boundary, *Ph.D Thesis, University of Alaska, Fairbanks*, 1997.

Chen, Q., A. Otto, and L. C. Lee, Tearing instability, Kelvin-Helmholtz instability, and magnetic reconnection, *J. Geophys. Res.*, *102*, 151, 1997.

Clauer, C. R., and A. J. Ridley, Ionospheric observations of magnetospheric low-latitude boundary layer waves on August 4, 1991, *J. Geophys. Res.*, *100*, 21873, 1995.

Clauer, C. R., M. A. McHenry, and E. Friis-Christensen, Observations of filamentary field-aligned current coupling between the magnetopsheric boundary layer and the ionosphere, *Geophysical Monograph*, *Physics of Magnetic Flux Ropes*, 565, 1990.

Clauer, C. R., A. J. Ridley, R. J. Sitar, H. J. Singer, A. S. Rodger, E. Friis-Christensen, and V. O. Papitashvili, Field line resonant pulsations associated with a strong dayside ionospheric shear convection flow reversal, *J. Geophys. Res.*, *102*, 4585, 1997.

Crooker, N. U., R. A. Greenwald, M. Hesse, M. K. Hudson, W. J. Hughes, L. R. Lyons, N. C. Maynard, C. T. Ryssel, and G. L. Siscoe, Report from the first geopspace environment modeling GEM campaigns: 1991-1997, p. cover, Space science center, IGPS, UCLA, 1999.

Drake, J., Magnetic reconnection: A kinetic treatment, in *Physics of the Magnetopause,* Geophys. Monogr. Ser., vol. 90, edited by P. Song et al., p. 155, AGU, Washington, D. C., 1995.

Dungey, J. W., Interplanetary magnetic field and the auroral zones, *Phys. Rev. Lett.*, *6*, 47, 1961.

Elphic, R. C., Multipoint observations of the magnetopause: Results from ISEE and AMPTE, *Adv. Space Res.*, *8*, 223, 1988.

Elphic, R. C., Observations of flux tranfer events: A review, in *Physics of the Magnetopause,* Geophys. Monogr. Ser., vol. 90, edited by P. Song et al., p. 225, AGU, Washington, D. C., 1995.

Escoubet, C. P., M. Fehringer, and M. Goldstein, The Cluster mission, *Ann. Geophys.*, *19*, 1197, 2001.

European Space Agency, Cluster Mission, *www.esa.int*, 2001.

Fairfield, D. H., and et al., Simultaneous measurements of magnetotail dynamics by IMP spacecraft, *J. Geophys. Res.*, *86*, 1396, 1981.

Fairfield, D. H., A. Otto, T. Mukai, S. Kokubun, R. P. Lepping, J. T. Steinberg, A. J. Lazarus, and T. Yamamoto, Geotail observations of the Kelvin-Helmholtz instability at the eqatorial magnetotail boundary for parallel northward fields, *J. Geophys. Res.*, *105*, 21159, 2000.

Fujimoto, M., and T. Terasawa, Ion inertia effect on the Kelvin-Helmholtz instability, *J. Geophys. Res.*, *96*, 15725, 1991.

Fujimoto, M., and T. Terasawa, Anomalous ion mixing within an MHD scale Kelvin-Helmholtz vortex, *J. Geophys. Res.*, *99*, 8601, 1994.

Fujimoto, M., and T. Terasawa, Anomalous ion mixing within an MHD scale Kelvin-Helmholtz vortex, 2, Effects of inhomogeneity, *J. Geophys. Res.*, *100*, 12025, 1995.

Fujimoto, M., T. Terasawa, T. Mukai, Y. Saito, T. Yamamoto, and S. Kokubun, Plasma entry from the flanks of the near-Earth magnetotail: Geotail observations, *J. Geophys. Res.*, *103*, 4391, 1998a.

Fujimoto, M., T. Mukai, A. Matsuoka, Y. Saito, H. Hayakawa, S. Kokubun, and R. P. Lepping, Plasma entry from the flanks of the near-Earth magnetotail: Geotail observations, *J. Geophys. Res.*, *103*, 4391, 1998b.

Hesse, M., J. Birn, and M. Kuznetsova, Collisionless magnetic reconnection: Electron processes and transport modeling, *J. Geophys. Res.*, *106*, 3721, 2001.

Huba, J. D., Hall dynamics of the Kelvin-Helmholtz instability, *Phys. Rev. Lett.*, *72*, 2033, 1994.

Huba, J. D., The Kelvin-Helmholtz instability: finite larmor radius magnetohydrodynamics, *Geophys. Res. Lett.*, *23*, 2907, 1996.

Kan, J. R., A globally integrated substorm model: Tail reconnection and magnetosphere-ionosphere coupling, *J. Geophys. Res.*, *103*, 11787, 1998.

Kaufmann, R. L., and A. Konradi, Explorer 12 magnetopause observations: Large-scale nonuniform motion, *J. Geophys. Res.*, *71*, 1481, 1969.

Keller, K. A., and R. L. Lysak, A two-dimensional simulation of Kelvin-Helmholtz instability with magnetic shear, *J. Geophys. Res.*, *104*, 25097, 1999.

Kistler, L. M., B. Klecker, V. K. Jordanova, E. Moebius, M. A. Popecki, D. Patel, J. A. H. Reme, A. M. DiLellis, A. Korth, M. McCarthy, R. Cerulli, M. B. Bavassano-Cattaneo, L. Eliasson, C. W. Carlson, G. K. Parks, G. Paschman, W. Baumjohann, and G. Haerendel, Testing electric field models using ring current ion energy spectra from the Equator-S composition (ESIC) instrument., *Ann. Geophys.*, *17*, 1611, 1999.

Kivelson, M. G., and C. T. Russel, *Introduction to space physics*, Cambridge University Press, New York, 1995.

La Belle-Hamer, A. L., Z. F. Fu, and L. C. Lee, A mechanism for patchy reconnection at the dayside magnetopause, *Geophys. Res. Lett.*, *15*, 152, 1988.

La Belle-Hamer, A. L., A. Otto, and L. C. Lee, Effects of sheared plasma flow on magnetic reconnection, in edited by T. Chang et al., *Physics of Space Plasmas (1993),* SPI Conference Proceedings and Reprint Series, Vol. 12, Scientific Publishers Inc., Cambridge, MA, 1995.

Lee, L. C., A review of magnetic reconnection: MHD models, in *Physics of the Magnetopause,* Geophys. Monogr. Ser., vol. 90, edited by P. Song et al., p. 139, AGU, Washington, D. C., 1995.

Lee, L. C., and Z. F. Fu, A theory of magnetic flux transfer at the Earth's magnetopause, *Geophys. Res. Lett.*, *12*, 105, 1985.

Lee, L. C., and Z. F. Fu, Multiple x-line reconnection, 1, a criterion for the transition from a single x-line to a multiple x-line reconnection, *J. Geophys. Res.*, *91*, 6807, 1986.

Lee, L. C., and J. V. Olson, Kelvin-Helmholtz instability and the variation of geomagnetic pulsation activity, *Geophys. Res. Lett.*, *7*, 777, 1980.

Lee, L. C., Z. W. Ma, Z. F. Fu, and A. Otto, Topology of magnetic flux ropes and formation of fossil flux transfer events and boundary layer plasmas, *J. Geophys. Res.*, *98*, 3943, 1993.

Lennartsson, W., A scenario for solar wind penetration of the Earth's magnetic tail based on ion composition data from the ISEE 1 spacecraft, *J. Geophys. Res.*, *97*, 19221, 1992.

Liu, Z. X., and Y. D. Hu, Local magnetic field reconnection caused by vortices in the flow field, *Geophys. Res. Lett.*, *15*, 752, 1988.

Lui, A. T. Y., D. Venkatesan, and J. S. Murphee, Auroral bright spots on the dayside oval, *J. Geophys. Res.*, *94*, 5515, 1989.

Ma, Z. W., and A. Bhattacharjee, Hall magnetohydrodynamic reconnection: The Geospace Environment Modeling (GEM) challenge, *J. Geophys. Res.*, *106*, 2001.

Ma, Z. W., A. Otto, and L. C. Lee, Core magnetic field enhancement in single x line, multiple x line and patchy reconnection, *J. Geophys. Res.*, *99*, 6125, 1994.

Ma, Z. W., L. C. Lee, and A. Otto, Generation of field-aligned currents and Alfvén waves by 3D magnetic reconnection, *Geophys. Res. Lett.*, *22*, 1737, 1995.

McHenry, M. A., and C. R. Clauer, Relationship of solar wind parameters to continuous, dayside, high latitude traveling ionospheric convection vortices, *J. Geophys. Res.*, *95*, 15007, 1990.

McHenry, M. A., C. R. Clauer, E. Friis-Christensen, P. T. Newell, and J. D. Kelly, Ground observations of magnetospheric boundary layer phenomena, *J. Geophys. Res.*, *95*, 14995, 1990.

Miura, A., Anomalous transport by magnetohydrodynamic Kelvin-Helmholtz instabilities in the solar wind magnetosphere interaction, *J. Geophys. Res.*, *89*, 801, 1984.

Miura, A., Simulation of the Kelvin-Helmholtz instability at the magnetospheric boundary, *J. Geophys. Res.*, *92*, 3195, 1987.

Miura, A., Kelvin-Helmholtz instability at the magnetospheric boundary: Dependence on the magnetosheath sonic Mach number, *J. Geophys. Res.*, *97*, 10655, 1992.

Miura, A., Kelvin-Helmholtz instability at the magnetopause: Computer simulation, in *Physics of the Magnetopause,* Geophys. Monogr. Ser., vol. 90, edited by P. Song et al., p. 285, AGU, Washington, D. C., 1995.

Miura, A., and P. L. Pritchett, Nonlocal stability analysis of the MHD Kelvin-Helmholtz instability in a compressible plasma, *J. Geophys. Res.*, *87*, 7431, 1982.

Nikutowski, B., J. Büchner, A. Otto, L. M. Kistler, C. Mouikis, G. Haerendel, and W. Baumjohann, Equator-S observations of reconnection coupled to surface waves, *Adv. Space Res.*, *In Press*, 2000.

Nykyri, K., and A. Otto, Plasma transport at the magnetospheric boundary due to reconnection in Kelvin-Helmholtz vortices, *Geophys. Res. Lett.*, *28*, 3565, 2001.

Nykyri, K., A. Otto, J. Büchner, B. Nikutowski, W. Baumjohann, L. M. Kistler, and C. Mouikis, Equator-S observations of boundary signatures: FTE's or Kelvin-Helmholtz waves?, *Geophysical Monograph*, *Chapman Conference on the Low Latitude Boundary Layer*, In press, 2002.

Ohtani, S., G. Rostoker, K. Takahashi, V. Angelopoulos, M. Nakamura, C. Waters, H. Singer, S. Kokobun, K. Tsuruda, W. J. Hughes, T. A. Potemra, L. J. Zanetti, J. B. Gary, A. T. Y. Lui, and D. J. Williams, Coordinated ISTP satellite and ground observations of morningside Pc5 waves, *J. Geophys. Res.*, *104*, 2381, 1999.

Olson, J. V., ULF signatures of polar cusp, *J. Geophys. Res.*, *91*, 10055, 1986.

Olson, J. V., and G. Rostoker, Longitudinal phase variations of P_c 4-5 micropulsations, *J. Geophys. Res.*, *83*, 2481, 1978.

Otto, A., The role of magnetic reconnection in magnetotail plasmoid dynamics, in *Reconnection in Space Plasma,* ESA SP-285 (Vol. II), edited by T. D. Guyenne and J. J. Hunt, p. 223, ESA, Noordwijk, Netherlands, 1989.

Otto, A., 3D resistive MHD computations of magnetospheric physics, *Comput. Phys. Commun.*, *59*, 185, 1990a.

Otto, A., Three-dimensional magnetic reconnection at the Earth's magnetopause, in *Plasma Astrophysics,*ESA SP-311, edited by T. D. Guyenne and J. J. Hunt, p. 57, ESA, Noordwijk, Netherlands, 1990b.

Otto, A., Three-dimensional MHD-computations of magnetic reconnection, in S. J. B. edited by H. K. Biernat and M. Heindler, *Plasma Theoretical Problems in Astro- and Fusion Physics*, p. 125, Austrian Academy of Sciences, 1992.

Otto, A., Forced three-dimensional magnetic reconnection due to linkage of magnetic flux tubes, *J. Geophys. Res.*, *100*, 11863, 1995a.

Otto, A., Magnetic reconnection at the magnetopause: A fundamental process and manifold properties, *Reviews of Geophysics*, *33*, 657, 1995b.

Otto, A., Properties of pressure pulses and magnetic reconnection at the dayside magnetopause, in *Physics of the Magnetopause,* Geophys. Monogr. Ser., vol. 90, edited by B.U.Ö. Sonnerup and P. Song, p. 303, AGU, Washington, D. C., 1995c.

Otto, A., Properties of two-and three-dimensional magnetic reconnection, *Physica Scripta*, *T74*, 9, 1998.

Otto, A., Geospace Environment Modeling (GEM) magnetic reconnection challenge: MHD and Hall MHD–constant and current dependent resistivity models, *J. Geophys. Res.*, *106*, 3751, 2001.

Otto, A., and U. Arendt, Numerical simulation of flux transfer events at the magnetopause - electron dynamics, *Advances in Space Research*, *11*, 129, 1991.

Otto, A., and D. H. Fairfield, Kelvin-Helmholtz instability at the magnetotail boundary: MHD simulation and comparison with Geotail observations, *J. Geophys. Res.*, *105*, 21175, 2000.

Otto, A., and K. Nykyri, Kelvin-Helmholtz instability and magnetic reconnection: Mass transport at the LLBL, *Geophysical Monograph*, *Chapman Conference on the Low Latitude Boundary Layer*, In press, 2002.

Otto, A., M. Hesse, and K. Schindler, General magnetic reconnection in 3-D systems, in *Topological Fluid Mechanics*, edited by H. K. Moffatt and A. Tsinober, p. 225, Cambridge University Press, Cambridge, UK, 1990.

Otto, A., L. C. Lee, and Z. W. Ma, Plasma and magnetic field properties associated with pressure pulses and magnetic reconnection at the dayside magnetopause, *J. Geophys. Res.*, *100*, 14895, 1995.

Potter, D. E., *Computational Physics*, John Wiley, New York, 1973.

Pritchett, P. L., Geospace Environment Modeling (GEM) magnetic reconnection challenge: Simulations with a full particle electromagnetic code, *J. Geophys. Res.*, *106*, 3783, 2001.

Rasinkangas, R., I. Usoskin, T. Ulich, R. Manninen, J. Jussila, and J. Manninen, Oulu space physics textbook, in *http://www.oulu.fi/ spaceweb/textbook/*, F. edited by University of Oulu, 1998.

Rème, H., C. Aoustin, J. M. Bosqued, I. Dandouras, B. Lavraud, J. A. Sauvaud, and et al., First multispacecraft ion measurements in and near the Earth's magnetosphere with the identical Cluster ion spectrometry (CIS) experiment, *Ann. Geophys.*, *19*, 1303, 2001.

Ridley, A. J., and C. R. Clauer, Characterization of the dynamic variations of the dayside high-latitude ionospheric convection reversal boundary and relationship to interplanetary magnetic field orientation, *J. Geophys. Res.*, *101*, 10919, 1996.

Russel, C. T., and R. C. Elphic, Initial ISEE magnetometer results: Magnetopause observations, *Space Sci. Rev.*, *22*, 681, 1978.

Schindler, K., Kinematics of magnetic reconnection in three dimensions, in *Physics of the Magnetopause,* Geophys. Monogr. Ser., vol. 90, edited by P. Song et al., p. 197, AGU, Washington, D. C., 1995.

Schindler, K., M. Hesse, M. Kiessling, and A. Otto, On magnetic reconnection and its consequences in magnetospheric tails, in *Proceedings of the International Conference of Plasma Physics*, edited by A. G. Sitenko, p. 772, World Scientific Publ. Co., Singapore, 1987.

Scholer, M., Magnetic flux transfer at the magnetopause based on single X line bursty reconnection, *Geophys. Res. Lett.*, *15*, 291, 1988.

Scholer, M., and A. Otto, Magnetotail reconnection - current diversion and field-aligned currents, *Geophys. Res. Lett.*, *18*, 733, 1991.

Scholer, M., and R. A. Treumann, The low-latitude boundary layer at the flanks of the magnetopause, *80*, 342, 1997.

Scholer, M., A. Otto, and G. Gadbois, Three-dimensional numerical simulations of magnetotail reconnection, in *Magnetic Substorms,* Geophys. Monogr. Ser., vol. 64, edited by T. Iijima et al., p. 171, AGU, Washington, D. C., 1991.

Schopper, R., and A. Otto, Reconnection in multiple current sheets, in *Astronomische Gesellschaft Meeting Abstracts*, vol. 15, p. 17, 1999.

Shay, M. A., J. F. Drake, B. N. Rogers, and R. E. Denton, Alfvénic collisionless magnetic reconnection and Hall term, *J. Geophys. Res.*, *106*, 3759, 2001.

Sibeck, D. G., Transient events in the outer magnetosphere: Boundary waves or FTEs?, *J. Geophys. Res.*, *97*, 4009, 1992.

Sibeck, D. G., and et. al., The magnetospheric response to 8-minute period, strong-amplitude upstream pressure variations, *J. Geophys. Res.*, *94*, 2505, 1989.

Sibeck, D. G., and M. F. Smith, Magnetospheric plasma flows associated with, boundary waves and flux transfer events, *Geophys. Res. Lett.*, *19*, 1903, 1992.

Song, P., and C. T. Russell, Model for the formation of the low-latitude boundary layer for strongly northward interplanetary magnetic field, *J. Geophys. Res.*, *97*, 1411, 1992.

Sonnerup, B. U. Ö., and M. Scheible, Minimum and maximum variance analysis, in *Analysis methods for multi-spacecraft data, ISSI Scientific Report*, edited by G. Paschmann and P. W. Daly, p. 185, The International Space Science Institute, Hallerstrasse 6, CH-3012 Bern, Switzerland, 1998.

Sonnerup, B. U. Ö., G. Paschmann, I. Papamastorakis, N. Sckopke, G. Haerendel, S. J. Bame, J. R. Asbridge, J. T. Gosling, and C. T. Russel, Evidence for magnetic reconnection at the earth's magnetopause, *J. Geophys. Res.*, *86*, 10049, 1981.

Sonnerup, B. U. Ö., G. Paschmann, and T.-D. Phan, Fluid aspects of reconnection at the magnetopause: In situ observations, in *Physics of the Magnetopause,* Geophys. Monogr. Ser., vol. 90, edited by P. Song et al., p. 167, AGU, Washington, D. C., 1995.

Terasawa, T., M. Fujimoto, H. Karimabadi, and N. Omidi, Anomalous ion mixing within a Kelvin-Helmholtz vortex in a collisionless plasma, *Phys. Rev. Lett.*, *68*, 2778, 1992.

Terasawa, T., M. Fujimoto, T. Mukai, I. Shinohara, Y. Saito, T. Yamamoto, S. Machida, S. Kokubun, A. J. Lazarus, J. T. Steinberg, and R. P. Lepping, Solar wind control of density and temperature in the near-Earth plasma sheet: WIND/Geotail collaboration, *Geophys. Res. Lett.*, *24*, 935, 1997.

Thomas, V. A., Three-dimensional kinetic simulation of the Kelvin-Helmholtz instability, *J. Geophys. Res.*, *100*, 19429, 1995.

Thomas, V. A., and D. Winske, Kinetic simulations of the Kelvin-Helmholtz instability at the magnetopause, *Geophys. Res. Lett.*, *18*, 1943, 1991.

Thomas, V. A., and D. Winske, Kinetic simulations of the Kelvin-Helmholtz instability at the magnetopause, *J. Geophys. Res.*, *98*, 11425, 1993.

Treumann, R. A., and W. B. Baumjohann, *Advanced Space Plasma Physics*, Imperial College Press, London, 1997.

Tsyganenko, N. A., Effects of the solar wind conditions on the global magnetospheric configuration as deduced from data-based field models, in *Proceedings of the ICS-3 Conference on substorms (Versailles, France May 12-17, 1996)*, p. 181, ESA SP-389, 1996.

Wei, C. Q., and L. C. Lee, Coupling of magnetopause-boundary layer to the polar ionosphere, *J. Geophys. Res.*, *98*, 5707, 1993.

Wiechen, H., J. Büchner, and A. Otto, Reconnection in a dipole-dominated magnetosphere: A two-dimensional model, *J. Geophys. Res.*, *100*, 19259, 1995.

Wiechen, H., J. Büchner, and A. Otto, Reconnection in the near-earth plasma sheet: A three-dimensional model, *J. Geophys. Res.*, *101*, 24911, 1996.

Wiechen, H., J. Büchner, and A. Otto, Driven reconnection in the near-earth plasma sheet, *Advances in Space Research*, *19*, 1939, 1997.

Wu, C. C., Kelvin-Helmholtz instability at the magnetopause boundary, *J. Geophys. Res.*, *91*, 3042, 1986.

Zhou, X.-Y., H. U. Frey, J. F. Watermann, B. T. Tsurutani, D. G. Sibeck, S. B. Mende, and J. K. Arballo, Dawn/dusk auroras and geomagnetic fluctuations: Ionospheric effects of intense solar wind ram pressure, *Geophysical Monograph*, *Chapman conference on the Low Latitude Boundary Layer*, In Press, 2002.